UNIVERSITY OF SOUTHAMPTON

Natural and Environmental Sciences

Ocean and Earth Science

Indian Ocean Dipole impacts on northwestern Indian Ocean climate variability

By

Kasem Elfadli

Thesis for the degree of Doctor of Philosophy

Dec 2015

UNIVERSITY OF SOUTHAMPTON

ABSTRACT

NATTURAL AND ENVIRONMENTAL SCIENCE

Ocean and Earth Science

Thesis for the degree of Doctor of Philosophy

INDIAN OCEAN DIPOLE IMPACTES ON NORTHWESTERN INDIAN OCEAN CLIMATE VARIABILITY

KASEM ELFADLI

The Indian Ocean Dipole (IOD) is a coupled ocean-atmosphere phenomenon in the equatorial Indian Ocean, with a positive mode characterized by anomalous warming of sea surface temperatures in the west and anomalous cooling in the east. The IOD has been shown to affect inter-annual variability of the Indian monsoon. There is also evidence that the IOD may affect the formation, strength and duration of monsoon-related oceanic features in the North West Indian Ocean (NWIO), including fronts and eddies, the Somali upwelling and the 'Great Whirl' system. However, the mechanism by which the IOD develops and details of its connection with monsoon-related oceanic phenomena in the NWIO remain unclear.

Satellite datasets of sea surface temperature anomalies (SSTA) and sea surface height anomalies (SSHA) over the past two decades have been examined, mainly to investigate the relationship between the IOD and large-scale climate modes like the Indian monsoon, El Niño Southern Oscillation (ENSO) and Rossby/Kelvin Waves. Early results show SSHA in NWIO; is more correlated with the IOD than with the ENSO. Also the results indicate an impact of Rossby wave patterns on the Somali Current system.

Standard Empirical Orthogonal Functions (EOF) and rotated EOF are applied for SSTA and SSHA at different spatial and temporal scales, to demonstrate the climate variability of the NWIO, a significant variability in late 1994 and 1997 is observed in the SSHA EOFs, which were strong positive IOD events. Also the EOFs indicate that the Somali Current and Great Whirl have the highest variability in the NWIO. The development of indices for the features of the Somali Current and the Great Whirl, to investigate their variability, is a key factor to see whether major climate mode indices like the IOD and ENSO are correlated with them.

Table of Contents

List of Tables

List of Figures

Acronyms

- Arabian Sea (AS).
- Climate Data Assimilation System 1 (CDAS1)
- Climate Prediction Center (CPC)
- Dipole Mode Index (DMI)
- Dissolved Inorganic Nitrogen (DIN)
- Earth Gravitational Model 1996 (EGM96)
- El Niño Southern Oscillation (ENSO)
- Empirical Orthogonal Functions (EOF)
- Expendable bathythermograph (XBT)
- Geographic Information System (GIS)
- Geophysical Fluid Dynamics Laboratory (GFDL)
- High Frequency (HF)
- Indian Ocean (IO)
- Indian Ocean Dipole (IOD)
- Inter-decadal Pacific Oscillation (IPO)
- International Comprehensive Ocean-Atmosphere Data Set (ICOADS)
- Intra-seasonal Variability's (ISVs)
- Joint Global Ocean Flux Study (JGOFS)
- Lamont-Doherty Earth Observatory (LDEO)
- Madden-Julian oscillations (MJO)
- National Centre for Environmental Prediction (NCEP)
- National Oceanic and Atmospheric Administration (NOAA)
- Negative IOD (nIOD)
- North Brazil Current (NBC)
- North Equatorial Current (NEC)
- North West Indian Ocean (NWIO)
- Positive IOD (pIOD)
- Quick Scatterometer (QuikSCAT)
- Reynolds and Smith Optimum Interpolation version 2 (Reyn_SmithOIv2)
- Sea level altitude (SLA)
- Sea level pressure (SLP)
- Sea Surface Height (SSH)
- Sea surface height anomalies (SSHA)
- Sea Surface Salinity Anomalies (SSSA)
- Sea Surface Temperature (SST)
- Sea surface temperature anomalies (SSTA)
- Southwest Monsoon Current (SWMC)
- Surface air temperature (SAT)
- Sverdrup (Sv)
- TOPEX/Poseidon (T/P)
- TRMM microwave imager (TMI)

DECLARATION OF AUTHORSHIP

I, **Kasem Elfadli**

Declare that this thesis and the work presented in it are my own and have been generated by me as the result of my own original research.

[Title of thesis] **Indian Ocean Dipole impacts on northwestern Indian Ocean climate variability**

I confirm that:

1. This work was done wholly or mainly while in candidature for a research degree at this University;
2. Where any part of this thesis has previously been submitted for a degree or any other qualification at this University or any other institution, this has been clearly stated;
3. Where I have consulted the published work of others, this is always clearly attributed;
4. Where I have quoted from the work of others, the source is always given. With the exception of such quotations, this thesis is entirely my own work;
5. I have acknowledged all main sources of help;
6. Where the thesis is based on work done by myself jointly with others, I have made clear exactly what was done by others and what I have contributed myself;
7. [Delete as appropriate] None of this work has been published before submission [or] Parts of this work have been published as: [please list references below]:

Signed: .....

Date: .....

1 Introduction

The complex nature of climatic and oceanographic phenomena in the Indian Ocean (IO) region have resulted in considerable debate in the scientific community, regarding its climate variability and potential response to future climate change. The interconnected nature of the Indian Ocean Dipole (IOD) and the El Nino Southern Oscillation (ENSO) have implications for modelling and predicting recurrent and anomalous events over time in both the Indian and Pacific Oceans. For this reason additional research is needed to understand connections between these systems and improve prediction of their future behavior. The emergence of more reliable satellite data and a broadening spectrum of analytical tools provide an opportunity to advance research in this field. This study will extend existing knowledge through the analysis of IOD anomalies over the past two decades.

The IOD is a coupled ocean-atmosphere phenomenon whereby a 'positive (negative) IOD is characterized by low (high) SST anomalies in the southeastern equatorial Indian Ocean (90°-110°E, 0°-10°S) and high (low) SST anomalies in the western equatorial Indian Ocean (50°-70°E, 10°N-10°S). Saji et al., (1999) narrate the following description of the dipole mode response:

> Cool SST anomalies first appear in the vicinity of the Lombok strait by May-June, accompanied by moderate southeasterly wind anomalies in the southeastern tropical Indian Ocean. In the following months, the cold anomalies intensify and appear to migrate towards the Equator along the Indonesian coastline, while the western tropical Indian Ocean begins to warm up. Zonal wind anomalies along the Equator and alongshore wind anomalies off Sumatra intensify together with the SST dipole then a dramatically rapid peak in October. In spite of its relative consistency and seasonal patterning, the IOD continues to spark widespread interest amongst researchers as empirical and theoretical studies struggle to establish a more constant pattern of variability and predictability.

The developing mechanism of the IOD and details of its connection with monsoon-related oceanic phenomena in the NWIO remain unclear. Little is known about its interaction with the Somali upwelling, the 'Great Whirl', Socotra Gyre system, the formation and movement of eddies in the NWIO, and seasonally variable circulation patterns in the Arabian Sea. A strong Somali-Oman upwelling is known to restrict the westward extent of the Indian Ocean warm pool, which is the main moisture source for Indian monsoon rainfall. Conversely, decreases in upwelling caused by anomalously weak southwesterly winds lead to increased sea surface temperature (SST) and may be linked to warm SW Indian Ocean.

This research aims to explore the IOD interaction with oceanographic phenomena in northwest Indian Ocean through visual and statistical analysis of available satellite data. In particular, although satellite data are widely used to address geospatial relationships associated with oceanic phenomena, this study will incorporate a multivariate exploration of such key variables as sea surface temperature anomalies (SSTA) and sea surface height anomalies (SSHA). Capturing the distinctive and interrelated principal components of these key variables will provide insight into distinctive conditions and features associated with this unique dipole. Through a comprehensive exploration of previous studies, the literature review shows that many researchers have tried to correlate the impact of the IOD on the landmasses surrounding the Indian Ocean, yet a study of the climate mode impact on features like the Somali Current system, is lacking and needed to better understand the climate variability of such features.

The research has the following objectives:

- To identify the impact of the interannual variability associated with the Indian Ocean monsoon on key climatic conditions including the Somali upwelling, the Great Whirl, hot and cold eddies, and seasonally variable circulation patterns in the Arabian Sea.
- To identify links between key climate phenomena occurring in NWIO and IOD behaviour and oceanic circulation patterning.
- To draw correlations between the IOD and NWIO climate variability in order to highlight interactivity, conditional optimisation, and impact potential.

Much of the variability in the region is likely to be linked to monsoonal or ENSO influences. Accordingly, before this research explores links between oceanographic variability in the NWIO and IOD events, the research will address the relationship between the IOD and such large-scale climate modes like the monsoon, ENSO and even Rossby/Kelvin waves. If anomalous behaviour linked to the IOD can be separated from responses to ENSO or to the monsoonal cycle, it may be possible to quantify the relationship between climate variability in NWIO and positive IOD events.

The IOD has been shown to affect interannual variability of the Indian monsoon and rainfall patterns in Indonesia, Western Australia, Kenya and the Horn of Africa (Marchant et al., 2007). There is also evidence that the IOD may affect the formation, strength and duration of monsoon-related oceanic fronts in the western Indian Ocean (Nagar et al., 2005). It is therefore important to characterize potential impacts of the IOD on the climate and oceanography of the region.

The following hypothesis will be tested:

- Independent of ENSO-related moments and events, the Indian Ocean and its interannual monsoonal forces propagate a dipole mode, which is characterised by distinct oceanic (internal) and climatic (external) features that may be understood through time series analysis of satellite data.

There is a broad range of research questions associated with the problematic and complex climatic features of the NWIO, some of them are proposed as follows:

- What is the interannual climate variability of monsoon-related phenomena in the NWIO?
- If the IOD has an effect on the interannual climate variability over the NWIO, then how does that influence the formation, strength and duration of monsoon-related phenomena in the NWIO such as the Somali Current and upwelling, and the formation and movement of eddies (the 'Great Whirl' – Socotra Gyre system); is there any correlation between the IOD and the climate variability of these phenomena?

2 Scientific Background

2.1 Introduction

In tropical climates away from the equator, annual precipitation is high; however, there is usually a wet and a dry season. Some tropical locations are prone to monsoonal affects, or inter-annual climatic variations in which rainfall and weather patterns increase to a more extreme degree. Often, areas of tropical climates with wet and dry seasons are characterised by savannah areas between wet tropical and drier subtropical locations. Particular locations featuring this seasonal variation include the southern Mexican Pacific coast, Venezuela, Brazil, the African Savannah regions, India, Southeast Asia, and northern Australia. The tropical monsoon climates record the greatest wet-to-dry precipitation features and are most prevalent on the African tropical west coast and tropical Southeast Asia. In some locations, precipitation during the wet season amounts to more than 5,000 millimetres. The tropical monsoon climates occur where there are seasonal changes in the surface heating of the land and the oceans. During the season when more solar energy is directed over the oceans, dry air flows over the land toward the ocean, where convection occurs and the land areas remain dry. When the season changes and more solar energy is directed over the land surface, the winds shift and bring moisture from the ocean surface over the land, where convection and precipitation occur (Tomczak and Godfrey, 2003).

The Indian Ocean is different from the Atlantic and Pacific Oceans in several ways. The first and probably the largest difference is the seasonal reversal of the monsoon winds and its effects on the ocean currents. This is due mainly to the presence of the Indian subcontinent with its hot subtropical climate just north of the Indian Ocean, unlike the other two Oceans, which extend into the temperate zone north of the equator and lack the presence of a large land mass. The Indian Ocean is also the smallest of the three, which is another distinction leading to heavy consequences for the circulation and hydrology.

The following sections emphasise a broad spectrum of research oriented towards the distinct climatologic and geographic phenomena associated with the Indian Ocean. Although this particular investigation focuses on the dipole and the influence of climate change, the research in this field is diverse and for this reason, a range of empirical studies have been evaluated and incorporated into this review.

The high degree of methodological variability was considered an important factor in the design and development of the particular research methods employed in this study. Particular phenomena are investigated including SST variations, air-sea fluxes, the IOD, circulatory variations,. The findings from particular studies introduced in the subsequent sections have influenced the scope and focal points of the current empirical investigation. One priority of this research is to identify within the research focus of leading theorists and empiricists, demonstrating areas in which significant gaps and methodological complications have resulted in a need for a more comprehensive, contributory study.

2.2 Northwest Indian Ocean and the Monsoon

Two marginal seas influence the properties of northwestern Indian Ocean and Arabian Sea water masses. The Persian Gulf is the smaller of the two with a mean depth of 25 m and a maximum depth of only 90 m. The other is the Red Sea, which has a deep basin with maximum depths of around 2740m and a mean depth of about 490 m.

A monsoonal climate dominates the northern Indian Ocean, The Northeast or Winter Monsoon (Figure 1) determines the climate of the northern Indian Ocean during the northern hemisphere winter (December–March). It is characterized by high pressure over the Asian land mass and northeasterly winds over the tropics and northern subtropics. Since most of the air pressure gradient is retained behind the Tibetian Plateau, air pressure gradients over the ocean are small. This protects the ocean from the full force of the winds blowing off the Mongolian high-pressure region and results in a wind of moderate strength. The wind also carries dry air, and the Winter Monsoon season is the dry season for most of southern Asia.

The Southwest or Summer Monsoon (Figure 2) dominates the climate of the northern Indian Ocean during the northern hemisphere summer (June–September). A deep heat low develops over Pakistan and extends west to northern Arabia. Whereas during the winter monsoon the north-south pressure difference from Arabia to Madagascar barely exceeds 6hPa, there is now a difference of 22hPa acting in the opposite direction. As a result the winds in the northern Indian Ocean reverse completely and are no longer like the Trade winds elsewhere.

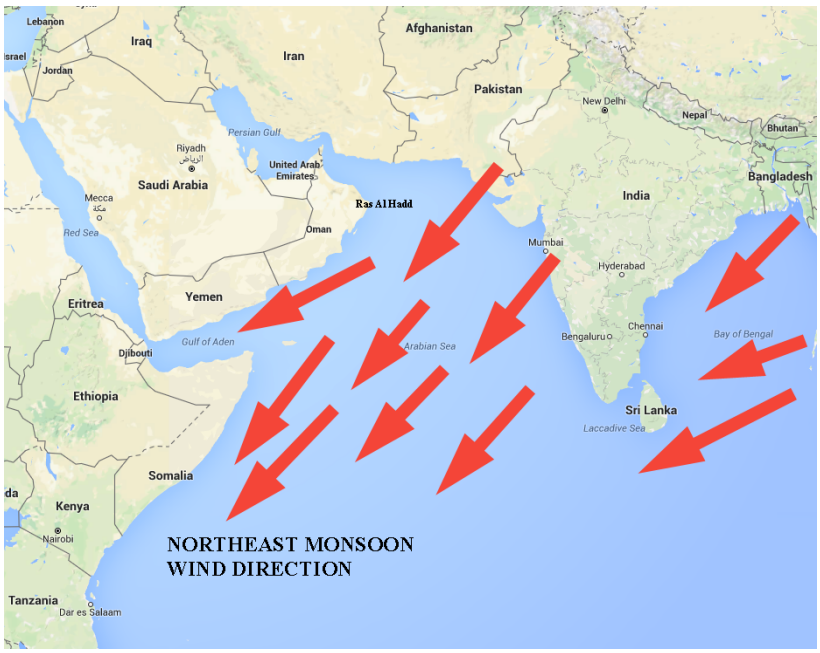

Figure 1 Northeast Monsoon wind direction that determines the climate of the northern Indian Ocean during the northern hemisphere winter (December–March).

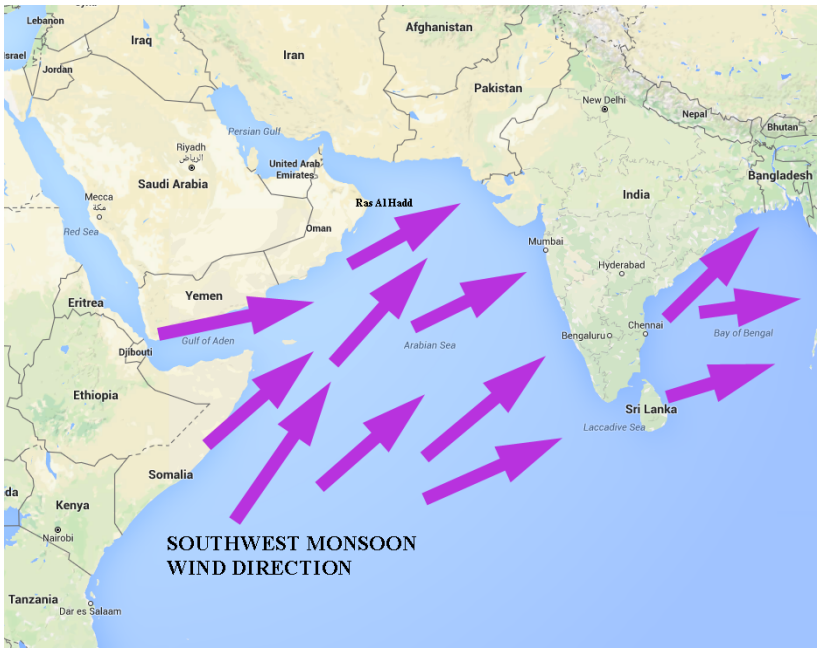

Figure 2 Southwest Monsoon wind direction that dominates the climate of the northern Indian Ocean during the northern hemisphere summer (June–September).

The Southwest Monsoon, as this wind is called in the northern hemisphere, is the continuation of the southern hemisphere Trades, which between 10° and 20°S are strong during this time of year. The Southwest Monsoon deposits rain on the Himalayas, thus bringing with it the monsoon rains and floods that are so crucial to Asian agriculture.

The most striking characteristic of the rainfall distribution over the Indian Ocean is the difference between the eastern and western regions in the north. Annual mean precipitation varies between 10 cm per year in the west (on the Arabian coast) and 300 cm per year or more in the east (near Sumatra). This is the opposite of the situation usually encountered in the subtropics, where the Trades bring dry continental air out over the sea in the east and rain to the western coast. The usual situation of little rain in the east and high rainfall in the west prevails in the southern Indian Ocean; Western Australia receives less than 50 cm per year but Madagascar some 200 cm per year. The monsoonal influence is restricted to the surface mixed layer and the western boundary currents; the distribution of hydrological properties in the Indian Ocean is much less affected by the seasonal monsoon cycle than the near-surface current field (Tomczak and Godfrey, 2003). The two most important factors which, make the Indian Ocean different from that of the other oceans, are the closure of the Indian Ocean in the northern subtropics and the blocking effect of the equatorial current system (Figure 3) for the spreading of water masses in the thermocline (Tomczak and Godfrey, 2003).

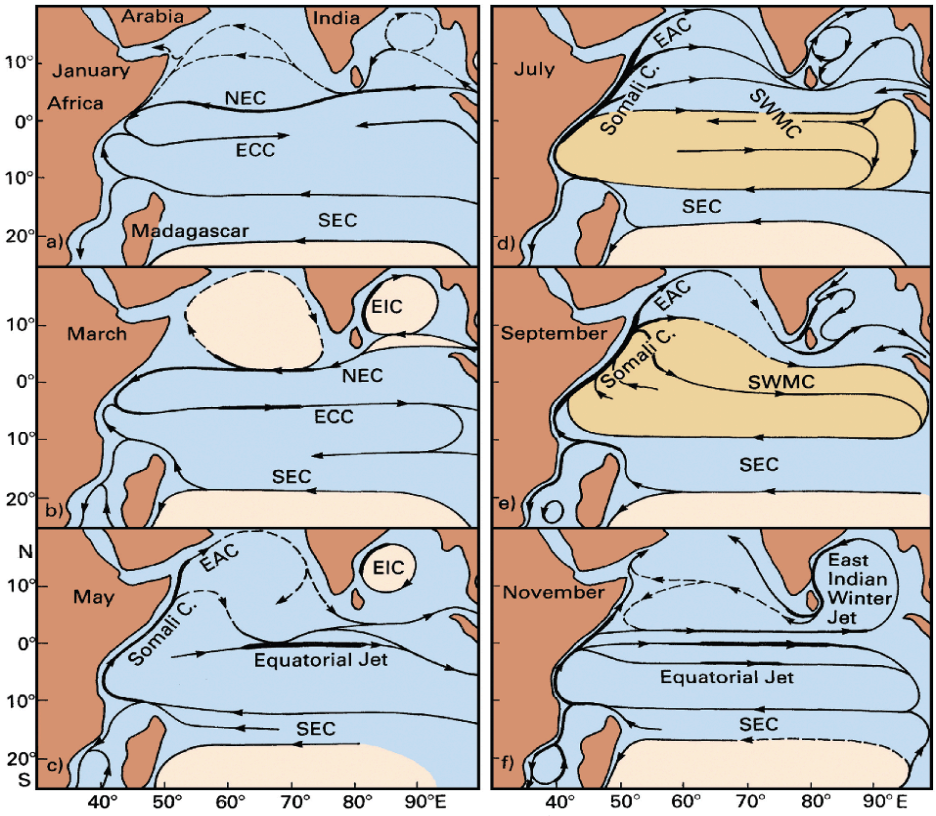

Figure 3 Surface currents in the northern IO as derived from ship drift data with the yellow colour referring to the gyre created by the current. SEC: South Equatorial Current, NEC: North Equatorial Current, ECC: Equatorial Countercurrent, SWMC: Southwest Monsoon Current, EAC: East Arabian Current and EIC: East Indian Current (Tomczak and Godfrey, 2003).

2.2.1 Monsoon Related Phenomena

The Indian summer monsoon is the most dominant mode of variability in the Indian Ocean. Wind values are at a maximum in the western Arabian Sea with the southeast trade wind extending north of the equator in the summer months. The strongest winds occur off the coast of Somalia, in association with the Findlater Jet (Findlater et al., 1969). Monsoon-related phenomena need to be explored to understand the variability in this region.

The following sections offer an overview of past research studies findings regarding the Somali Current, Great Whirl gyre, Arabian Sea and the dipole mode. This research introduces a range of phenomena that are linked to both seasonal periodicity and oceanic features. These findings demonstrate the importance of climatologic assessments of this region, particularly in relation to the departure from what is normal, which is manifest as a result of particular influences.

2.2.1.1 Somali Current

A key component of the circulatory dynamic in the Arabian Sea and Indian Ocean, the Somali Current has been widely researched in relation to the influence of its SST and cooling behaviour. In order to evaluate the possibility of upwelling and a distinct variance between surface-air temperatures and the cooling properties of this current, (Beal and Chereskin, 2003) used empirical evidence from one of the earliest periods of satellite record, the 1995 monsoon season. Through targeted temporal-spatial analysis, the authors studied the propagation and effects of the Somali Current during the monsoonal seasons of June-September. Their results differed from more widely recorded conditions, in June, highlighting a lack of current transport during this period and instead the presence of a shallow, anticyclonic eddy (the Great Whirl). In spite of these new findings, the authors concluded that their evidence was merely an indication of a high degree of transient variability in the Somali Current transport with a 20-30 day periodicity (Beal and Chereskin, 2003).

In the summer monsoon phase transports can exceed 70 Sverdrup (Sv) (Shankar et al., 2002). During this time, the Somali Current flows generally northward along the coast. Finally, at the end of the Southwest monsoon season the Somali Current turns offshore at 2-3°S. During this time of the year, the flow continues to propagate northward; however, its strength is reduced significantly. During the winter northeast monsoon season, the winds blow southward away from the Indian subcontinent.

Due to this reversal of the wind pattern, the Somali Current also reverses its flow towards the south. During the winter, the southward flowing cross-equatorial Somali Current meets the northward flowing East African Coastal Current (EACC) in a confluence at about 2-4°S. Then, both flows lead into the eastward flowing South Equatorial Counter Current. At the equator, the southward Somali Current is shallow, carrying 5 Sv in the upper 150 m. This shallow penetration depth has been attributed to a northward undercurrent flowing during this time frame. Winds in the Indian Ocean blow from the southwest during May-September (summer monsoon) and from the northeast during November-March (winter monsoon) (Shankar et al., 2002). This cyclical wind action has a direct influence on the coastal currents, which can be explored through satellite-based remote sensing techniques. Shankar et al. (2002) highlight the characteristics of these seasonally reversing currents (particularly those in the Arabian Sea), describing both spatial variability and a seasonally anomalous depth of gyre movement. Recognising that there are divided opinions regarding the cause of this reversing current pattern, Shankar et al. (2002) realised that additional observation and analysis was needed in order to determine if the current movement are related to the monsoonal winds or the result of slow moving Rossby waves. Through a comprehensive analysis of satellite datasets, the authors concluded that both Ekman drift, 'estimated from climatological wind stress, and surface geostrophic currents contribute to the net surface current (Shankar et al., 2002).

2.2.1.2 Great Whirl and Socotra Eddies

The Great Whirl is defined by Wirth et al. (2002) as a 'large anti-cyclonic eddy that develops every year after the onset of the summer monsoon causing substantial upwelling along the coast of Africa and also transporting and mixing the cold upwelled water eastward into the interior Arabian Sea. Specifically, the Great Whirl develops during the onset of the monsoon in June in the 4-10°N latitude range, with a second cold wedge (Socotra Gyre) at 10-12°N (Wirth et al., 2002). During the summer monsoon, the Great Whirl operates as a relatively closed circulation cell, limiting the exchange between the offshore recirculation branch and the interior Arabian Sea (Wirth et al., 2002). In spite of best efforts to classify the formation of the Great Whirl, Wirth et al. (2002) show that as a direct result of localised, anti-cyclonic eddies, and the lifecycle formation of this event is extremely turbulent and unpredictable. Through temporal analysis of both internal and external characteristics, the authors propose that internally caused variability decreases the predictability of this event and limits our ability to simulate actual oceanic dynamics.

Although such conclusions may be realistic given the authors' particular methodological restrictions, they are not indicative of consensus and therefore require additional investigation and discussion. Subrahmanyam and Robinson (2000) recognise that the number of eddies formed in the Arabian Sea each year 'could be an indicator of the strength of the monsoon', potentially providing quantifiable evidence of distinct monsoonal activity. They also suggest that in this particular region Kelvin and Rossby waves that are triggered through monsoonal activities lead to the growth of eddies in the western boundary currents, directly affecting the sea temperature throughout the region. The existence of a two large, semi-permanent eddies in the western tropical Indian Ocean has been observed in numerous regional field expeditions. The Great Whirl and the Socotra Gyre, located respectively to the south and southeast of Socotra Island, have re-circulating transports of the order of 50 Sv (Schott et al., 1997).

Both in-situ and remote observations indicate that these eddy features evolve over time, but occur in approximately the same location each year. These eddies are transient features with an identifiable formation event, a measurable westward translation speed, and an assumed decay mechanism. In the western tropical Atlantic, a similar physical mechanism results in the formation of anticyclonic rings from the retroflecting North Brazil Current (NBC) (Barber et al., 2001). Unlike NBC rings that are thought to play a significant role in the inter-gyre transport of mass and tracers, the Somali Current rings are effectively trapped in the Gulf of Aden; however, the rings may provide considerable regional impacts (figure 3).

2.2.1.3 Arabian Sea Circulation Pattern

The Arabian Sea is bounded by India (to the east), Iran (to the north), and the Arabian Peninsula (in the west). The Gulf of Oman is located in the northwest corner of the Arabian Sea. The continental shelf in the region is widest off the northwest coast of India which experiences wind-induced upwelling. The circulation of the Arabian Sea is affected by the Northeast and Southwest monsoon seasons. The dynamics and thermodynamics of the surface layer of the Arabian Sea, north of about 10°N, are dominated by the monsoon-related annual cycle of air-sea fluxes of momentum and heat. The currents in the open sea regime of this layer can largely be accounted for by Ekman drift and the thermal field is dominated by local heat fluxes.

The geostrophic currents in the open sea subsurface regime are represented by a seasonal cycle, where there is evidence to suggest that this cycle penetrates as deep as 1000 m. The forcing due to Ekman suction is an important mechanism for the geostrophic currents in the central and western parts of the Arabian Sea (Tomczak and Godfrey, 2003).

In the North Arabian Sea, there is a broad eastward flow during the summer monsoon across the entire latitude range of the Arabian Sea. Research such as Schott and McCreary (2001) have observed the presence of a Laccadive Low off the southwest tip of India during the summer Monsoon season. By October, the circulation of the Laccadive Low is clearly identifiable along the southwestern tip of India moving in an anti-clockwise direction. During this time of year, the South Equatorial Countercurrent (SECC) has started flowing eastward almost along the equator. The southwest monsoon current flows eastward along the southern tip of India. As part of the Joint Global Ocean Flux Study (JGOFS), for the years 1994 and 1996, the North Arabian Sea was studied in detail.

In the JGOFS study during the summer monsoon, it was observed that a northeastward coastal jet develops along the south coast of Oman in early May and persists throughout the summer months (Arabian Sea Process Study report, JGOFS). This jet flows past Ras al Hadd at the southeast corner of Oman and then maintains course into the Gulf of Oman. As explained by Flagg and Kim (1998), this jet has been linked to an anticyclonic gyre just south of its offshore turning point and a cyclonic gyre to its north.

During the winter circulation pattern in the North Arabian Sea, a basin-wide clockwise gyre and weak easterly currents (along the northern coast) can be identified. In the southern regions of the sea, westerly currents similar to those in the Northern regions can be identified. In January and April, the western current of the Gulf of Oman north of Ras al Hadd is comparatively weak as observed by Flagg and Kim (1998). The SECC is flowing eastward and the northeast monsoon current is flowing in the westerly direction. In general, during the winter monsoon, the characteristic flow is westward. Shi et al. (2000) also explained that this westward flow is accompanied by downwelling along the coast and an offshore-directed pressure gradient. Further offshore, a mesoscale eddy along the equator at 71°E can be identified, rotating in an anti-clockwise direction. As the winter northeast monsoon dies down in April, the general circulation pattern is still the same in the northern Arabian Sea with some weak westward flow (Shi et al., 2000).

The circulation in the coastal region off Oman is driven primarily by local winds and there is no remotely driven western boundary current. Local wind forcing is also important to the coastal circulation off Western India during the southwest monsoon; but not during the northeast monsoon when a strong current moves poleward against weak winds (Shi et al., 2000). This current is driven by a pressure gradient that forms along this coast during the northeast monsoon due to either thermohaline-forcing or the arrival of Kelvin waves from the Bay of Bengal.

The dramatic change in forcing over the Arabian Sea leads to an equally dramatic response in the basin's western boundary current, the Somali Current. During the Southwest (SW) monsoon, the northward flowing Somali Current has a strong transport of 65 Sv, mostly confined to the upper 200 m, and reported currents up to 2 m/s (Shi et al., 2000). During the NE monsoon, the surface current is southwards, but is weaker and more diffuse. During the SW monsoon, this dynamic current system gives rise to a strong mesoscale eddy field, which has been reported around the basin from the Somali coast to Pakistan. The southwesterly winds during the summer monsoon also lead to upwelling along the coast of Oman (Shi et al., 2000).

The resultant forces include persistent jets and streams of cold, upwelled water that extend from the capes along the Omani coast, often extending far into the interior. These phenomena have been observed in satellite SST images, as well as surveyed by SeaSoar, an open ocean towed data acquisition vehicle (Shi et al., 2000). During the Northeast (NE) monsoon, Bruce et al. (1994) reported the persistent formation of a large anticyclonic eddy in the eastern Arabian Sea, with a subsequent westward propagation and decay. The mean current system and in particular, the strong mesoscale eddy field developed primarily during the SW monsoon, playing an important role in the upper ocean evolution. While affected by these large-scale circulatory patterns, the upper ocean has a more direct observable response to the wind in the form of Ekman transport convergences and divergences. Especially during the southwest monsoon, the effects of Ekman pumping can be seen in shallow mixed layers, on the order of 20-50 m, and high biological productivity to the north and west of the Findlater Jet, and in deep mixed layers down to 100 m, to the south and east with reduced biological productivity. Bauer et al. (1991) found that Ekman pumping plays a first order role in the evolution of the mixed layer and productivity, during both the NE and SW monsoons.

2.3 Geochemical Patterning and IO Variability

The study of various phenomena in the IO has expanded rapidly over the most recent decade as technological modelling advances have explored distinct and variable climatologic phenomena. Wiggert et al. (2006), for example, applied a profile-based Geographic Information System (GIS) mapping technique to time series modelling of biogeochemical variance across monsoon patterns in the Indian Ocean. Localising their research to the Bay of Bengal and the Arabian Sea, empirical data gathered from a range of expert sources were divided into phenomenological components (chlorophyll concentration, phytoplankton concentration, etc.) and modelled according to geo-spatial sectors over a yearlong time frame. The value of this particular research model is obvious, as Wiggert et al. (2006) were able to identify periodic bloom phenomena and causally link them to monsoonal forcing, the initial objective of their particular study. In addition to these targeted, hypothesised findings, the authors also modelled current movement including the Great Whirl and the Southern Gyre to demonstrate seasonal variability, biological responses, and the associated summer bloom. Ultimately, the modelling of causal links between current, monsoon, and nutrient patterns effectively demonstrated spatial heterogeneity and seasonal evolution of the diverse, localised ecosystems.

There are other similar studies that have been conducted in the IO in recent years in order to model the biochemical variance associated with monsoonal patterning and hydrospatial characteristics (e.g. cold core eddies, etc.). Thompson et al. (2007), for example, recognised that cold core eddies lead to an increased standing stock of chlorophyll and physical concentration of phytoplankton is recognised as causally linked to the injection of dissolved inorganic nitrogen (DIN), whilst warm core eddies are characterised by low primary rates of phytoplankton production and a reduced standing stock of chlorophyll. Through fluorometric analysis of physical samples from the IO region, the authors endeavoured to identify phenomenological anomalies that arise as a result of current patterns and mesoscale eddies. The results indicated that formative influences including cold and warm current eddy movement patterns had direct influence on the nutrient availability for phytoplankton sustenance, causing persistent stratification of organic concentration.

Yet Thompson et al. (2007) also reported that, given the influence of a variation of sinking rates, differential growth associated with light and nutrients, and differential growth due to grazing pressures, simulation models may fail in their ability to distinguish between key phenomena, attributing movement observations to inaccurate features and occurrences. These findings are indicative of the methodological uncertainty of an extensive variability amongst mapping techniques and analytical tools. Recognising the fundamental role, which the geography of the coast of Java and Sumatra plays in the tropical Indian Ocean Dipole mode, Andruleit (2007) conducted an empirical analysis of the coastal upwelling region through comprehensive field studies. Based on monsoonal-linked response of phytoplankton groups in this region, and built upon previous recognition of the surface water conditions associated with algae blooms and behaviour, concentration levels were measured and compared.

Particular research methods employed in this investigation involved the capture and analysis of abundance levels from particular geographic regions with recorded surface temperature phenomena (Andruleit, 2007). Cluster analysis and quantification was correlated with seasonal variations and evolving environmental conditions over time in order to mirror the seasonality and compositional variations associated with these organisms (Andruleit, 2007). For the current study, the practical application of these modelling techniques has valuable implications for the design of comparative methods for climate-related phenomena.

2.4 SST, Height, and Circulation Anomalies

Monsoonal variability and its impact are cited and discussed in many research studies. Specifically, Kantha et al. (2008) reports that 'progress in understanding the fundamental physical processes underlying the variability of the monsoonal circulation of the Indian Ocean has been hamstrung by the sparse in situ observations'. Yet emergent satellite datasets from TOPEX/Poseidon (T/P) and Jason 1 imaging have provided baseline evidence for comparison of time series evidence regarding Indian Ocean events, circulatory anomalies, and SST characteristics. Testing the value and reliability of these datasets through hindcast analysis Kantha et al. (2008) demonstrated a positive correlation between statistical tests and in situ observations that validated these techniques for more widespread applications in future modelling. In particular, however, Kantha et al. (2008) reported weaker current representation and underestimates regarding various wind stresses than expected.

Citing distinctive influences including the equatorial waveguide (disturbances trapped in the vicinity of the equator) and the coastal waveguide (disturbances trapped along the coast), the authors suggested that regional anomalies are not only distinct, but they are indicative of unique localised conditions. Further, local changes in conditions are communicated to the eastern boundary by equatorial Kelvin waves and to the western boundary by equatorial Rossby waves (Kantha et al., 2008). Unique to this region are strong monsoon currents that 'transport mass, heat, and salt across the basin in a narrow meridional channel', characteristics that can be represented through hindcasting; however, only on a descriptive level (Kantha et al., 2008). Accordingly although this research methodology is valuable for identifying anomalies, the underlying dynamic causes of these climatological and geographical phenomena cannot be properly modelled through such data-limited research techniques.

Intra-annual SST variability is recognised by Subrahmanyam et al. (2011) as particularly 'interesting in the equatorial Indian Ocean wherein anomalous cooling occurs by October-November off the Sumatra coast in the eastern Equatorial Indian Ocean (EIO) and warming occurs in the western/central EIO, a phenomenon widely known (e.g. Saji et al., 1999) as the positive IOD event'. In spite of what the authors recognise as a large and growing literature base emphasising temperature measurements and variations, they suggest that salinity observations are not only sparse and temporally distant, but there are no existing satellite salinity measurements to use for spatio-temporal analysis.

Using the limited evidence available from the 506 active Argo floats in the Indian Ocean today, salinity and temperature vertical profile data were captured at 10-day intervals (Subrahmanyam et al., 2011). The findings revealed evidence of through flow variations that contribute to advection of low salinity waters and a large negative sea surface salinity anomalies (SSSA) (freshening), findings that describe a linear trend fitted to the intra-annual variation of salinity profiles in particular geographic regions of the Indian Ocean. The research methods employed demonstrate that in spite of evidential limitations, in this field, emergent technology and measurement tools continue to advance phenomenological research regarding a broad spectrum of causal and event-associated variables.

2.5 Climatological Influences and Indian Ocean Perturbations

Madden-Julian oscillations (MJO) have been widely researched in academia in relation to the Pacific Ocean and other related climatological phenomena. Discovered by Madden and Julian (1971), Wang (2006) reports that these oscillations were initially detected in tropical wind and surface pressure data, later to be validated through satellite imaging and various observational studies. In a recent study conducted by Zhou and Murtugudde (2010) in the Indian Ocean, these oscillations have been linked to intraseasonal variabilities (ISVs) due to atmospheric forcing and internal oceanic instabilities. The authors defined their related MJO events according to the MJO index, a phenomenological development that characterises eastward-propagating events (westward propagating events are independent). The MJO forces are identified through depth and temperature comparisons, wherein the authors recognise that 'coherent SST anomalies in the two phases indicate that the MJO influence on the SST anomalies in the maritime continent is not solely dominated by surface heat fluxes but also oceanic processes' (Zhou and Murtugudde, 2010).

Zhou and Murtugudde (2010) findings are derived from satellite and mooring observations, demonstrating how ISVs are the direct response to the different phases of the MJOs responsible for atmospheric intraseasonal forcing. This study is valuable because it documents a causal link between MJO-related low frequency variations and the evolution of the Indian Ocean dipole; however, Zhou and Murtugudde (2010) emphasise that the complexity of long series analysis limits the definitive linkage between these phenomena without additional research and data review.

One key component of the modern analysis of IO phenomena and perturbations is based on advanced methods, particularly those that are afforded by more diverse spectral imaging via satellite technologies. Manghnani et al. (2002) exploited the T/P reports in a study of heat transports throughout the IO region in order to demonstrate the predictive nature of this climatic feature. The authors recognise that 'satellite altimetry, with its abundant spatiotemporal coverage of the ocean provides an excellent opportunity to study the heat propagation' (Manghnani et al., 2002). Accordingly, the researchers employed several key objectives including a comprehensive test of the validity of sea level altitude (SLA) data from T/P altimetry for time series modelling of heat content anomalies over the Indian Ocean, an assessment of the hydrosphere heat budget, and an analysis of spatio-temporal variability in oceanic heat transports (Manghnani et al., 2002).

The formation of low and high-pressure regions in the IO is greatly influenced by the atmospheric Rossby waves, which was first identified in 1939 by Carl-Gustaf Rossby and is characterised as 'large, slow moving planetary scale waves, which manifest in the troposphere due to orographic forcing as well as temperature contrasts between the land-ocean atmosphere' (Murty, 2011). In a baroclinic atmosphere, Murty (2011) reminds that Rossby waves have been found to 'owe their existence to the isentropic gradient, which is an idealized thermodynamic process that is adiabatic, of potential vorticity and are a potential vorticity conserving motion'. It is for this fundamental reason that the Rossby wave is considered one of the most significant measures of meteorological phenomena.

This study has particular relevance to this investigation, as it demonstrates a unique variable resolution mapping technique relating to an enhanced resolution study of the Indian Ocean heat transport over time. Feature based comparison and validation studies indicated that T/P-derived heat content anomalies could be used on a larger scale in order to study variability in the Indian Ocean. Further, the evidence demonstrates monsoonal variability in this region, whilst simultaneously arguing that atmospheric-induced oceanic heat gain plays a secondary role to ocean dynamics in redistribution of heat content. Practical applications of satellite imaging technologies focus on predictability and the unique characteristics associated with the IOD and zonal gradient of SST across the equatorial Indian Ocean (Wajsowicz, 2005). Of priority for such studies is the ability to predict such severe phenomena as extreme flooding or severe drought in relation to coupled ocean-atmosphere phenomena.

To test this theory, Wajsowicz (2005) explores extreme IOD events over a century-long time period, attempting to derive a canonical event as defined by a composite image of the individual events. Such analysis allows the researcher to evaluate particular anomalies in relationship to their regional influences, drawing correlations that could serve as benchmark characteristics for more predictive future models. The results of this empirical study indicated that due to the well-defined signature of the SST associated with an extreme positive event and the role of the subsurface ocean processes in its evolution and decay, a one to two season predictive model could be effectively developed (Wajsowicz, 2005). As a result of this study, the author was able to determine that current datasets regarding subsurface real time reports were largely limited, restricting the validity of such analysis and presenting particular methodological challenges that need to be resolved in future analyses through integration of TOPEX or JASON altimetry readings with subsurface Argo data.

The Indonesian throughflow is a key phenomenon associated with a tropical cyclonic gyre in the South Indian Ocean, which ultimately discharges waters into the eastern Atlantic via the Agulhas retroflection (Matano et al., 2008). As a direct result of the exchange and geostrophic circulation of the gyres in the IO, Matano et al. (2008) recognise that in order to understand the particularities associated with interocean exchanges, the processes which control this variability must be explored and defined more specifically. Comprehensive satellite imaging of seasonal variabilities between the tropical and subtropical Inter-decadal Pacific Oscillation (IPO) was conducted in order to describe the net impact of the Indonesian throughflow in comparison with wind stress forcing (Matano et al., 2008). One key test, which was performed in this analysis, was an altimeter-based harmonic analysis of sea surface elevation wherein predictive modelling of this temporal-spatial phenomenon was then compared with satellite observations in order to validate the accuracy of the model. The results from this particular study provide an important confirmation of findings from early controversial theorists such as Saji et al. (1999), as throughflow variability was determined to have only minimal influence on the easternmost portion of the basin, whilst wind stress forcing was important across the entirety of the IO. For this reason, eddy anomalies and recirculation cells could be described as key factors in seasonal variations in the Mozambique Channel (MC), findings that contravene any arguments that throughflow variability was responsible for these anomalies (Matano et al., 2008).

2.6 Indian Ocean Dipole Mode

In the tropical Indian Ocean a pattern of internal variability exists independently of ENSO. The spatial/temporal pattern is termed the IOD mode. First discovered by Saji et al. (1999), its distinguishing characteristics are anomalously low sea surface temperatures off Sumatra and high sea surface temperatures in the western Indian Ocean, the spatial anomalies are coupled with anomalous precipitation and wind patterns through ocean-atmospheric dynamics (Ashok et al., 2004). IOD is an inter-annual phenomenon occurring in the tropical parts of the Indian Ocean. It is represented by the zonal dipole structure of various coupled ocean-atmosphere parameters such as SST, wind, surface pressure and SSH anomalies. The strength of the IOD is largest in the boreal autumn months with a typical peak in October.

Like other climate oscillations the IOD climate mode also has a 'positive' and a 'negative' phase (Figure 4). The positive dipole mode is characterized in part by warm (SST) anomalies in the western Indian Ocean and cold SST anomalies in the eastern Indian Ocean (Saji et al., 1999). The SST anomalies are accompanied by easterly wind anomalies in the equatorial Indian Ocean and upwelling-favorable alongshore wind anomalies off Sumatra.

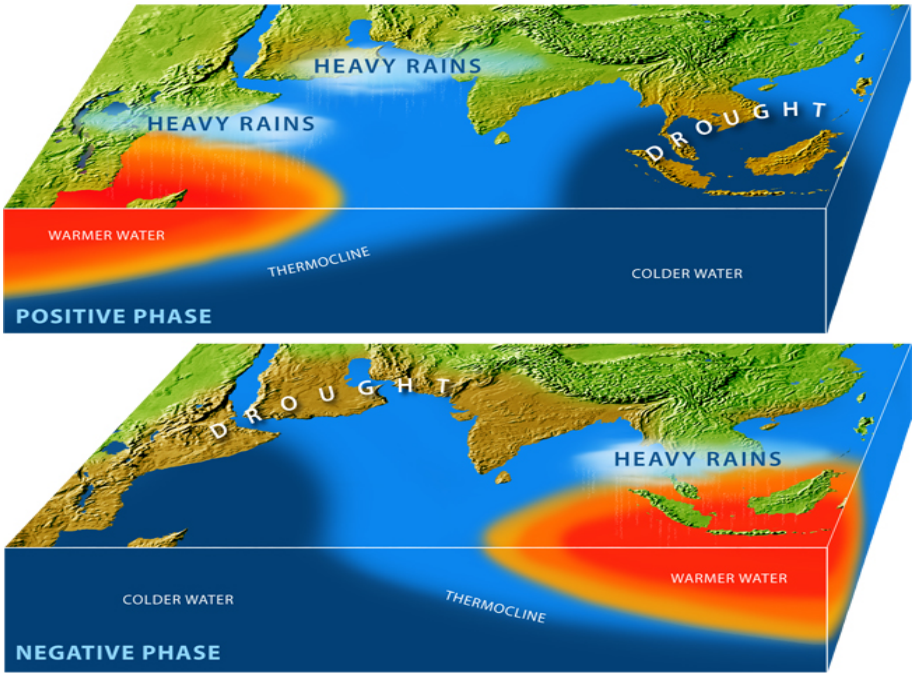

Figure 4 Positive phase of IOD mode with warm SST anomalies in the western Indian Ocean and cold SST anomalies in the eastern Indian Ocean and the negative phase of IOD mode with a reversed pattern. Illustration by E. Paul Oberlander, Woods Hole Oceanographic Institution

The positive IOD leads to droughts in Indonesia, enhanced monsoonal rainfall over India, and increased East African rainfall. The pattern reverses during a negative dipole mode event. The negative phase is much weaker than the positive phase and is sometimes referred to as a normal phase. Westerly wind anomalies in the northern Indian Ocean are the dominant feature in the negative IOD event. In a negative IOD, the increased rainfall over East Africa and India is suppressed with typical monsoon conditions prevailing, and heavy rainfall over Indonesia. The Indian Ocean Dipole peaks in autumn and is an important mode of interannual variability at that season in the Indian Ocean. Interestingly, it does not seem to influence rainfall during the following summer monsoon where the correlation is 0.03 with the IOD index, As already discussed, late spring SST/precipitation anomalies in the southwest Indian Ocean can influence summer SSTs and monsoon through changes in Somalia–Oman upwelling.

The IOD events is represented by the Dipole Mode Index (DMI) shown in Figure 5, which is defined as the zonal difference of SST anomaly between the tropical western Indian Ocean and the southeastern Indian Ocean.

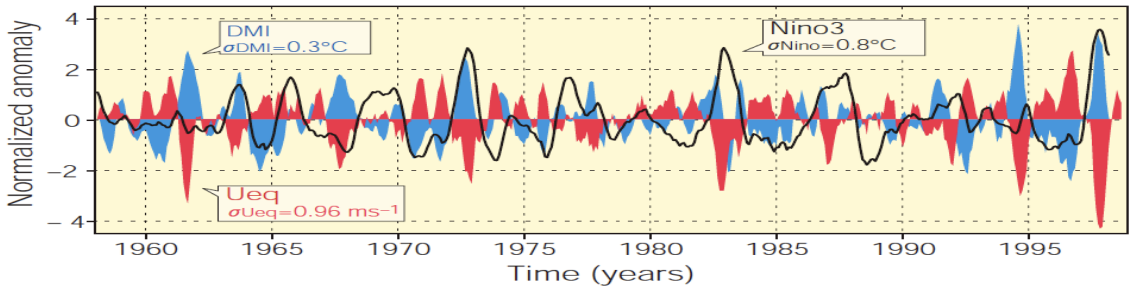

Figure 5 Dipole mode index (DMI), equatorial zonal wind anomalies (Ueq), and the Nino3.4 SSTA (Saji et al., 1999)

The late spring anomalies are mostly caused by westward propagation of oceanic equatorial Rossby waves. The Rossby waves generated by an Indian Ocean Dipole in fall are closer to the equator and propagate much faster (c~10°/month at 5°S) than those generated by ENSO in winter (c~3–4°/month at 10°S. Thus, the oceanic Rossby waves generated by IOD variability impact southwest Indian Ocean conditions only in winter and early spring and cannot influence Indian rainfall the following summer. During its developing phase in summer the IOD is somewhat correlated to the West Indian monsoon rainfall in the same period (corr: +0.38 in JJA). However, this correlation is mostly due to the western pole of the IOD index (corr: +0.40), whereas the correlation between the IOD eastern pole and the West Indian monsoon rainfall is insignificant (r = 0.14) (Izumo et al., 2008).

Webster et al., 1999 confirmed these findings, suggesting that in spite of previous arguments that forcing phenomena such as El Nino or the Southern Oscillation were the cause of the coupled climate variability in the Indian Ocean, empirical evidence was demonstrative of an internal mode directly linked to a self-contained Indian Ocean climate system. By choosing specific dates from a 40-year span, Webster et al. (1999) were able to compare events, identifying any particularities that might be attributed to links between ENSO and the Indian Ocean Dipole. Accordingly, phenomenological variability served to identify particularities that could not be sufficiently explained by historic reasoning based on ENSO effects; instead, suggesting that the Indian Ocean 'exhibits strong coupled ocean-atmosphere-land interactions that are self-maintaining, and are capable of producing significant perturbations to the annual cycle (Webster et al., 1999).

Saji et al. (1999) proposed that as a direct result of changes in SST throughout the region, the dipole mode is strongly dependent on monsoonal circulation, a relationship that could not be explicitly defined by this research. Ultimately, however, these two studies would serve as baseline stimuli for additional investigation and analysis relating to this dipole phenomenon. Basing their research on the Webster et al. (1999) and Saji et al. (1999) evidence, Vinayachandran et al. (2002) endeavoured to prove or disprove the dipole phenomenon through exploration of dipole mode events using 'an ocean general circulation model forced by National Centre for Environmental Prediction (NCEP) reanalysis fluxes for more than 25 years. As a subcomponent of signature analysis, the authors also included the role of Rossby waves in this analytical model.

Analysis of dipole mode anomalies revealed that positive events occurred during 1994 and 1997, whilst negative anomalies occurred during 1996. The cooling of the Eastern IO during the positive phases is governed by oceanic processes (upwelling and advection), whilst during the negative dipole mode events, the warming is attributed to net surface heat flux (Vinayachandran et al., 2002). Within this analysis, the authors also recognise that both Kelvin and Rossby waves play important roles on the seasonal and thermodynamics of the Indian Ocean, contributing to warming, and possibly altering the thermal structure of the Indian Ocean from more normal seasonal patterns (Vinayachandran et al., 2002). Conclusions from the empirical study results reveal that the positive dipole mode is characterised by cold SST anomalies in the eastern equatorial Indian Ocean and warm SST anomalies in the west, with a shallower thermocline in the eastern IO and deeper in the west. Characterised through visual analysis of satellite data and statistical correlations, these findings indicate surface depth fluxes and upwelling characteristics that are further influenced by Kelvin and Rossby wave propagation.

Continuing the evolutionary interpretation of the IOD events Saji et al. (2005) completed another evaluation of these anomalies in order to draw correlation between surface air temperature (SAT) anomalies and IOD events. The particular methodologies employed during this later study are valuable from a modelling perspective, as they are designed to exclude climate variability that was previously identified in relation to ENSO (Saji et al., 2005). Partial correlation analysis was employed in order to control the effect of a second independent variable on the relation between two other dependent variables, incorporating a correlation coefficient to indicate the strength and direction of the relation between the independent and dependent variables (Saji et al., 2005).

Remarkably, the authors were able to demonstrate how land temperatures over the southern hemisphere were anomalously warm during positive IOD events (SST is cool and convection suppressed over eastern western equatorial IO) (Saji et al., 2005). Quantitatively, the partial correlation coefficient attributes anomalies to the activities of the IOD, whilst simultaneous evaluation of possible correlation with El Nino events was determined to be insignificant. Generalisation of this association suggests that positive IOD events are associated with warm anomalies and negative IOD events with cool anomalies over the southern hemisphere regions (Saji et al., 2005). These statistical findings suggest a teleconnection between IOD events and SAT anomalies, the result of which is a possible IOD role in climate variability across Southern Hemisphere continents, findings that raise a broad spectrum of questions regarding climatological relationships and causal linkages. Past research on SSH conducted by Valsala (2008) revealed a consistently similar anomalous phenomenon, which was associated with variability in the baroclinic modes (the density distribution of the ocean that varies due to different temperature and salinity) across the IO region. Specifically, they show that 'the IOD responses in the equatorial Indian Ocean are coupled between the first two normal modes. The first three to four month response of SSH is consistent with a single period of wind forcing resulting in Rossby and Kelvin waves, while subsequent months are an anomalous signature which is recorded as a replication of this initial behaviour (Valsala, 2008).

In one particular negative IOD year (2002), the researchers determined that a low sea level involved a first baroclinic mode, whereby a subsequent high sea level propagated a second baroclinic mode as a Rossby wave from the eastern boundary of the ocean, which validated the previous hypothesis that IOD responses in the equatorial Indian Ocean were a combination of the first two baroclinic modes (Valsala, 2008). Such findings are consistent with the evidence presented, establishing a baseline linked waveform patterning which is likely explained by the propagation of Rossby and Kelvin waves throughout the IOD.

Empirical and predictive observations of this geographic region indicate a potential increase in IOD events, a theoretical indication of the impact of global warming (Cai et al., 2009). For this reason, additional research regarding the IOD phenomenon and its impact on monsoonal conditions and characteristics is essential to predicting regional impacts and indicating potential shifts in weather patterns that could potentially lead to substantive changes in the future in monsoonal effects.

A recent study by Kug et al. (2009) addressed particular anomalies that are related to Madden-Julian oscillations and ENSO dynamics. Using the dipole mode index (DMI), Kug et al. (2009) calculated 'seasonally moving lag-correlation coefficients', evaluating equatorial SST and zonal wind anomalies in order to address a possible correlation between the DMI index and High Frequency (HF) atmospheric variability. Based on this quantitative model, the authors concluded that HF variability over the IO is modulated by IOD events wherein the MJO and synoptic eddies become 'significantly energetic during negative IOD events' (Kug et al., 2009). Distancing their findings from the more rigid non-correlated theories of Saji et al. (1999, 2005) and Webster et al. (1999), the authors argued that this correlation is influenced by ENSO.

Accordingly, there remains a standard belief whereby IOD phenomena are systemic and qualitatively linked mainly to conditions of several regions that have not yet been investigated, which define the extent of climatological variations, and possibly address the imperativeness of further exploration regarding monsoonal anomalies and influences. Although the phenomenological influence of IOD events on multiple geographic regions is theoretically stimulating, this research focuses on the manifestation of climate events within the IO region specifically.

3 Large Scale Climate Modes Impact on the Indian Ocean in relation to the IOD

3.1 Introduction

Assessment of Indian Ocean characteristics and correlations with other regional phenomena such as the ENSO continue to provide researchers with a behavioural understanding of regional interrelationships and possible correlations that may impact upon either monsoonal manifestation. Tiwari et al. (2004) conducted a highly relevant study of sea level variations in the Indian Ocean, engaging datasets from Topex/Poseidon altimetry, temperature data, and tide gauges in order to investigate possible correlation with the ENSO. Such research, in essence, postulates that there is a correlated relationship between Indian Oceanic events and the tropical Pacific behaviour via atmospheric teleconnections (Tiwari et al., 2004). Other researchers such as Saji et al. (1999) and Webster et al. (1999) associate intraseasonal variability in climatic features throughout the Indian Ocean with a dipole mode, discounting the effects that ENSO has on various characteristics including temperature, wind patterns, and currents.

Across the Indian Ocean, sea level changes are the direct result of what Tiwari et al. (2004) recognise as responses to temperature and salinity variations within the water column, mass change through water exchanges with continents and atmosphere, and long Rossby Waves. Given their direct association with the IOD and variable climatic phenomena, these unique wave structures will be evaluated over the course of this research in order to identify any potential link between their manifestation and anomalous events within the Indian Ocean region. The Indian Ocean is a unique system of climatic and oceanographic responses, resulting in temporal and spatial variations that have been widely explored throughout the past two decades. Although the range of methods and focal points of these researchers have been diverse, it is clear that there are two broad aims of such exploratory studies: first to identify whether or not there is a link between ENSO and the IOD, second to define the characteristics of the dipole mode and its coupled responses within this particular oceanic region. Leading studies in this field, including Saji et al. (1999), Webster et al. (1999), Rao et al. (2002), Feng and Myers (2003), have established the empirical and conceptual foundations for IOD analysis, describing an EOF methodology which serves as a valuable link between evidence and conceptual application.

In spite of such findings, however, any emergent research in such a complex field raises questions regarding its validity and relevance, as subsequent empirical studies have intended to either disprove or confirm the existence of a dipole mode in the Indian Ocean. Based on the research studies assessed over the course of this chapter, we will study the IOD and compare it with a range of climatic modes using remote sensed data analysis over the past two decades focusing on the IO anomalies and coupled phenomena.

3.2 Data and methods

3.2.1 Sea Surface Height (SSH) Data

SSH is measured using altimetry which measures the time taken for a radar signal to reach the earth and return to the satellite "e.g. T/P", then the SSH are calculated from the combination between the return signal and precise satellite location data. SSH is the distance at a certain time from the sea surface to a reference ellipsoid (Figure 6), where the SSH anomalies (SSHA) are the difference between the observed and an average SSH as observed by the satellite for a certain period where longer period leads to a better average. A correction that should be considered is the geoid variation. The ocean responds to the earth's gravity field, the level of equal gravity potential is called the Geoid (Robinson, 2004).

The difference between the heights above the reference ellipsoid and the altitude above the ocean surface is approximately equal to the geoid height (Figure 6). Absolute SSH is relative to the geoid and dynamic topography is used to calculate the SSHA. Dynamic topography is obtained by subtracting the Earth Gravitational Model 1996 (EGM96) geoid model from the altimetric observations (LeGrand et al., 1998).

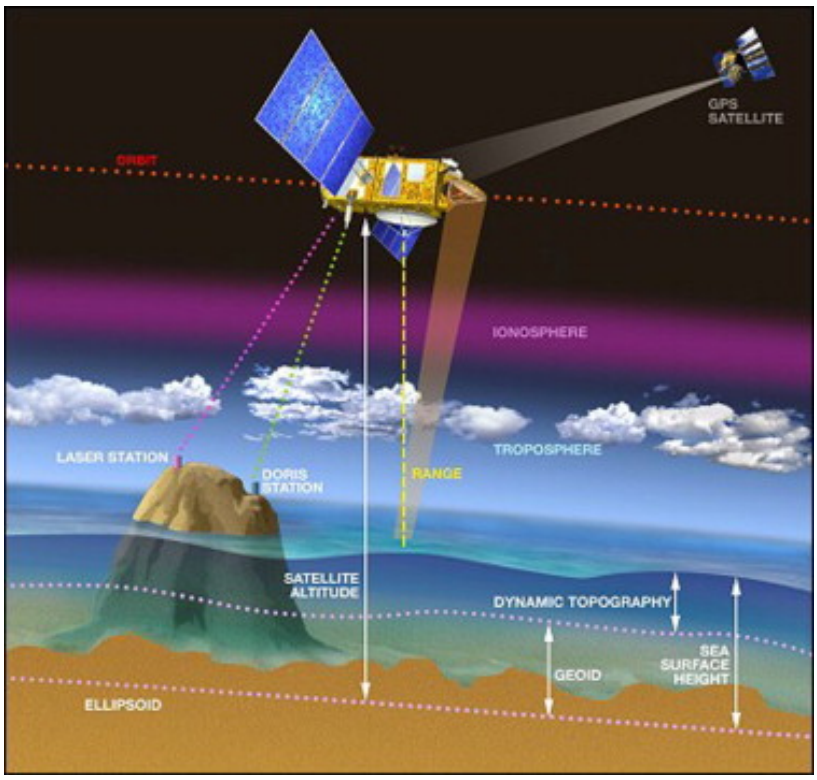

Figure 6 Altimeter principle (archiving, validation and interpretation of satellite oceanographic data, AVISO)

SSH can be used for calculating current velocity at a time scale equivalent to the satellite repeat period (e.g. 10 days for Jasons-1 and T/P). SSH can show the current flow in eddies, where in the Northern Hemisphere cyclonic eddies are turning counter clockwise and shows negative SSH field, these are usually known as cold-core eddies because there is low SST in the core of eddies. On the other hand anticyclonic eddies turn clockwise and are indicated by a positive SSH field. In the Southern Hemisphere both cyclonic and anticyclonic eddies turn in the opposite direction to Northern Hemisphere eddies. In this chapter the Monthly SSHA is used for the time between Oct of 1993 until Feb 2010 from the T\P+Jason1 satellite missions over the IO.

3.2.2 Sea Surface Temperature (SST) Data

SST and SSTA that is a measure of the difference between the best estimates of the satellite-observed SST and the mean SST for each month from a specific time period called the variable climatology, both variables are used in the following section from two different sources starting from Jan 1998 to Dec 2011, the first source is the Tropical Rainfall Measurement Mission (TRMM) and the second being the Reynolds/Smith OI.v2 SST data.

TRMM obtain the SST using a microwave radiometer on board the satellite called TRMM Microwave Imager (TMI), the measurement of SST through clouds by satellite microwave radiometers has been an elusive goal for many years. The early radiometers in the 1980s (i.e., SMMR) were poorly calibrated, and the later radiometers (i.e., SSM/I) lacked the low frequency channels needed by the retrieval algorithm. Finally, in November 1997, the TMI radiometer with a 10.7 GHz channel was launched aboard the TRMM satellite.

The important feature of microwave retrievals is that SST can be measured through clouds, which are nearly transparent at 10.7 GHz. This is a distinct advantage over the traditional infrared SST observations that require a cloud-free field of view. Ocean areas with persistent cloud coverage can now be viewed on a daily basis. Furthermore, microwave retrievals are not affected by aerosols and are insensitive to atmospheric water vapor. However, the microwave retrievals are sensitive to sea-surface roughness, while the infrared retrievals are not. A primary function of the TRMM SST retrieval algorithm is the removal of surface roughness effects. The microwave and infrared SST retrievals are complementary and can be combined to obtain a reliable global data set with better special resolution of about ¼ degree.

3.2.3 Methodology

Before we introduce applications derived using regression and correlation tools, one must keep in mind that these methods show statistical relationships only, and can not indicate cause and effect, which is one of the most common misuse of interpretation for practical application using the real-world data, one has to look at the correlation with extra care when confined to a limited sample size because the significance of a correlation depends on the few independent samples among the whole sample size.

The mathematical equation used in regression is straightforward therefore we will just explain the concept behind the technique, which can be illustrated by a simple plot (Figure 7) of two variables that one reacts to fluctuations in the other therefore there is a relation between them, which can be quantified by the regression line that represents the sensitivity of relationship between the two variables.

In Figure 7 show a basic explanation of linear regression between two data sets, slope (a) shows that an increase in (x) relates to almost twice of an increase in (y) and therefore the slope is more sensitive to the (y) data set values. On the other hand the opposite occurs with slope (b) where a large increase in (x) relates to a small increase in (y) with magnitude change of four in (x) to one for y indicating that the slope is more sensitive to the (x) data set values. Regression can provide a value between +/- 1 when used on the data set to relate their sensitivity where the closer the values to +/- 1 the more sensitive the data set to each other.

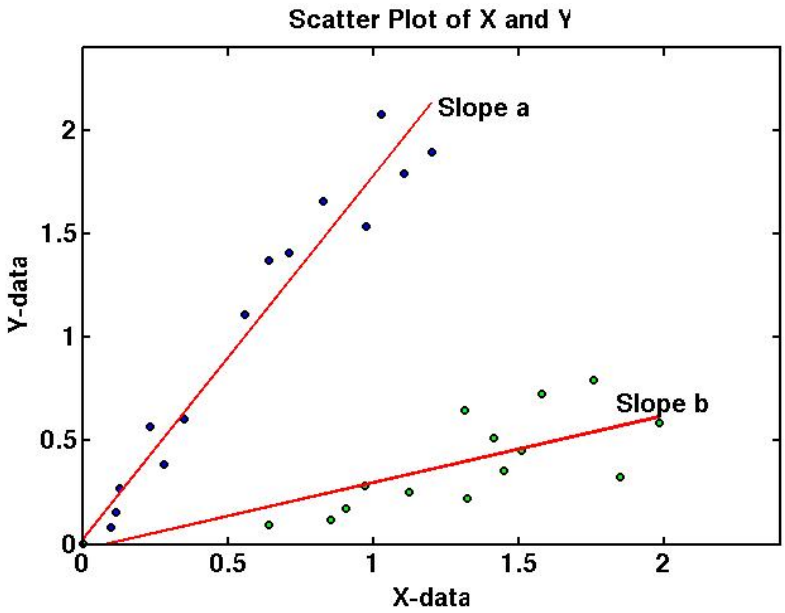

Figure 7 Linear regression lines representing best-fit line between two variables.

Another value obtained using the regression analysis on two variables or more is the Coefficient of determination (r^2) that represents the correlation between them where (r) is the Correlation coefficient for example to show how well a parameter like SSTA of a specific area is correlated to a large scale climate mode index like the southern oscillation index. Values of r^2 in Figure 7 indicate a stronger correlation in slope a than b, where in slope a the points lie closer to the line causing higher r^2-values, which is always between 0 and 1 where 0 represent no correlation and 1 is a perfect linear fit. The remainder of the methods and techniques applied in this chapter for processing the data are fairly simple, basically using visual analysis and interpolation through plotting and incorporating means and standard deviations of the data. The statistical operation of simple correlation techniques (auto, lag and cross-correlation) is then used for time series correlation between the data examined. Also used is the time vs. longitudes plots (Hovmöller Diagram) to investigate variable behavior for areas of interest.

3.3 The Indian Monsoon and the IOD

3.3.1 Recent research results on the impact of monsoon on NWIO

The monsoon is one of the most significant, recurrent, and influential variables of the Indian Ocean climate, a force that has both predictable and unpredictable influences on the behaviour of multiple elements throughout this region (e.g. the Somali Current, the Great Whirl etc.). In their study of this annual phenomenon, Tomita and Kubota (2004) stated that perhaps the most dominant characteristic of monsoonal influences in the IO is a 'reversal of wind direction', directly affecting air-sea interactions and heat flux characteristics during monsoonal periods. In addition to the mean seasonal pattern, the researchers determined three distinct patterns. Pattern A has a peak in the boreal summer, Pattern B is the opposite and peaks in the boreal winter, and Pattern C have a bi-annual cycle with peaks in the boreal spring and fall. The value of a zone-based, flux-based analytical tool was evident in this particular study indicating the occurrence of phenomena in the IO and might have an impact on the Indian monsoon.

Characteristic of monsoonal variability, anomalous rainfall and weather patterns are of concern to researchers, particularly considering their significant implications for regional residents. Francis and Gadgil (2010), for example, identified an event in 2009 whereby the Indian monsoon patterns differed from their annual norms. Specifically, there was a massive deficit in all-India rainfall of around 48% in June, and a significant deficit of 27% in August (Francis and Gadgil, 2010). In order to causally link this phenomenon to other climatologic features, the researchers explored several potential impact factors including a drought-leading Rossby wave in the Indian Ocean and a strong correlation of ENSO-related impacts that may have simultaneously precipitated the drought. Using surface zonal winds from the NCEP reanalysis, SST from TMI sensor data of the TRMM, the National Oceanic and Atmospheric Administration (NOAA) ENSO index, and all-India tropical rainfall datasets Francis and Gadgil, (2010) tested methods and gathered evidence that showed results of a highly anomalous SST pattern that preceded the normal monsoonal period, resulting in lower surface temperatures and a lower potential for convection to occur.

One of the methods used to identify trends and anomalies in SST is based on a time series analysis whereby comparative analysis of the spatial pattern variations highlight substantive heating and cooling fluctuations. Simon et al. (2008) identified distinctions between SST patterns in four different annual periods, linking temperature variability to rainfall levels in order to highlight any potential influence of monsoonal warming. Their findings showed warming characteristics in 1998, which distinguished this year from the other three by the greater number of depressions over the Bay of Bengal. Simon et al. (2008) argued that such variability maybe related to the change in positioning of the convective heat source that year, altering the overall development of the monsoon according to the relationship between climatic and oceanic elements. Their research was essentially designed to test the validity of the TRMM/TMI satellite imaging as a valuable means of evaluating characteristics within this region.

3.3.2 NWIO Monthly SSHA in relation to the monsoon and IOD

The collected results are based on SSHA data from T/P+Jason1 that have been chosen to reflect their distribution during the primary period of the southwest monsoon and northeast monsoon. Further, these data demonstrate high ocean variation during the period of the northeast monsoon. Temporal restrictions by analyses of four years from the data (1994,1996,1997 and 1998) have been imposed in order to highlight strong events of climate modes including both positive and negative IOD.

In Figure 8, the small circular high and low SSHA regions are indicative of eddies. The primary variation in the SSHA images shown in Figure 8 is viewed at 45-60°E occurring on the northwestern side of the ocean during Jul, Aug and Sep, just off the Somali coast between 5°N and 10°N and is most likely representative of the Great Whirl. The strength of the largest eddy is particularly noticeable against the lower SSHA region, which is adjacent to this phenomenon at the north and south. Finally, the majority of the SSHA map highlights high SSHA in the region around 10-15°N, accounting for the Socotra Gyre, with low SSHA along the Somali coast at 5-8°N indicative of an area of Somali upwelling.

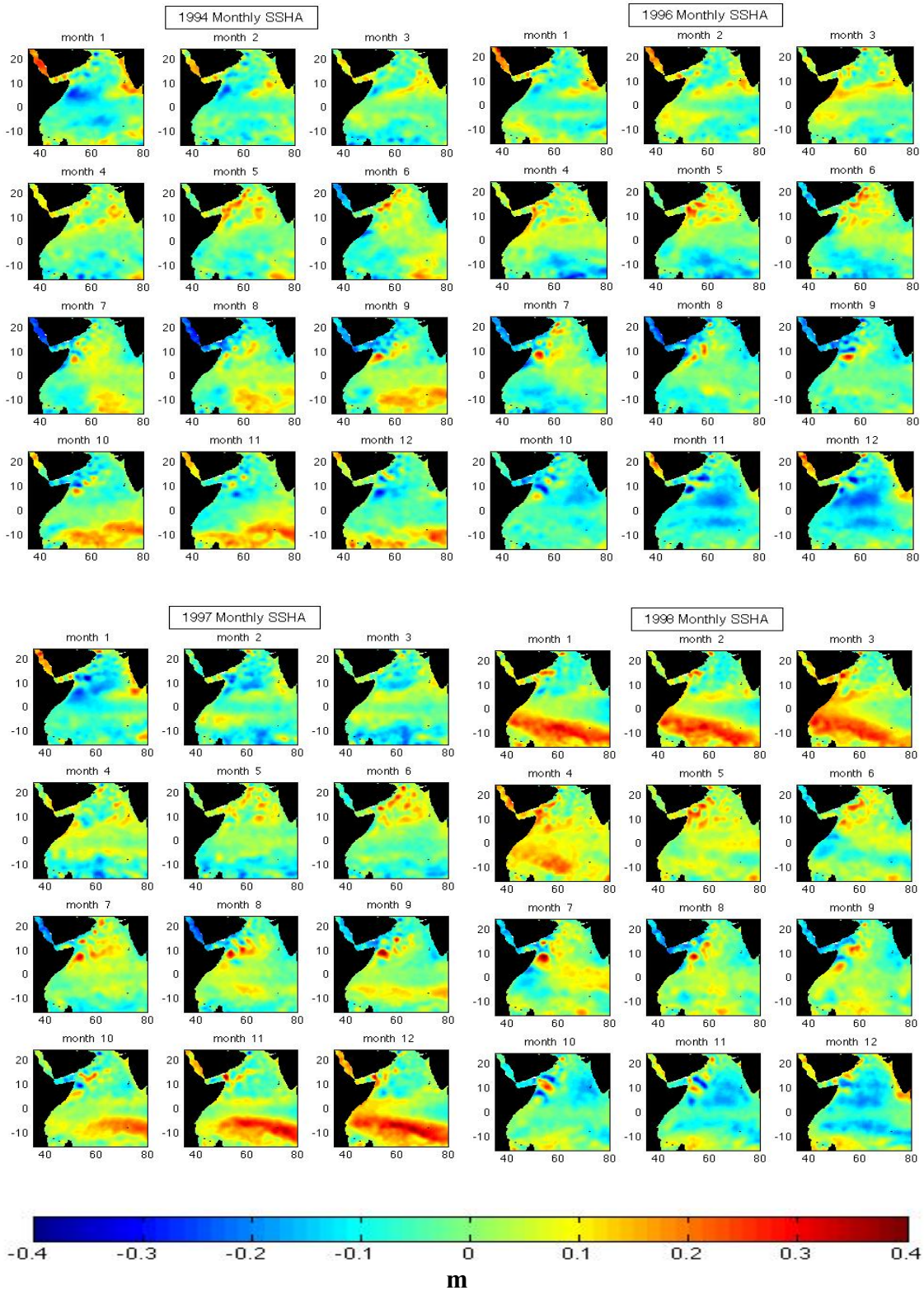

Figure 8 Monthly plots SSHA Data (m), showing the difference between the increase of SSHA in the western part of the Indian Ocean during the positive IOD events of 1994 and 1997 and the negative IOD event of 1996.

3.4 The ENSO Link Complications

3.4.1 Scientific views on the influence of ENSO on the Indian Ocean

In spite of widespread emphasis on dipole events in the Indian Ocean, researchers such as Rao et al. (2002) continue to see interannual variability of SST as related to a basin wide warming phenomenon that is directly linked to ENSO conditions. The authors removed the associated linear trend and applied empirical orthogonal function (EOF) analysis to find the dominant modes of interannual variability, to identify relevant anomalies in contrast with seasonal deviations. The application of the EOF methodology is a departure from other similar studies in this field, and in order to capture propagating signals, the authors employed a complex EOF with is better than standard EOF in detecting low-frequency propagating features in time and space. EOF mode modelling revealed a clear dipole pattern with positive loading in the east and negative loading in the west, indicative of what the authors refer to as a 'seesaw oscillation' (Rao et al., 2002).

To resolve the ENSO argument the authors suggest that in direct contrast to the surface and subsurface forcing of ENSO, identified in the tropical Pacific, the dipole mode in the Indian Ocean results in an interannual variability both at the surface and the subsurface, which is correlated with IOD events and surface level variability as a result of monopole correlation with ENSO forces (Rao et al., 2002). These findings are valuable because they related events of IOD to the thermocline variations and SST forces outside of ENSO influence.

To reconcile the variation in SST and IOD related events, Feng and Myers (2003) suggested that because there is a non-negligible correlation between ENSO and IOD indices, it is difficult to empirically determine independence for IOD events. The authors recognised that the role of the subsurface ocean structure in the IO had yet to be sufficiently addressed in research studies for a possible link between IOD events and patterns of SST. The dataset for the Feng and Myers (2003) analysis was derived from a 'ship of opportunity network'. The data were binned by lattitude/depth and optimally averaged in order to highlight bimonthly values. Further modelling included a gridded altimeter SSH product that was based on TOPEX Poseidon and ERS-1/ERS-2 missions wherein annual and semi-annual harmonics were calculated through linear regression and subtracted from the dataset to define the interannual SSH.

EOF analysis of altimeter and expendable bathythermograph (XBT) subsurface temperature data revealed that IOD events were initiated by anomalous upwelling along the Sumtra-Java coast at the start of the normal upwelling season in May-June. Based on modelling and a comparison of two distinct IOD anomalies, Feng and Myers (2003) concluded that there is coupled ocean-atmosphere instability in the IO, which is possibly initiated by ENSO during the early upwelling season. The justification of these conclusions empirically requires more advanced modelling strategies in future research.

Furthering this argument, Shinoda et al. (2004) recognised the merits of past studies in their treatment of the IOD/ENSO correlation. Their focus was designed to explore correlations between these two seemingly interrelated events. Through a comprehensive comparison of EOF models and fluid dynamic analysis, the researchers determined that the 'surface dipole is strongly correlated with ENSO, while the subsurface dipole is mostly independent of ENSO' (Shinoda et al., 2004). The composite analysis revealed that due to the upper ocean heat budget, ENSO induces a shallow surface dipole controlled by surface heat flux variations, whilst wind forced ocean dynamics simultaneously influence the development of the SST dipole that accompanies the subsurface dipole (Shinoda et al., 2004). In spite of these findings, the authors were unable to directly correlate these SST anomalies with an interconnection between ENSO and IOD events; giving the possibility that there is independence for the subsurface dipole that dissociates its behaviour from ENSO phenomena.

3.4.2 ENSO/IOD Indices Linear Regression Correlation analysis

Before starting to apply linear regression correlation analysis on the indices we need to recognize which years represent El Nino or La Nina conditions and for that we adopt the definition of NOAA, which classify the full-fledged El Nino and La Nina when the SST anomaly of the Nino 3.4 index exceed +0.5 (El Nino) or -0.5 (La Nina) for at least five consecutive months (www.noaa.gov) with the adjustment of the threshold from +/- 0.5° C to +/- 1° C to consider only the significant events, which is approximately the standard deviation of the index three months running mean using the Reynolds OIv2 SST analysis (Table 1).During the period investigated here (1993 to 2012), there were four significant episodes of El Nino (1994\5, 1997\8, 2002\3 and 2009\10) where the 97\98 event is twice the strength of the other three events and lasted for almost a year, six months more than the others. Four major La Nina events also can be seen over the same period that occurred in (1998\9, 1990\2000, 2007\8 and 2011\12). They are fairly equal in strength and duration.

Table 1 Three monthly SSTA running mean of El Nino 3.4 index calculated monthly from1993 to 2012.

Year	DJF	JFM	FMA	MAM	AMJ	MJJ	JJA	JAS	ASO	SON	OND	NDJ
1993	0.3	0.4	0.6	0.7	0.8	0.7	0.4	0.4	0.4	0.4	0.3	0.2
1994	0.2	0.2	0.3	0.4	0.5	0.5	0.6	0.6	0.7	1	1.2	1.3
1995	1.2	1.1	0.7	0.4	0.3	0.2	0	-0.2	-0.3	0.4	-0.5	-0.6
1996	-0.7	-0.6	-0.4	-0.3	-0.1	-0.1	0	-0.1	-0.1	-0.2	-0.3	-0.4
1997	-0.4	-0.3	0	0.4	0.8	1.3	1.7	2	2.2	2.4	2.5	2.5
1998	2.3	1.9	1.5	1	0.5	0	-0.5	-0.8	-1	-1.1	-1.3	-1.4
1999	-1.4	-1.2	-0.9	-0.8	-0.8	-0.8	-0.9	-0.9	-1	-1.1	-1.3	-1.6
2000	-1.6	-1.4	-1	-0.8	-0.6	-0.5	-0.4	-0.4	-0.4	-0.4	-0.6	-0.7
2001	-0.6	-0.5	0.4	-0.2	-0.1	0.1	0.2	0.2	0.1	0	-0.1	-0.1
2002	-0.1	0.1	0.2	0.4	0.7	0.8	0.9	1	1.1	1.3	1.5	1.4
2003	1.2	0.9	0.5	0.1	-0.1	0.1	0.4	0.5	0.6	0.5	0.6	0.4
2004	0.4	0.3	0.2	0.2	0.3	0.5	0.7	0.8	0.9	0.8	0.8	0.8
2005	0.7	0.5	0.4	0.4	0.4	0.4	0.4	0.3	0.2	-0.1	-0.4	-0.7
2006	-0.7	-0.6	-0.4	-0.1	0.1	0.2	0.3	0.5	0.6	0.9	1.1	1.1
2007	0.8	0.4	0.1	-0.1	-0.1	-0.1	-0.1	-0.4	-0.7	-1	-1.1	-1.3
2008	-1.4	-1.4	-1.1	-0.8	-0.6	-0.4	-0.1	0	0	0	-0.3	-0.6
2009	-0.8	-0.7	-0.5	-0.1	0.2	0.6	0.7	0.8	0.9	1.2	1.5	1.8
2010	1.5	1.3	1	0.6	0	-0.5	-0.9	-1.3	-1.5	-1.6	-1.6	-1.5
2011	-1.5	-1.3	-1	-0.6	-0.4	0.2	0.2	0.4	-0.7	-0.8	-0.9	-1
2012	-0.9	-0.6	-0.5	-0.3	-0.2	0	0.1	0.4	0.5	0.6	0.2	-0.3

The same principal used by NOAA to recognize the ENSO episodes is considered here to identify the IOD events only applied on the data from Hadley Centre SST anomaly observation to define the Dipole Mode Index (DMI) to be able to correlate the mode with features occurring in the NWIO and also with the ENSO index, the positive IOD (pIOD) is reflected when exceeding +1°C in the DMI and -1°C as the negative IOD (nIOD).

Table 2 shows that there were four significant episodes of pIOD (1994, 1997, 2006 and 2012) with three major nIOD events (1996, 1998 and 2010). The pIOD events of 94 and 97 are by far much stronger than the other two pIOD events and had longer duration, although the 94 event started earlier than the others where the 97 lasted for a little longer.

Table 2 Three monthly SSTA running mean of DMI calculated monthly from1993 to 2012.

Year	DJF	JFM	FMA	MAM	AMJ	MJJ	JJA	JAS	ASO	SON	OND	NDJ
1993	-0.6	-0.5	-0.3	-0.2	-0.2	-0.1	-0.1	-0.1	-0.2	-0.2	-0.2	-0.1
1994	0	0.4	0.8	**1.4**	**1.9**	**2.3**	**2.6**	**2.7**	**2.7**	**2.3**	**1.9**	**1.3**
1995	0.8	0.3	0	-0.2	-0.3	-0.3	-0.3	-0.3	-0.4	-0.4	-0.3	-0.3
1996	-0.3	-0.4	-0.6	-0.9	**-1.2**	**-1.6**	**-2**	**-2.3**	**-2.6**	**-2.5**	**-2.2**	**-1.7**
1997	**-1.1**	-0.5	-0.1	0.2	0.6	**1**	**1.7**	**2.4**	**3.1**	**3.4**	**3.3**	**2.8**
1998	**2.1**	**1.3**	0.7	0.3	-0.1	-0.5	-0.9	**-1.4**	**-1.8**	**-2**	**-1.8**	**-1.5**
1999	**-1**	-0.7	-0.4	-0.3	-0.2	-0.1	-0.1	0	0	-0.2	-0.3	-0.4
2000	-0.3	-0.1	0.1	0.3	0.4	0.5	0.5	0.3	0.1	-0.2	-0.5	-0.6
2001	-0.6	-0.3	0.1	0.4	0.5	0.4	0.2	-0.1	-0.3	-0.3	-0.3	-0.2
2002	-0.2	-0.2	-0.2	-0.3	-0.3	-0.1	0.2	0.4	1	1.1	0.9	0.5
2003	0.3	0.1	0.2	0.4	0.4	0.6	0.8	0.8	0.5	0.4	0.4	0.4
2004	0.5	0.4	0.2	-0.2	-0.4	-0.6	-0.4	-0.2	0	0.1	-0.1	-0.4
2005	-0.5	-0.8	-0.7	-0.6	-0.4	-0.6	-0.7	-0.8	-0.8	-0.9	-1.1	-1.2
2006	-1.1	-1	-0.9	-0.8	-0.5	-0.1	0.3	**1.2**	**1.4**	**1.5**	**1.2**	**1.0**
2007	0.5	0.2	0.1	0.1	0.2	0.3	0.4	0.4	0.3	0.1	-0.1	-0.3
2008	-0.5	-0.5	-0.3	0	0.2	0.4	0.5	0.6	0.4	0.2	0	0
2009	0	0.2	0.4	0.5	0.5	0.4	0.3	0.2	0.2	0.4	0.5	0.6
2010	0.3	0.1	0.6	0.4	0.1	-0.1	-0.3	**-1.1**	**-1.3**	**-1.4**	**-1.4**	**-1.1**
2011	**-1.0**	-0.2	0.1	0.2	0	0.2	0.3	0.5	0.4	0.6	0.5	-0.1
2012	0.1	0	0.2	-0.2	-0.2	0.5	**1.0**	**1.1**	**1.2**	**1.3**	**1.2**	**1.0**

This climate variability in ENSO and IOD climate modes will hopefully help us understand the variability of the NWIO region by comparing and correlating the indices of the climate modes using linear regression analysis, when we apply the method on the DMI and Nino 3.4 indices from Table 1 and Table 2 that very much indicates the same relationship between the two as previous studies like Ashok et al. (2004) who found the relationship lies somewhere between 0.3 and 0.4 correlation factor using different correlation analysis methods like EOF and linear regression, Figure 9 shows a coefficient of determination (R^2) of almost 0.35, this value is not very strong considering the number of samples, but most likely suggests that the two modes are independent of each other and this relatively moderate correlation exists due to the co-occurrence of the second mode in some years, as Rao et al. (2002) shows that 35% of IOD events co-occur with ENSO events between 1877 and 1997. However the strong events of 97 pIOD and 97/98 El Nino seem to be connected.

One possible reason is that both modes are coupled with the equatorial zonal winds in the central Indian Ocean that year, unlike the other times where ENSO events have some relationship with the equatorial zonal winds in the central Indian Ocean but in the same phase corresponding to IOD do not (Ashok et al., 2003). This indicates that the equatorial zonal winds in the IO can be affected by either an ENSO or DMI event separately occurring or during the same year where the effect becomes greater.

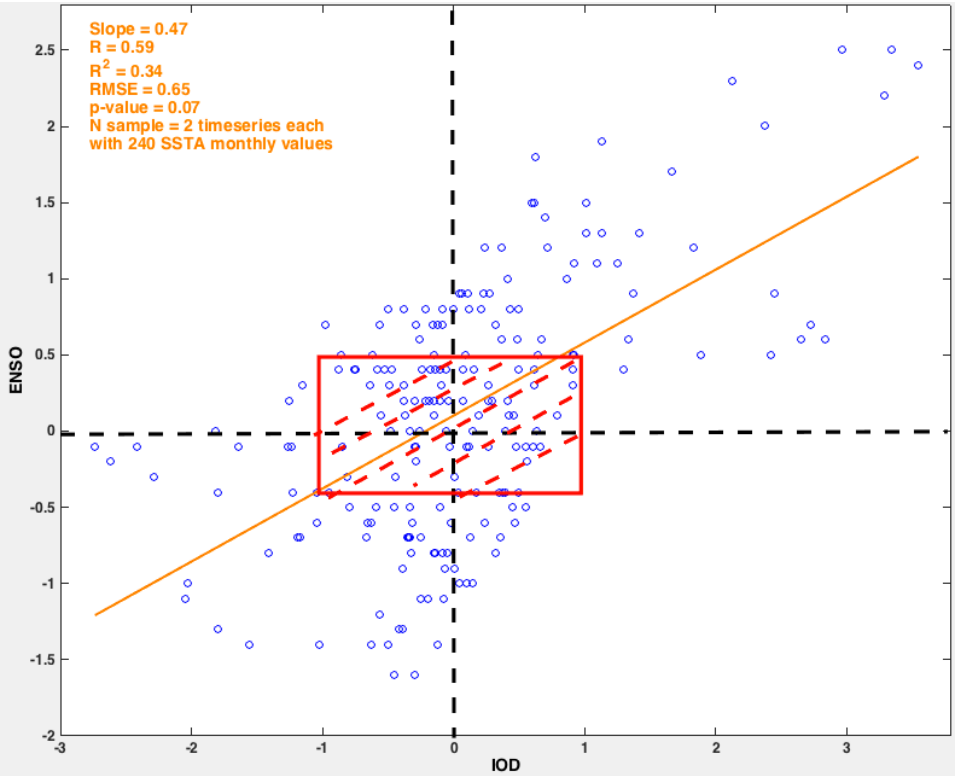

Figure 9 linear regressions showing a level of relationship between IOD and ENSO with a slope of 0.47 and a coefficient of determination (R^2) of about 0.34 for a 95% level of confidence.

3.4.3 IOD and ENSO signal along the equator over the Indian Ocean

To differentiate between IOD and ENSO phenomena, it was important to establish some bounding mechanism that could introduce a degree of correlation with the dipole mode itself. Figure 10 offers a combinative illustration of the Indian Ocean Dipole mode index (DMI), the Nino 3.4 index, and between the two indices a Hovmöller diagram of the Indian Ocean SSHA for a time frame between November 1992 and February 2010. This representation is localised to the equatorial Indian Ocean at 0°, highlighting a stronger correlation between the SSHA increase and the DMI especially towered the later years of 2007, 2008 and 2009 which a weak to moderate IOD events occur with no El Nino events as the ENSO index reflect, with the exception of the 1994 pIOD that is not reflected because the influence of the IOD was further to the south below the equator that year (Figure 8).

This diagram also demonstrates similarities in strength of events occurring at in the same periods between the two indices, characterised by similar strong highs and deep low over particular seasonal periods. Yet in spite of these findings, it is equally clear that the DMI is not directly associated with ENSO and caused by its manifestation, operating autonomously and in direct response to coupled ocean-atmosphere conditions characteristic of the Indian Ocean.

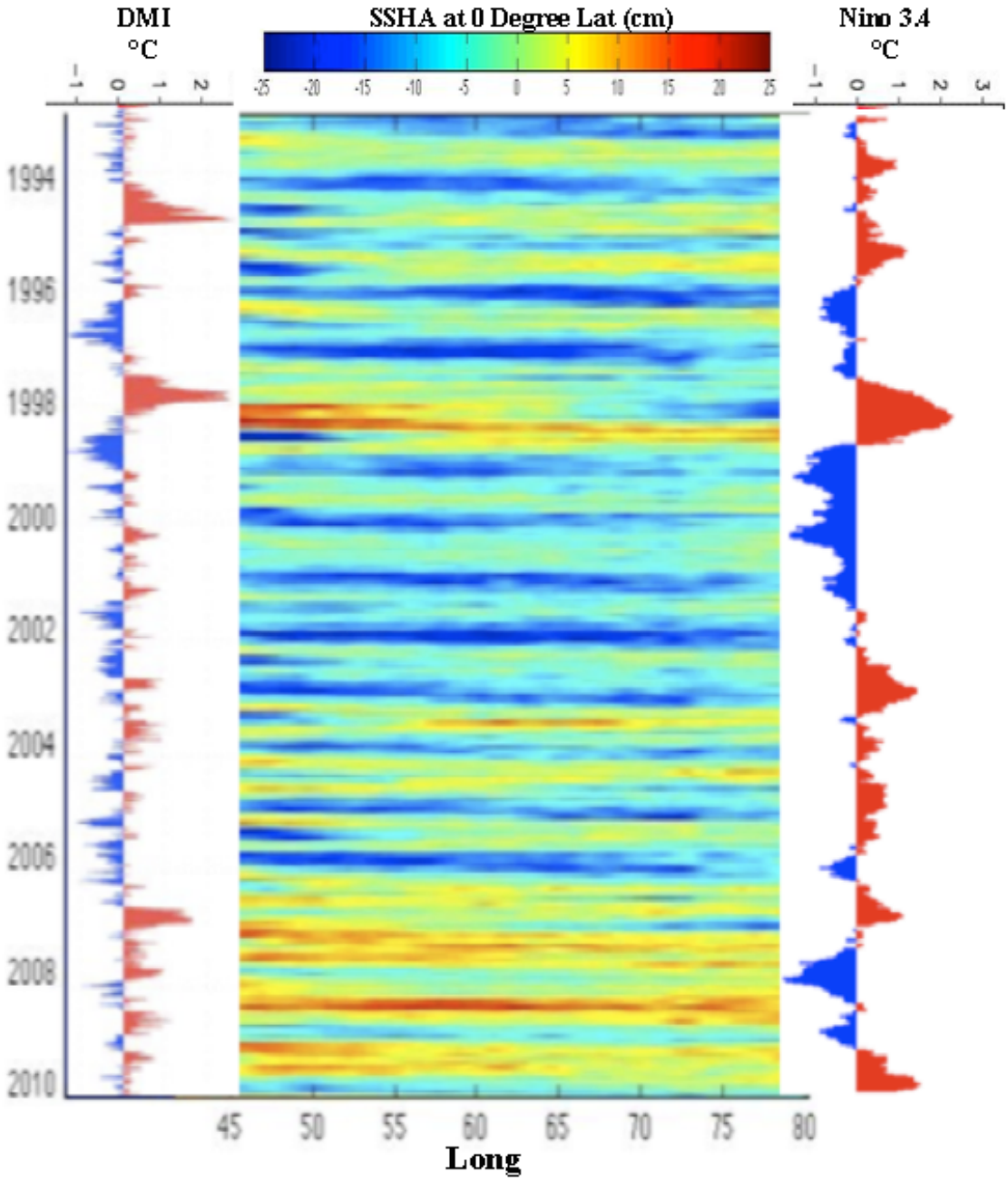

Figure 10 Plot of indices comparison of DMI and Nino 3.4 with Hovmöller Diagram of SSHA at 0° Latitude.

3.4.4 ENSO Lagged Correlation Analysis

Figure 11 represents a lagged correlation analysis in which the lagged characteristics of SSTA in the Indian Ocean were compared with the unlagged characteristics of the Nino 3.4 index. The lag function in this analysis resulted in a lag range of -6 to 6 months in order to highlight any potential correlations over the assessment period. The outcomes indicate that there is a negative correlation between the Nino 3.4 and the IO SST, particularly in latitudes between 5° and 16° N covering most of the Arabian Sea area. This pattern of negative SSTA is reflected at the same area of the Great Whirl and could be related to its geospatial anomalies, particularly when considered in relation to ENSO propagation and the periodicity of impacts.

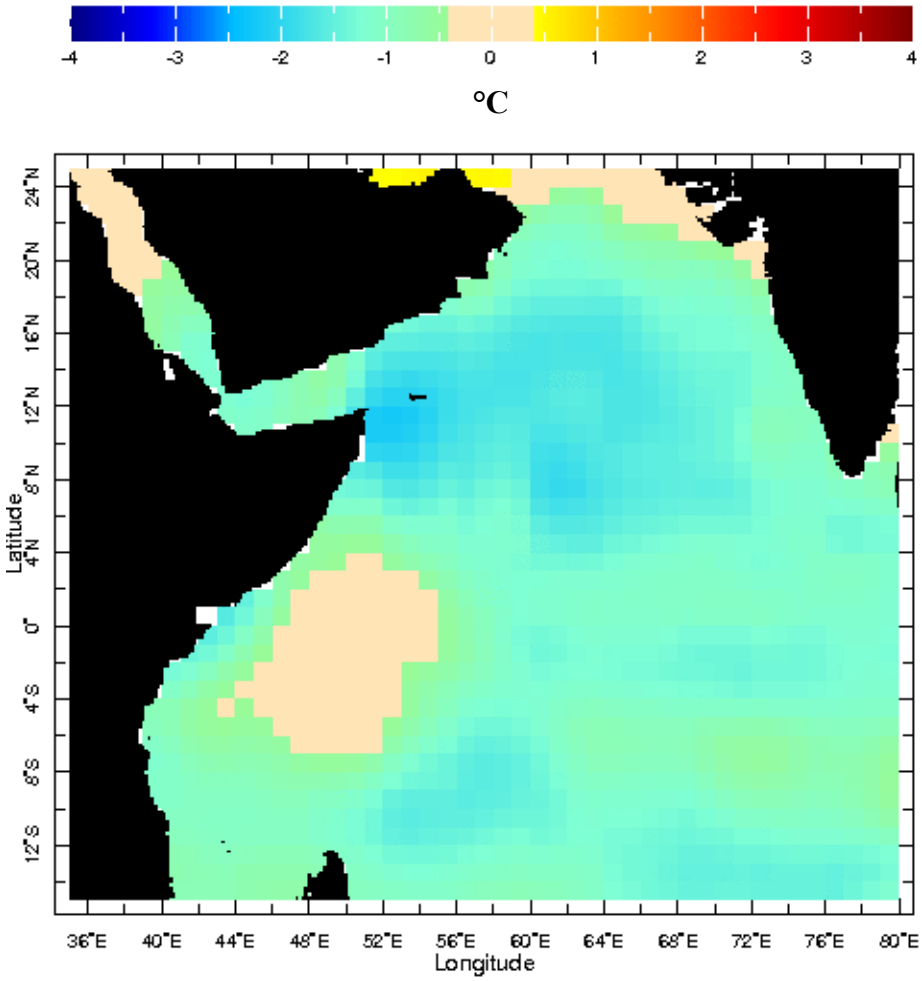

Figure 11 correlations at peak lag (-6 to 6 months) analysis of SSTA vs. El Nino 3.4

3.5 Regression and Correlation maps

One of the common techniques used in climate statistical analysis is a regression/correlation map, in this section we produce these maps using the application Matlab (appendix E) to regress and correlate both the IOD and ENSO indices against two main variables parameters that is SST and sea level pressure (SLP) at each grid point to generate the maps. The first variable SST is considered to its importance of reflecting characteristics of the ocean behavior, where SLP due to its direct relationship with several atmospheric variables such as precipitation, relative humidity, wind and air temperature that can possible impacts of ENSO and IOD on Indian Ocean and the surrounded land masses. Before we generate the maps, the indices are standardized and we use the monthly climatology of the variables data to remove the seasonal cycle. The regression maps are the covariance of the indices multiplied with each matrix column of the data, which represents the coefficient of determination (R^2) divided by the standard deviation of the indices. The correlation maps are calculated slightly differently, where first we divide each column of the variable by its standard deviation, and then acquire the indices covariance to get the correlation coefficient (R).

3.5.1 ENSO regression and Correlation

Figure 12 (A&B) represents the seasonal summer SST (colour shaded) and SLP (contours) regression/correlation maps of May to September monthly Nino 3.4 index for the period of 1993 to 2012, the figure as expected shows an El Nino pattern event with the sign reversed which does not make any difference here because the data scale is arbitrary, it reflects a high negative values correlation of SST in the central Pacific Ocean which appears to have a proportional relationship with the majority of central and north west of the Indian Ocean SST, but inverse relationship with south west of the Pacific extending to the south east in the Indian Ocean. From these maps we can estimate that during an ENSO event, there is a weak to moderate relationship with the western Indian Ocean in the order of 0.2 according to (R^2), which also agree with the SLP although it indicates a strong relationship with Indonesia and Australia leading to the severe droughts associated usually with an El Nino event influence over those regions.

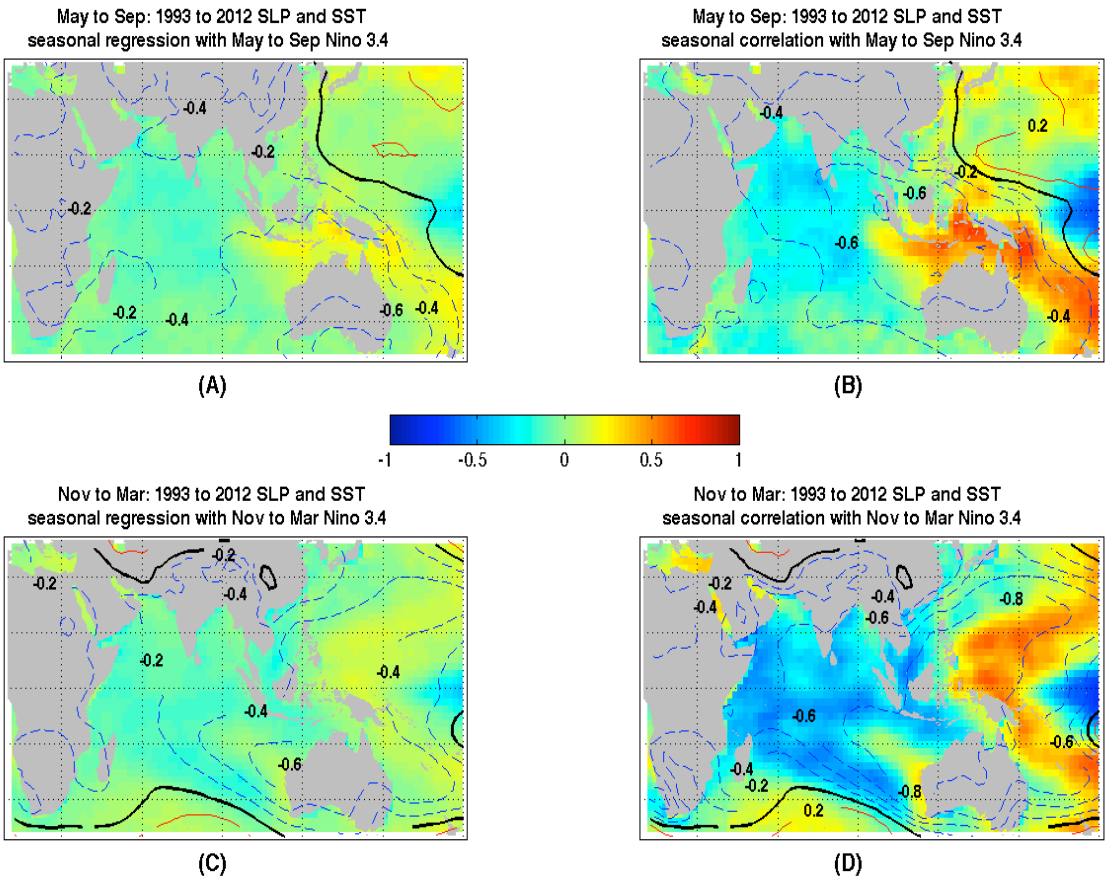

Figure 12 Standardized SST (colour shaded) and SLP (contours) regression maps (left, r^2) and correlation maps (right, r) with Nino 3.4 index from table 1.

The maps in Figure 12 (C&D) reflect the relationship during winter and shows high negative values for the central Pacific and the Indian Ocean with high positive over the west Pacific, although its similar to the pattern during the summer (A&B), it indicates much more intense relationship in both SST and SLP especially over the majority of the Indian Ocean, where it could be argued that this is most likely because November to March is the period of maturity of ENSO. The SLP values reach as high as -0.8 (r), which is why it is one of the key elements in identifying an El Nino year. The map indicates a strong positive correlation between ENSO and the Indian Ocean and hence leading to a high degree of variance in the rainfall that is received throughout each year throughout this region due to the altering of atmospheric pressure distribution by ENSO through the shifting of the Walker Circulation (the surface easterly trade winds) over the tropics that define the ascending air associated with surface lows and descending air with highs, both cumulatively and according to more transient periodicity of the Indian monsoon with its associated ocean phenomena like the Somali Current and the Great Whirl.

3.5.2 IOD Regression and Correlation

A positive IOD shape is clear in both summer and winter of the regression and correlation maps in Figure 13, The spatial distribution of the SLP and SST in Figure 13 can be attributed to the reduced strength of a key current influencer, the Wyrtki jet (Tomczak and Godfrey, 2003), when a combination of the direct effect of weaker off-equatorial easterly wind stress and weaker equatorial westerly stress promote easterly equatorial surface winds.

Figure 13 shows high negative values correlation of SST in the south east of the Indian Ocean along the Indonesian west coast and high positive SST correlation over the west and central Indian Ocean especially, the relationship is stronger during the summer along the Indonesian coast than winter but along the Somali coast it is the opposite with higher values for (r) during the winter, the SLP relationship with the IOD appear to be weaker than ENSO suggesting a less linked system of atmospheric and oceanic responses. On the other hand the high correlation of SST over west Indian Ocean reaching values of 0.6 (r) explain the increase in the east Africa rainfall during a positive IOD event that induce water vapour through the rise of SST off the east coast of Africa.

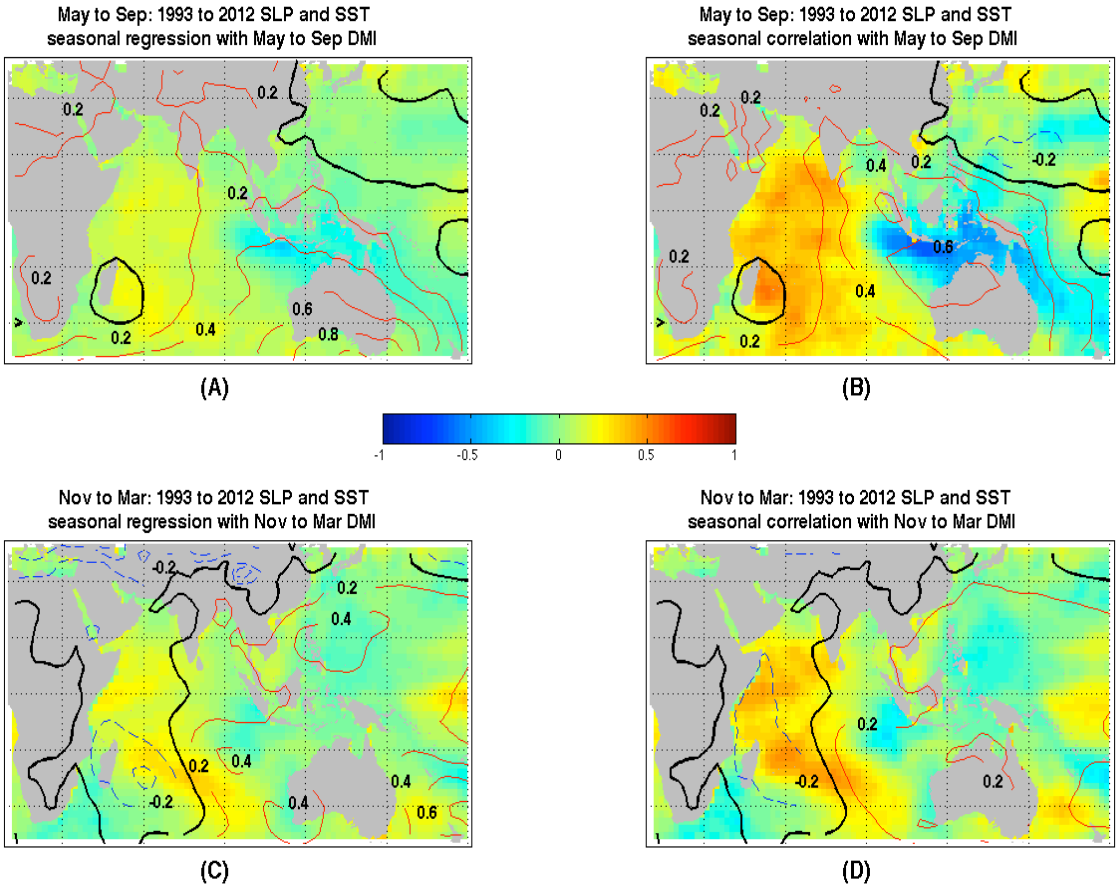

Figure 13 Standardized SST (colour shaded) and SLP (contours) regression maps (left, r^2) and correlation maps (right, r) with IOD index from Table 2.

3.6 Rossby and Kelvin Waves

3.6.1 The Role of planetary waves in the Indian Ocean

The manifestation of Rossby and Kelvin waves throughout the Indian Ocean is a topic of much debate today. Bondarenko et al. (2004) remind us that for a closed oceanic system, Rossby waves manifest in a form consistent with continental shelf waves, maintaining for a period of time and associated with variable oscillations that are affected by regional characteristics such as jet currents. Through in-depth assessment of a range of past empirical studies, Bondarenko et al. (2004) concluded that Rossby waves are most likely to have a direct influence on current behaviour, forming large scale currents in cohort with wind and thermohaline factors according to the wave transport hypothesis. Such behaviour has particular implications for the Indian Ocean where Rossby waves play a key role in the dynamics of current and hydrological patterns throughout this region, particularly during seasons of high climatic activity such as during monsoonal periods.

In order to model the propagation of Rossby and Kelvin waves throughout the Indian Ocean, one study in particular conducted by Valsala (2008) established a forcing model in order to test the location, range, and periodicity of baroclinic responses of the ocean. This purely experimental exercise demonstrates how variability in wind forcing generates a range of wavelengths among the Rossby waves in the zonal direction. Particularly, the researchers demonstrated how poleward Kelvin waves were directly responsible for modulating the annual cycle of the Indonesian throughflow water into the Indian Ocean (Valsala, 2008; Vaid et al., 2007). The extended time solutions (from 0-100 days) revealed that 'the energy imparted to the ocean by IOD wind anomalies of one month duration generates a range of Kelvin-Rossby waves which reflects in the equatorial beta-plane' (Valsala, 2008).

Further, under a second baroclinic mode assessment, the researchers demonstrated how oceanic responses to IOD related wind anomalies could remain within the IOD forcing region for upwards of eight months following the initial propagation of Kelvin and Rossby waves. Such findings are indicative of wave propagation that is affected by wind forcing and SST anomalies throughout the IO region.

3.6.2 Demonstration of impact by Rossby and Kelvin waves on NWIO

Figure 14 presents a slope in the reflected SSHA from west to east, which represents a westward-propagating signal, the indication of a first mode Rossby waves, for the 208 months of SSHA at 8°N on the same latitude as the Great Whirl which propagate between 6°N and 10°N. The onset of the Great Whirl is potentially the response to strong anticyclonic wind stress curl offshore from the Somali coast by long Rossby waves. These waves probably reflected into short Rossby waves at the boundary, accumulating energy and propagating westward (Schott and Quadfasel, 1980). This plot is indicative of a Rossby wave propagates over an extended 6 month period before transferring energy at the westward boundary of the Indian Ocean and dissipating under the force of various eddies and jets.

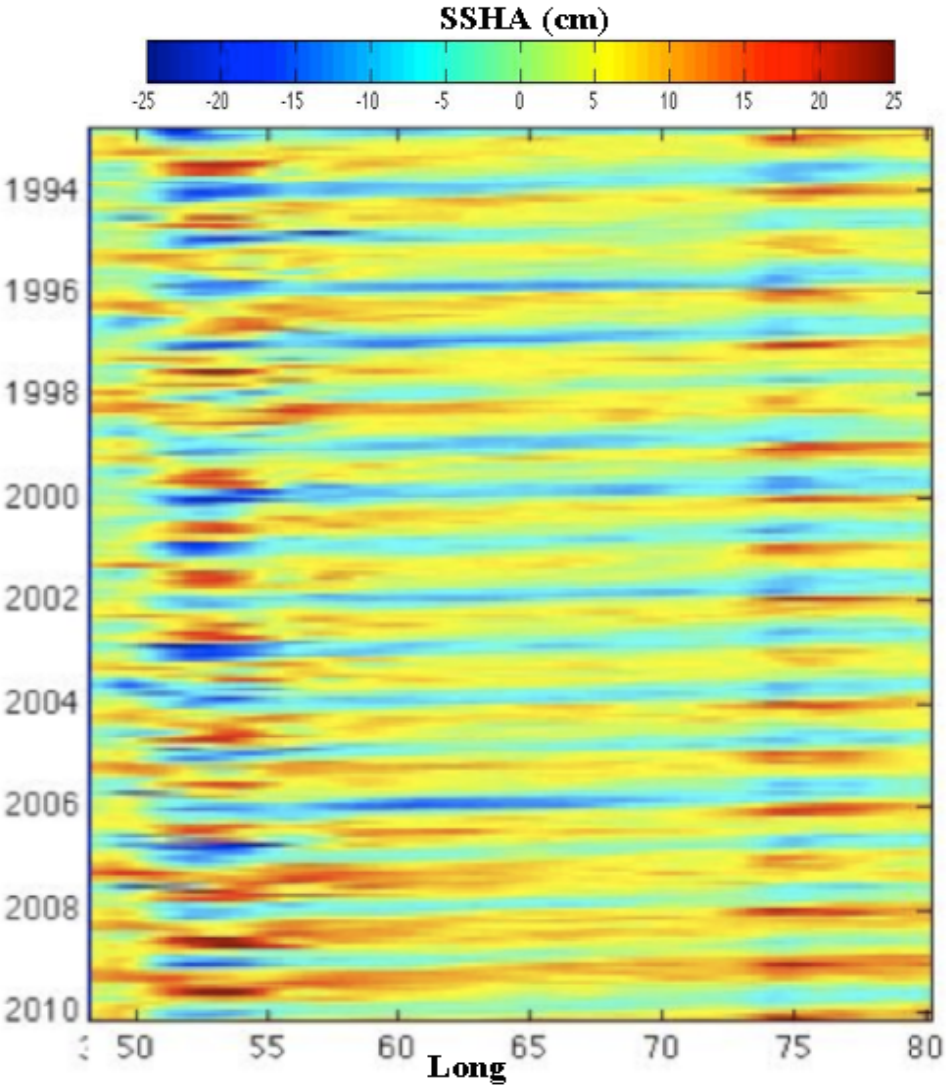

Figure 14 Hovmöller Diagram of SSHA at 8° North.

The monsoonal impact on the Indian Ocean results in strong winds and a high degree of seasonality in the ocean currents, potentially triggering the formation of Kelvin and Rossby waves that 'control the propagation of energy across the ocean' (Subrahmanyam and Robinson, 2000). In order to test this anomaly and evaluate its degree of impact, the authors employed satellite SSH datasets over a set period of time in order to determine the propagation characteristics of both Kelvin and Rossby waves. Their analysis of 1993 data revealed an excitation of Rossby waves by remotely forced Kelvin waves, which were localised around the equator and had a direct correlation with the circulation of the eastern equatorial Indian Ocean.

A key impact of monsoonal behaviour is the manifestation of eddies along the Somali coast, the authors determined that only in strong monsoon seasons are all three energetic eddies observed, the Southern eddy, the Great Whirl and Socotra eddy whilst during a weaker period only the Great Whirl was observed. Equatorial Kelvin waves were identified in direct response to the onset of the NE and SW monsoons wherein the energy contained within these wave streams was entirely dependent on the monsoon strength. Rossby waves were identified as key factors in the formation of the Somali Current and the generation of the Somali eddies of wind reversal (Subrahmanyam and Robinson, 2000). Ultimately, this analysis, although fundamentally limited by the scope of the temporal period, offers a valuable insight into feature-based satellite altimetry modelling, and demonstrates the viability of identifying anomalies of various climatological and oceanographic phenomena that have influence on localised events and patterns.

The abrupt change in the wind direction along the equatorial region in April and May (Figure 15) causes depressions in the thermocline along with a rise in the ocean surface, which is expected to propagate eastward along the equator as a downwelling Kelvin wave. By this process Kelvin waves deepen the thermocline in the eastern Indian Ocean and also cause significantly higher sea levels of the order of 5 to 10 cm in the east (Somayajulu et al., 2006). Such a height change should be detectable, however Kelvin waves cross the Indian Ocean within 30 days, and it is difficult to explicitly identify their propagation using SSH anomaly maps, although the maps do show positive anomalies. Along the equator these tend to appear as band-like structures with a spacing of 6-8 degrees. The theoretical phase speed for a Kelvin wave in the equatorial Indian Ocean is 2.4 ms^{-1} (McCreary et al., 1993).

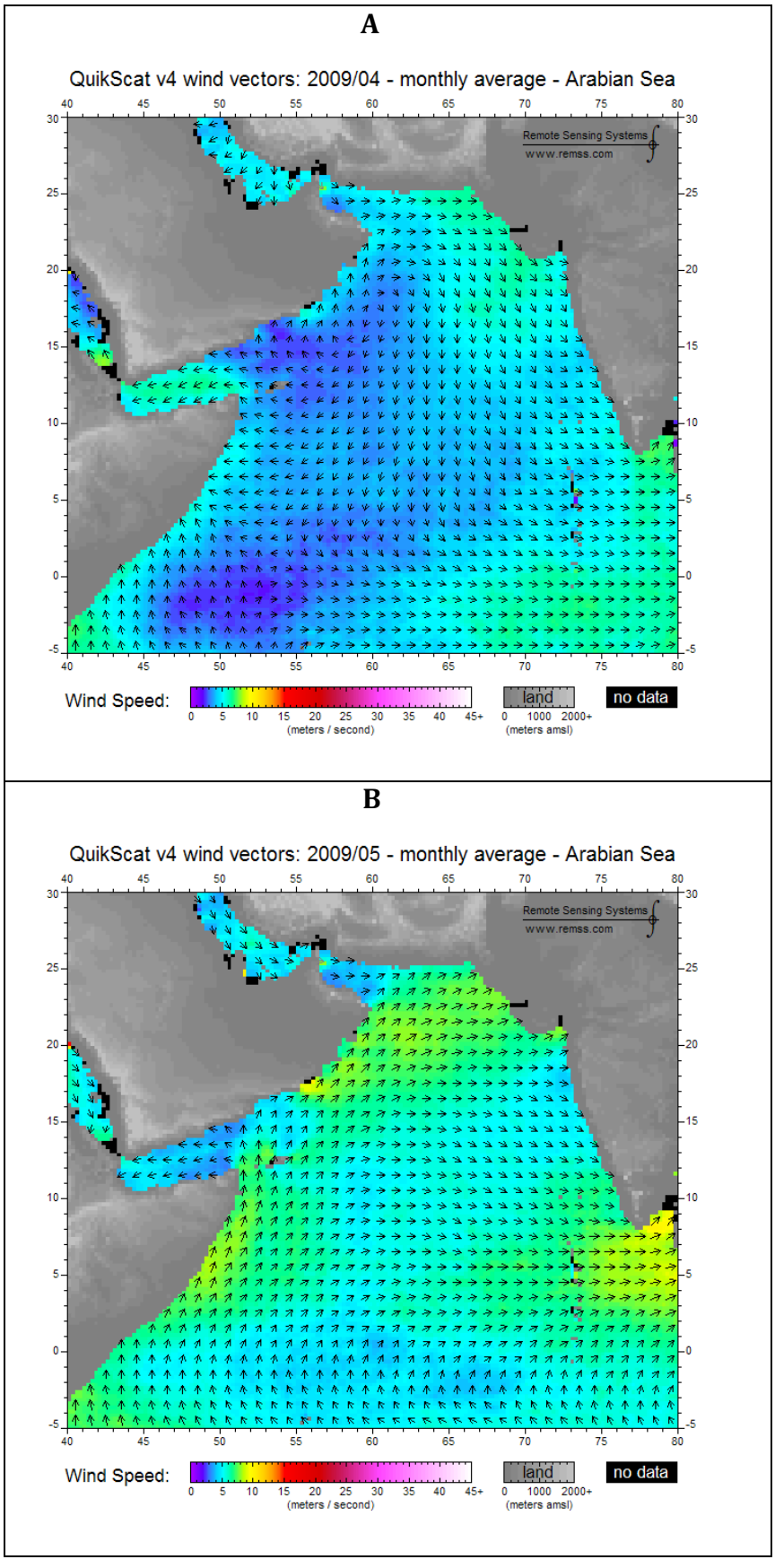

Figure 15 Wind direction change from northeasterly April 2009 (top) to May 2009 (bottom) southwesterly.

According to this scenario, the Kelvin waves, after reaching the eastern boundary, propagate as two coastally trapped Kelvin waves, one northward and the other southward. Some of the energy can also reflect back as a Rossby wave along the equator. There is some evidence for this; the high SSHA over the eastern boundary when the Kelvin wave arrives (in May) is reduced later on (in Aug), and appears to have moved westward. Such reflected Rossby waves would reach the western boundary (Somali Coast) around July.

On the other hand the coastally trapped Kelvin waves, which are generated at the eastern boundary, propagate northward along the perimeter of the Bay of Bengal and reach the west coast of India during Dec/Jan. This means that these coastally trapped Kelvin waves are much slower and take about 6 months to travel from the eastern boundary to the southern tip of the Indian subcontinent. After reaching the west coast of India, they may radiate as westward propagating Rossby waves to the interior of the Arabian Sea. The propagating Rossby waves would reach the Somali coast around March, taking about 3-4 months to travel from the west coast of India to the Somali coast. Jensen (1991) suggest that these wave like structures propagate as a ridge of high pressure, and when reaching the Somali Coast in April/May, they trigger the Somali Current after the onset of the strong south westerly wind, It is believed that sometimes the strength of the monsoon winds is not enough to generate a strong Kelvin wave along the equator in April, it may delay or create a weaker Kelvin wave in weak monsoon years. Ultimately the reflected Rossby waves may have less energy to feed to the western boundary currents and the surrounding eddies.

3.7 Summary

This chapter has described the research methods employed by various authors to capture and assess evidence for any relation between the IOD and major climate modes and to point out the correlation between these phenomena.. The most interesting result here was that when comparing the IOD and ENSO with SSHA along the equator over the Indian Ocean show closer relationship with the DMI than El Nino 3.4 index but from the regression and correlation maps of ENSO and IOD over the entire Indian Ocean it indicate that the ENSO has a broader influence beyond the equator. Rossby waves play an important role in the NWIO in particular over the manifestation of the Somali Current eddies.

4 NWIO Climate Variability Based on EOF Analysis

4.1 Introduction

In climate research, there are a myriad methods, many of which have been employed to success in modelling exercises and analytical studies over the past several decades of research. Given the advancement of satellite imaging and data collection tools, there is an increasingly rich spectrum of databases from which to pull empirical evidence that was gathered according to regular periodic intervals throughout a given geographic region. Although many of these records are specialised (e.g. coastal temperatures in North America, precipitation records in Japan, etc.), the breadth of evidence relating to the Indian Ocean and its surrounding regions is now rich and extremely detailed.

This chapter will introduce a closer look at the NWIO region through research methods that were employed over the course of this investigation in later chapters as well. Focusing on a leading method of oceanic and geospatial assessment over time, the EOF, the primary methods employed in this research is designed to not only model anomalous phenomena, but to identify potential links between hydrographical features and regional oceanic responses. In the literature review, a variety of recognised phenomena including the Great Whirl, the Socotra Eddy, Rossby and Kelvin Waves, and the Somali Current were all introduced as indicators of interest in this study. Each of these factors is largely tied to seasonal and climatological variations. The IOD also involves the unique opportunity to explore coupled events, whereby atmospheric factors have a direct influence on the evolution and manifestation of this phenomenon. For this reason, the focus of this research provides the opportunity by empirical study, to examine the characteristics of the IOD and its time-variant influence on climate variability and impact factors. The following sections will introduce the underlying theoretical and empirical background of the techniques employed, discuss the diverse range of data sources used, and compare datasets and assessment techniques. Then we introduce the findings and provide an in-depth assessment of the broad scope of methods and datasets that were explored over the course of this investigative process.

4.2 Data and Resources

The data captured over the course of this chapter was focused on the north western Indian Ocean and Arabian Sea, an area bounded on the east by the Central Indian Ocean, on the west by the African continent, by the Arabian Peninsula to the north and by the south Indian Ocean to the south and located between latitude 25^{o} N- 15^{o} S and longitude 35^{o} E - 80^{o} E. The major oceanographic processes occurring in this region such as eddy formation, upwelling and currents and have high seasonal variability because of the monsoon and its impact on variations in climate.

This study uses the altimetry data (SSHA) after being smoothed from the oceanography missions monitoring the global ocean circulation, T/P and Jason-1. The selected period of this study within this data set is January 1993 to December 2009 The data sets has monthly temporal scale and has a spatial resolution of (0.25^{o} x 0.25^{o}) covering over NWIO (15S to 25N and 35E to 80E). As correlated variables, SST captured through the Tropical Rainfall Measuring Mission (TRMM) satellite launched in 1997, which was measured by the TMI, the assessment here is for the period from January 1998 to December 2011. Validation techniques include algorithmic removal of surface roughness effects and comparative in-situ measurements, demonstrating a degree of variance that is minimal and sufficiently accurate for modelling temporal-spatial patterns. For the TMI-recorded SST binary files, data was automatically delimited according to the geographic and temporal (monthly) limitations, providing an accurate measurement of localised variations with minimal quantitative interference.

Also the monthly SSTA of Reynolds and Smith Optimum Interpolation version 2 (Reyn_SmithOIv2) (iridl.ldeo.columbia.edu) is used in this chapter for the same time period and spatial coverage used for the TMI data. The data is a monthly one-degree global SSTA climatology that is derived from monthly Optimum Interpolation (OIv2) SSTA analyses with an adjusted base period of 1971-2000, constructed by the Climate Prediction Center (CPC) at NOAA, that was used in computing the SSTA field by a weighted monthly mean and the current observed Reynolds SST field. The satellite data is adjusted for biases using the method described by Reynolds and Marsico (1993). A description of the data can be found in Reynolds and Smith (2002).

4.3 Methodology

4.3.1 Empirical Orthogonal Function (EOF)

EOF methodology of site mapping, variable identification, and time series control is widely embraced to help in smoothing and prediction and reduce the larger number of variables of the original data without compromising much of the variability of the data. Throughout the past several decades, researchers have largely accepted EOF as an authoritative mechanism in climatological and remote sensing applications, simply because the EOF analysis has several advantages like it is a convenient method for characterizing dominant spatial pattern of variability with a time series explaining the greatest amount of variability which are linearly independent. In their application of this analytical technique to the Spanish coastline, Baldacci et al. (1998) define EOF as 'a statistical method used to decompose a multivariate data set into a linear combination of uncorrelated separate functions of the original variables'. Within these calculations, these stratified modes are organised according to their energy level, whereby first order modes remain of primary interest as they represent the 'principal behaviour of the decomposed signal; in fact, higher order modes represent marginal motions and noise effects that may be discarded' (Baldacci et al., 1998). Singular value decomposition (SVD) is widely recognised as the optimal method for calculating EOFs, decomposing the data matrix into three distinct matrices that contain the eigenvalues, eigenvectors, and eigenfunctions.

Essentially, the SVD ranks the 'modes in order of decreasing variance' whereby 'the size of a mode's eigenvalue in relation to the size of the other modes eigenvalues gives the amount of variance in that mode relative to that of the other modes' (Keiner and Yan, 1997). As such, the first mode represents the majority of the degree of variance, findings that can be then compared with known climatic or environmental phenomena in order to identify the relative impact and importance of a given phenomenon. In his comprehensive analysis of variance and anomalous geographic behaviour in the North Indian Ocean, Rojsiraphisal et al. (2007) recognised the principal component analysis (PCA), widely known, as EOF is a valuable quantitative technique that can remove redundancies from a multivariate dataset. The following is a mathematical representation of this analytical model that has been adapted from the Rojsiraphisal et al. (2007) discussion in order to highlight the underlying quantitative decomposition that enables multivariate analysis through EOF.

The initial dataset is relatively straightforward and consists of *K* locations (space) and *N* samples (time). From a quantitative perspective, the comparison of these variables is expressed as a matrix operation, whereby analysis may be completed as *N* points in *K*-dimensional variable space (spatial variation) or *K* points in the *N*-dimensional sample space (temporal variation). In order to describe this relationship according to the SVD function, the following equation is defined according to the vector-based comparison of columns with orthonormal properties:

$$A = U\Omega V^{\tau} = \sum_{ixt}^{r} \varpi_1 U_1 V_1^{\tau}$$

Equation 4.1

A: EOF mode, U: left singular vector, V: right singular vector
r: number of modes contained in the field,

In this particular equation, $U_{(Kxr)}$ and $V_{(Kxr)}$ are defined as the left and right singular vectors whose columns have orthonormal properties while $\Omega_{(rxr)}$ is a singular matrix whose elements are non-negative numbers called the singular values. Based on calculation of the eigenvector according to traditional orthogonal assumptions, PCA may be used to separate the uncorrelated variables from each other (Rojsiraphisal et al. 2007). Due to underlying property of the singular values in which $\omega_1 \geq \omega_2 \geq \omega_3 \geq \cdots \geq \omega_k \geq 0$ then the first term of the estimation of data matrix $\omega_1 U_1 V_1^{\tau}$ accounts for the largest percentage of variance of A^i, whilst subsequent terms account for the largest possible variances in lower indices (Rojsiraphisal et al. 2007). It is through recognition of this maximum degree of variance that the application of EOF to single variable analysis of Indian Ocean variability can be effectively and accurately described.

In spite of the widely accepted value of the SVD/EOF analysis, eigenvectors are weighted by the square root of their corresponding eigenvalues, so that the weights represent the correlations between each variable and the principal component (Lamont-Doherty Earth Observatory, LDEO, 2012). As such, the primary rotations are simple expressions, which approximate a simple structure through the application of algorithms that distributed the PC loadings so that the dispersion is maximised. An alternative technique known as Varimax rotation has been accepted as a means of reducing the variances of the projection of the data onto the rotated basis, where the projection is the principal component time series (LDEO, 2012).

Accordingly, such analysis improves alignment of the basis with the actual data and improves the relationship between their spatial and temporal patterns and known physical mechanisms. Varimax effectively rotates the axes of a plot such that the eigenvectors remain orthogonal as they are rotated. The rotations are used in the principal component analysis so that the axes are rotated into a position in which the sum of the variances of the loadings is the maximum possible (LDEO, 2012). Although this unfortunately do not solve the disadvantages of the EOF method like the sensitivity to choice of spatial domain and time period and the possibility of the EOF analysis creating patterns from noise meaning the features reflected do not necessary relate to a physical meaning.

There are a broad range of methodological techniques employed in the collection and analysis of geospatial datasets related to oceanic anomalies and climatologic phenomena. Specific to modelling climatic events, there are a broad range of studies that have employed EOF in describing and analysing data sources ranging from SST (Armstrong, 1995) to SSH to rainfall in order to characterise the impact of distinct events and anomalies. This research extends such past examples, focusing on leading indicators associated with anomalous IOD phenomena including SST, SSH, wind, and rainfall patterns.

Shinoda et al. (2004) employed EOF analysis of the IOD in a correlated analysis of ENSO-related phenomena and IOD patterns. Their analysis endeavours to address the key concern of interoperability between ENSO and IOD variability related to the tropical Pacific. This particular research methodology focused on a 40-year simulation model, which integrated a comprehensive comparison of experimental evidence collected from the Geophysical Fluid Dynamics Laboratory (GFDL) with EOF applied on remote sensed data to investigate the IOD anomalies variation. Although the authors recognise that the subsurface dipole variability is 'efficiently identified by EOF analysis of equatorially averaged temperatures', previous concerns regarding ENSO correlation were inadequately addressed using these quantitative models. Accordingly, composite analysis of the subsurface dipole correlation with ENSO phenomena demonstrated the relationship between surface warming and surface zonal winds, positive horizontal temperature advection, and vertical upwelling. Conversely, the EOF modelling of SST anomalies and temporally-linked climatic variability was recognised as of particular importance to this study and these particular techniques were incorporated into the evaluation of IOD phenomena.

4.3.2 Rotated EOF

Although the EOF served as the primary mechanism for modelling variance and the degree of periodicity associated with distinctive IOD phenomenon, the widespread application of this technique in geo-spatial modelling should not be interpreted as validation of its accuracy. Navarra and Simoncini (2010) remind that there is a fundamental difficulty associated with identifying real physical patterns from EOF stems due to their relative orthogonal nature.

Specifically, the authors argue that 'orthogonality translates into the fact that typical patterns appear in the secondary (higher order) EOF' whereby, 'the first EOF has little structure, the second has a positive and a negative centre, and the third more centres and so on, in a way so as to maintain orthogonality' Navarra and Simoncini (2010). For this reason there is a high potential for modelling misleading or inaccurate representations via EOF analysis, particularly in relation to artificiality and an inaccurate or over-represented degree of variance. For this reason, the technique of rotated EOF modulation was employed beside the standard EOF.

Rotated EOF reflects the transformation of the EOF into another set of coordinates, whereby in the revised matrix, the non-orthogonal, reflects a correlation between the various columns (Navarra and Simocini, 2010). As a direct result, patterns can be generated and reconciled according to distinctive physical relations in the data. In the rotated EOF, spatial variance is concentrated over as few points as possible in order to identify simpler patterns, or a revised concentration of EOF coefficients into a few modes so that for each variable, only a few number of EOFs are needed to explain a large degree of variance (Navarra and Simocini, 2010).

The value of the rotated EOF will be highlighted throughout the data presentation section, as key variables such as SSHA and SSTA are compared according to their standard EOF representation and their rotated EOF outcomes. Distinctively, these secondary patterns offer reflection of climatologic and oceanic phenomena that progress research in this field towards a more comprehensive understanding of NWIO fluctuations and singularities.

4.3.3 Research Instruments

The International Research Institute for Climate and Society (IRICS, 2011) is an online collaborative database management server, which integrates quantitative modelling techniques into a large-scale programming-based research tool. Sponsored by such leading institutions as Columbia University and supported by a range of researchers including Reynolds et al. (2002) this wealth of oceanographic and climatologic indicators is designed to provide an online, reliable, and accessible tool for oceanographers and climate researchers across the globe. There are currently over 400 climate-related datasets ranging from station and gridded observations to atmospheric and satellite sensing models.

The most significant value identified within this database is the expert level data assessment tools that are provided. Stepwise data assessment guidelines for SVD (EOF), Varimax Rotated EOF, time series, and correlation analyses have been included in the Appendix. By focusing on anomalous datasets over monthly records, it was possible to compare the IRICS outputs with those downloaded and described via local assessment using Matlab (appendix E) from NASA databases. Further, the IRICS database allowed for seamless exploitation of findings, providing time series and spatial analyses, statistical assessment of eigenvalues, and mouldable, targeted comparisons of visual time series datasets. Ultimately, it was determined over the course of this research that the IRICS tools were invaluable in not only validating the output results from the local analysis, but they were a mechanism for capturing more in-depth datasets that would have otherwise been inaccessible due to their methodological and data-based complexity.

4.4 SSHA Empirical Orthogonal Function Analysis

4.4.1 SSHA Standard EOF Assessment

The following section starts with the application of the standard EOF analysis in Matlab on SSHA from T/P+Jason1. Table 3 offers an overview of the level of variance that has been explained by each EOF. What is immediately clear is that around 60% of the total variance in this model is explained by the first three EOFs, with 25.54% of the variance explained by the first EOF. Although higher order EOFs can contain information about single events for example, in general the evidence offered in EOFs 4 and 5 have a relatively limited impact on anomalies in this dataset, restricting conclusions and inferences in this data assessment to first-degree impacts.

Table 3 Percent variance explained by first 3 SSHA EOF modes

Mode	Percentage Variance
1st Mode	25.54%
2nd Mode	19.70%
3rd Mode	15.43%

It is essential that the EOF be compared in terms of their spatial and temporal patterns, thereby describing the geospatial response and intra-regional phenomena affecting the variance in SSHA. The spatial patterns are presented in Figure 16, whilst the temporal patterns are offered in Figure 17.

In all the spatial and temporal EOFs plots, the sign is arbitrary and only represents the variance degree, therefore the regions with negative values don't necessary means that they are actually lower than the mean value and show low SSHA rather it describe how far they are away from the mean and the same is for those regions with positive values. The temporal patterns of variability are described by the eigenvectors and show how the values of the spatial patterns vary over time. The main modes of variability can be related to the original data by considering that negative regions are areas with lower eigenvector (troughs). Conversely, when there is a peak in the eigenvector it reflects a positive area. The green colour regions that are little affected by the peaks and troughs show areas near the temporal mean value.

As reflected in Table 3, most of the variance is explained by the first three EOFs (Figure 16); therefore, it is necessary to consider all three EOFs when relating the spatial patterns back to the original data. EOF 4 and 5 explain only about 9% between them. These recorded patterns are not likely to be significant.

EOF1 shows a very similar pattern during the southwest monsoon from the SSHA image between July and September (figure 8) with a strong positive pattern in the northwestern Indian Ocean, with marked circular features off Somalia. A negative stripe along the coast of Somalia contrasts with the positive feature offshore. There is also a positive pool running in the Arabian Sea at 60-70°E, there is also a process of coastal upwelling that can be identified, characterised by low SSHA near the Somali coast.

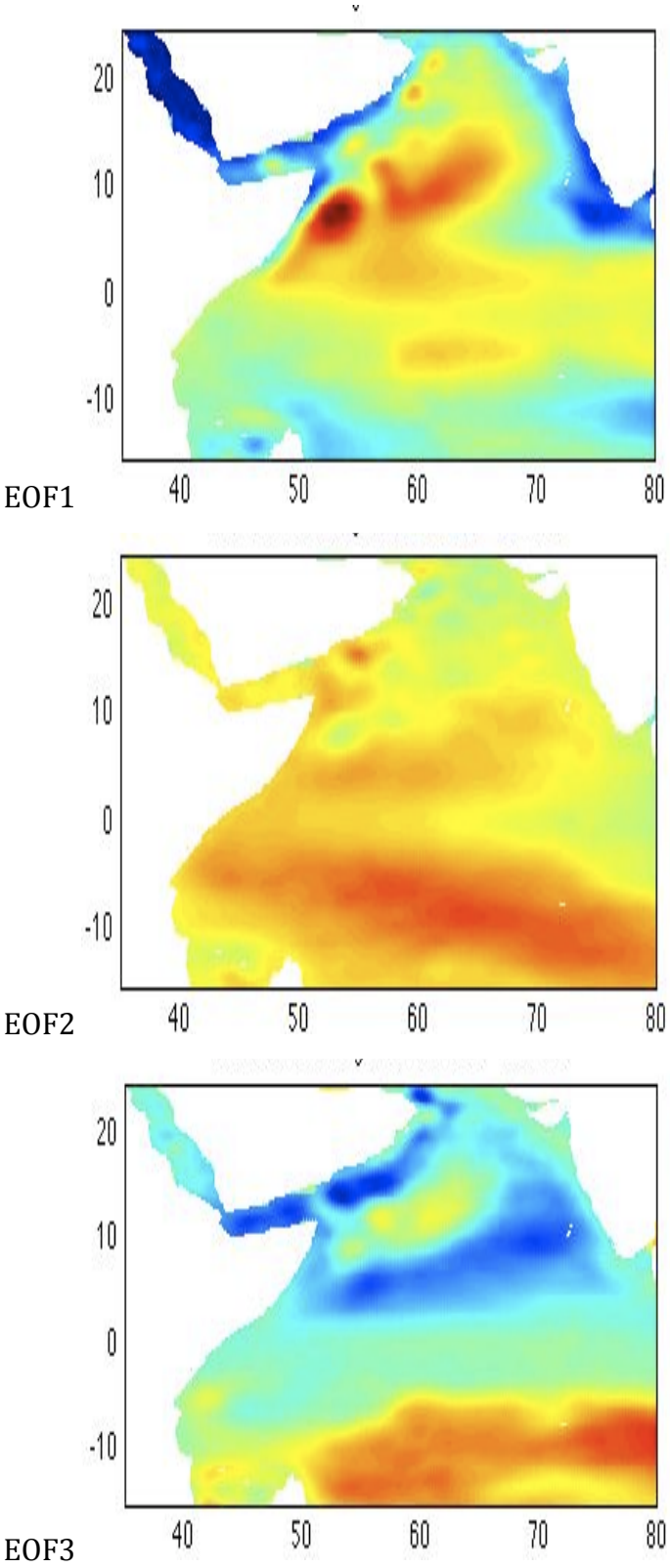

Figure 16 SSHA EOF 1st, 2nd and 3rd Modes, all three EOFs is relating the spatial patterns back to the original data, with EOF1 clearly showing the most variability at a positive round feature indicating the Great Whirl and a negative stripe along the coast of Somalia that is related to the Somali Current.

The upwelling off the Somali coast is geostrophic; a further factor affecting the variation of SSHA is the horizontal mixing along the exterior of eddies (Bruce, 1984). When eddies form, they trap coastal water, and when they propagate offshore, they carry the trapped water. There are cyclonic and anticyclonic eddies that can be identified through spatial analysis. At the centre of a cyclonic eddy, there is an upwelling of water to the surface wherein water diverges, resulting in a low SSHA. In contrast, at the centre of an anticyclonic eddy, there is downwelling, in which the water converges and sinks, resulting in an increase in the SSHA. In EOF1, this phenomenon is identified, with a stark contrast between positives and negatives localised just above the equator and around the 50° longitude. In EOF2 a diffuse green region of little spatial variability and values close to the mean is recognisable in the east over the equator. A strong positive pool extends along the basin just south of the equator. In contrast to EOF1, there are no negative values in EOF2 and both the positive round features and the negative stripe are less marked.

EOF3 is indicative of a high degree of periodicity associated with anomalous SSH in NWIO. There is a central pool of medium values in the Arabian Sea surrounded by negative values between 55 and 65°E. North of the equator there is a pool of negative values and south of the equator it is the opposite with positive values, whilst along the equator, the data is directly linked to the mean. Essential to the degree of variability in the SSHA are a range of internal forces, wherein variability and anomalous behaviour are largely attributed to the degree of nonlinearity of the equations, which govern the characteristic dynamics of the IO (Wirth et al., 2002).

Figure 17 presents the seasonal pattern in PC1 where the sign changes every 6 months during which the maximum value of the eigenvector is reached at the beginning of June and the minimum at the beginning of December, decreasing gradually and then increasing from December through to the following June. The presentation of the associated time series PC2 reveals that such variation is not constant over time (when compared with PC1). In fact, PC2 highlights primarily negative values of eigenvectors from the start of the data set until around 2003 with the exception of 1994 and an extremely high positive value in 1997. Subsequent positive values are relatively consistent until manifestation of aberrations in 2005. These findings indicate an interannual cycle at PC2 (possibly an inter-decadal cycle) with trend variations prominent towards the last 7 years of the total 17 years of data.

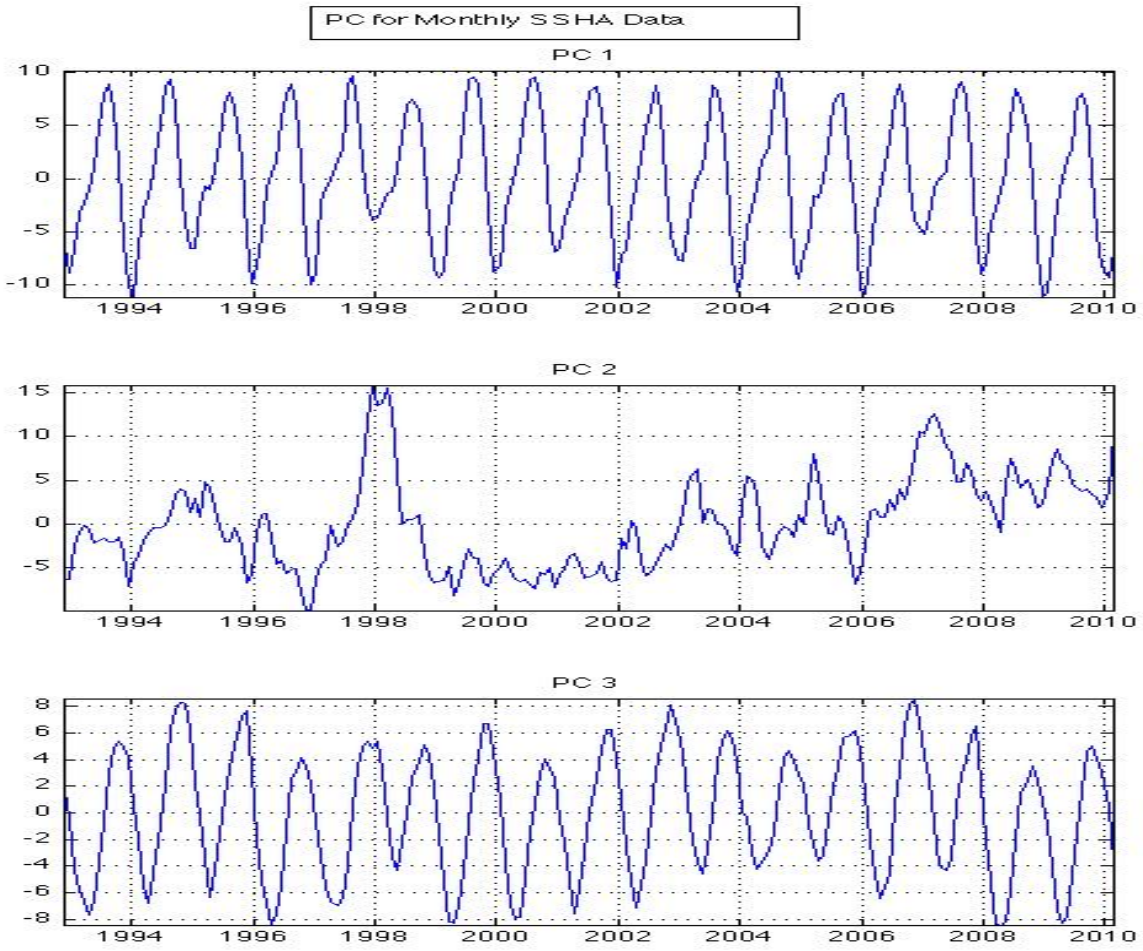

Figure 17 PC For Monthly SSHA Data, from T/P+Jason for the period of 17 years indicating a seasonal cycle in PC1 and PC3, with a interannual cycle at PC2 (possibly an inter-decadal cycle).

In their assessment of interannual variability, Li et al. (2006) referenced the leading EOF mode as a representation of intraannual variability, whilst the second EOF mode reflected an interdecadal mode that was characteristic of the coupled anomalous surface-atmosphere relationships. A similar pattern to PC1 is presented in PC3 with a fall of the eigenvector in October and finishing in March. Subsequent increases occur from March to October with a 3-4 month phase shift between the peaks of PC1 and PC3. Accordingly, the evidence in PC's 1 and 3 is largely reflective of seasonal variability, whilst SSHA over an intradecadal period are reflected in PC2, demonstrating a degree of inconsistency, which has experienced a gradual positive increase since around 2002. Such findings may reflect evidence of climatological patterns that are shifting; however, the evidence captured by this singular EOF analysis will need to be compared with other indicators, particularly SSTA in order to identify any significance in this remarkably constant anomalous progression.

In EOF1 there are two anticyclonic eddies at 5-15°N that can be identified in the majority of the monthly SSHA images from July to September. Identified by Fischer et al. (1996) as the Great Whirl and Socotra Eddies, they are geographically fixed and they can be traced to a similar temporal period to that of the southwest monsoon (Bruce, 1984). The temporal variability of these eddies demonstrates a strong seasonal pattern across all PC, but particularly in PC1 and PC3. This 3-4 month phase shift is indicative of a diverse seasonal pattern for the two modes and could also indicate a propagating feature. In order to identify the key processes, which are involved in the modes of the EOFs, a more in-depth discussion of the spatial pattern will be conducted.

The negative and positive regions in the first three EOFs (Figure 16) demonstrate key features that are most highly variable in the NWIO and the Arabian Sea (AS). One of these key features manifests in the region adjacent to the coast of Somalia, which is strongly influenced by monsoon patterns. This conclusion is supported by several previous studies in which Vialard et al. (2012) identified an upwelling along the Somali Coast in the Arabian Sea during the southwest monsoon. The small round positive feature identified in EOF1 in this region is likely related to the Great Whirl. The second feature to the north is likely to indicate the Socotra Eddy that shows lower amplitude and smaller spatial scale. Both of these eddies form in around the same geographical location each year and are able to be captured via the EOFs. In EOF3, the spatial pattern is similar with the north-south seesaw seasonal time scale, but the Somali region is represented by more negative values.

The Great Whirl is known to move north from 5° to 10°N. This movement is consistent with the phase shift that is indicative of a moving feature. Another marked feature is the positive value identified along the region south of the equator in EOF3. The pattern in this region is nearly reversed from EOF1 to EOF3. These findings could indicate an alternating equatorial jet, one that is strong during the transition months of April to May and October to November (Wyrtki, 1973). Whilst PC1 and PC3 are marked primarily by seasonal variation, PC2 indicates inter-annual variability. Fluctuations in 1998 are higher than in other years, most likely associated with the strong positive IOD event occurring in the end of 1997 and the strong ENSO event in 1998, Figure 18 shows a correlation between the IOD mode index (DMI) and PC2 of about $r = 0.6$ at a time step lag of -2, Also PC2 shows a change in the average of the eigenvector with a higher mean after 2002, a potential indication of the effect of global climate change.

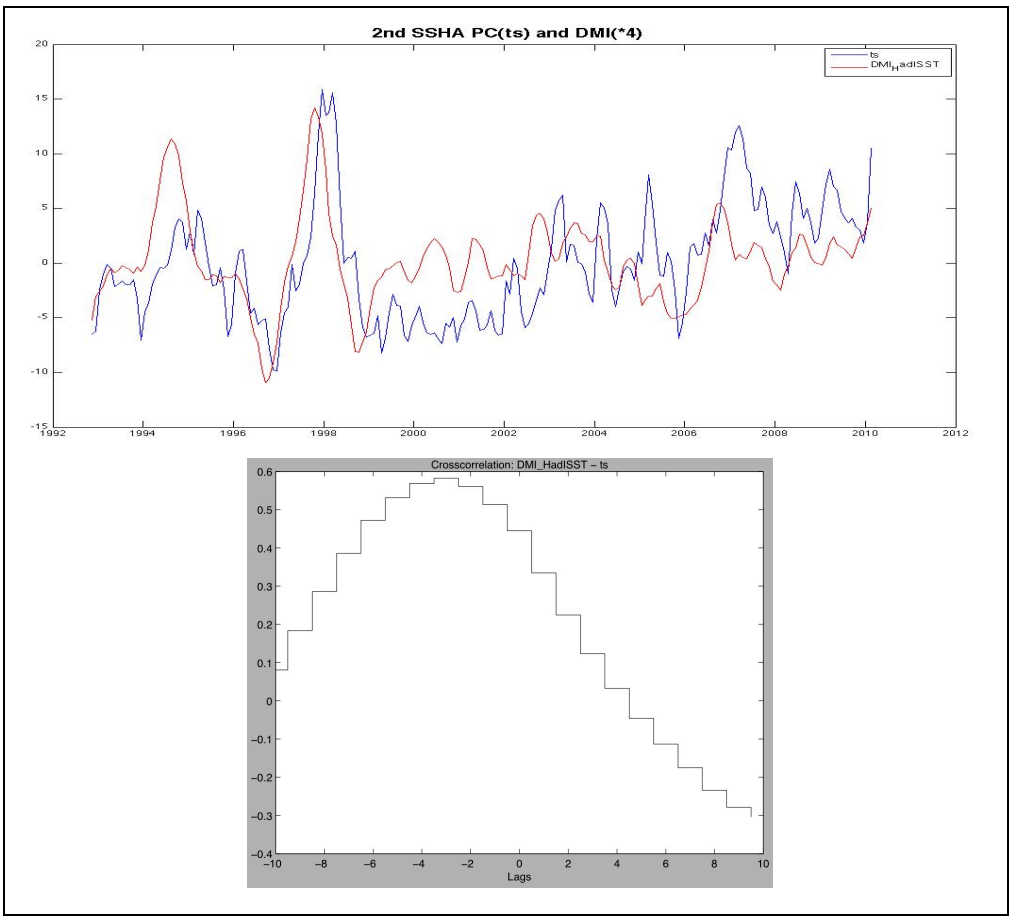

Figure 18 Monthly time series of SSHA PC2 blue line and the IOD mode index (DMI) derived from Hadley Centre for Climate Science SST multiplied by red line (top), with the correlation of about r = 0.6 at a time step lag of -2 between the two time series (bottom).

4.4.2 SSHA Rotated EOF

Although the EOF itself offers a valuable interpretation of SSHA data, rotated EOF provides a reduced degree of variance of the projection of the data, wherein the projection is the principal component time series (IRICS, 2011). Figure 19 reveals the first three EOF modes that similar to the unrotated EOFs account for just over 63% of the total variance of this model. There is a high degree of correlation between these two particular analyses, with the first EOF mode exhibiting a similarly strong southern negative with minor positives along the Somalia coast. In the second EOF mode, there is a strong central positive which is consistent with hydrographical patterns including the Great Whirl and the Socotra eddies. The third EOF mode, on the other hand, reverses its emphasis, showing a range of negative values as opposed to the previously indicated positives throughout the northeastern and northwestern segments of this particular geographic segment.

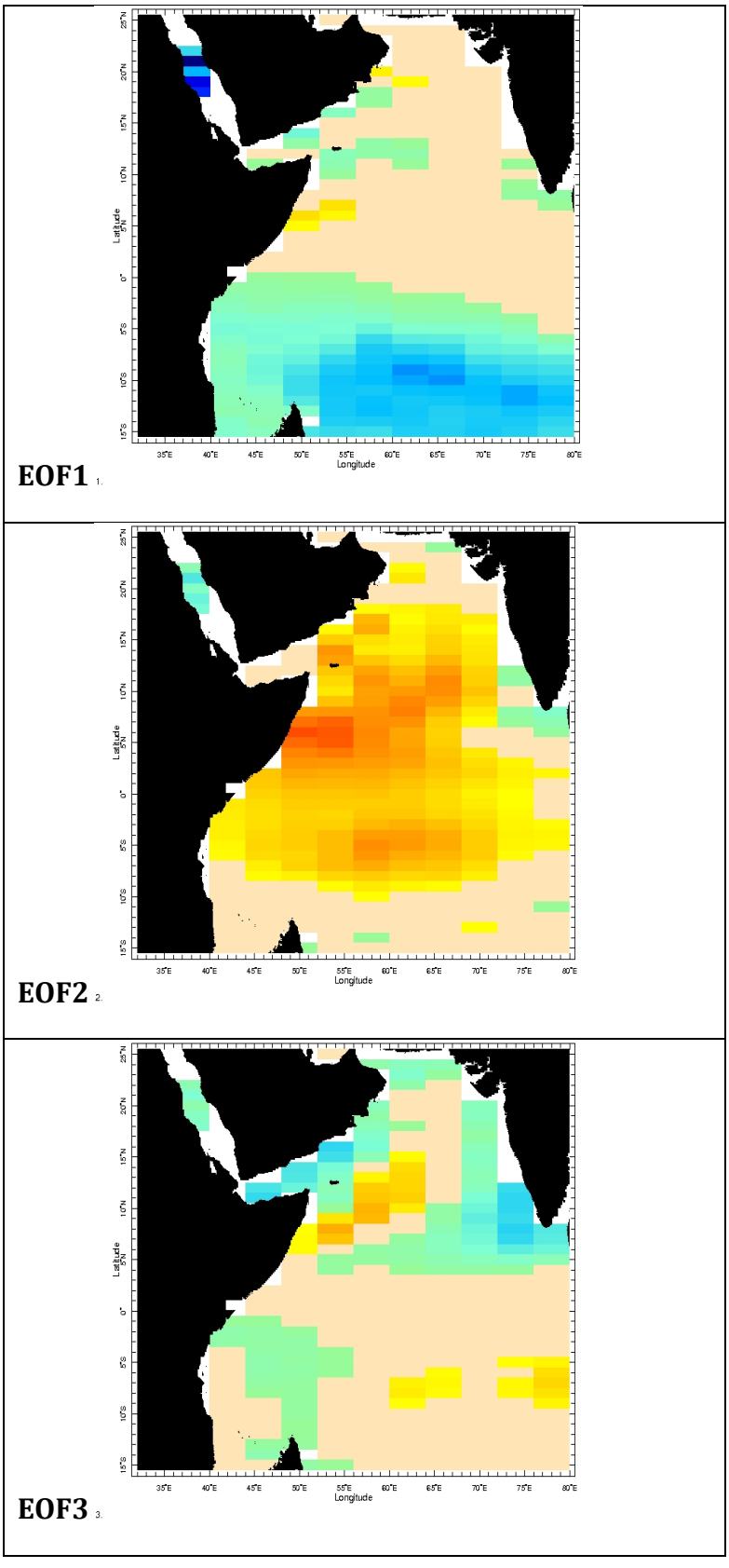

Figure 19 SSHA Spatial Rotated EOF 1st, 2nd and 3rd Modes

A comparison of the time series data captured via PC time series for these three rotated EOFs also reveals several distinctions between the rotated and non-rotated EOF mode. Figure 20 highlights the rotated PC of the 1st mode that offers consistent lows just prior to 1995 and 1998. Amongst the positive indicators of what is expected from the rotated EOF, however, there is a higher degree of variability, which is likely related to the narrowed depth of this assessment with different time periods.

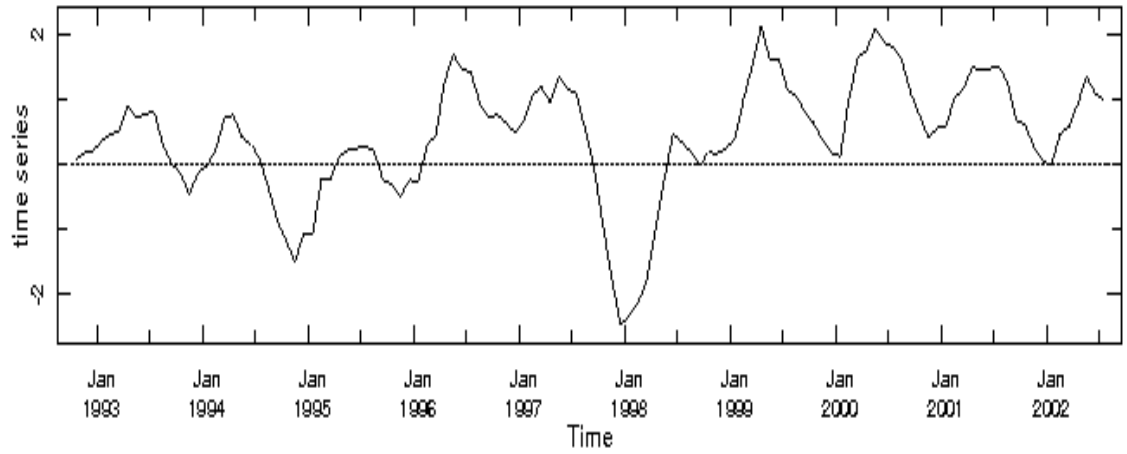

Figure 20 SSHA Rotated 1st PC Mode

Figure 21 offers a revised insight regarding the second PC mode, further restricting the degree of time series variance and indicating a cyclical mode with deep negative cycles on an annual basis with the exclusion of 1998. Considering this high degree of variance and the PC outcomes retrieved from the Matlab assessment, there is a high degree of likelihood that a replication of the 1998 anomaly would have been identified in 2008 had this data stream been extended beyond its 2002 threshold similarly to the 2nd PC from the Matlab assessment.

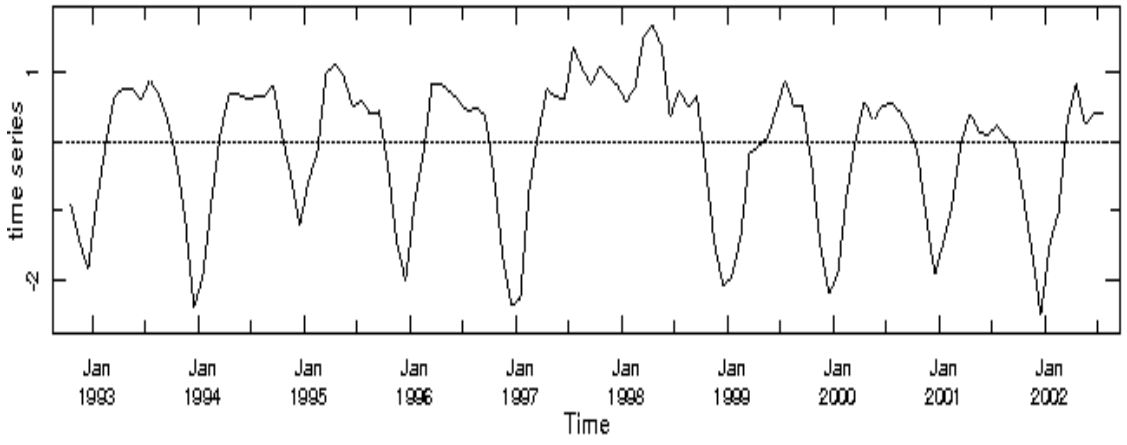

Figure 21 SSHA Rotated 2nd PC Mode

Finally, the rotated 3rd PC mode is a direct mirror of the periodic manifestation intervals of apparent IO SSHA phenomena, but that's only because the sign of EOF is arbitrary and it is multiplied by time varying factor which can be + or -, with a similar phase shift to previously recorded data of around 3-4 months. Such findings are indicative of the strong degree of consistency reflected in SSHA patterns throughout this region as a direct result of localised phenomenon and a linked oceanic-climatologic impact zone.

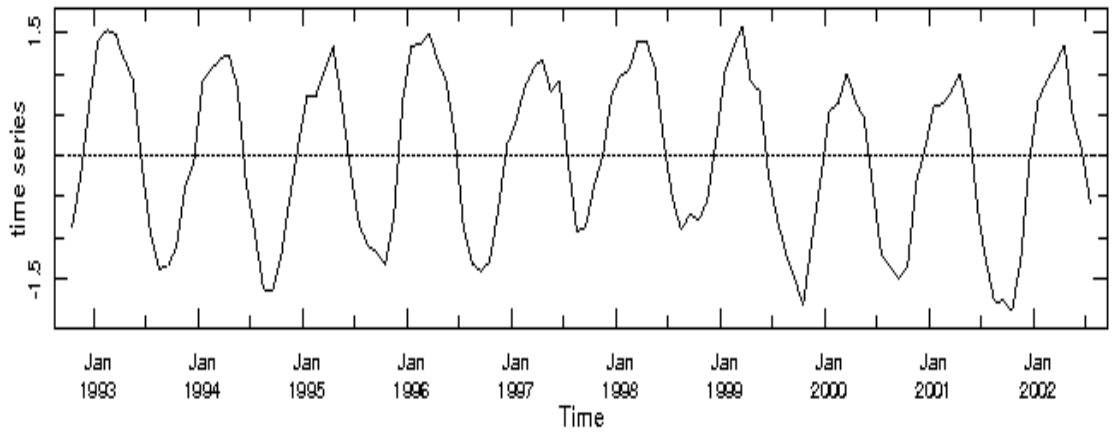

Figure 22 SSHA Rotated 3rd PC Mode

4.5 SSTA Empirical Orthogonal Function Analysis

4.5.1 Standard SSTA EOF Assessment

As an overview to the expectations in the anomalous and periodic datasets highlighted in this analysis, it is valuable to first introduce leading evidence captured in relation to SST data over several key past studies. For example, in their comprehensive analysis of SST anomalies in the 1990's, Salvekar et al. (2002) describe distinct changes in the cooling cycle of various sectors of the IO.

These findings of instability are indicative of a precursor trend, wherein cooling began prior to the more usual onset date as the currents adapted to monsoonal winds. The research also indicates anomalous cooling in particular years that raise the question what are the various factors influencing the climatic behaviour during these specific time periods. There are other factors relating to anomalous cooling and warming factors that have more recently been identified through empirical assessment as well. For example, Jayakumar et al. (2010) demonstrated that during the boreal winter, Madden-Julian oscillations are linked to a prominent maximum intraseasonal SSTA variability in the Southwestern Indian Ocean.

In this section we apply the standard EOF analysis on SST and SSTA, first using Matlab (SST) then the IRICS based assessment tool (SSTA), with each tool implying a different dataset. First, the Matlab tool that uses SST data via the TMI database, then the IRICS, which incorporates the Reynolds et al. (2002) model of SSTA data.

Table 4 highlights the significant percentage of variance that was explained by the first three EOF modes (90%). With 59.2% of the total variance, it is clear that EOF 1 is the most significant factor associated with anomalous SSTs over the past decade. EOF 2 accounted for just 27.7% of the variance, whilst the significance of EOF 3 was much lower in this model than under the SSHA calculations at just 2.5% of the variance and therefore it won't be discussed.

Table 4 Percent variance explained by first 3 SST EOF modes

Mode	Percentage Variance
1st Mode	59.2%
2nd Mode	27.7%
3rd Mode	2.5%

Figure 23 presents the spatial relationships reflected by these SST EOFs and their respective variances. Under the first EOF, there is clearly a strong negative across the western region of the IO, with the most significant variance accounted for at or below the equatorial region indicating the seasonal cycle on the NWIO and strong positives in the regional seas (Red Sea, Persian Gulf and Arabian Sea). There is a strong positive pool in EOF 2 in the northern region of the Arabian Sea with a cool negative pool bordering the lower boundaries of this model below the equator.

It is equally clear that EOF 3 did have impact on the degree of SST variance calculated by this model; however, due to its relatively insignificant level, the results are likely due to oceanic or climatological anomalies, which manifested throughout this region without constancy.

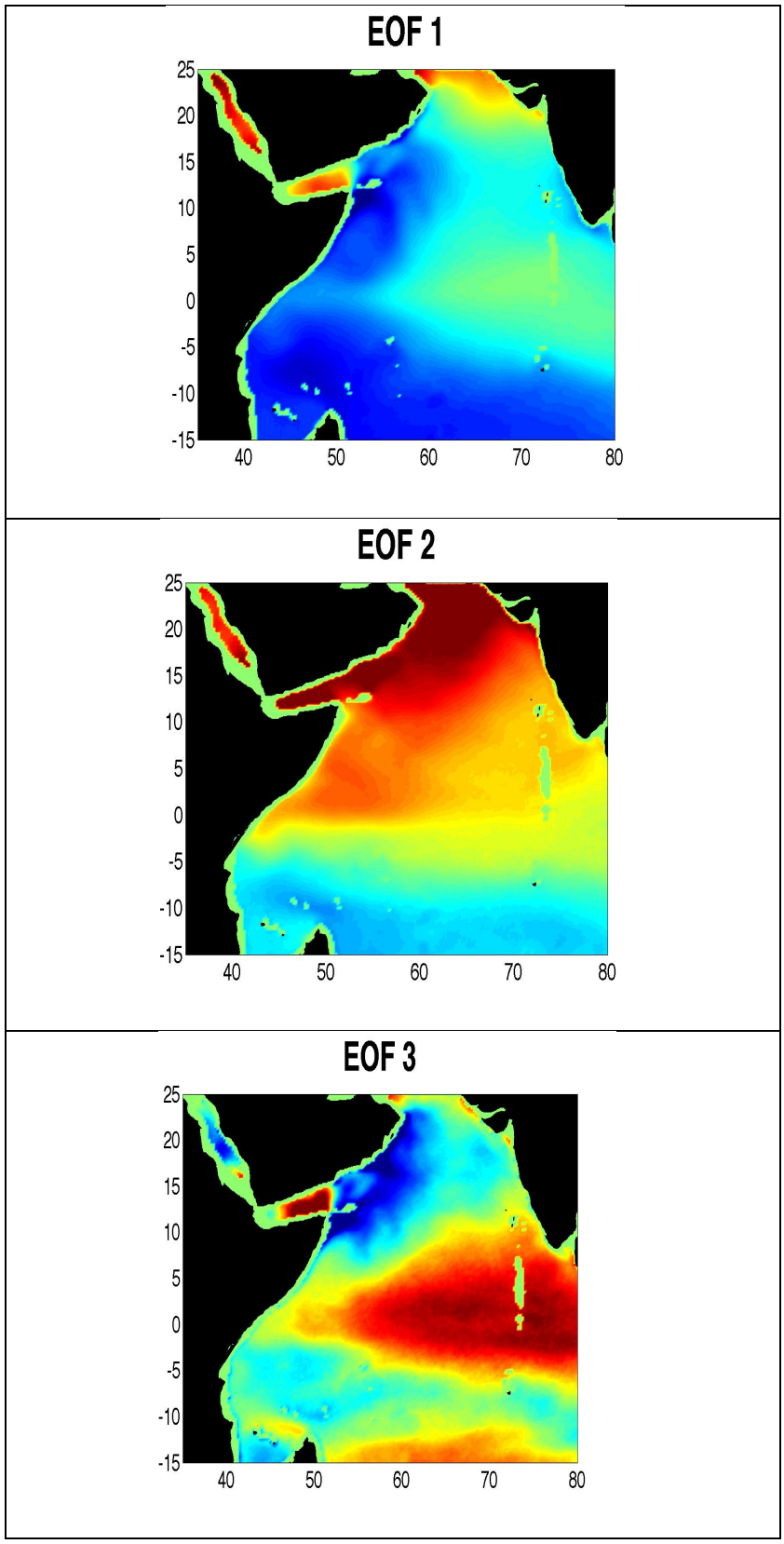

Figure 23 SST EOF 1st, 2nd and 3rd Modes

In order to demonstrate the temporal effects of SST anomalies and variability, Figure 24 highlights the periodicity of the SST according to the EOF assessment. One primary distinction between this particular model and the features observed within the SSHA assessment is that SST periodicity is reflective of 14 years of a high and low seasonal pattern, which is particularly demonstrated in PC1. In PC2 there is clearly an opposite direction of the PC1 highs that is preceded or followed by peaks and troughs at 6-months intervals, with one peak/trough stronger than another most probably the higher peaks and lower troughs is associated with summer monsoon while the lower peaks and the deeper troughs is reflecting the winter monsoon. Consistent with the high degree of variance in the EOF spatial model, PC3 is reflective of relatively limited impact on this particular model, and is more likely linked to anomalous records, missing or inconsistent data records.

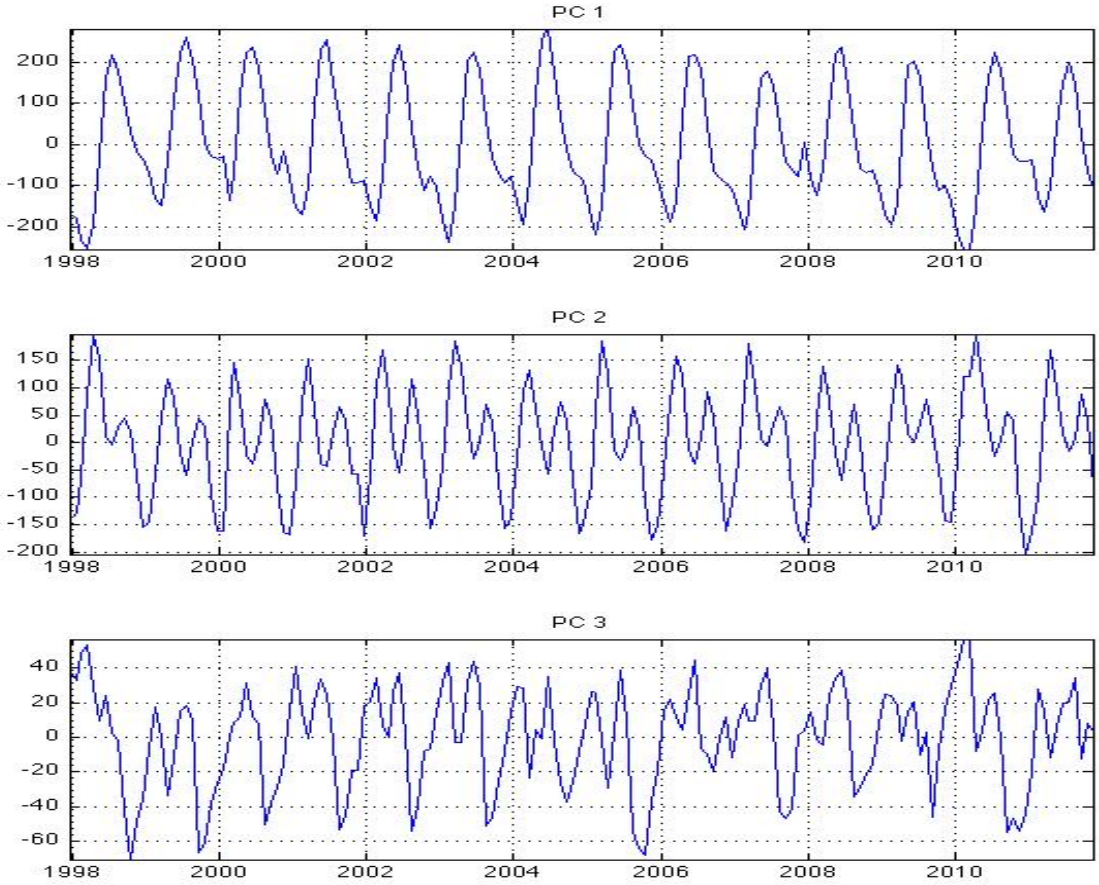

Figure 24 SST Temporal PCA For First Three EOF Modes

Given the evidence captured via the Matlab assessment of SST datasets, it was clear that a comparative model was needed in order to validate conclusions and insights relating to this distinctive spatio-temporal phenomenon.

The following sections will introduce an IRICS based assessment, which incorporates the Reynolds et al. (2002) model of SSTA data collection from the International Comprehensive Ocean-Atmosphere Data Set (ICOADS) and the NOAA NCEP global SSTA data model with seasonal cycle removed from the data. The first three EOF modes of the normalised eigenvalues are representative of a combined variance of 67.1% of the total, with the 1st EOF reflective of the vast majority of this variance at 54.5%. The variances expressed by EOF 2 and 3 are relatively minimal at 7.2% and 5.4% respectively. Table 5 highlights this decreasing curve of variance, suggesting that there is limited relevance associated with lower level EOFs.

Table 5 Percent variance explained by first 3 SSTA EOF modes

Mode	Percentage Variance
1st Mode	54.5%
2nd Mode	7.2%
3rd Mode	5.4%

Consistent with the findings presented by Saji et al. (1999), the IOD is characterised by warm SSTA in the Western IO and cold anomalies in the Eastern IO (Eastern section not included), a clearly seasonal phenomenon that has a direct influence on monsoonal properties and responses by increasing SSTA leading to more heat content release and increase of monsoonal rainfall. Considering that the leading mode in Figure 25 is reflective of 54% of the degree of variance recorded in this mode, it is clear that there is a relatively contiguous positive SSTA characteristic in this first EOF representation although it has a relatively small SSTA gradient. Such findings are consistent with the evidence captured via the Matlab assessment, suggesting that the degree of temperature variance in the NWIO is largely attributable to intraannual variability, and is largely reflective of seasonal patterns and climatologic phase shifts.

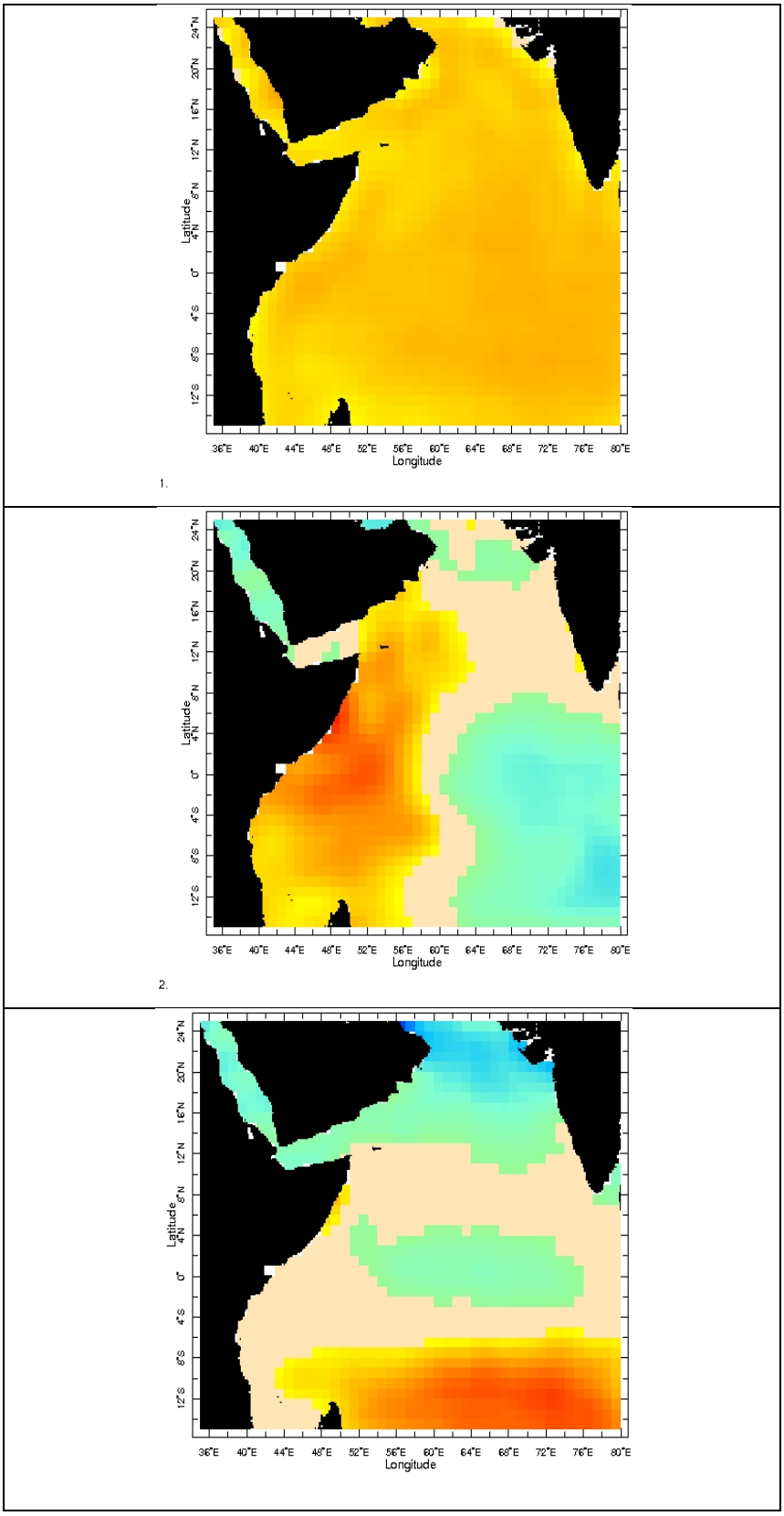

Figure 25 SSTA EOF 1st, 2nd and 3rd Modes

Figure 25 highlights a relatively constant positive associated with temperature anomalies across the Indian Ocean as calculated by the first EOF mode. Although only reflective of around 7% of the total variance, the second EOF mode demonstrates several of the unique regional characteristics that were similarly identified under the SSHA assessment, reflecting the current and hydrographical phenomenon that manifest throughout the western and eastern segments of this portion of the IO. The third EOF highlights a strong positive variance in the lower southwestern segment of the IO which is likely an indication of heat exchange properties and a strong southwardly current.

The following three figures show the time series representation of the EOF modes, highlighting several unique features in temperature variance, which will be discussed in greater detail. For example, PC 1 (Figure 26) indicates a temperature increase in 1998 and 2010 of about 1°C. There are several years with observable variations in this time series as well; however, their fluctuations are much more inconsistent in form.

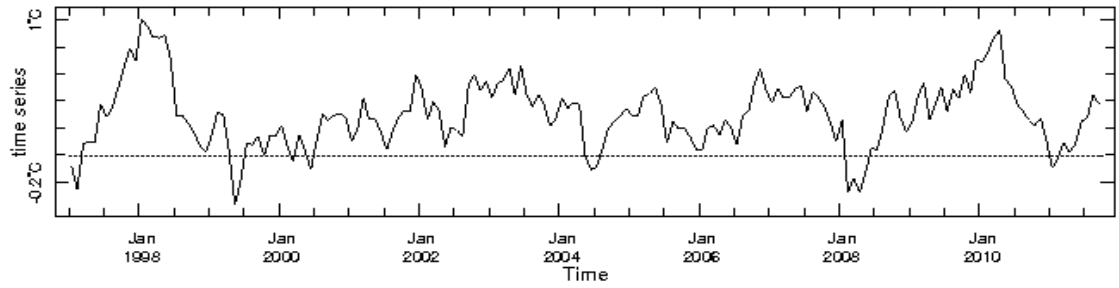

Figure 26 SSTA EOF PC 1st Mode

The second PC mode (Figure 27) also reflects the aberrant 1998 and 2010 periods, highlighting deep interim depressions in mid 2002 and mid 2004. It is clear that the SSTA cycles involve a higher regional temperature from January through May, with a negatively manifested temperature during the early summer months, which Gualdi et al. (2003) equate to strong upwelling activities. Ultimately, the fluctuations in PC 2 do not follow a consistent pattern, with the exception of the 1998 and 2010 peaks.

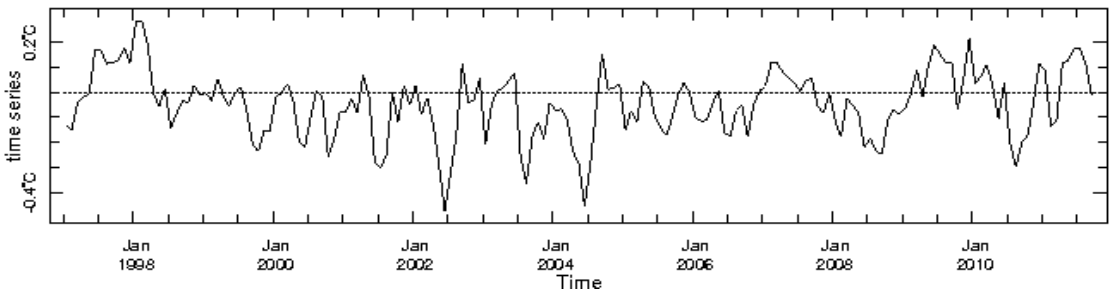

Figure 27 SSTA EOF PC 2nd Mode

Presented by Figure 28, PC 3 does indicate a range of temperature anomalies over the term of the assessment period; however, the degree of variance is much more compact than in the previous time series models. Further, in PC3, the aberrations in 1998 and 2010 are much less marked and a range of other periodic variances is shown over the term of this model. Given the relatively low representation of this mode in the variance findings, such evidence is consistent with more regionally localised variability, rather than distinctive patterns or universalities throughout the IO.

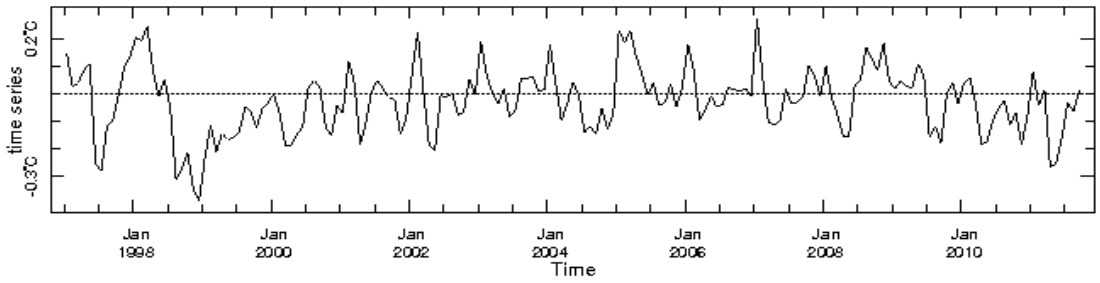

Figure 28 SSTA EOF PC 3rd Mode

4.5.2 SSTA Rotated EOF

In their assessment of SSTA in the IO, Zhao et al. (2011) demonstrated what they referred to as 'typical biases in the tropics', or geographically oriented bias points associated with warm and cold tongue phenomenon. Specifically, the researchers argued that the westward, anticyclonic currents along and to the south of the equator reflected a weakening of the eastward flowing equatorial counter current (Zhao et al., 2011). Specifically, the authors attributed this weakening to a decline in strength of the Wyrtki jet, reducing the ability of the atmosphere to generate near-equatorial convection or westerlies (Zhao et al., 2011). For this reason, the authors cautioned that there is a potential bias for numerical models to include surface currents to an inappropriate degree, particularly when the currents are most westward. Given the potential for inaccuracies in temperature assessments, a varimax rotated EOF was also calculated for the Reynolds et al. (2002) temperature field, providing a phase shifted, alternative interpretation of the principal modes.

Figures 29-32 reflect the spatial analysis of the Varimax rotated EOFs for the first three modes of this model, with a fourth visual indicative of a unique communality merge to demonstrate cumulative variance throughout the NWIO region. Figure 29 shows a strong positive value with particular highs in the northern Arabian Sea and east of the region, indicative of anomalous variance. Figure 30 highlights the 2nd mode wherein a strong westerly positive is also reflected that is consistent with the Somali Current and coastally linked phenomenon.

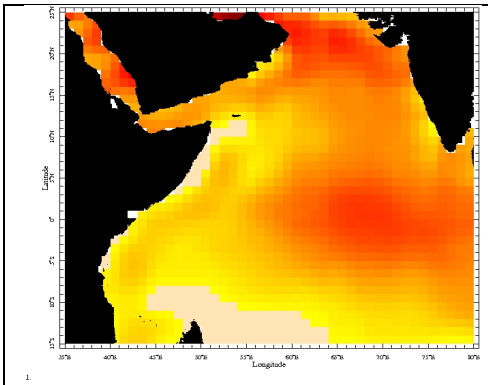

Figure 29 SSTA Rotated EOF 1st Mode

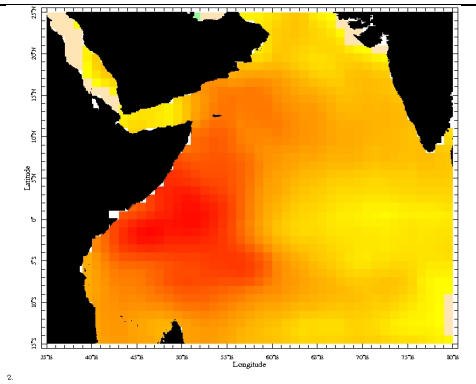

Figure 30 SSTA Rotated EOF 2nd Mode

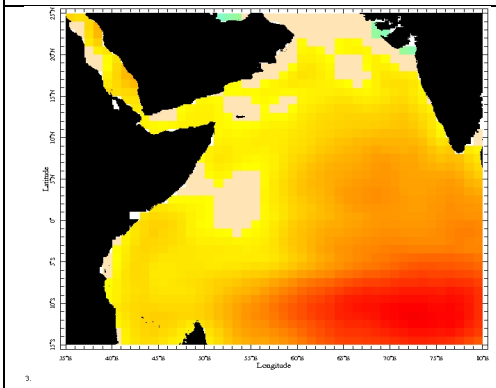

Figure 31 SSTA Rotated EOF 3rd Mode

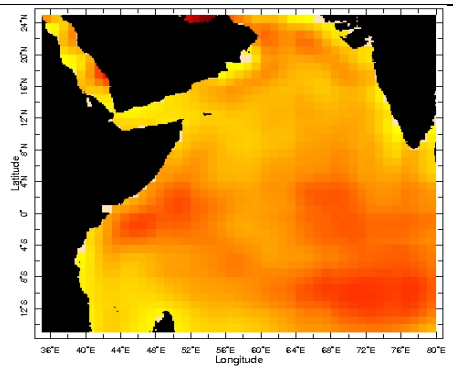

Figure 32 SSTA Common 1, 2 and 3 Rotated EOF

The 3rd mode in Figure 31 returns to a southerly high with a strong positive consistently linked to a heat transfer mode south of the equator in the IO. The value of Figure 32 is the combination of key areas of variance from 1st, 2nd and 3rd SSTA rotated EOFs, whereby distinctive temperature-linked phenomenon continue to manifest over the term of this assessment. The time series representation of these first three rotated EOFs indicate data patterns that are consistent with the previously recorded indices under traditional EOF calculations.

Specifically, Figure 33 (PC1) suggests that although there are two distinct anomalies in temperature levels, the first occurred in 1999 (not 1998), whilst the second remained in 2010. Such a shift is likely the outcome of the EOFs rotation; however, it will be considered in later assessment models.

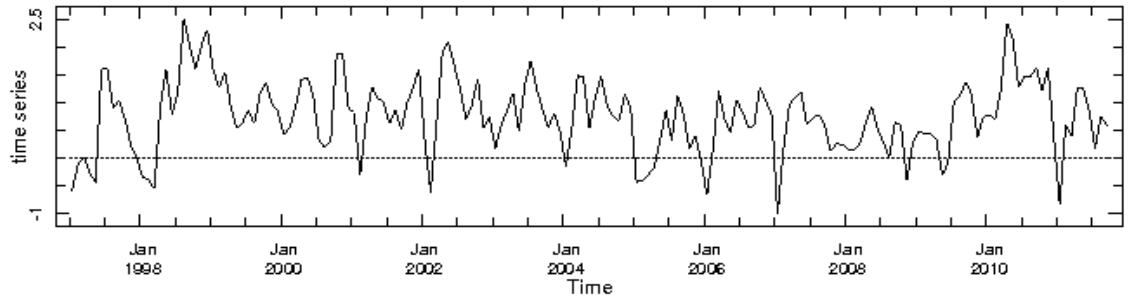

Figure 33 SSTA Spatially Rotated EOF PC1

Underscoring the variance reflected in Figure 34 (PC2) is a seasonal constant whereby January temperatures are recorded at a higher level than their mid-year counterparts, suggesting an interannual seasonality, which is likely characteristic of monsoonal forces, where the SSTA is lower during summer than winter due to the higher wind speed.

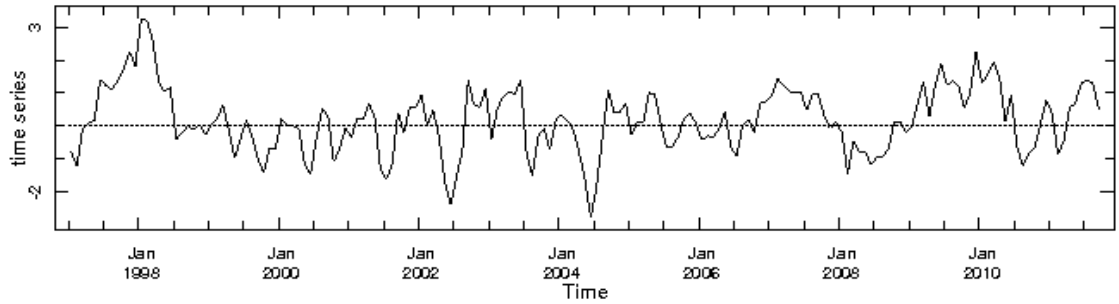

Figure 34 SSTA Spatially Rotated EOF PC2

In Figure 35, PC3 is represented, highlighting a much broader range of variability, with significant peaks and troughs identified in 2003 and 2005. Such findings are likely reflective of the heat exchange properties of the southerly segment of the IO and may be linked to ENSO-specific phenomenon during these various time periods.

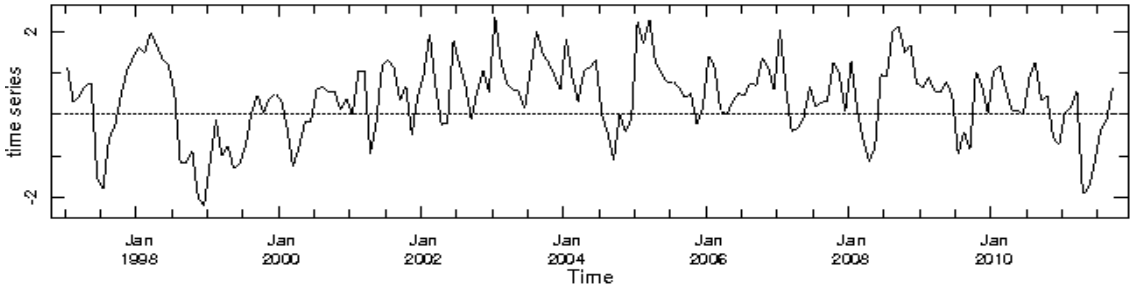

Figure 35 SSTA Spatially Rotated EOF PC3

4.6 SSTA Annual Variance Comparison

Although the SSTA EOF datasets reveal phenomena associated with variance across the NWIO, an additional assessment of key temporal indicators was also conducted in order to compare the degree of temperature anomalies across a given standard periodicity. Figure 36 to Figure 40 reflect temperature anomalies taken at four year intervals in January, whereby the mean characteristics have been averaged over the spatial domain.

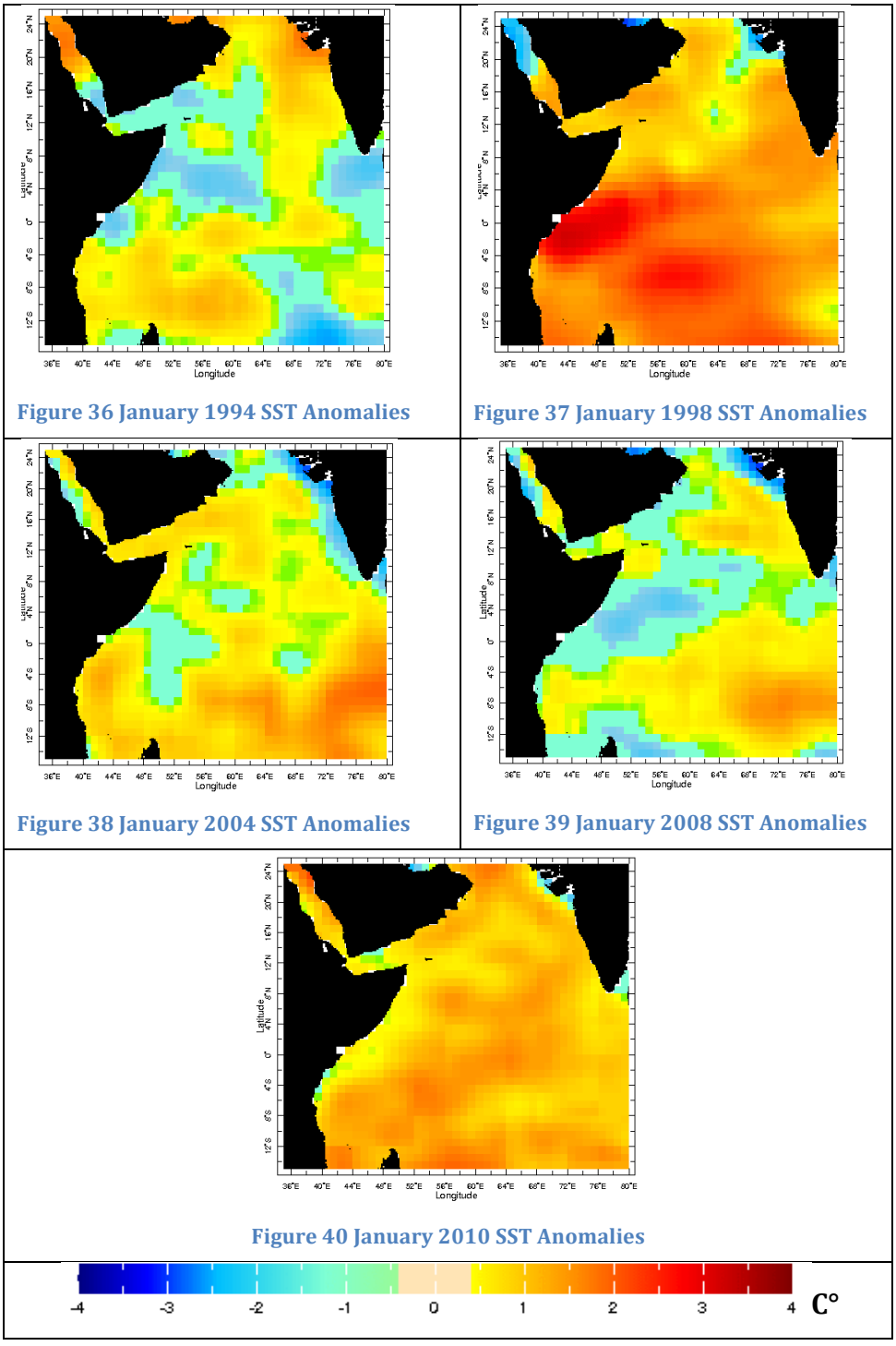

Figure 36 January 1994 SST Anomalies

Figure 37 January 1998 SST Anomalies

Figure 38 January 2004 SST Anomalies

Figure 39 January 2008 SST Anomalies

Figure 40 January 2010 SST Anomalies

These findings demonstrate a relatively constant decadal response between 1994 and 2004; however, it was clear from these figures that in spite of similar phenomenon in the western segment of the IO, there was a distinctive positive difference in the southeastern section of the 2004 data.

When compared across a decadal link between 1998 and 2008, there is clearly a difference between these two datasets with 1998 recording the most significant difference in temperature to date in this region. However, the 2008 data reveals a relatively similar distribution of positive and negative anomalies, with a southeastern pattern in 2004.

In fact, later years were targeted in order to determine whether there was some form of periodic shift associated with IO SSTA, revealing that in 2010, a very similar anomalous mode to the 1998 dataset manifested, as is shown in Figure 40. Bordering years of 2009 and 2011 revealed very similar SSTA patterns to 1994, 2004, and 2008, suggesting that there might be another factor correlated with this degree of variance. In order to emphasize the changes of SSTA throughout the central NWIO, a Hovmöller diagram was developed across the latitude 8^{o} N. Figure 41 shows the standardisation of SSTA over the time period 1997 through 2011, revealing patterning which is consistent with time series comparison of anomalous SST phenomenon in this region revealed in Figure 36 through Figure 40.

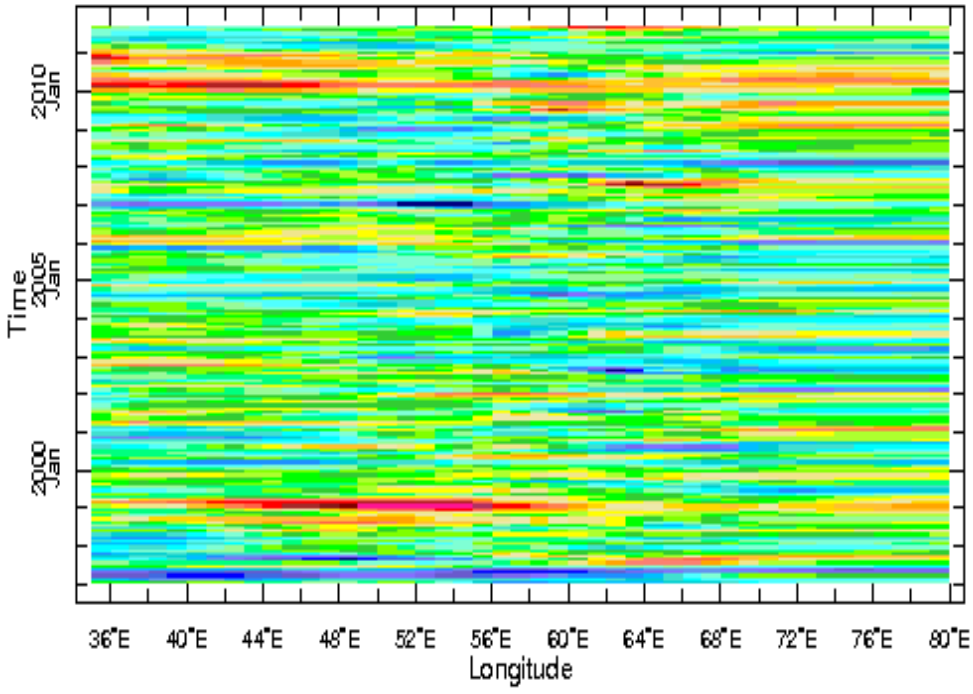

Figure 41 Monthly SSTA standardised over time across latitude 8^{o}

These findings demonstrate that around 1998 and 2010 the most significant positive anomalies were recorded in this region in relatively widespread orientation, particularly across the 2010 SSTA values. What is clear is that there are two sharp events that are 12 years apart, which might be correlated with other climatological factors within the IOD or active within the manifestation of ENSO.

4.7 Summary

This chapter's aim is to investigate a critical assessment of the role that climate variability factors maybe playing in anomalous patterns throughout the NWIO. Although the findings may be considered inconclusive, on the basis of the anomalies throughout the NWIO, it is suggested that regional factors rather than climate factors have had a much more influential role on the variability throughout the region, this due to the strong impact of the monsoon, which is why the seasonal cycle in the NWIO has the greatest degree of variance reflected by monsoon related phenomena such as the Great Whirl and the Somali Current. On the other hand there is over whelming evidence of the influence of climate modes like the IOD and ENSO on the region based on the 2nd spatial pattern and temporal timeseries that is consistent with Saji et al. (1999), this is evident without removing the seasonal cycle from the data before using them in the EOF analysis, and even more when the data are de-seasoned (appendix F) where the inter-annual variance becomes the dominant variance instead of the seasonal one, this research has also discussed the regionally specific characteristics, which show the possible influence of the dipole mode on the climate variability of the NWIO; however, there is also sufficient evidence to suggest that there is a correlation between NWIO characteristics and ENSO manifestation. Ultimately, the conditions themselves (e.g. change in SSHA or SSTA) all reflect a severe weather pattern that is tied to ENSO emergence and recession.

5 Somali Current Variability Indices using Remote sensing data

5.1 Introduction

Amongst members of the scientific community, the analysis of the Somali Current and its annual reversal cycle has remained of key interest. This chapter highlights the current movement patterns between January and July, to demonstrate the substantial shift in flow and direction. The summer Somali Current which is located to the north of 2-3°S has been proven by Luther and O'Brien (1989) to gradually break up during a fall transition period, and is subsequently replaced by the south-westward Winter Somali Current following the onset of the northeast monsoon in December. This shift will be clearly evident in the July and January data of several variables like SSHA, SST/SSTA and surface wind speed, which is focused on for the region of the Somali Current.

An ideal way to characterize the circulation pattern of a geophysical system is through a climate index because it is a simple diagnostic quantity. A variety of methods can be used to derive indices, the most popular ones uses selected station or grid point data (eg., Southern Oscillation Index, Nino 3.4). However less basic and conventional indices are based upon EOFs (e.g. Arctic Oscillation Index) or a Rotated EOFs (e.g. Pacific-North American Index). Most indices use a single variable (e.g. sea level pressure) while others, such as the Multivariate ENSO Index (MEI) use a combination of six variables (e.g. SST, SSHA est.). One of the issues for consideration is that the use of different source data sets and different base periods can yield different index values (National Center for Atmospheric Research, NCAR).

The following points will be the focus of this chapter:

- Generation and analysis of Indices for the Somali Current, using Sea Surface Temperature (SST/SSTA) and Sea Surface Height Anomaly (SSHA) Remote sensing Data plus surface wind speed.
- Use of the indices to quantify the strength of the Somali Current, identify its characteristics and establish how it behaves differently from one season to the other.
- Recognize the patterns of climate variability of the Somali Current during the summer and winter monsoon.

5.2 Data and Methodology

5.2.1 Data and Resources

This chapter focuses on a targeted geographic area within the region of NWIO, an area bounded on the east by the Arabian Sea, on the west by the Somali coast, by the Arabian Peninsula to the north, and by the Equatorial Indian Ocean from the south. The primary coordinates indicate a latitude of 00°N -12°N and longitude 44°E-54°E. The main reason to chose this area is because it includes the Somali Current. The Somali Current climate has been previously linked to the interannual monsoon and variability in climate conditions. This analysis presents multiple assessments of key variables like sea surface height anomalies (SSHA) plus others, to look at the factors that play a fundamental role in describing the climatological characteristics of this phenomenon, as well as crafting the interrelationships between forces that are responsible for its variability.

The main dataset used here is sea surface height anomalies (SSHA) that has been readily accessed from NASA's Topex/Poseidon+Jason1 satellite images for over the past two decade. Fu (2010) emphasises that since the 1990s, 'satellite altimetry has revolutionized oceanography', allowing for unprecedented mapping of oceanic currents and sea level changes that are reflective of both periodic and anomalous behaviours. Beginning in October of 1992, Topex/Poseidon analysis of SSH anomalies was accessible via the NASA database, offering complementary visualisation of phenomenological change over time.

Another key remote sensing data source used is the TMI that has very good resolution coverage for the tropics, which provided two important variables, SST and surface wind speed starting from January 1998 onward. Also we use NASA's Quick Scatterometer (QuikSCAT) Level-3 satellite vector wind product, with each vector component (zonal and meridional) and wind speed for both ascending and descending tracks gridded on a daily, 0.25°x0.25° grid.

Finally one of the most widely used database management sites was incorporated as a secondary mode of validation and methodological diversification through the International Research Institute for Climate and Society (IRICS). This evidence involved similar temporal and geospatial records of SST and Wind; however, it employed a more diverse range of methodological choices like the NCEP model-based product, the Climate Data Assimilation System 1 (CDAS1), often called NCEP/NCAR Reanalysis1.

5.2.2 Procedures and Methods

The following sections include a comprehensive study of anomalies on both temporal and spatial scales. The analytical methods will include a primary focus on time series of the data sets to create indices for the Somali Current. Data analysis methods included a Matlab routine (appendix E), which provides baseline measurements and presentations for each of the leading indicators (SSHA\SST). The following methods for creating indices for the Somali Current are considered:

- Generate an index for the Somali Current strength from the time series of the SSHA across the geostrophic current by calculating the slope steepness between near-shore and offshore.
- Produce an index based on the horizontal extension and width of the Somali Current variation using the SSHA.
- Analyze the surface wind speed with in the vicinity of the Somali Current, and examine its fluctuations and behavior throughout the seasons.
- Form an index represented by the different spatial patterns and characteristics of the SST\SSTA adjacent to the Somali Current.
- Apply an EOF on SSHA and surface wind speed in July and January for a specified area, which includes mainly the Somali Current and use the principal component that indicates the current variability as an index.

All evidence is presented visually and assessed quantitatively in order to establish justification for the conclusions herein; further, validation of these findings is also introduced, by linking it with those findings previously captured in prior leading studies. It is hoped that analysis of anomalous behavior of the Somali Current will provide a specific insight into the patterns of climate variability influencing the surrounding area of the Somali Current. It is important to note, however, that this can be influenced by a variety of climatological factors – resulting in a high degree of transient variability, which is characteristic of this area, as evidenced by Beal and Chereskin (2003). The research will try to identify the magnitude of internal variability of the Somali Current from the possible external causal links that may be responsible for its high degree of variability.

5.3 SSHA slope gradient across the Somali Current index

The basis for measuring ocean circulation and currents using satellite altimetry is that at large scales the surface current is proportional to the surface slope. The surface slope is simply the gradient of the sea surface height. The current is deflected by 90° to the right of the direction of the slope in the northern hemisphere, and 90° to the left in the Southern hemisphere.

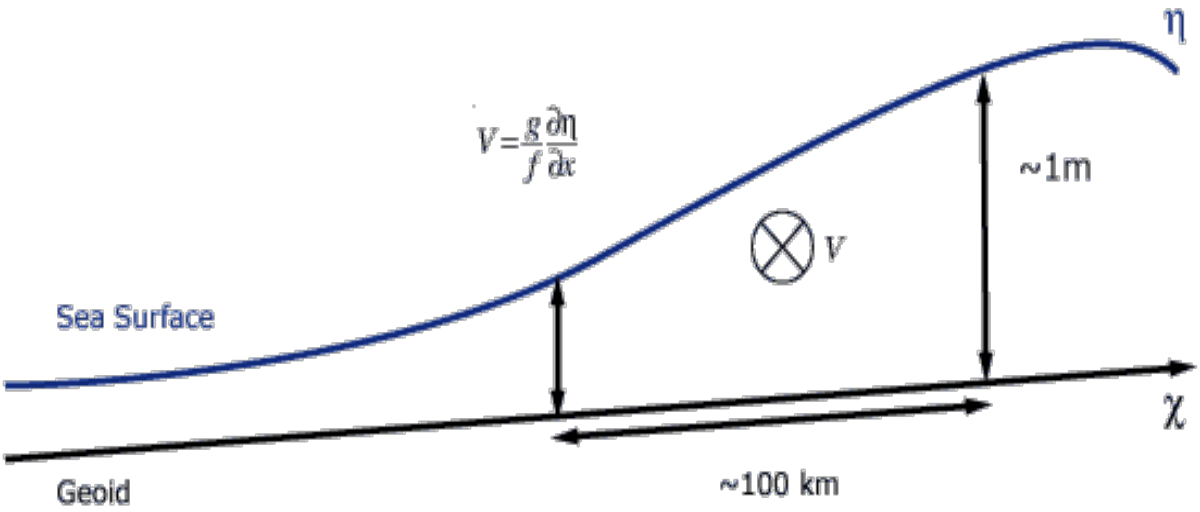

Figure 42 Diagram showing the calculation of current from SSH in the northern hemisphere.

The geoid is a theoretical surface to which the ocean would conform, given a non-rotating Earth without any currents. The accuracy of measurement of the geoid is the limiting factor in the calculation of absolute SSH. The force of gravity is denoted g, f is the Coriolis parameter and η is the dynamic topography – the height related to the ocean current. The current, with a velocity V flows into the page (Figure 42). In the southern hemisphere, it would flow out of the page. To measure the absolute slope (and therefore the absolute current) using satellite altimeters is presently beyond technological capabilities. However, taking advantage of the fact that a satellite altimeter repeats its orbit exactly every cycle, it is possible to measure the difference in sea surface height from the mean – the Sea Surface Height Anomaly (SSHA). This gives us a useful measure of changes in ocean circulation.

5.3.1 Somali Current near-shore and offshore SSHA time series

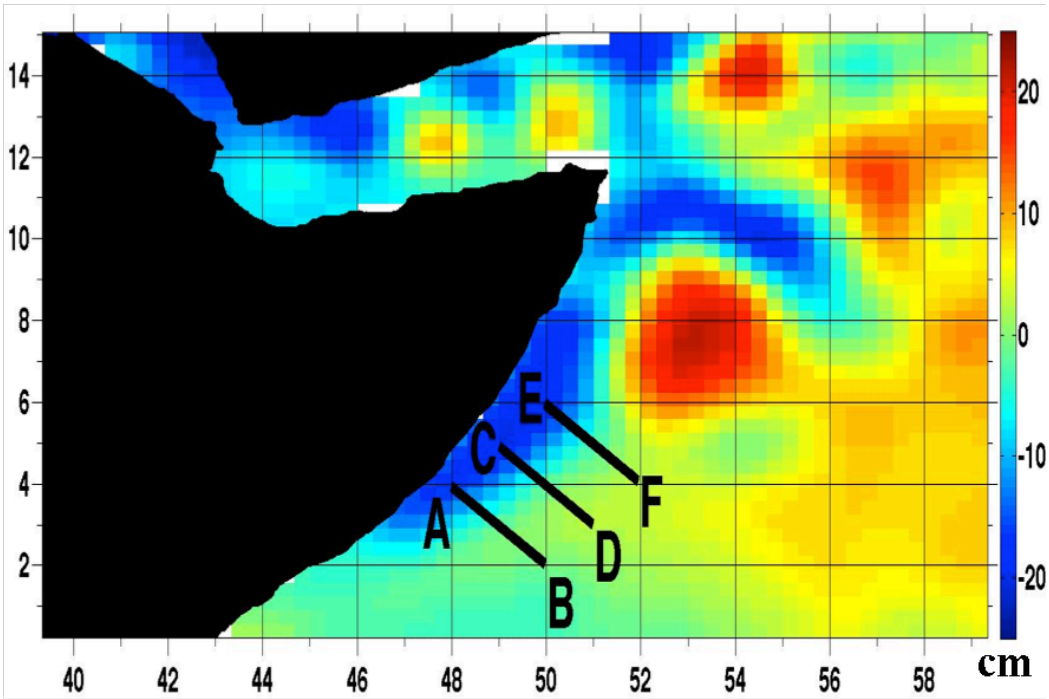

Figure 43 Points of near-shore and offshore selected across the Somali Current using SSHA during July 1994.

Table 6 shows the location of data chosen to produce the indices for the Somali Current from calculating the gradient between the near-shore (A / C / E) and the offshore (B / D / F) points (Figure 43), SSHA of July 1994 is used in the background to indicate the Somali Current position, where studies suggest that SSHA and ocean colour provides better information about the location of currents than other remote sensing products like SST (Bonjean and Lagerloef 2002), especially for regions close to the tropics where the temperature gradient is very small.

Two main considerations were taken into account when choosing the position of the points, the first is to move north as much as possible away from the equator to capture the characteristics of the geostrophic Somali Current, the second is not to get close to the Great Whirl and its much higher SSHA than the Somali Current area.

Table 6 Locations of the points chosen and their distance from the coast of Somalia.

Point Name	A	B	C	D	E	F
Position	04°N/48°E	02°N/50°E	05°N/49°E	03°N/51°E	06°N/50°E	04°N/52°E
Distance to coast	50 Km	530 Km	80 Km	450 Km	110 Km	380 Km

At distances of about 50 km or closer from the coast, satellite altimetry is of limited value because of land contamination in the altimetry, large footprints of 10 km to 50 km of the radar echoes reflected off water, and off a combination of water and land, will not be identical, and only the former undergo processing. Also the computation of some required corrections is more difficult, e.g., tides are much more complex near the shore than in the open ocean, and require a very precise knowledge of the coastal geography. Wet tropospheric corrections are also less precise near the coast (ESA, 2013).

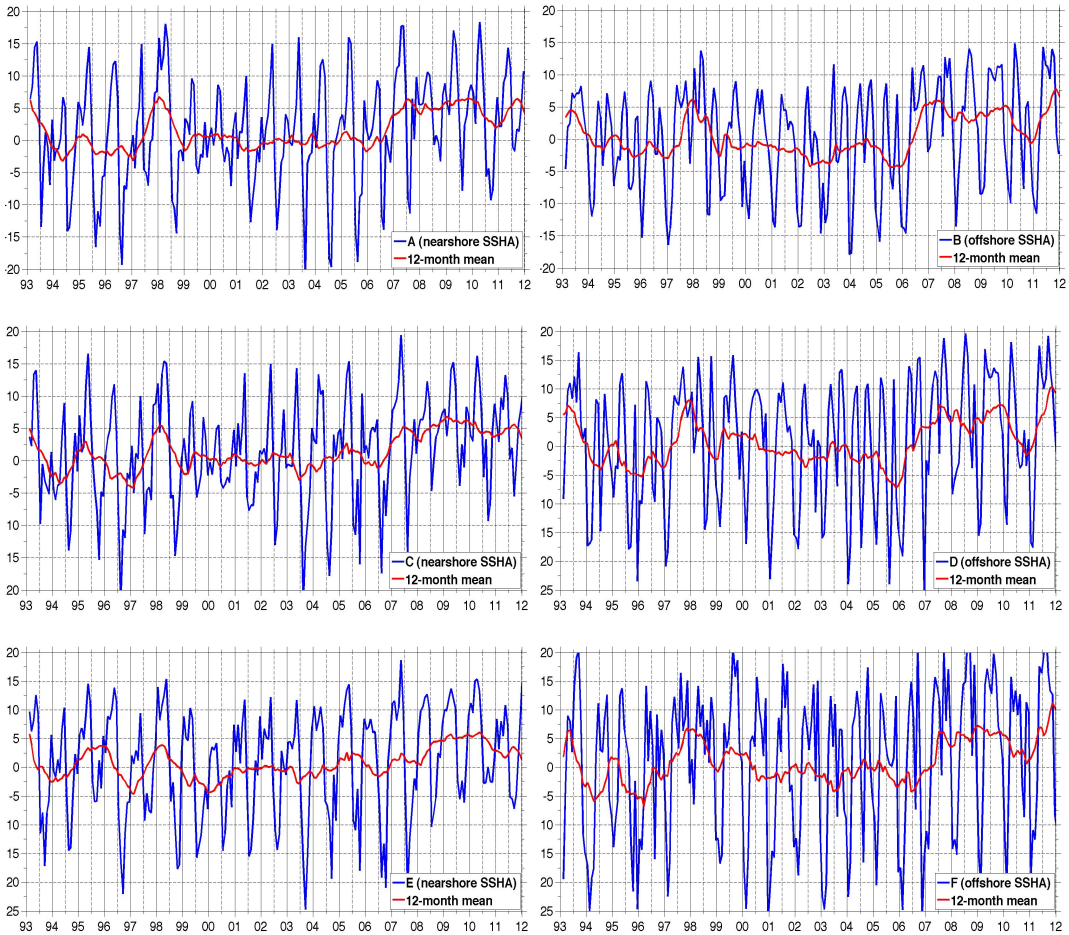

Figure 44 SSHA (cm) data from 1993 to 2012 for the near-shore points (A, C, E) and the offshore points (B, D, F) represented by the blue lines, and the 12-month running mean for the same data by the red lines.

Figure 44 present the time series for the SSHA between 1993 and 2012 at each point selected across the Somali Current, also included is the time series of a 12-month running mean for the same data. The SSHA along the Somali Current seems to amplify slightly as we move northward away from the equator, which is expected due to the increase of the Coriolis force (f), especially in the seasonal signal for the offshore.

In the seasonal SSHA the second min/max of SSHA during the year is smaller in the near-shore than the offshore as shown by Figure 44. The data in the offshore time series changes sign considerably more frequently in each year, which is expected as further from the coast, there is less influence of the Findlater jet and wind stress, which drive the geostrophic current of Somalia during the summer monsoon. The summer monsoon is much stronger than the winter monsoon near the Somali coast.

The time series of the seasonal signal indicates that SSHA starts to decrease rapidly around May in general and it reaches its minimum in July, corresponding to the coastal upwelling through Ekman suction induced by the surface wind stress. Thereafter the SSHA begin to increase gradually as the coastal upwelling gets weaker turning to coastal downwelling in October, as the SSHA further increases, reaching its maximum in May. This appears clearer in the near-shore data than the offshore. Near-shore seasonal signal data of SSHA gradient between max/min indicate four phases during the entire time series in the order of high\low\high\low SSHA with the 1st phase occurring between 1993 to 1999, the 2nd 1999-2002, the 3rd 2003-2007 and finally the 4th phase between 2008 to 2012.

To get a better sense of the inter-annual changes in the seasonal cycle of the SSHA, a 12-month running mean is performed; its main purpose is to point out the climate variability over the entire period of the data. The 12-month running mean time series for the SSHA at all six positions is similar and reflects a significant increase in 1995, 1998 and for three consecutive years after 2007. The strongest increase in the 12-month running mean time series occur in 1998 which is corresponding to the very large EL-Nino event, however it is rather interesting that all the years of SSHA increase come straight after a positive Indian ocean dipole event.

5.3.2 Gradient between the Somali Current near-shore and offshore

Figure 45 includes two plots each with two time series of near-shore SSHA (blue line) and offshore SSHA (red line), which are the average SSHA at A, B and C. The top plot is during January (winter monsoon) where the bottom one is during July (summer monsoon). The first obvious difference that can be noticed between the two plots of SSHA in January and July is the reversal between the near-shore and offshore SSHA values, this is expected because of the direction of the geostrophic Somali Current during the northeast monsoon, and its reversal in July by the southwest monsoon.

The plot for January indicates an increase in SSHA for both the near-shore and the offshore during 1995, 1998 and 2007 with the offshore SSHA increase being greater than the near-shore, resulting in less difference between the two time series and bringing them closer to each other for these years, suggesting a decrease in the Somali Current. As for the July plot the two time series get closer to each other and even overlap during the years 1998 and 2010, which suggest a reversal in the normal direction of the current during July.

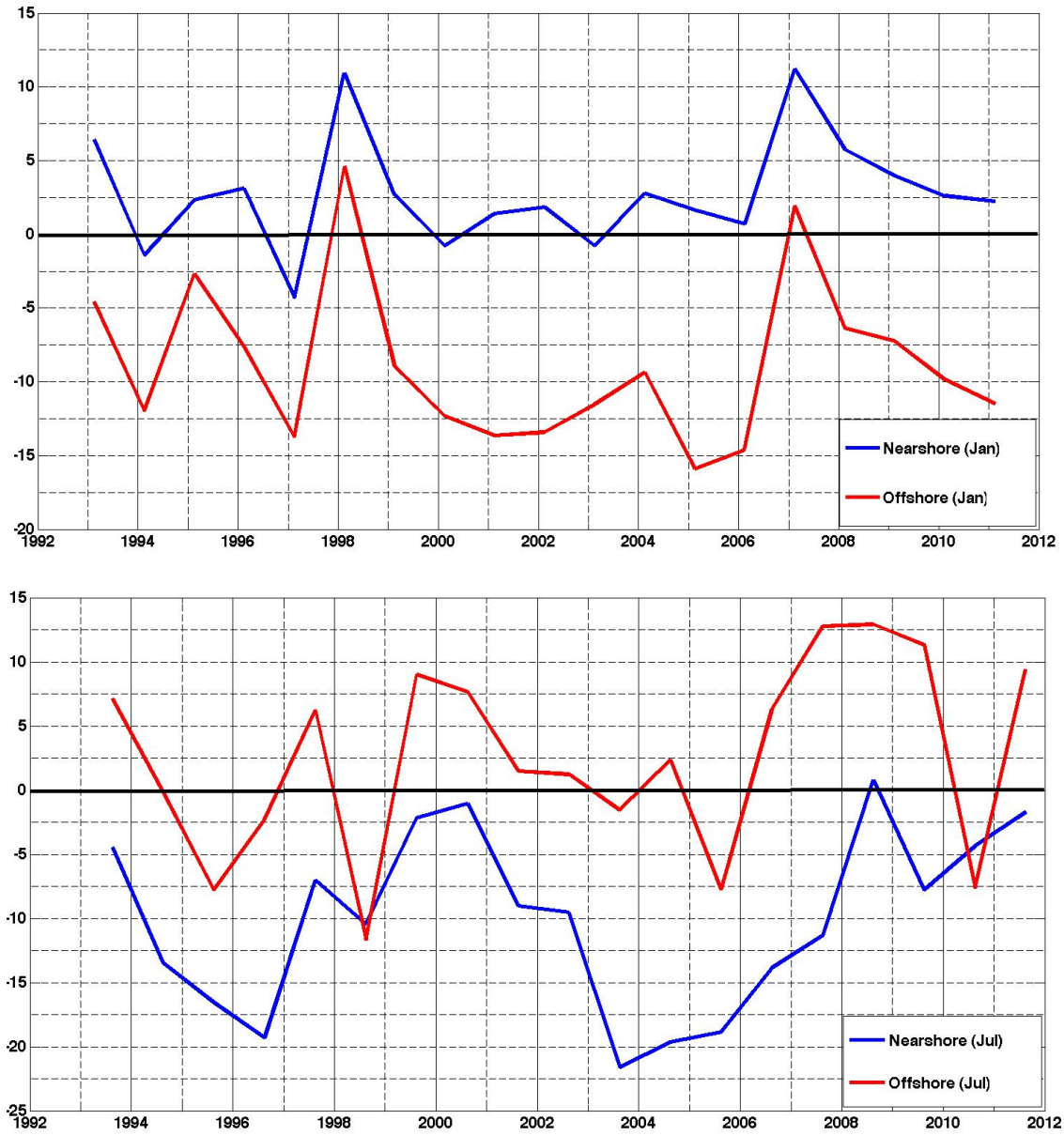

Figure 45 Time series for the SSHA (cm) of near-shore (blue line) and offshore (redline) during the winter monsoon in January (Top) and summer monsoon in July (Bottom).

The time series getting closer to each other can be interpreted as a horizontal expansion in the coastal upwelling\downwelling of the summer\winter for those years, in other words a wider, slower Somali Current.

The SSHA slope is more flat between the near-shore and the offshore during the years where the time series get closer to each other, this can be seen more clearly from Figure 46 that shows the calculated difference between the near-shore and the offshore where higher\lower bars from the difference in January\July means stronger or steeper slope.

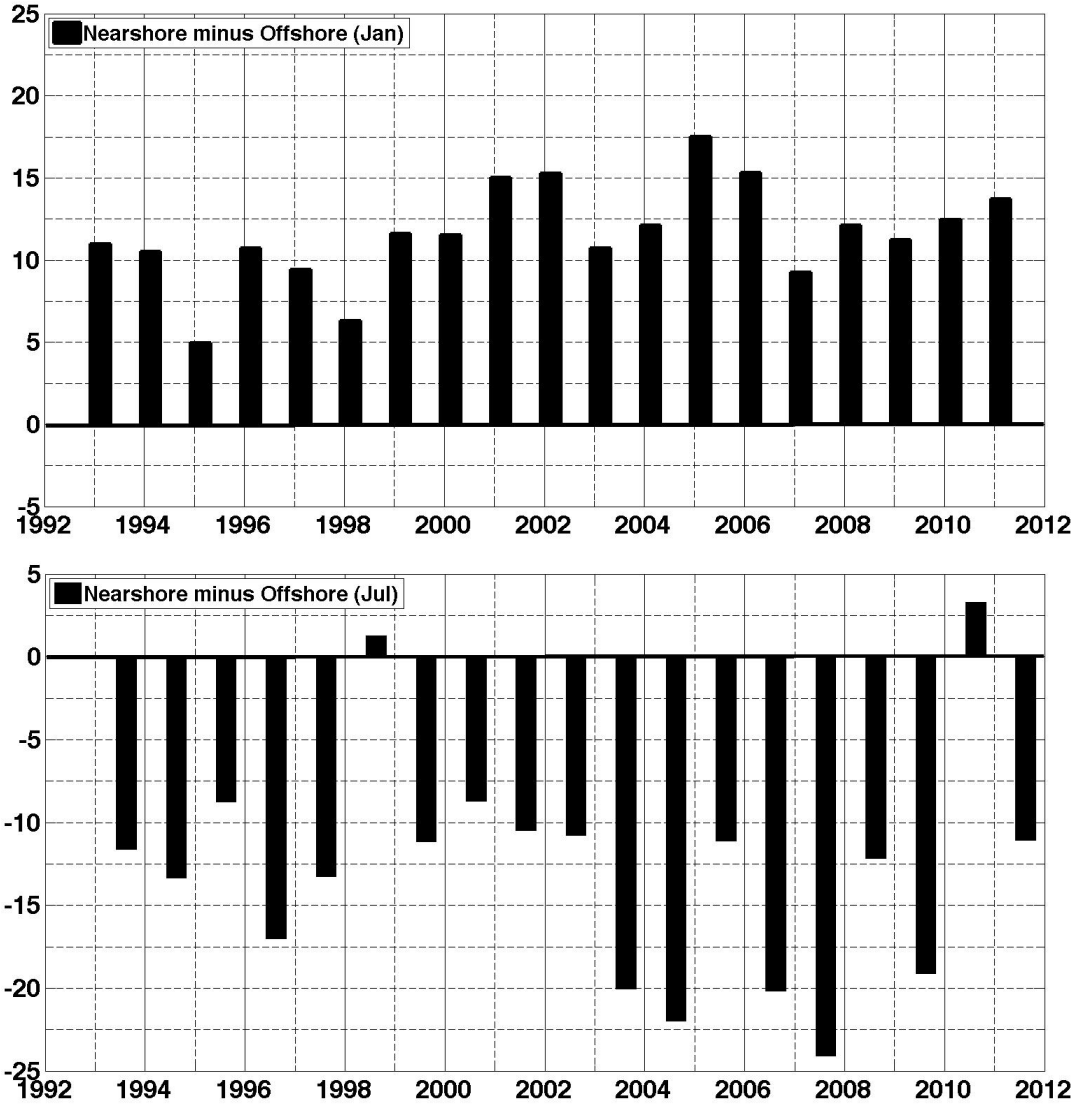

Figure 46 Difference between the near-shore and the offshore SSHA (cm) in January (Top) and July (Bottom).

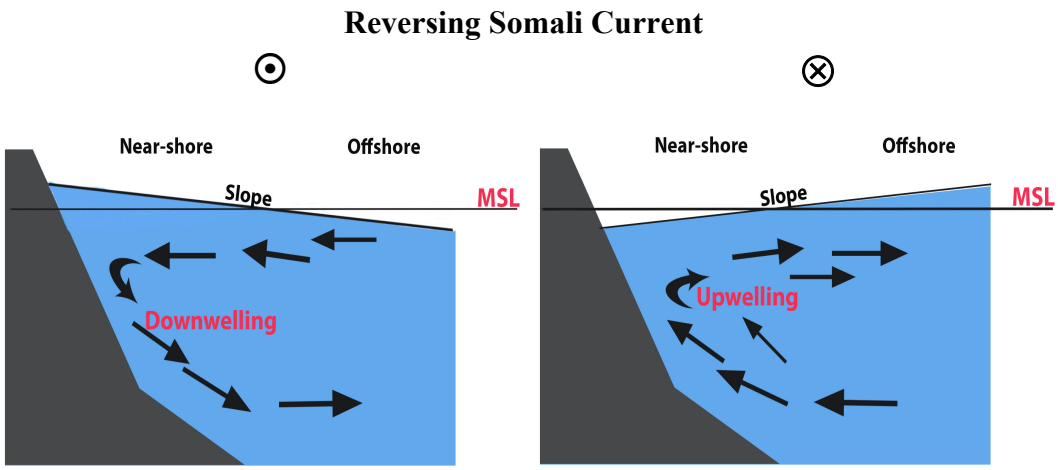

Figure 47 Illustration of the coastal downwelling (right) and upwelling (left) in the north hemisphere

Another factor to be considered for the SSHA between the near-shore and the offshore is the Ekman transport that is associated with the geostrophic current and moves to the right of the wind in the north hemisphere, the near-shore SSHA in January is higher than the offshore SSHA because of the downwelling induced by the Ekman transport of water at the surface during the NE monsoon and vice versa in July during the SW monsoon (Figure 47). The current continues to accelerate and deflect due to the Coriolis force until it flows parallel to surface elevation contours. At this point the Coriolis force balances the pressure gradient force and the geostrophic balance are reached (Figure 48).

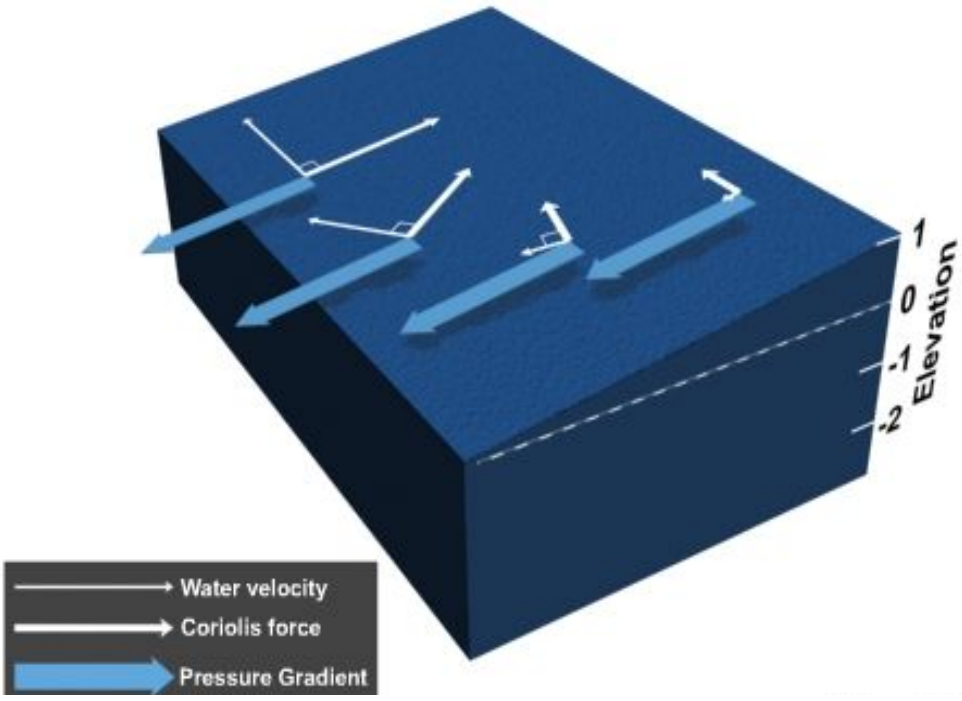

Figure 48 Origin of the geostrophic current over sea surface (www.comet.ucar.edu).

5.4 Horizontal extension and magnitude of the Somali Current

5.4.1 Somali Current Horizontal extension from SSHA in July

The Somali Current shows a tropical analogue to a mid-latitude western boundary current recirculation region that is directly affected by the presence of the equatorial wave-guide as well as seasonal reversals of the wind (Luther and O'Brien, 1989). The width of the Somali Current SSHA varies in July from one year to another during the past two decades (Figure 49), which correspond to the wind stress caused by the southwest monsoon. It seems that the larger horizontal expansions becomes, the lower SSHA to be within the Somali Current. Figure 49 indicates that the greatest horizontal expansion of the Somali Current mostly occurs at latitudes between 4˚ to 6˚ N, whereas less horizontal expansion of the current is further north between 7˚ to 9˚ N.

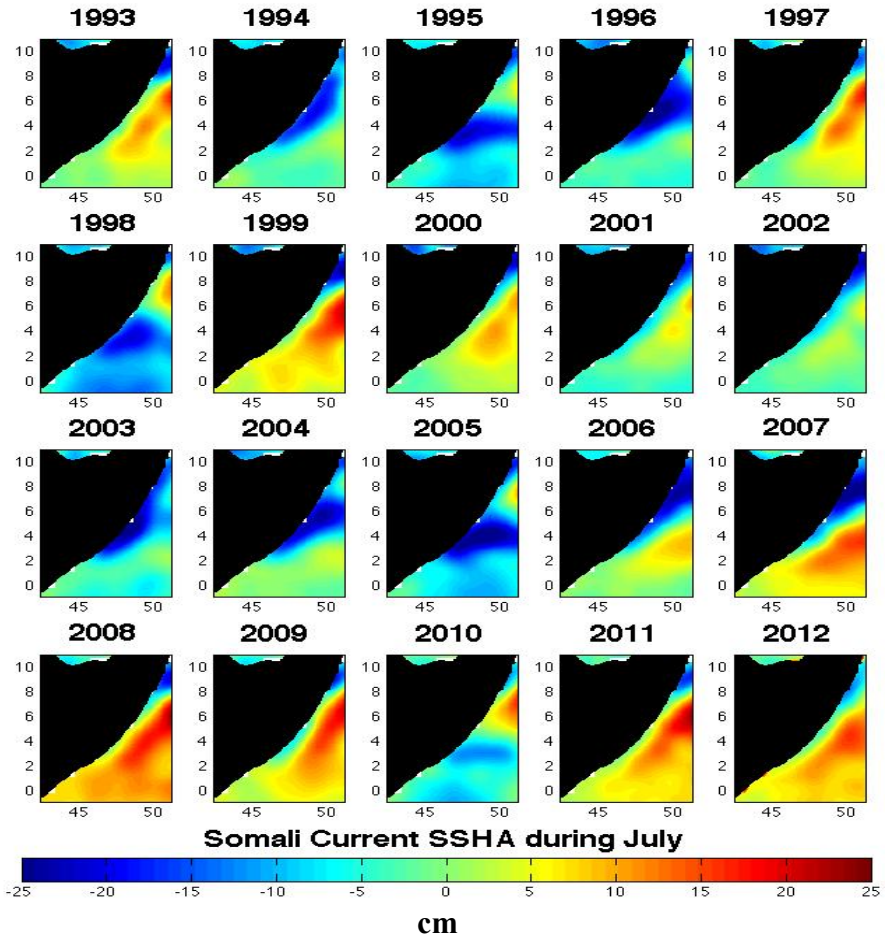

Figure 49 Somali Current SSHA during July for the past two decades

Roughly about 50% (around 10 years) of the years during the past two decades for the July months show a strong horizontal extension according to Figure 50 and Figure 51, which are the Hovmöller diagrams of latitude at an interval of one degree from 4° to 9°N where the longitude for each diagram is between 46° to 52°E and for the time period from 1993 to 2012.

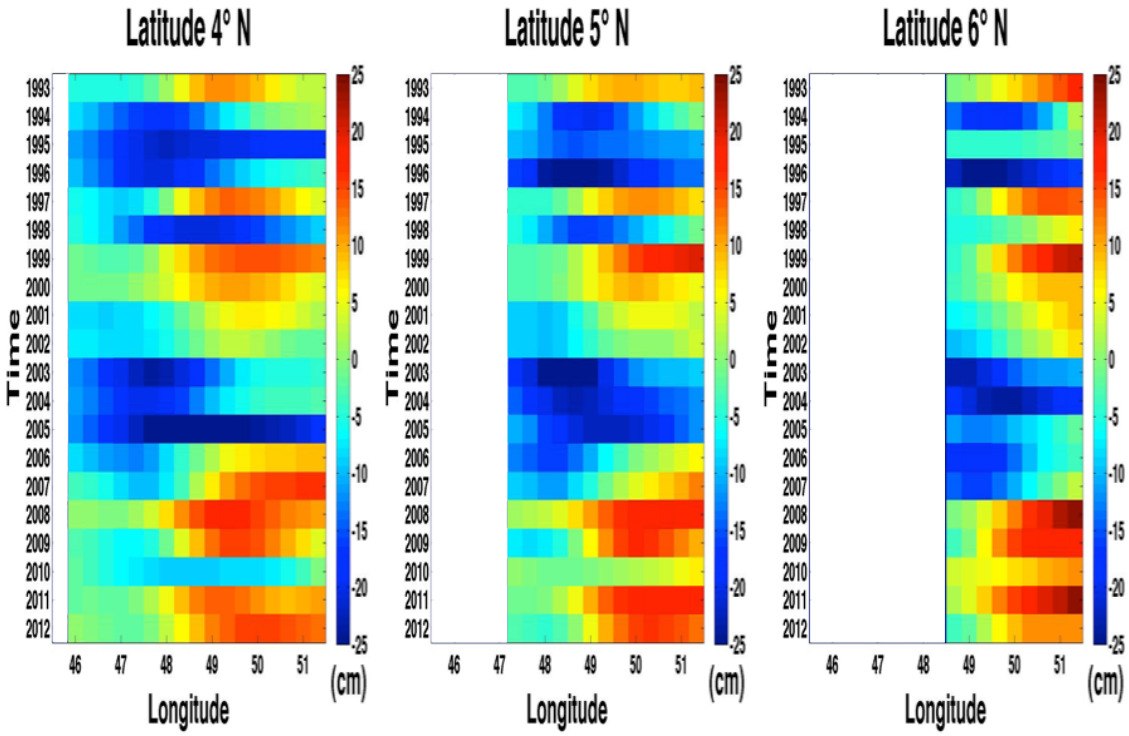

Figure 50 Hovmöller diagram of SSHA at 04°, 05° and 06° N

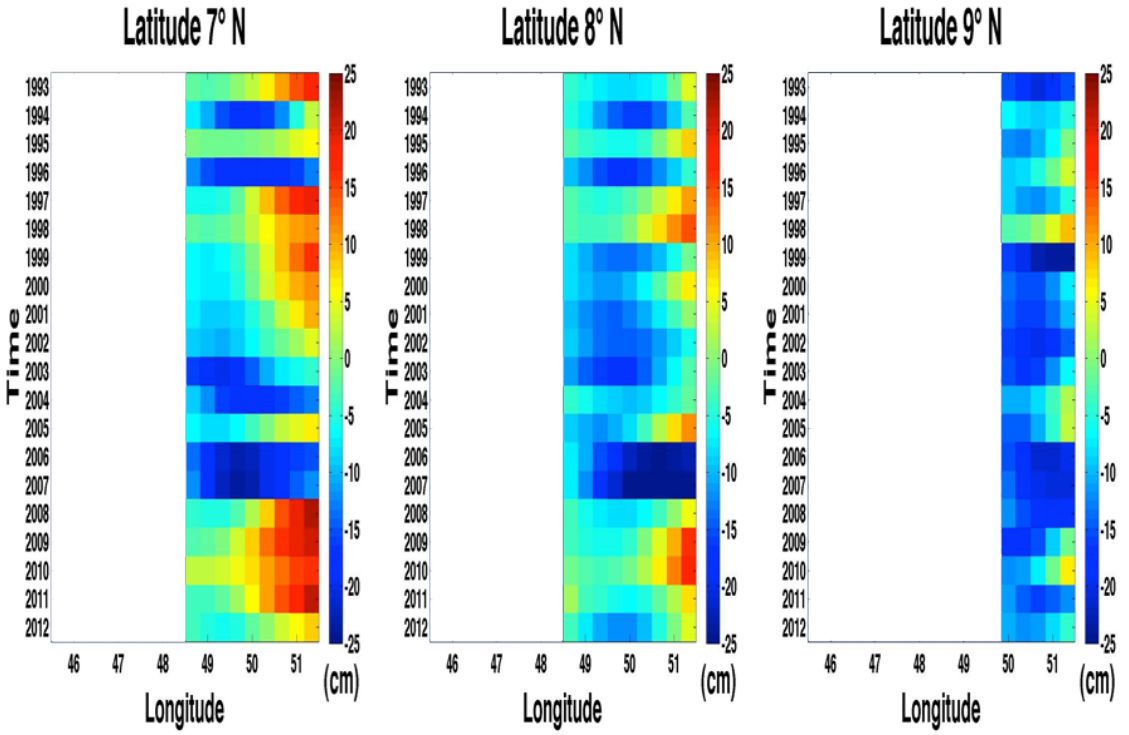

Figure 51 Hovmöller diagram of SSHA at 07°, 08° and 09° N

The distance of the Somali Current extension offshore in each year is corresponding to the number of boxes of SSHA that are less than 0 cm, where a grid point is represented by one box, which is 1/4 of a degree (Table 7).

Table 7 Greatest horizontal extension represented by number of grid points less than 0 cm of SSHA at latitudes 04°, 05°, 06°, 07°, 08° and 09° North at each year from 1993 to 2012.

Latitude / Year	Grid Num at 04°N	Grid Num at 05°N	Grid Num at 06°N	Grid Num at 07°N	Grid Num at 08°N	Grid Num at 09°N	Mean of Grid Num
1993	6	3	1	3	8	5	4.3
1994	14	13	8	8	9	5	9.5
1995	17	13	9	5	7	5	9.3
1996	17	13	9	9	9	4	10.1
1997	7	4	2	4	6	5	4.6
1998	17	13	5	4	5	2	7.6
1999	5	4	2	5	9	5	5
2000	4	4	2	5	7	5	4.5
2001	8	6	4	6	8	5	6.1
2002	17	8	5	7	9	5	8.5
2003	17	13	9	9	9	5	10.3
2004	17	13	9	9	9	4	10.1
2005	17	13	9	6	6	4	9.1
2006	9	9	9	9	9	5	8.3
2007	8	7	8	9	9	5	7.6
2008	3	0	1	4	7	5	3.3
2009	7	5	2	3	6	5	4.6
2010	17	5	0	0	5	4	5.1
2011	5	3	0	3	7	5	3.8
2012	5	4	2	5	8	5	4.8

The mean of grid points with less than 0 cm SSHA for all six latitudes in each year is a better representation of the horizontal extent of the Somali Current because of its variability where in some years the greatest extension is between 04°N to 06°N and in other years its more to the north between 07°N and 09°N.

Figure 52 shows more clearly that indeed there were roughly 50% of the years with above average horizontal extent of low SSHA, implying a wider Somali Current during the summer of those years. Another indication is that there was a two phases of strong horizontal extent and two weak ones of the Somali Current: in the years between 1997 to 2001 and 2008 to 2012 the Somali Current width is small with an average of 4 grid points (130 Km); years 1994 to 1996 and 2002 to 2007 the current width is between 8.5 to 10.5 grid points (285 to 350 Km), indicating that it is twice as wide as in the weak phases.

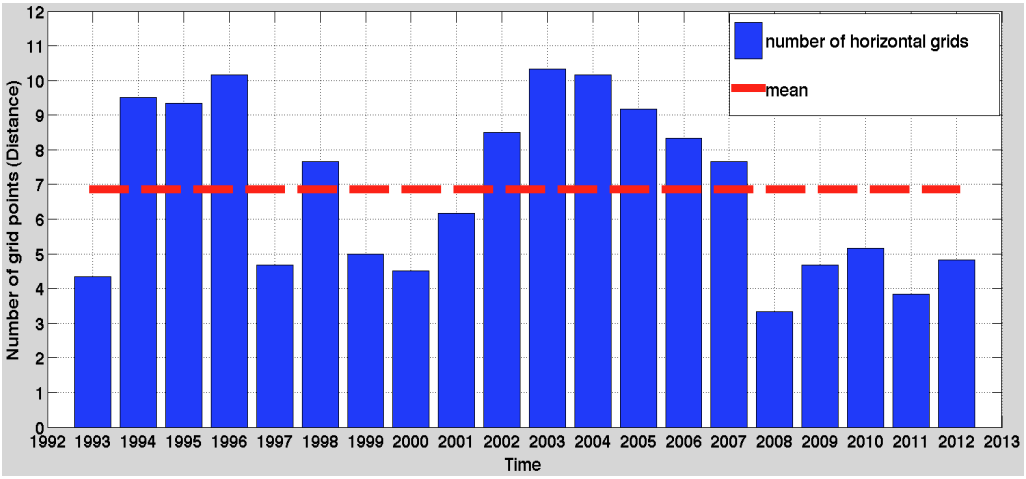

Figure 52 Number of grid points mean with SSHA of less than 0 cm across the Somali Current for latitude between 04°, 05°, 06°, 07°, 08°, 09°N in July of every year from 1993 to 2012, where each grid point is 1/3 of a degree.

Although the extension of the Somali Current can be represented by the number of grid points with negative values of SSHA spreading eastward (Figure 52), it does not illustrate the magnitude of how low these values are, for example some years has the same number of negative SSHA grid points, but with very different values like in the year 1996 that is very close in the number of grid points to years 1994 and 1995, but has much higher values of negative SSHA as could be noticed from the standard deviation for only the negative SSHA grid points mean at latitudes 4,5,6,7,8 and 9 degrees north (Figure 53).

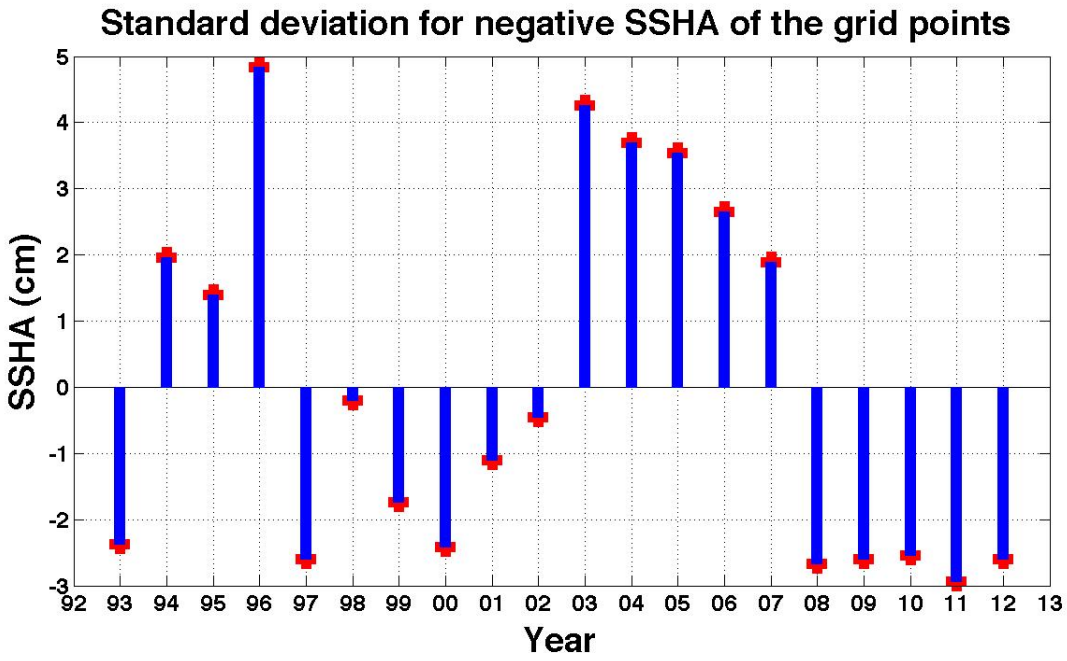

Figure 53 Standard deviation for only the negative SSHA of the grid point in all the latitudes 4°N, 5°N, 6°N, 7°N, 8°N and 9°N associated with each year.

5.4.2 SSHA intensity of the Somali Current during summer season

Where persistent wind blows along the coast, the Coriolis force acts to move surface water in the Northern Hemisphere to the right and to the left in the southern hemisphere. When winds move water offshore, leading to cold water replacing it from the bottom. This upwelling usually results in a depression in sea surface height and temperature (Figure 54).

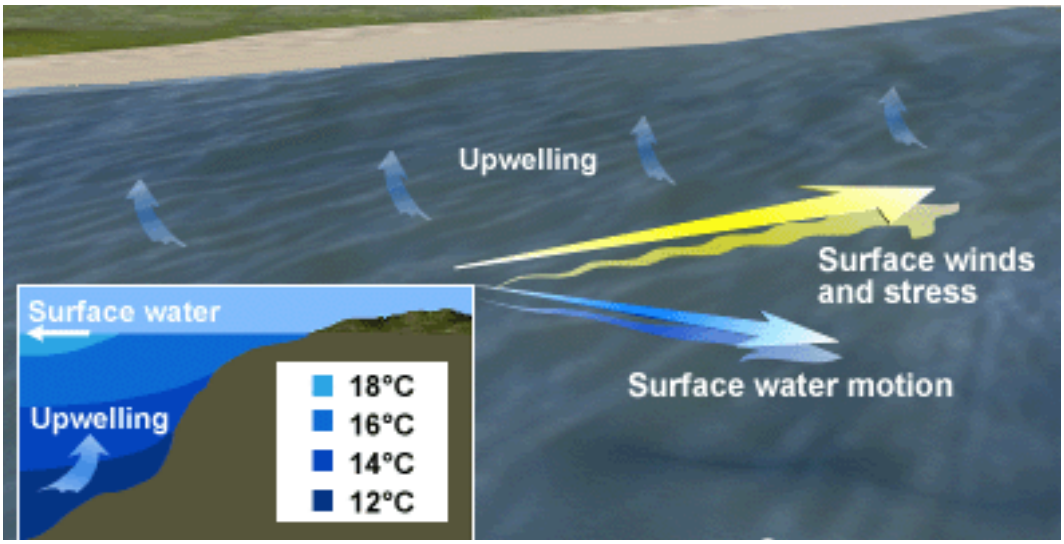

Figure 54 Along the coast wind moves surface waters offshore resulting in upwelling and lower sea surface height (www.comet.ucar.edu).

The Somali Current can be characterized as a coastal geostrophic current with large-scale strong surface wind forcing during the southwest monsoon, this winds drive the intense northeastward Somali Current along the coast of Somalia, whose surface currents can exceed 200 cm/s (e.g., Schott and Quadfasel 1980), lower SSHA indicate a stronger current, therefore we can use the SSHA covering the Somali Current area to produce an index that correspond to its intensity.

In most years, the month of July has lower SSHA than June or August (Figure 55). This index is calculated by averaging the SSHA during the summer months (Jun, Jul and Aug) over the Somali Current area over the past two decades, which indicate a low SSHA meaning strong Somali Current for the years 1993 to 2006 with the exception of 1993, 1999 and 2000 then high values suggesting weak current thereafter with the exception of years 2007 and 2010.

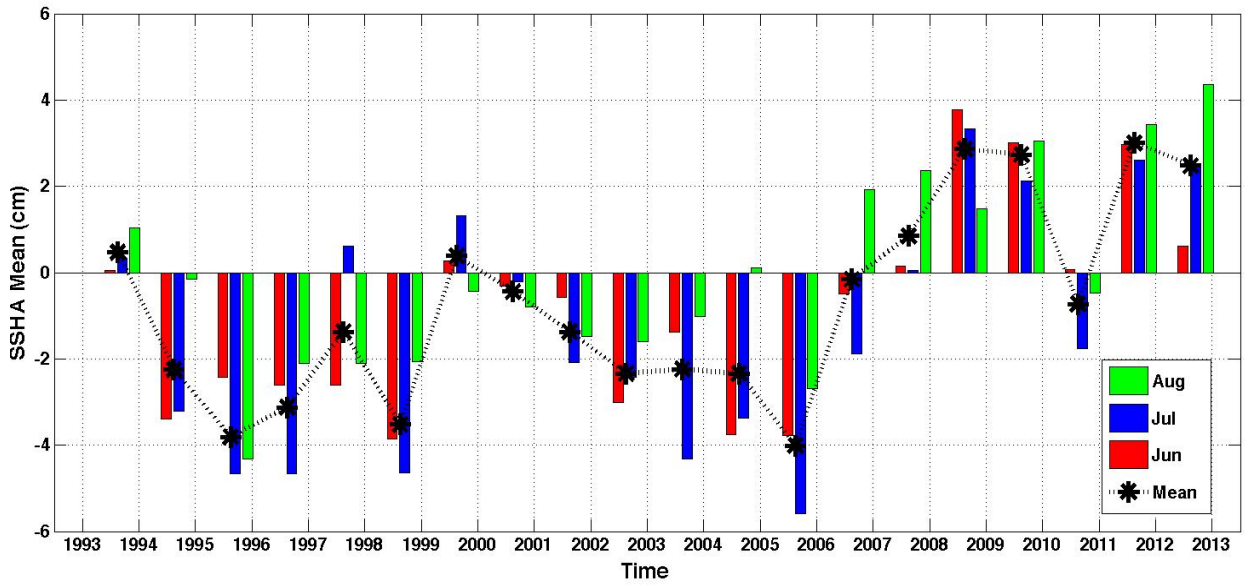

Figure 55 SSHA mean over the coastal area of the Somali Current during the summer months.

The probability density frequency (PDF) method is used on Figure 55 to illustrate the distribution of the SSHA in the area of the Somali Current. PDF are the percentages per unit of measure of the x-axis. Figure 56 is a histogram where the vertical axis is the frequency density of SSHA, It clearly points out the years with the lowest SSHA per bin with obvious similarity to Figure 49. Low values of SSHA (in red bars) characterize the intensity and sign of magnitude of the Somali Current.

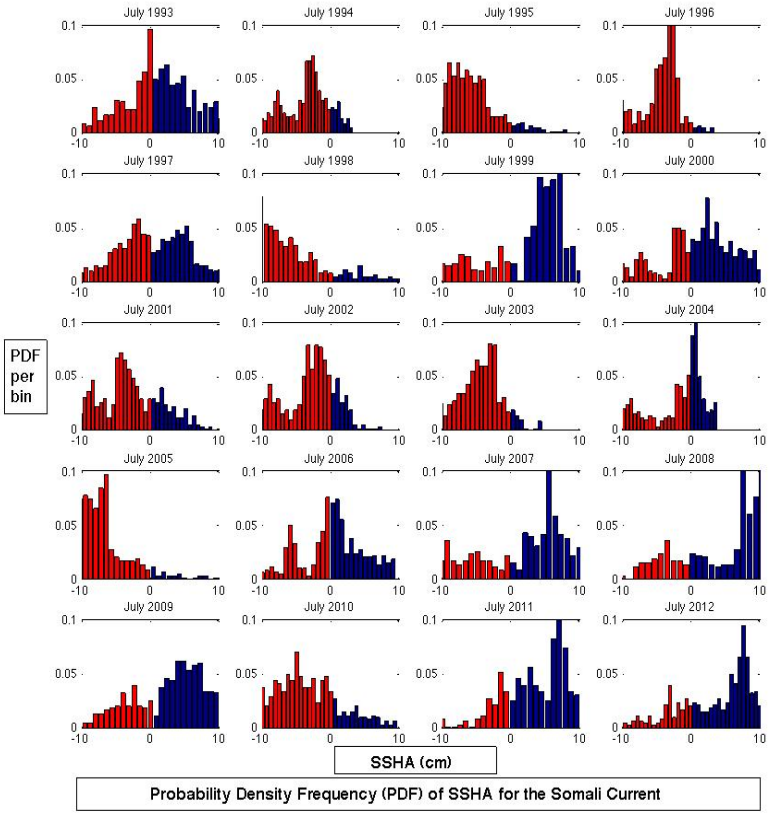

Figure 56 Probability density frequencies (PDF) per bin of SSHA for the Somali Current during the month of July 1993 to 2012, with negative SSHA is shown in red and positive in blue.

5.5 Analysis of the Somali Current surface wind and SST/SSTA data

Strong wind speeds during the summer monsoon lead to large dynamical ocean response that yields large SST gradients on the coastal ocean. In this section, we use satellite data to describe the variability in the surface wind and SST\SSTA within the region, where cold (warm) SSTs are associated with weak (strong) surface winds.

Over warmer SSTs, the near-surface atmosphere (1000 m) becomes unstable, leading to enhanced vertical mixing, bringing down high winds from aloft and accelerating the surface winds. Over cold waters on the other hand, the atmospheric stability and hence the vertical wind shear increase, decelerating surface winds. In situ soundings indeed show that the atmospheric boundary layer (ABL) stabilizes over the cold phase and deepens over the warm phase of tropical instability waves (TIW) (Hashizume et al. 2002).

5.5.1 Surface Wind variability and fluctuation in the region

Distinctive variability in oceanic dynamics is attributed to the degree of interannual mean value in atmospheric forcing as a direct result of mean values in the wind field. Characteristic of major periods of mean values during the summer monsoon, there is a measurable coupling of large scale atmospheric dynamics and deep convection that can be modelled through analysis of the surface signature including key surface wind variations that 'induce changes in both upper ocean mixing and latent heat fluxes uptake' (Vialard et al., 2012). Previous studies based on sparsely distributed in situ observations depicted the Findlater jet as a smooth wind jet off the coast of Somalia. One work using surface wind from a variety of satellites indicates that the Findlater jet is not a smooth feature at the ocean surface, but rather, it exhibits significant spatial variability (Halpern and Woiceshyn 2001).

As a result, surface wind patterns especially during winter and summer seasons will be assessed in this section as a significant impact variable associated with the variability of the Somali Current. It is well known that winds shift from being strong northeasterly (monthly mean wind speed 8 m\s) during boreal winter months, to being strong southwesterly (monthly mean wind speed 14 m\s) during the boreal summer months as it appears in Figure 57.

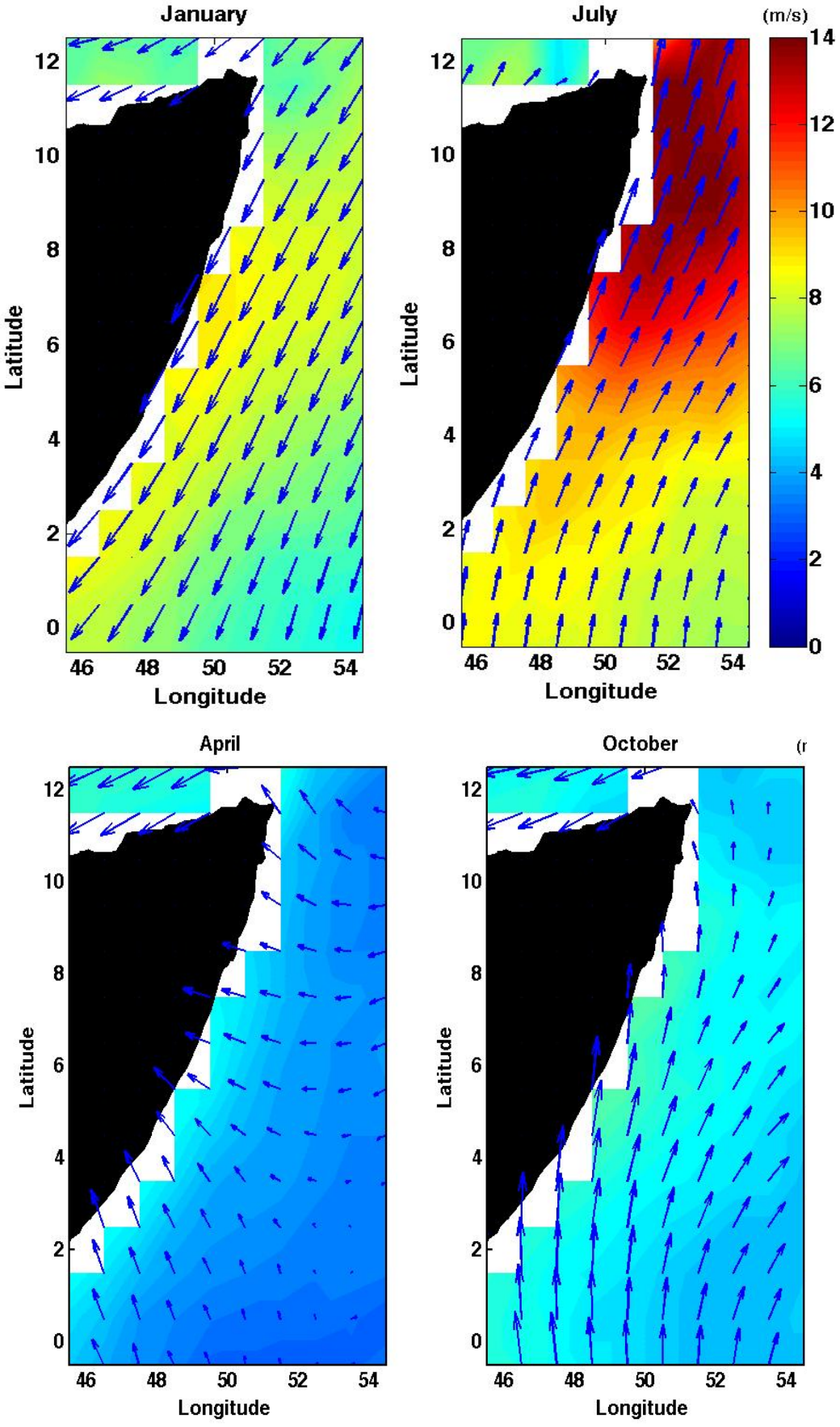

Figure 57 Wind speed and direction mean for all the January, July, April and October months between 2000 and 2009, from QuickSCAT

Figure 58 Show strong wind speeds at the first two summer seasons (1998,1999), and then it decreases for about a decade between 2000 and 2009 only to record high values again in the last four years. One interesting point is that when the values are high during the summer, they are considerably low the previous spring, another observation is the very strong wind speed of the spring of 2004, so strong it recorded the same values of wind speed as the summer season in the same year.

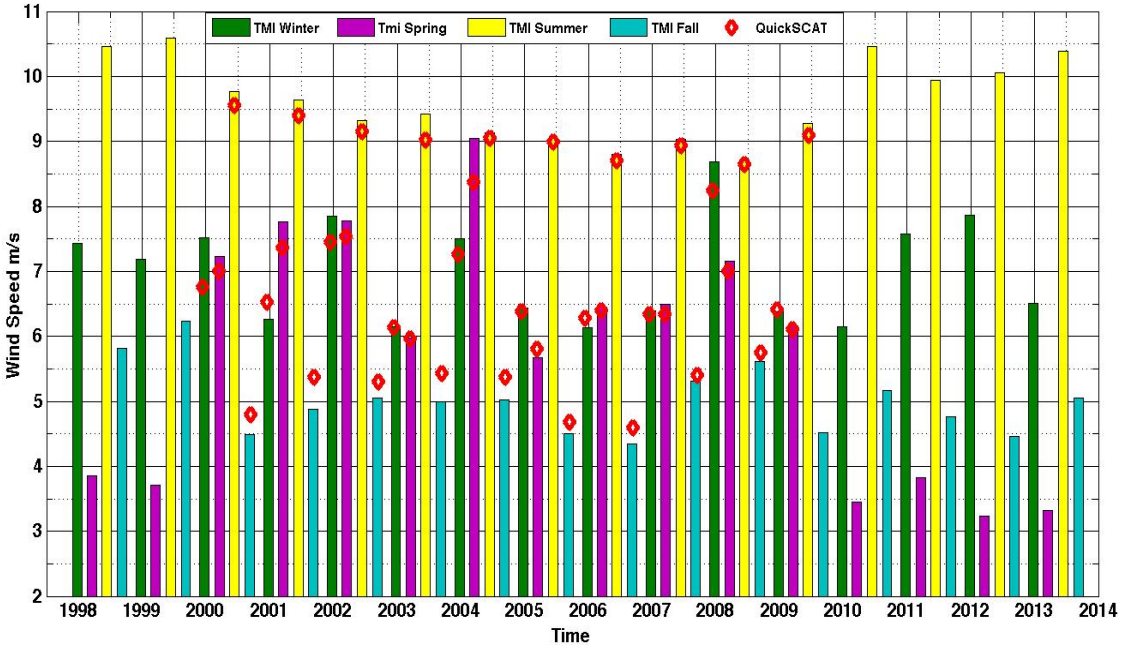

Figure 58 Somali Current area (0 to 12°N and 46 to 54°E) Wind Speed average from QuikSCAT (red marker, Jan 2000/Jul 2009), and TMI (color bar, Jan 1998/Dec 2014) during winter (green), spring (magenta), summer (yellow), fall (blue) seasons.

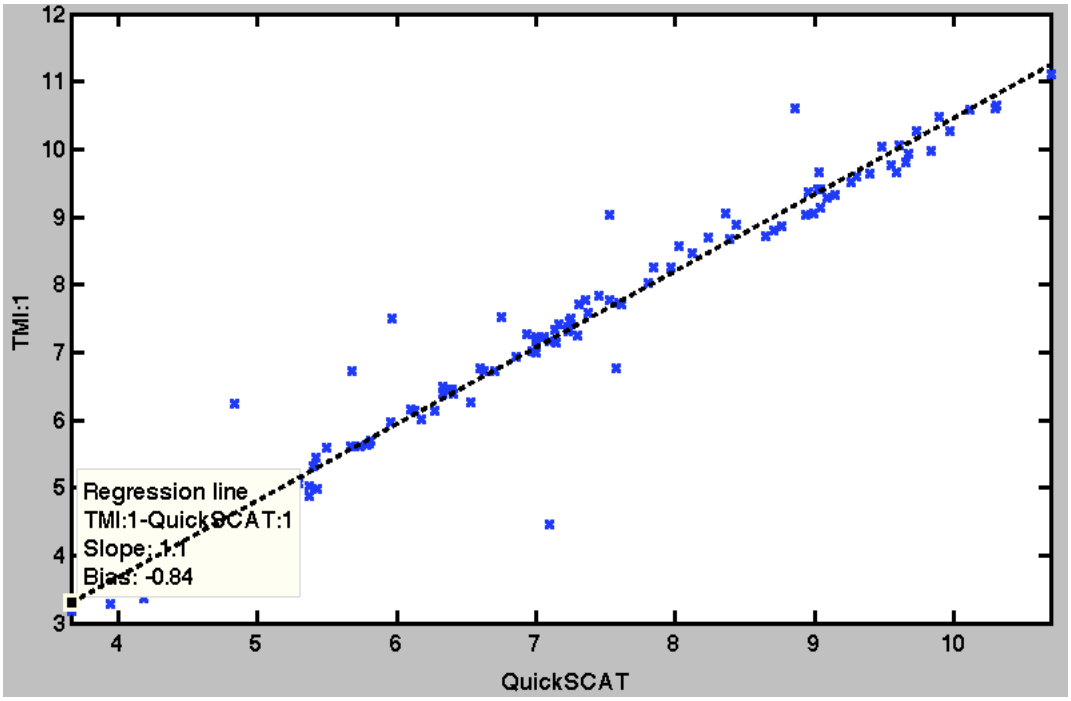

Figure 59 Scatter plot correlation between QuickSCAT and TMI indicating the strong similar values of wind speed observed by the two.

In order to visualise the nature of wind variability, Figure 60 introduces a visual plot of the zonal wind speed variability through the pressure levels from the NCEP model-based product, the Climate Data Assimilation System 1 (CDAS1, Kalnay et al. 1996), often called NCEP/NCAR Reanalysis1, which is mapped over the monthly temporal periods since 1997 to 2011 wind speed is averaged over the Somali Current area between 46°-52°E and 02°-10°N.

Although this plot is complex, it simply shows that the wind flow, eastward (northward) during the summer monsoon (May–September) and westward (southward) during the winter monsoon (November–February). It is clear that there is annual strong zonal wind reaching up to 14 m/s over the surface pressure level (1000mb) toward the east (positive) in July, with subsequent weak to moderate wind between 4 to 7 m/s toward the west (negative) during January throughout the Somali Current region. On the other hand in the upper pressure levels, at around the level 300mb, the situation is reversed, which is expected due to the equatorial Walker circulation. These strong, winds are likely linked to monsoonal activity and can be additionally correlated with wind pattern variability.

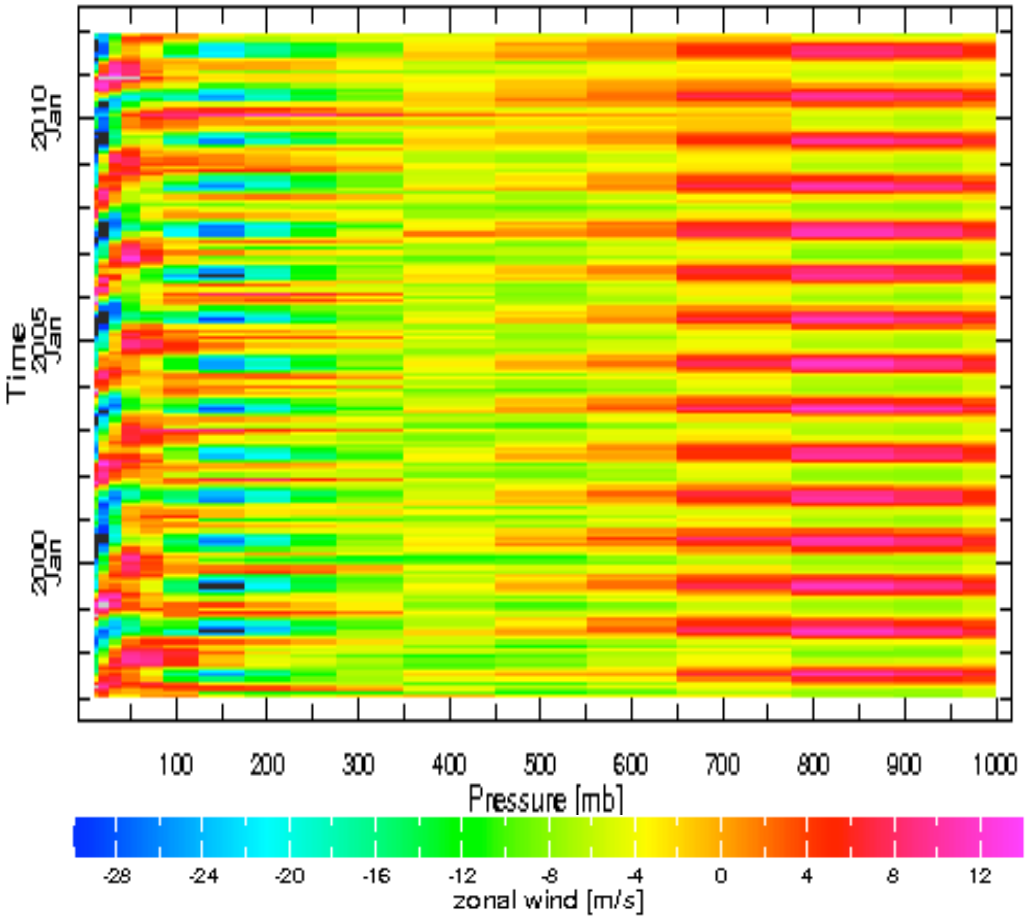

Figure 60 Intrinsic pressure levels mapped monthly of zonal wind speed averaged for the Somali Current area.

When we take a closer look at years 1998 and 2010 from Figure 60 as shown in Figure 61 we can notice that the zonal wind for those years at the upper levels are slightly stronger in the negative speeds (wind direction) during July, and significantly stronger in the positive speeds at the surface (1000 mb) compared with the other years zonal wind speed, where it is only at the upper level it is stronger in the positive during January, which is caused by the ENSO events of 1998 and 2010.

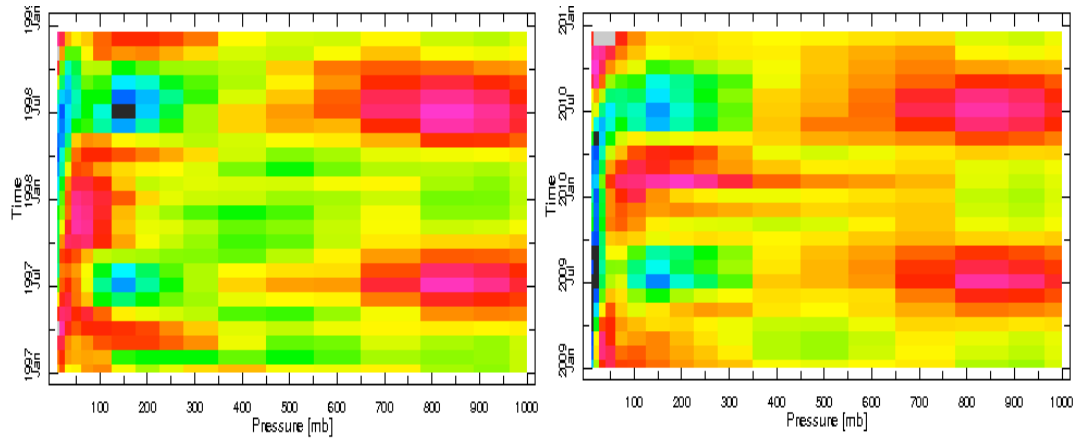

Figure 61 Zonal wind speeds Jan 1997 to Dec 1998 (left) and Jan 2009 to Dec 2010 (right)

By averaging the anomalous wind behaviour over time at the surface, Figure 62 indicates the broad range of variability in wind speeds that is linked to annual variability in weather patterns, particularly arising with sharp declines in wind force in January of each year. Such gathered strength ultimately peaks in mid July, regressing to its previous decayed position by the following winter season. One unique characteristic of this particular time series is that since 2008, wind speeds have not degraded as significantly, resulting in a more compressed mode of fluctuation which may be reflective of either changes in the assessment standards or a marked shift in climatic conditions that are altering regional wind patterns.

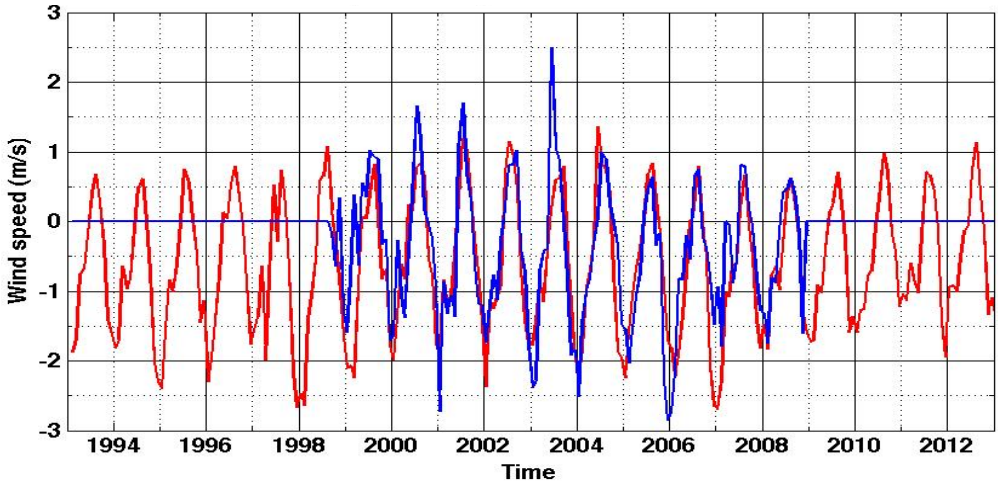

Figure 62 Temporal averages of regional surface wind speed anomalies from QuickSCAT 1999-2009 (Blue) and NOAA NCEP-NCAR CDAS-1 1993-2013 (Red).

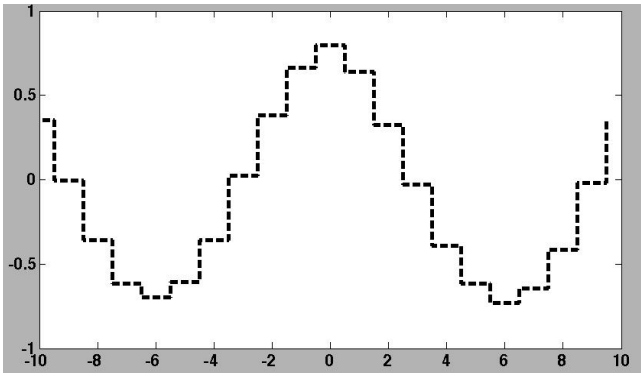

Figure 63 Cross-correlation between QuickSCAT and CDAS-1 zonal wind speed averaged over the Somali Current from Aug 1999 to Sep 2009.

Figure 63 shows the strong correlation between the QuikSCAT data and the CDAS1 reaching correlation around +/- 0.8, which is repeated every 12 lags due to the seasonally change. The main reason of interest in the zonal wind speed is that by examining its variability, hopefully we can identify if it has a connection with the Somali Current width (strength) where it might be that strong zonal wind speed leads to a wider and stronger Somali Current.

5.5.2 Analysis of the SST/SSTA in the Somali Current area

There are large changes in the ocean near-surface currents and thermal structures in the western Indian Ocean including the Somali Current area, Driven by the wind reversals. Figure 64 displays a time series of the averaged SST over the Somali Current area from the TMI mission between 1998 and 2012, and the NOAA NCEP EMC CMB GLOBAL Reyn_SmithOIv2 from 1993 to 2013 between 1997 and 1998, SST anomalies were recorded within the Indian Ocean that were significant and have been recognised in several studies as distinctive in relation to regional consistency and the intra-annual climatic anomalies (Murtugudde et al., 2000).

It is clear from Figure 64 that there is pronounced seasonality with SST within the Somali Current peaking during spring and followed by a strong decrease of SST during the late summer early autumn which Gualdi et al. (2003) equate to strong upwelling activities during this period.

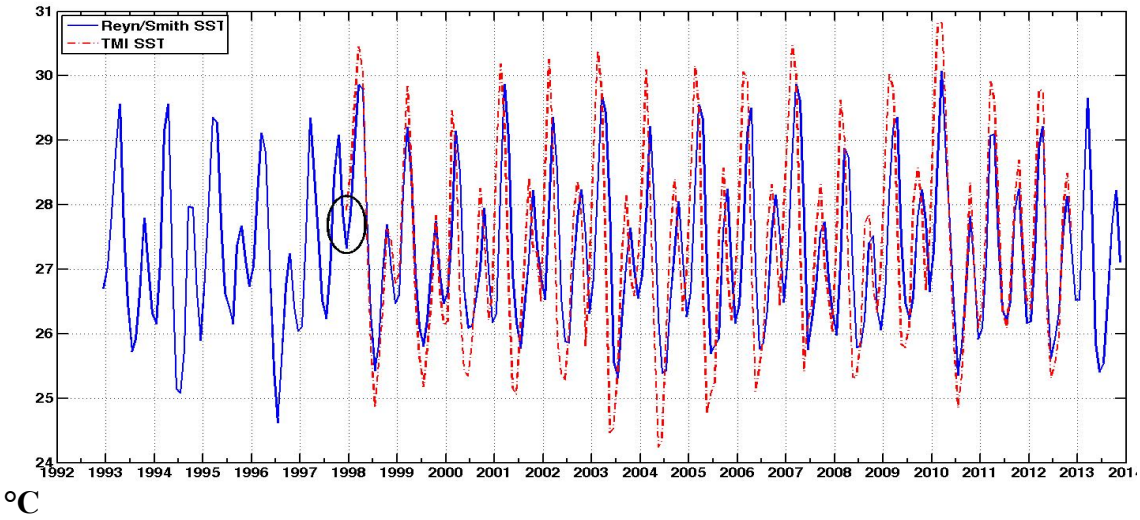

Figure 64 SST from NOAA NCEP EMC CMB GLOBAL Reyn_SmithOIv2 (Blue) and TMI SST (Dashed red), circled in Black is the anomalous warm winter of the year 1997/1998.

Based on empirical quantitative study by Reynolds et al. (2002), the IRICS database offers an opportunity to plot SST anomalies over an extended period. Figure 64 highlights the results from using this analytical technique, demonstrating a wide degree of variability. The data plot takes an average of SST readings during each month from the NOAA database for a given latitude (Y) and longitude (X) during a comparative temporal period. In this case, Y=(02N, 10N) whilst X=(46E, 52E) between the period 1993 and 2013.

When seasonal variations are present within a set of data, it often helps to express the data in terms of standardized anomalies. Standardized anomalies, also referred to as normalized anomalies, are calculated by dividing anomalies by the climatological standard deviation. They generally provide more information about the magnitude of the anomalies (www.iridl.ldeo.columbia.edu).

Figure 65 represents a measure of difference between the SST value and its monthly mean, which help remove the influences of location and spread from data therefore makes it easier to discern normal vs. unusual values. The SST standard anomaly in Figure 65 is calculated by subtracting the monthly mean from each observation, then dividing by the standard deviation.

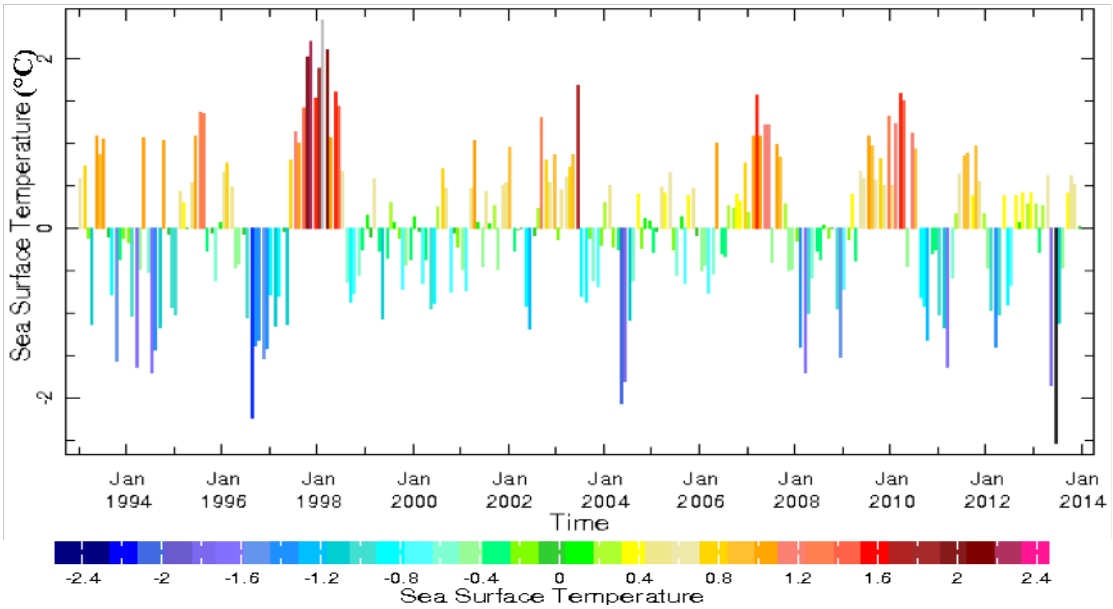

Figure 65 Reyn_SmithOIv2 monthly SSTA averaged over longitudes [46E, 52E] and latitudes [2N, 10N] between 1993 and 2014.

Again like the plot of the SST (Figure 64), the highly anomalous positive temperatures at the end of 1997 early 1998 (Figure 65) stand out reaching as much as 2.5°C, other strong positive anomalies occur in 2003, 2007 and 2010, where there is a considerable negative value in 1996 and parts of the years of 2004 and 2013. Figure 66 illustrate examples of strong negative, positive and neutral spatial pattern distribution of SSTA.

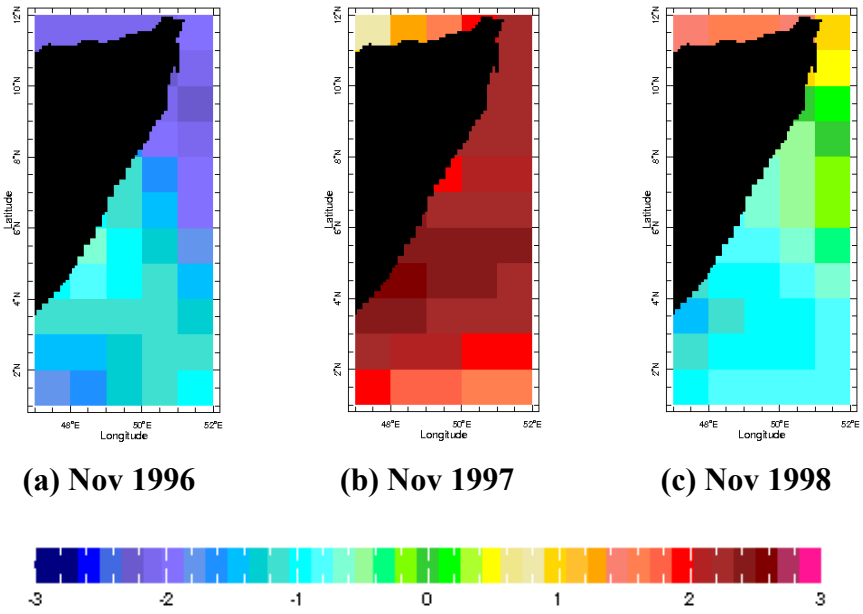

(a) Nov 1996 **(b) Nov 1997** **(c) Nov 1998**

Figure 66 Example of a strong negative (a), positive (b) and neutral (c) Monthly standardized SSTA in the Somali Current area.

5.6 Somali Current indices derived from EOFs products

5.6.1 SSHA Somali Current area EOFs during summer and winter

Although the EOF was applied on the SSHA monthly data in a previous section of this study covering the NWIO region, here we apply it again on the same data but on a smaller scale that only includes the Somali Current area and for January/July separately, to achieve the analysis of variability and anomalous SSHA and wind speed. For January (Figure 67) the cumulative variance, which is explained by the first three leading EOF modes reflect around 81% of the total variance. The first EOF is the most significant with just over 60% of the total variance; however, the second EOF is also important in this model, as it captured around 11% of this variance as well.

EOF1 offers representation of spatial patterning results that highlight positive variance toward the south coast and offshore which seems particularly characteristic of inter-annual modes of variability and the corresponding PC detects the strong ENSO signal in 1998 and probably the positive IOD modes during 1994, 1997 and 2006. EOF 2 reflects an inherently negative pattern alongshore extending to the north all the way to the African horn where it starts to move horizontally to the east most likely due to the northeast Somali Current, also with values close to the zero offshore and the PC indicate a decreasing trend from 1994 onward. Spatial pattern of the 3rd EOF is dominated by a strong increase of SSHA representing the GW just off the coast with its PC fluctuated between +/- 20 only.

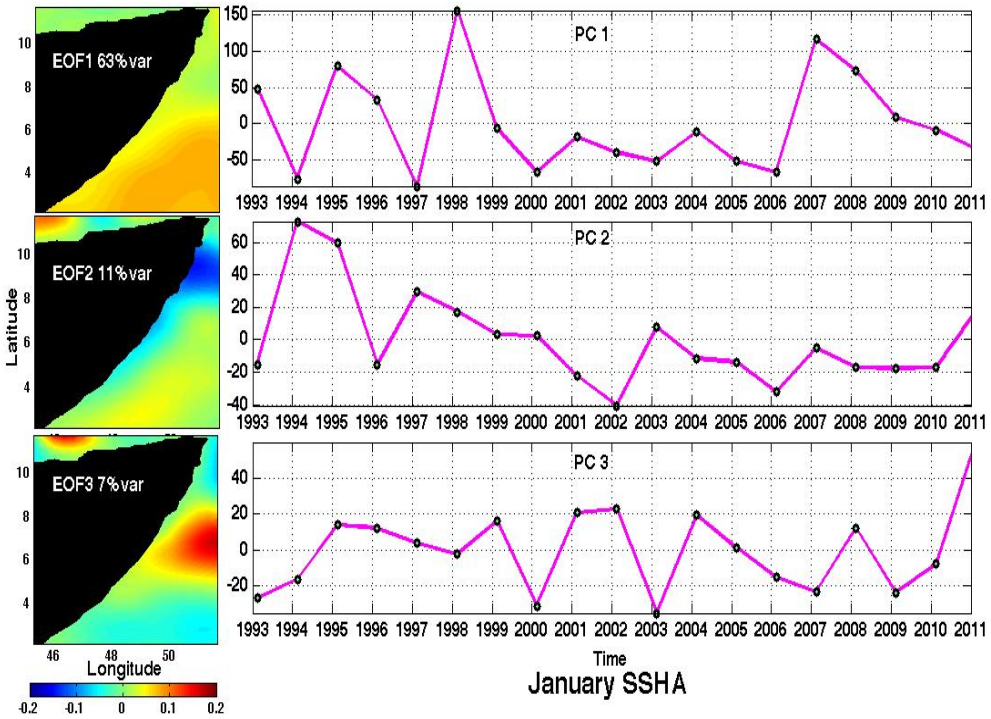

Figure 67 First three EOF's & PC's of SSHA for the January months.

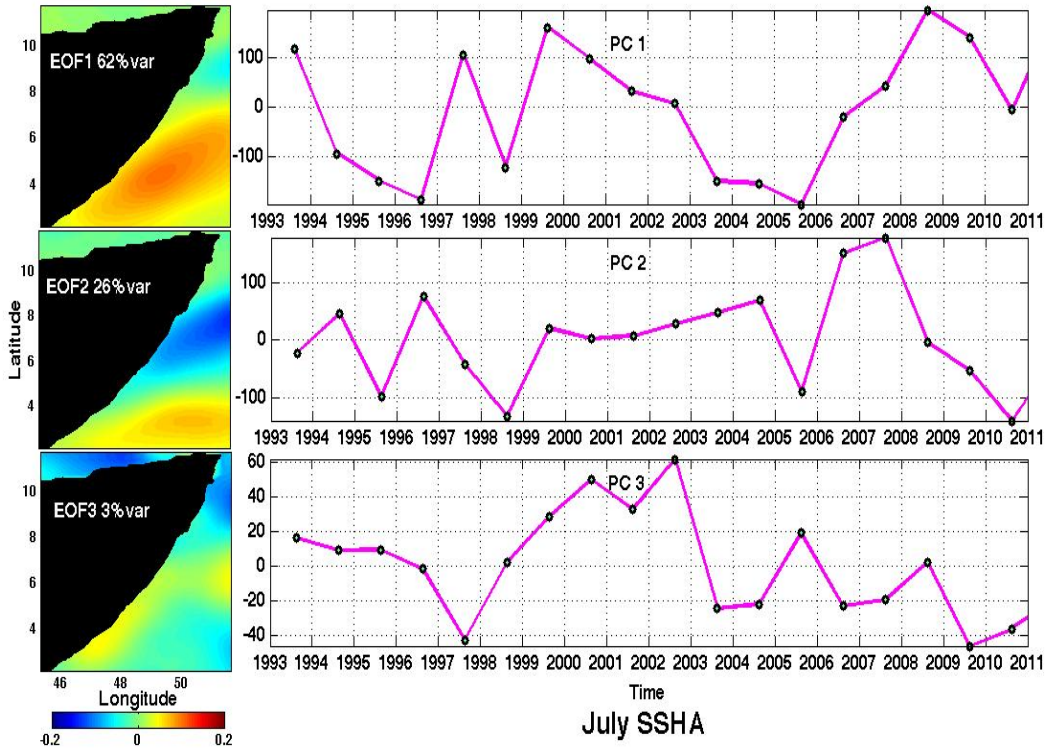

Figure 68 First three EOF's & PC's of SSHA for the July months.

Figure 68 highlights the first three leading EOF for SSHA of July months, of these three EOFs, the 1st mode was again representative of the majority of variance in this assessment at around 62%. This output is similar to the January one with slightly stronger contrast where its characteristic of a strong positive trend to the south and a wide negative trend in SSHA variance to the north in particularly between 6° and 10° N. This downwelling characteristic is indicative of variability in zonal currents or atmospheric patterns, which was assessed in previous sections.

EOF2 reflects a N-S gradient pattern demonstrating variability off the coast possibly reflecting the SW monsoon, which is at its strongest time of the season causing low SSHA along the Somali Coast, while the corresponding PC indicate an increasing trend opposite to the second PC of January. 3rd EOF spatial pattern has weak variation with figures close to zero and its PC is significant in the negative direction at 1997 and 2009 reaching as low as -40 of the time series scale and in the positive values of about 60 from 2000 to 2003.

5.6.2 Sea Surface Wind Speed Somali Current area EOFs

The cumulative percent variance from the first EOF mode mostly accounts for the majority of the wind speed variability in the Somali Current area, emphasising the high degree of variance that is captured. In particular EOF 1 accounts for 89% of the total variance, whilst EOF 2 and 3 account for 4.7% and 1.5% respectively. Such findings indicate that there is a much higher degree of variability associated with the first mode calculations, which then reflect behaviour of the monsoon phenomena; however, EOF 2 is also significant and will be discussed in relation to forcing patterns and regional variability.

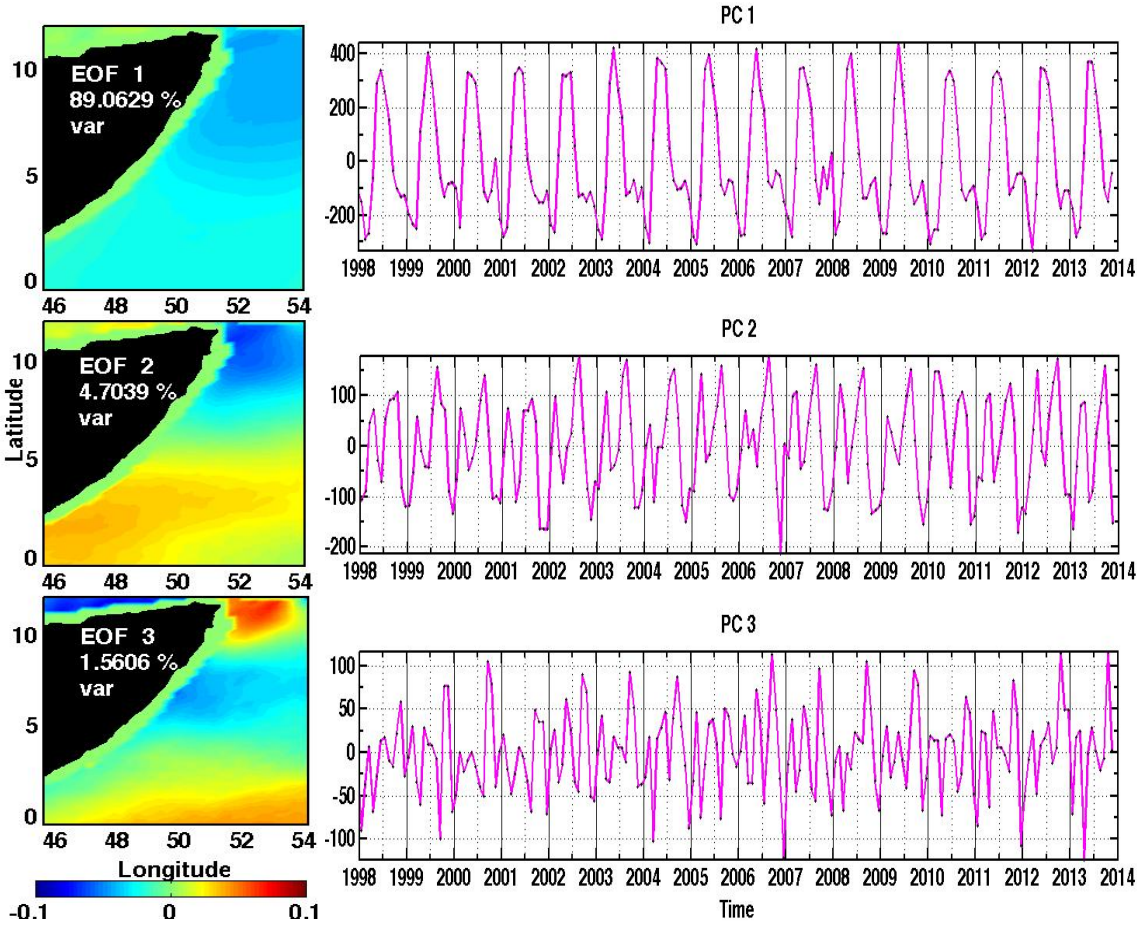

Figure 69 The first three spatial EOF and temporal PC modes of TMI wind speed.

From the spatial wind speed patterns (Figure 69), the green colour along the shores represent the NaN from the data, it is not very clear but there is a weak gradient towards the northwest forming a pool of negative values in EOF1. Emphasising the ocean characteristics associated with this variability, the high level of central western flux is characteristic of the downwelling effects, stimulating such regional phenomena as the Great Whirl in relation to the wind stress. Further, these wind patterns are indicative of a continental effect, strengthening as they emerge from the Somali coast where a low level narrow atmospheric jet (Findlater jet) exists during the summer monsoon.

EOF 2 is reflective of a bi-annual phenomenon, one which is likely attributable to a wave pattern expression in the form of regional Rossby waves or monsoonal winds. With a strong northward negative and an extreme southern positive, such evidence is directly linked to regional constants and weather pattern characteristics. EOF 3 only accounts for a small portion of the total variance although characteristic of this mode, that reflects a strong northern and southern positive with a central negative, resemble a pattern that appears throughout the SSHA and the SST during the summer monsoon as a cold wedge.

Perhaps the most valuable interpretation of these spatially oriented phenomena comes from the time series representation especially PC 1&2, Such findings are indicative of a distinctive negative period each January which is consistent with higher SSTs and higher SSHA. In the subsequent 3-4 month period, the monsoonal rains are introduced to this region, resulting in strong wind patterns, elevated SSH, and a general decline in SST. As reflected in PC 1, in spite of anomalous regional patterns relating to ocean phenomena, wind patterns are constant and manifest over an extended period of time with little variance.

The wind speed is highest during the summer season and lowest in the spring. PC 2 is indicative of an intra-period fluctuation, whereby wind levels rise and fall according to seasonal variability as opposed to coupled atmospheric and oceanic factors. Under PC3, it is evident that there is a strong compression of variability that is largely restricted to minor wind changes reflected over the temporal period.

5.7 Somali Current indices vs. ENSO and DMI

Out of the indices produced for the Somali Current in this chapter, only two show significant correlation with both DMI and ENSO indices, where both Somali indices are calculated from the data during the winter in January when the two climate modes peak, as for the July indices they indicate only coincide with the ENSO events of 1998 and 2010, which indicates that the ENSO impact persists to the following summer season and the IOD have little impact on the Somali Current during July. The correlation is significant at the winter season because at this period the climate modes have the strongest influence on the equatorial zonal winds in the central Indian Ocean, which is related to the Somali Current system.

The first Somali Current index is the SSHA slope of the near-shore minus the offshore index (Figure 70), which clearly indicates that SSHA difference between the SC near-shore/offshore has an opposite direction in sign to the DMI&ENSO indices. Especially during the positive IOD and El Nino years like January of 95 and 98, which are the two strongest years of IOD&ENSO events in the past two decades where the SC index showing the highest negative SSHA difference. On the other hand, Figure 70 indicates that SC index slope do not react consistently during the negative IOD and La Nina years.

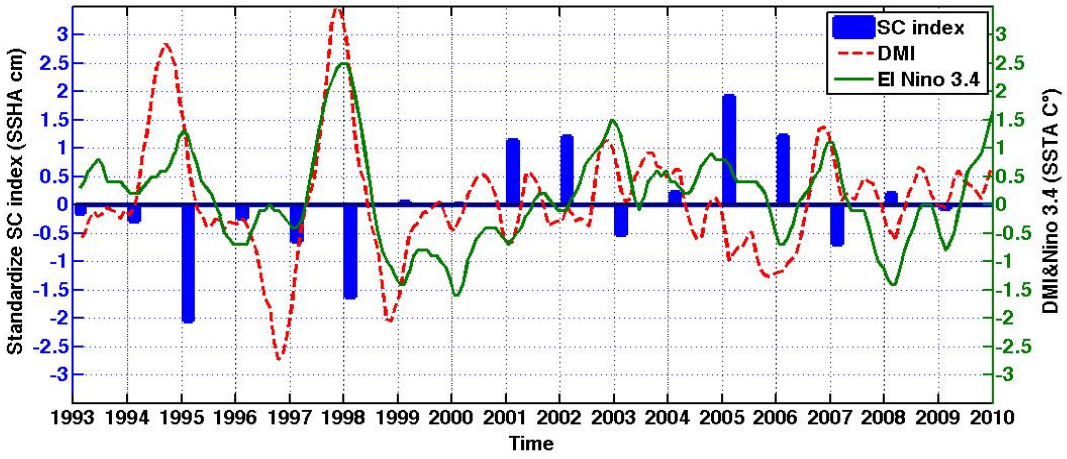

Figure 70 DMI SSTA (red), El Nino 3.4 index (green) and standardize Somali Current SSHA index from near-shore minus offshore of January months (blue).

Linear regression analysis show higher correlation with the IOD than ENSO for the Somali Current standardized SSHA of near-shore minus offshore, which has with ENSO a correlation coefficient of only 0.4 and coefficient of determination of about 0.18, but much higher than that with the IOD (Figure 71).

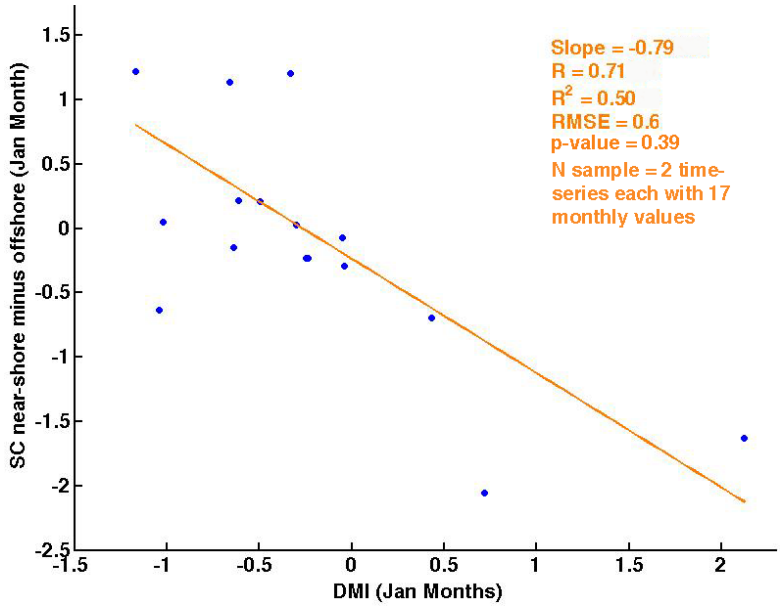

Figure 71 Linear Regression between IOD Jan months and Somali Current near-shore minus offshore SSHA Jan months with a slope of -0.79 and r^2 about 0.5 for a 95% level of confidence.

Figure 72 is the second SC index that has a significant correlation with IOD&ENSO, which is the 1st Principal Component of the SSHA over the Somali Current area. It also shows an inverse relationship with the climate mode indices major events from 1993 to 2010, but here the index is more correlated with the IOD because it shows a slightly better relationship to both positive and negative IOD as in January 97 high positive SSHA during the major negative IOD event.

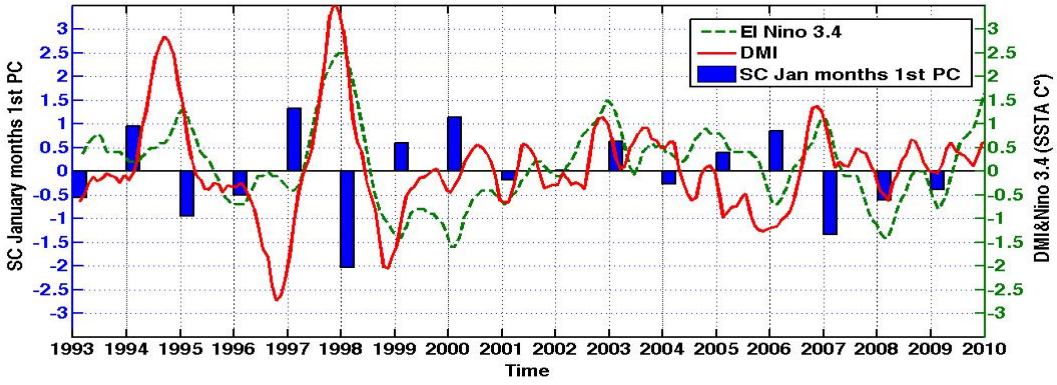

Figure 72 Time series for the first Principal Component (PC) of the SSHA Somali Current area for January months (1993-2009) and DMI&El Nino 3.4 indices.

The correlation coefficient is 0.73 and coefficient of determination is 0.53 for a 95% level of confidence (Figure 73&Figure 74) that is also higher than the correlation with ENSO, which is 0.5 for the correlation coefficient and 0.26 as the coefficient of determination.

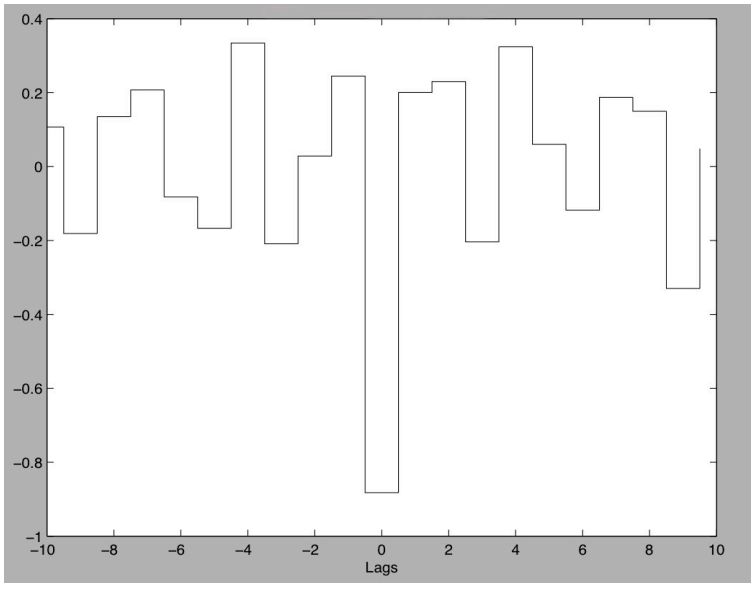

Figure 73 Cross correlation between PC1 of Somali Current SSHA for January months (1993-2009) and DMI.

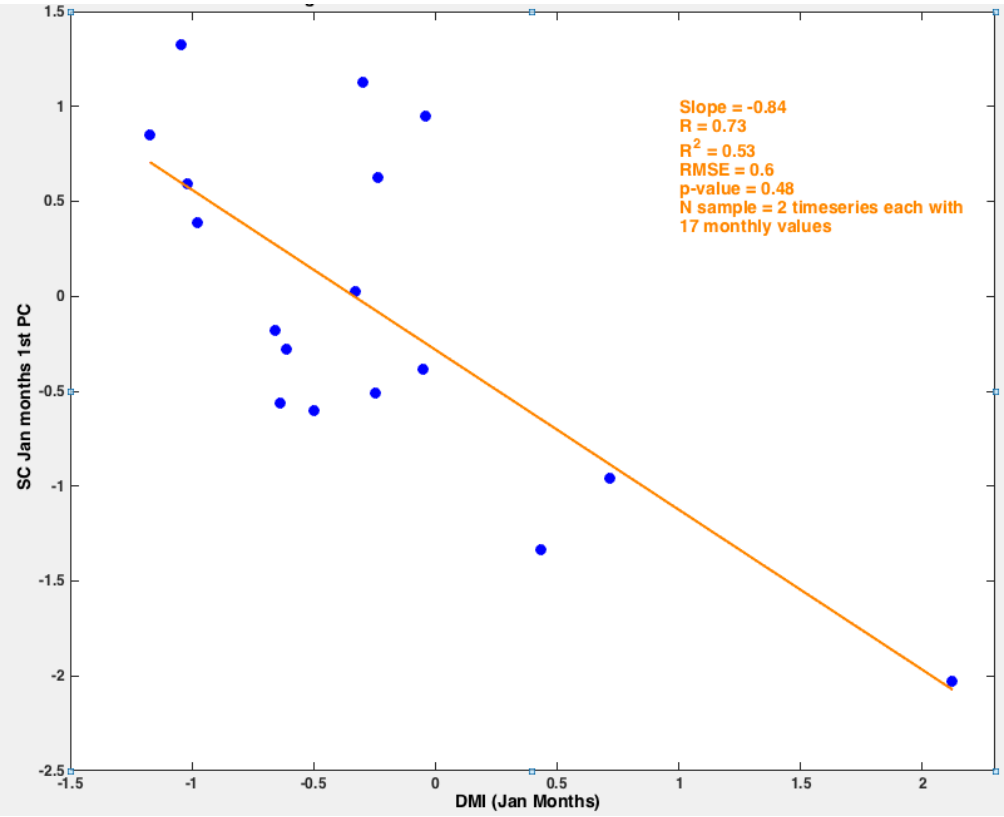

Figure 74 Linear regressions between IOD Jan months and Somali Current SSHA Jan months 1st Principal Component with a slope of -0.84 and r^2 of 0.53 for a 95% level of confidence.

5.8 Summary

The Somali Current is very intense, but unlike many other western boundary currents it is highly variable due to the complete seasonal reversal of the winds. One important consideration is in how to interpret the data from SST and SSHA readings. Indeed, there is an important distinction between SST and SSHA when used as remote-sensing signatures of meso-scale dynamics, because the SSHA field is hardly affected by small-scale thermodynamic processes in the surface layer (Robinson, 2010). By viewing both of these factors together, it was hoped that SSTA and SSHA would present a robust data set for addressing the climatologic annual and seasonal shifts in the Somali Current characteristics. This seems to have been validated across both data sets, which show elevations for the 1998 ENSO event in particular. For example, the SSHA data and SST observations showed a clear correlation between elevated sea surface height and significant ENSO events. However the intensity and variability of the Somali Current is influenced by a variety of climatologic and meteorological conditions associated with the reverse direction in response to semi-annual monsoonal wind forcing.

6 Great Whirl Variability Indices from Remote sensing data

6.1 Introduction

The area off the Somalia coast represents a highly dynamic oceanic environment characterised by seasonal evolution of oceanic current patterns and upwelling distributions that Wiggert et al. (2006) recognised lead to 'pronounced biogeochemical variability throughout the basin'. Therefore it is considered one of the most valuable geospatial regions for assessing and analysis. In fact, researchers including Schott et al. (1997) and Fischer et al. (1996) have attributed the summer bloom off the coast of Somalia to the upwelled waters that are entrained around the Great Whirl, an annual anti-cyclonic circulation pattern that is the northern component of the Somali Current's two-gyre system.

The Great Whirl gyre occurs in a region of a tropical climate and its strongest signal can be detected during the month of July when the climate of the region is dominated by incoming solar energy where it enters the atmosphere more directly than in higher latitudes throughout the year. There is also less of a seasonal shift in the solar energy coming into tropical areas than seasonal shifts that occur over higher latitudes. Characteristically, this means that throughout the year, the solar energy is high, and as a result, both the ocean and land surfaces at the tropical latitudes are warm year-round. As a result of these interrelated phenomena, tropical climates, particularly those localised over oceans, manifest a lower annual variation in mean temperature than any other climatic regions on earth. It is frequently recorded that the diurnal temperature range in tropical climates exceeds the annual temperature range which is typically only 3-6° C. Throughout the year, the night-time temperatures are typically between 21-27° C, whilst daytime temperatures are 30-35° C. Temperatures below 16°C or above 38°C are rare and anomalous in land and even more for the ocean. In other words the horizontal gradient of SST is very small making it difficult to identify mesoscale features such as the Great Whirl using remote sensing sea surface temperature product only.

Figure 75 is a schematic diagram of the Somali Current upper layer flow pattern during a given year based on measurements from different years, demonstrating the aforementioned movement of the Great Whirl and high degree of variability in current fluctuations.

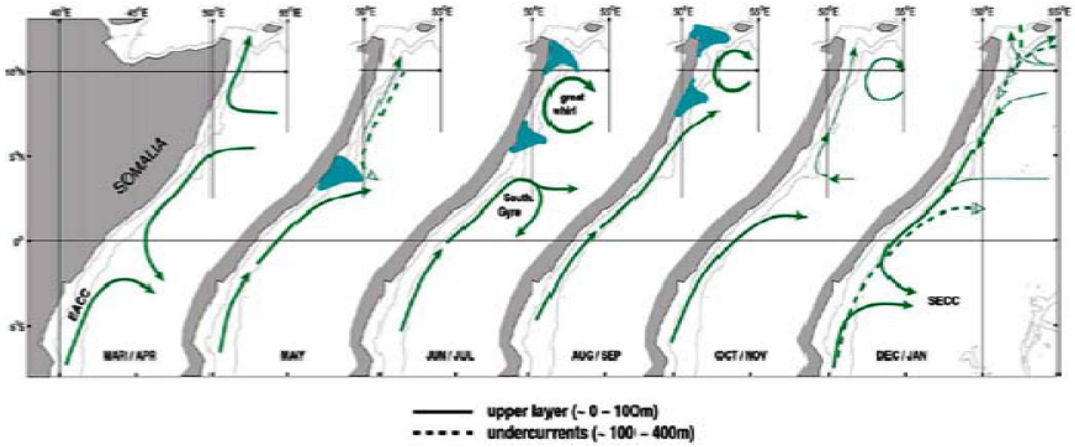

Figure 75 Schematic Diagram of Somali Current showing the Upper Layer Flow Pattern and the development of the upwelling region along the Somali coast up to the horn of Africa (Schott & McCreary, 2001)

The following chapter will be focusing on the generation and analysis of Indices for the Great Whirl, using SST and SSHA remote sensing data plus their anomalies, to recognize the patterns of climate variability of the GW during the summer monsoon and understand more about the Great Whirl system, e.g. how it behaves, its interaction with other features such as the Somali Current and with the larger scale aspects of the Indian Ocean. This phenomenon has a direct influence on the wave-based characteristics of this particular geographic region. For example, from March through May, The southern Somali Current can be identified as an extension of the EACC, flowing northward through the region. Between June and July, at the onset of the June monsoon season, the 'Great Whirl' manifests.

Schott and Quadfasel (1997) recognised through analysis of mooring data in the Northern Somali Current region that during their analytical period, there was an early onset of the 1995 Great Whirl eddy, after which they reported distinct, westward-propagating signals. The researchers attributed this behaviour to the first mode of Rossby waves, which possibly resulted in the initiation of the Great Whirl. These Rossby waves were initiated as a response to strong anticyclonic wind-stress curl offshore from the Somali coast. These waves were then reflected into short waves at the boundary, accumulating energy near the boundary.

6.2 Data and Methodology

6.2.1 Data and Resources

In this chapter we will be analyzing several data sets to explore the Great Whirl, one data set is the SST that can be a valuable measure of its climatic variability; however, such records must be defined over an extended temporal period because of both climatic anomalies and noise and the relatively extended nature of any temperature evolution processes. In fact, Singleton (2004) suggested that oceans and, more specifically, surface level temperature readings are generally regarded in climatology as the 'memory of the Earth's climate system'. Accordingly, measuring and analysing SST and surface wind speed changes over time within the area of the Great Whirl will allow us to identify particularities in its system behaviour over the past 15 years and identify any substantive changes that may have taken place, using SST/surface wind speed starting from Jan 1998 to Dec 2012 of TMI. One other dataset is the SST Anomalies, calculated by subtracting the monthly climatology from the SST. Miliaresis and Seymour (2011) defined a thermal anomaly as 'a region with distinct spatial and temporal temperature variance with respect to the surrounding areas'. Although relatively basic, the manifestation of SST has been empirically linked to constant geophysical behaviour including ocean dynamics, water circulation and deep-trough activity. Further, consistent with other global climatic events, thermal variance and sea surface temperature changes continue to reflect climate change (Miliaresis and Seymour, 2011).

Also the SSHA dataset from T/P+Jason1 for the same period of the SST will be used mainly to map variation in the Great Whirl, quantify their amplitude and diameter, track the trajectories, and examine the eddy dynamics to have a better understanding of its role in the ocean processes and climate variability. The primary datasets used in this research are measured by remote sensing mainly because of the emergence of more reliable satellite imaging and a broadening spectrum of analytical tools in recent years, especially for the region of interest. One way of validation of this dataset is to look at research based purely on remote sensing and validated by site-specific readings and comparison such as Rao et al. (2002) that have leveraged such advanced resources to generate a quantitative research model. Such justification of remote, rather than in-situ, observation and analysis of datasets allows researchers to leverage readily accessible records from such leading institutions as NASA and the Japanese Space Agency, who was responsible for the Tropical Rainfall Measurement Mission (TRMM).

6.2.2 Procedures and Methods

This study will contribute to the base of knowledge by improving upon existing methodologies and apply research to the Great Whirl SST, surface wind speed and SSH anomalies over a set period of time. By the analysis of anomalous behaviour in this area we hope to specify its climate variability, although as evidenced by Beal and Chereskin (2003) a high degree of transient variability is characteristic of the Great Whirl that is prone to climatological influences. The consequence of such a significant departure from behavioural patterns results in a methodological limitation, one which leads the research to try to identify the magnitude of internal variability of the Great Whirl from the possible external causal links that may be responsible for this high degree of variability. Statistical analysis tools such as MatLab (appendix E) are mostly used here to conduct in-depth analyses of changes in climatic and geographic features and behaviours over time.

- Using the SSHA within the area of the Great Whirl to develop an index based on the magnitude of strength derived from the maximum values of the SSHA at the center of the Great Whirl.
- Calculating the size of the Great Whirl by the area it covers at selected SSHA values representing the border of the Great Whirl.
- Generate an index for the Great Whirl strength from the time series of the SST and SSTA, by first identifying the min/max of SST in the area where the gyre is generated to locate the centre then calculating its size and the difference between values in the centre and the outer boundary of the gyre.

The main aim here will be to use the satellite-based measurements to describe strong ocean–atmosphere covariability linked to the Great Whirl area SST&SSHA variability during the southwest monsoon.

6.3 Magnitude and size of the Great Whirl using SSHA

6.3.1 Time series index based on the maximum SSHA at the center of the Great Whirl

Measuring the relative departure of sea surface height from its long-term mean level at the same location through remote sensing data offers an opportunity to view potential oceanic variability on both macro and meso-scales. These SSHA are an important aspect of analyzing variability in the Great Whirl and looking at the potential range of influences, which produce this variability. Analysis of ocean surface features such as these are valuable because they allow for basin-wide data coverage to be assessed over short time intervals and allow for inter-annual variations to be considered (Somayajulu et al., 2000). This is essentially because the temporal variability of surface currents can often be determined from the relative differences seen in this altimetry SSHA (when the temporal mean is removed) across the domain of a particular current. When assessing data relating to SSHA in the Great Whirl the difference between the dynamic and static ocean topography can be reviewed – differences which are the result of complex interactions between the ocean surface and atmosphere (Robinson, 2004). Where significant anomalies are observed, these interactions and the potential factors, which influence this variability, can then be considered through other observed or modeled data.

Data has been obtained from the T/P, Jason1 and Jason2 altimetry satellite missions and processed through Matlab. As the Aviso data sets have already been corrected for potential orbit and environmental errors it was considered that no further validation of this data set was necessary before the data could be analyzed. Previous research assessing SSHA data has tended to focus on seasonal variance and the onset of the Great Whirl. This has outlined seasonal variability: with the onset of the monsoon winds in early June, the Great Whirl intensifies, remaining at its peak throughout July, August and September, dissipating about one month after the winds have died (Beal and Donohue, 2013). The data obtained for this research focused on sea surface height anomalies in the Great Whirl maximum over a period of 20 years to allow for assessments of inter-annual data sets. July data sets were selected to represent a seasonal SSHA present at the peak strength of the Great Whirl and allow for assessments of SSHA when the Great Whirl would be at its most active – to assess if there are potentially significant influences beside the monsoonal influence as this is essentially a measure of the SSHA maximum of the Great Whirl.

Figure 76 shows SSHA data obtained for the month of July between 1993 and 2012. This was presented using a Matlab routine (appendix E) function to graph the data obtained and allowed for more effective time series patterns to be displayed and assessed. This allowed for information to be presented in relation to the ongoing evolution of the Great Whirl in terms of SSHA and the variability of its maximum height in each year. The data presented here represents a time series index based on the SSHA maximum at the centre of the Great Whirl.

The T/P and Jason1 along-track record of SSHA has been a widely utilized and respected data resource for many of the fields of ocean dynamics research, as discussed in Robinson (2010) and Fu (2010) and was considered particularly useful tool in assessing SSHA in this area in terms of providing valid and accurate data sets. Rather than analyzing individual eddies or defining the flow fields, the SSHA from altimetry can be used to measure the spatial distribution of the strength of meso-scale (10 – 100 km) turbulence (Robinson, 2010), allowing for more general assessments of variability over longer time frames. This allowed for data sets to be considered over a two-decade period to ensure that discussions relating to seasonal variability were more robust, although we need to consider that the whole region will be with higher than normal SSHA due to ENSO or IOD events.

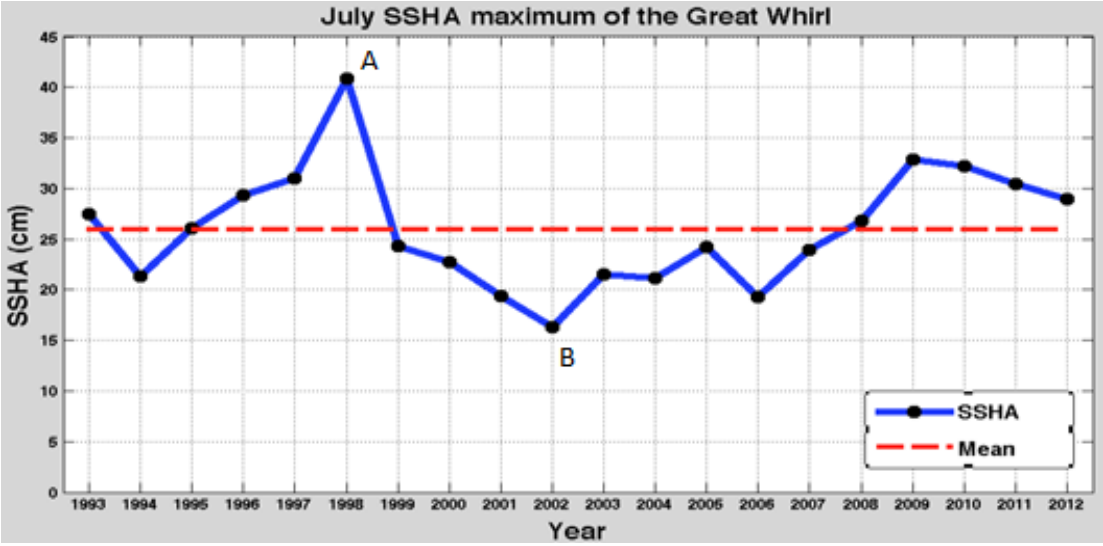

Figure 76 SSHA maximum at the center of the Great Whirl (blue-solid) and its mean (red-dashed) for the months of July from 1993 to 2012.

Points A and B on Figure 76 have been highlighted as the highest and lowest SSHA data recordings across this period, however in more generalized terms the data does not stray too far from the calculated mean for this period, with the positive SSHA showing further transition from the established mean result.

Despite this, there does appear to be some clear variability from year to year. This agrees with the work of Somayajulu et al. (2000) who indicates that numerous meso-scale cells of both positive and negative SSHA, with the magnitude of these cells varying from year to year, generally characterize the Arabian Sea.

Overall, across the two decades of data obtained for the central Great Whirl region of the Arabian Sea, 10 data points fall below the mean, 9 above, and 1 reading is right on the mean result. This suggests that there is inter-annual variability across this time period, and that there are significant anomalies affecting the overall mean result. During the years 1994, 1995 and 1999 the SSHA patterns show negative anomalies from the data sets obtained, with 1996, 1997 and 1998 showing an increasing positive anomaly. From 1999 onwards there is a prolonged period of negative anomalies, up to 2008 when the SSHA enters another period of positive results (up to the final result set in 2012). As well as seasonal variability this data does seem to suggest distinct patterns associated with more meso-scale oceanographic and climatological phenomena occurring on wider time-scales that the monsoonal shifts.

Results of the SSHA maximum across this time period for the Great Whirl area reflect a relatively even distribution. It appears that the larger anomaly observed in 1998 may have impacted upon the general mean of SSHA in July for this region across the 20 year period analyzed. In general, however, there is little variability across inter-annual assessments, with variability generally between 1 and 10cm of the mean. For the 1998 event this variance jumps to more than 15cm above this mean value and represents a data point of particular interest. Indeed, this degree of inter-annual variability for this particular data point is indicative of a wider pattern amongst this data, which suggests a potential seasonal signal that occurs over longer time frames (i.e. not a seasonal signal which is merely repeated year upon year).

These signals could potentially be from coastal currents, or the upwelling zones within the Great Whirl zone (as discussed in Kumar et al., 1998). Historically both in-situ and remote sensing observations of this area have indicated that the Great Whirl evolves slowly as a result to the development and eventual relaxation of the monsoon (Prasad et al., 2005). In this research it was also interesting to note larger-scale temporal differences, with the SSHA from the centre of the Great Whirl for July maximums appearing to be grouped in low and high data sets that occur over several years.

6.3.2 Index of the Great Whirl from boundary area

Boundary areas are an important consideration for quasi-stationary eddies. Rather than having a continuous boundary, the formation and development of the boundary areas associated with phenomena such as the Great Whirl can often vary quite considerably over time.

The Great Whirl eddy has a spatial horizontal scale of between 350 and 750 km with surface velocities typically varying between 1.5 and 2.0 ms^{-1} based on Peng and Olson (2004). It has been observed to form during late May and early June between 5 and 10 degrees north off the Somali coast (Peng and Olson, 2004; Jensen, 1991). Due to the varied location of the Great Whirl, assessments of available remote sensing data were undertaken to try and determine the extent of variability and the potential influences upon these fluctuations.

The Great Whirl size and volume was obtained to show the geographic positioning of this particular oceanographic phenomena and how the area and location of the Great Whirl may potentially change due to various oceanographic or climatologic influences. Figure 77 shows the SSHA of the Great Whirl of greater than 10 cm for July between 1993 and July 2010. The results showed that the Great Whirl area varies greatly year upon year, often shifting location and intensity across inter-annual patterns.

The results obtained show that there is strong variability from small area coverage of the Great Whirl of no more than 2x2 degrees in size (as in the examples of 2002 and 2006) to the strong contrast of 1998 and 2010 where the boundary area covered by the Great Whirl is much larger (increasing to around 5x5 degrees) as shown in Figure 77. Although the Great Whirl is considered to be geographically fixed (Frantanoni et al., 2006; Prasad et al., 2005), this data does provide fairly robust evidence that the Great Whirl boundary area is actually highly variable over inter-annual assessments, and may suggest that the area boundary of the Great Whirl is influence by both monsoonal conditions, and wider meso-scale oceanographic and climatologic influences such as ENSO events.

This is perhaps evidenced in Figure 77 by the larger area and northwesterly location of the Great Whirl in 1998 (strong ENSO year) when compared to other years, and the development of larger area Great Whirl eddies in 2010, the onset of another moderate-strong ENSO event.

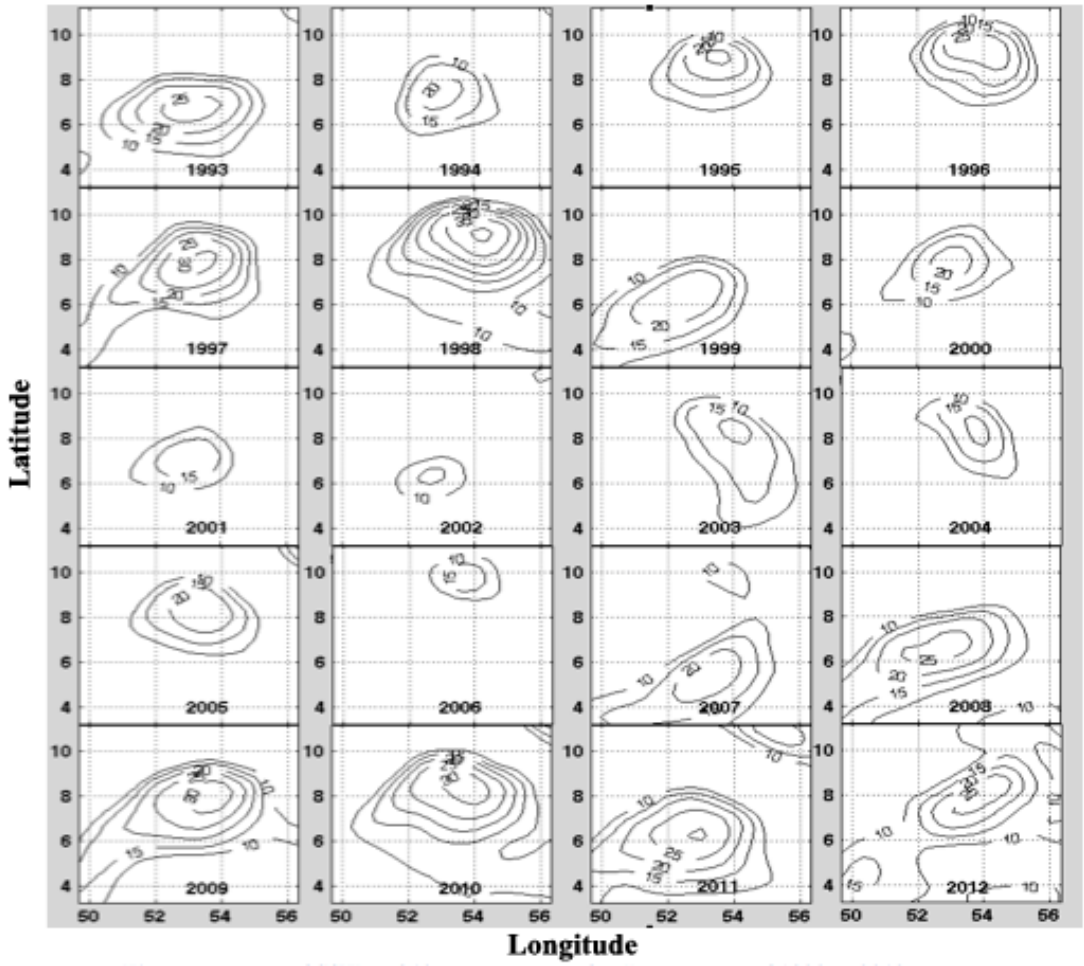

Figure 77 Maps of SSHA of 10 cm and above for July months of 1993 to 2012, showing the border of the area covered by the Great Whirl.

Figure 77 also shows that there is a definite propagation of the Great Whirl eddy towards the northeast over inter-annual patterns. This appears to be fairly cyclical with the change occurring over a period of roughly five to seven years and then restarting. When reviewing this data across the past two decades, Figure 77 does suggest that there have been three of these cycle of this propagation – the first happening between 1993 and 1998, the second between 1999 and 2006 and the third cycle between 2007 and 2012, we only assume the life cycles is from six to eight years because the second cycle lasted for eight years but for the first cycle we don't have the data before 1993 and the same for the third cycle in what happened after 2012.

By calculating the distance between the first year of the cycle and the last one (Figure 78) we can estimate the speed that the Great Whirl is propagating toward the northeast, which is presented in Table 8. It appears that the propagation has steady speeds between 50 to 55 km/year.

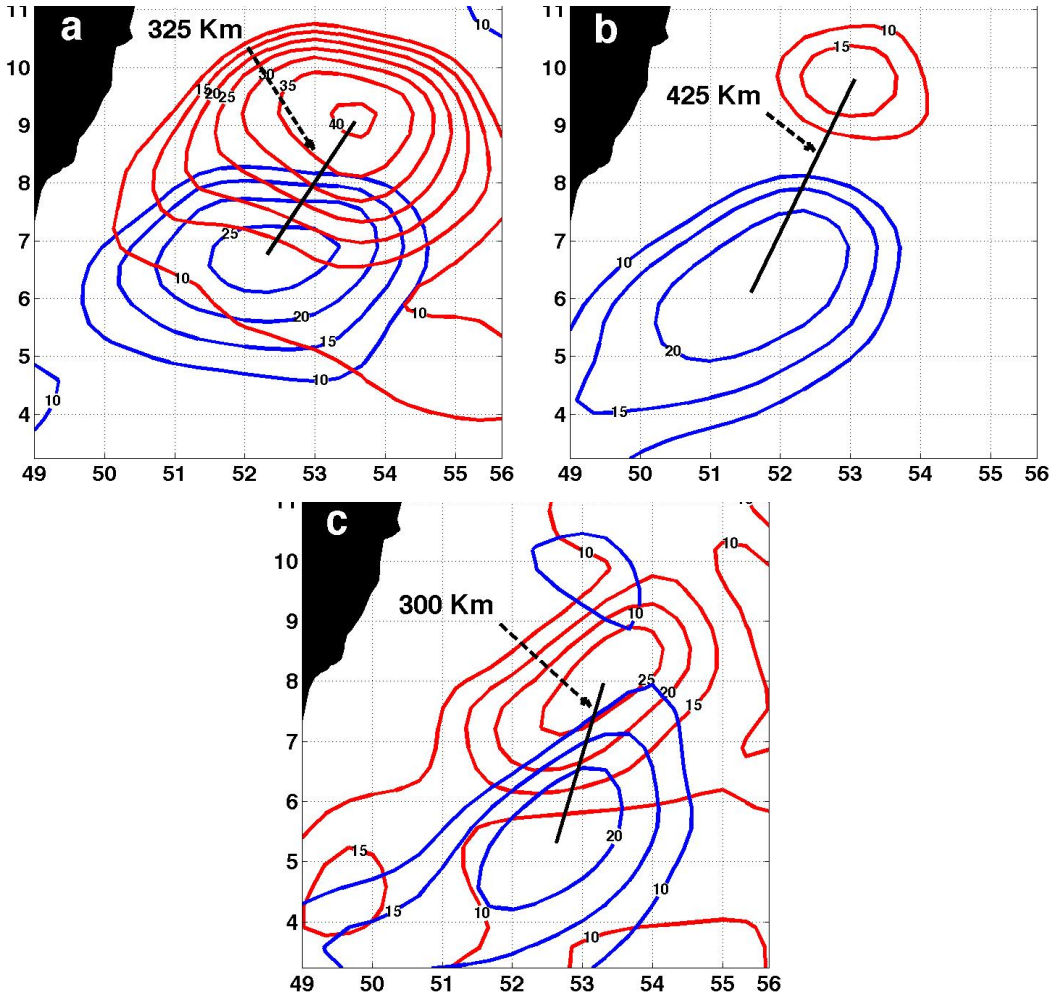

Figure 78 Maps of July SSHA for 1993/1998(a), 1999/2006(b) and 2007/2012(c), showing the distance of the Great Whirl center from the 1st year of the cycle to the last one.

We can conclude that the intensity of the SSHA does not necessary contribute to the propagation of the eddy, because the three cycles indicate different degrees of intensity for the SSHA of the last year of the cycle, this is clear in Figure 78 at which the first cycle end year (1998) has a high SSHA opposite to the last year in the second cycle (2006), whereas the third cycle last year SSHA is neither as high or low as the other two.

Table 8 The speed at which the Great Whirl is propagating at northeasterly yearly in each cycle.

Period of cycle	Distance	Number of years	Speed
1993 to 1998	325 km	5	55 km/year
1999 to 2006	425 km	7	53 km/year
2007 to 2012	300 km	5	50 km/year

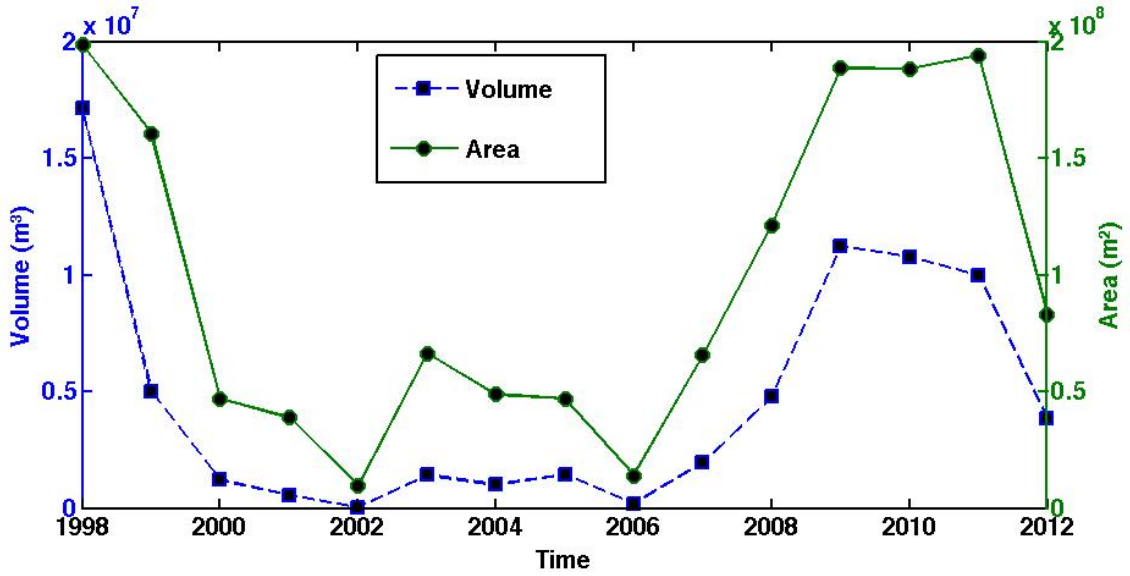

Figure 79 Great Whirl volume (blue) and area (green) during the month of July calculated using the SSHA.

Figure 79 shows a plot of the Great Whirl volume and boundary area data between 1998 and 2012. Both volume and area was calculated after specifying the Great Whirl boundary of 15 cm SSHA and above during July from Figure 77 where in some years the eddy took the shape of a circle and in others the shape of an ellipse, in which we used $\pi \cdot r^2$ (r = radius) to obtain the area in the case of the circular shape and $\pi \cdot a \cdot b$ (a = major long radius and b = minor short radius) for the ellipsoid, as for the Great Whirl volume when a circle the eddy take the shape of a circular base cone and ellipse base cone in the case of the ellipsoid and both can be calculated by 1/3 · base area · cone height.

As expected, there is a strong correlation between these two characteristics, with the period of 2006 to 2008 showing a rapid increase in both area and volume. Between 1998 and 2002 there was a strong decrease in both volume and area for the Great Whirl, and this may be reflective of conditions in the oceanic environments of the Arabian Sea and the Indian Ocean after a strong ENSO event in 1998.

Comparing the result of the SSHA area and volume we can see that the volume time series might be better then the area one to be considered as an index representing the magnitude of the Great Whirl, because of the variability of the SSHA within the Great Whirl from one year to another, in other words higher SSHA does not necessarily mean larger boundary area of the Great Whirl.

Past studies researching the Great Whirl depending on the in-situ data that was the only available sets of data for this region then, had difficulties with defining parts of the eddy's behaviour such as its whereabouts, size and life time during a year, the reason for that is the spatial and temporal limitations of the in-situ observations, but here with the use of remote sensed data observations especially the SSHA, that limitation is no more due to the spatial coverage and resolution that detects the onset of the eddy to its offset for the past two decades, which shows that the eddy present in most of the months during a year.

In fact the observations suggest that the Great Whirl is coherent and persistent even after the offset of the summer monsoon, therefore this observations can show new findings of the eddy characteristics. One of the potential limitations of SSHA data is that it has been presented from altimetry remote sensing resources alone. In many instances, it has been found that the use of altimetry to record SSHA may be variable by between 2-3cm – as this is the most accurate recording of SSHA that can be measured from current technologies and available resources (Robinson, 2010).

As a result, small-amplitude meso-scale signals can often be plus or minus that figure in which could slightly affect the data presented here that consider 5 cm SSHA intervals of gradient for the Great Whirl. This is an important aspect of the remote sensing data obtained as, although there have been multiple corrections undertaken with regards to the potential environmental and orbital factors, these discrepancies and slight variability do need to be considered as a potential limitation of the work and may have small impacts upon the data which has been obtained.

Despite this limitation, it has been considered to be a minor caveat of the available data and it is considered that the data presented through the Matlab routine (appendix E) does suggest that a strong ENSO event has resulted in a raised SSHA for this area of the Arabian Sea. Such as the level of variability and the SSHA difference between the 1998 data and the surrounding measurements, it would be considered that confidence could be placed in the data as a representation of a significant anomaly at this point in time. To be oceanographically useful the altimeter range needs to be correct to ensure that it can produce results, which are accurate within a few centimetres (Kumar et al., 1998), so it was considered that this data was representative of oceanographic conditions.

6.4 SST/SSTA distribution within the Great Whirl

The sea surface temperature (SST) data sets can help to provide indices of variability in the Great Whirl in a similar fashion to the SSHA datasets discussed earlier. Sea surface temperature assessments can also provide a framework for analysis of long-term variability (such as evidence for decadal change). This is increasingly important in modern research as it provides an avenue through which slow changes in ocean circulation and atmospheric composition and emerging issues such as climate change can be reviewed against patterns of sea surface temperatures (Rasch, 2012). Considering this potential, the data for the SST was obtained from the TMI temporal assessments of July months for 1998 to 2012. This date range from the TMI was considered most appropriate for July, the SST microwave image results would ensure that data from the summer monsoon season was utilized – helping to overcome issues associated with significant and, more importantly, long-term cloud cover problems which can often cause uncertainty or data gaps in remote sensing data.

The warm Great Whirl is quasi-stationary and transports around its edge cold, up-welled water (<20 °C in July) from the coast offshore, to the east until 55°E and then to the south at 5°N. The SST difference between the warm Great Whirl and the cold wedges north of it (Figure 80) exceeds as much as 5 °C meridionally. The Great Whirl is an important contributor to the upwelling along the Somali coast and to the eastward transportation of cold water towards the interior of the Arabian Sea (Brandt et al., 2003).

Figure 80 again shows a clear pattern for the inter-annual shifts associated with a significant ENSO event (as shown in the comparison of the July 1998 data with those of other years). In general, evidence suggests that during its progress the Great Whirl draws cold coastal waters from the upwelling off the Somali coast offshore, first eastward and then towards the south. Coastal upwelling brings cold water to the upper ocean surface, and the thermo-contrast (frontal) zone forms as this upwelling water mass encounters the warmer surface water mass (as outlined in Peng and Olson, 2004). The upwelling process brings cold, fresh, water to the surface and maintains a cold wedge in the SST. It has also been established that during an ENSO event SST can change dramatically and this needs to be considered in general patterns of SST across larger inter-annual temperature patterns.

This data shows that the Great Whirl is not a steady oceanic phenomenon, but can vary and shift position by a few degrees over a relatively short time period. This seems to support model simulations (as outlined in Beal and Chereskin, 2003), and suggests that the strength and intensity of the wider Somali Current also fluctuates rapidly in response to both wind field, and more slowly in response to annual monsoon forcing. These SST patterns are in line with the ENSO climate mode where high SSTA is present during the El Nino years, however some of the magnitude of these anomalies are not as significant as may have been expected (with the exception of the large ENSO event in 1998). Despite these patterns, they do appear to be consistent with other research, which postulates that SST will be more prominent in the midlatitudes where it has significantly more horizontal gradient than in the tropics with tropical SSTA often having a broader meridional extent (Rasch, 2012).

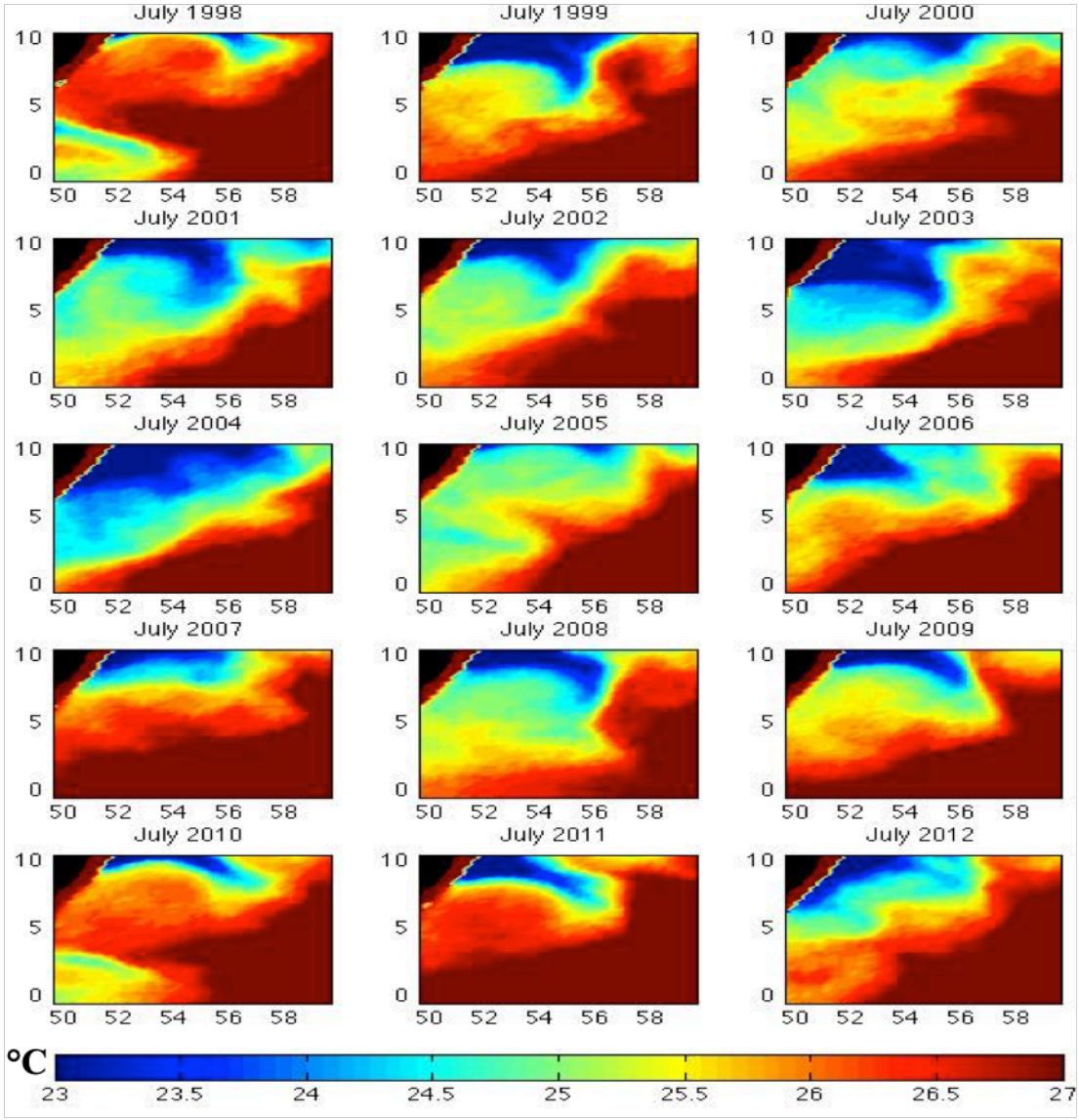

Figure 80 Maps of SST of July within the Great Whirl area between 1998 and 2012 from TMI.

The southwest monsoon wind is established across the Arabian Sea from May onwards and this continues to have an effect upon SSHA and SST during this time (Figure 81). It is also considered, however, that SSHA and SST also respond to seasonal conditions such as changing wind speed and direction (Kumar et al., 1998). At this time, the onset of the monsoon, along the Somali coast the southward flowing wintertime Somali Current reverses to a northward flow. Indeed, at a time where the net surface heat flux is often at maximum, and is directed into the ocean, it is interesting to note that the Arabian Sea generally experiences a rapid heat loss due, primarily, to the export of heat via the strong southeastward Ekman transport (Chereskin, 1995).

Figure 81 shows the pattern of the SST, SSHA and wind speed distribution within the Great Whirl area of May to September for 1998, 1999 and 2000, which indicate a forward shift of two months for 1998 and one month in 1999 than 2000 where most of the other years up to 2009 shows similar pattern to 2000 (appendix C). This probably suggests that the impact of the 1998 El Nino combined with the pIOD event was so strong it continued until the following year.

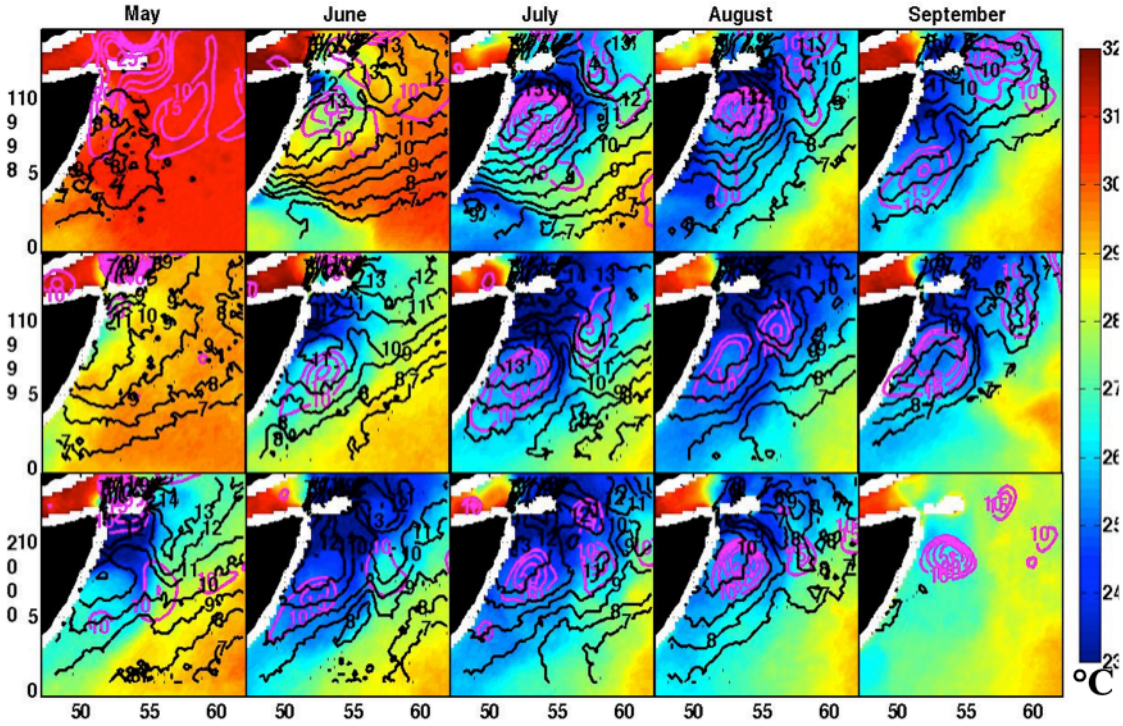

Figure 81 May to September of 1998, 1999 and 2000 SST (color map), above 10 cm SSHA (magenta contour) and surface wind speed (black contour).

6.4.1 SSTA Indices for the Great Whirl

The SSTA information was calculated by subtracting the monthly climatology information from the SST (Figure 82). This was in accordance with the definition of thermal anomalies as defined by Miliaresis and Seymour (2011) who postulate that a thermal anomaly should be considered to be a region with distinct spatial and temporal temperature variance with respect to the surrounding area.

Although this presents a relatively basic definition and calculation of SSTA, the manifestation of SST has been empirically linked to constant geophysical behavior including ocean dynamics and water circulation activity. Further, consistent with other global climatic events such as ENSO events that is reflected by Figure 82 during 1998 and 2010 causing higher SSTA of the Great Whirl, thermal variance and SST changes continue to reflect wider climatologic issues such climate change in addition to the seasonal influences of the summer and winter monsoons which affect patterns of SST in the Great Whirl and the wider Somali Current (Miliaresis and Seymour, 2011).

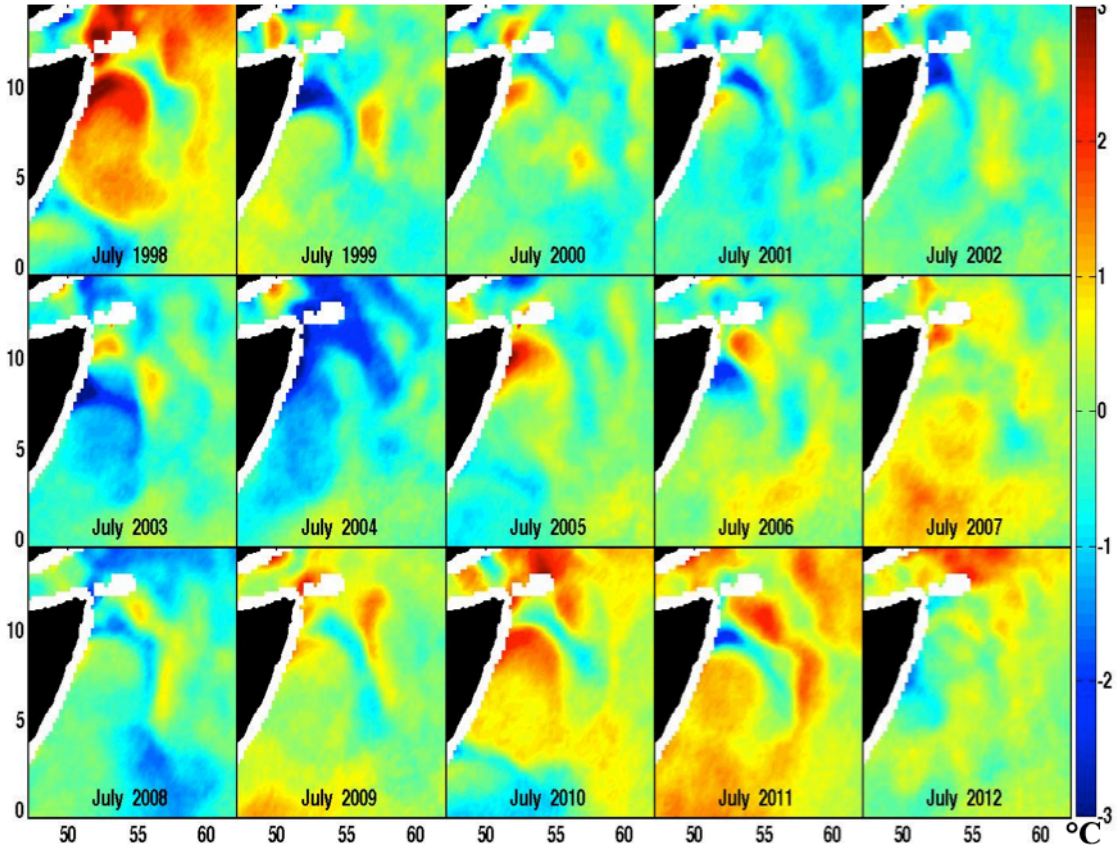

Figure 82 SSTA for the Great Whirl during July from 1998 to 2012

Figure 83 is an index using the SSTA mean within the Great Whirl area, which is 5x5 degrees from 5N to 10N and 50E to 55E during the July months between 1998 to 2012, the standard deviation of the index is approximately +/- 0.5°, five year exceed the standard deviation where three with a positive SSTA (1998, 2010 and 2011) and two with negative SSTA (2003 and 2004). Again the impact of the ENSO event is reflected in 1998 with high SSTA as in Figure 76 with the SSHA, which also can be in response to the weaker than normal surface wind speed during July that year (Figure 58), on the other hand the strong negative SSTA in 2004 corresponds to the higher than average of surface wind speed for the month of July happening that year as indicated by Figure 58. This lead us to assume that during the southwest monsoon there is a strong covariability of SST and winds on the oceanic meso-scale feature where Cold (warm) SSTs are coincident with locally strong (weak) winds.

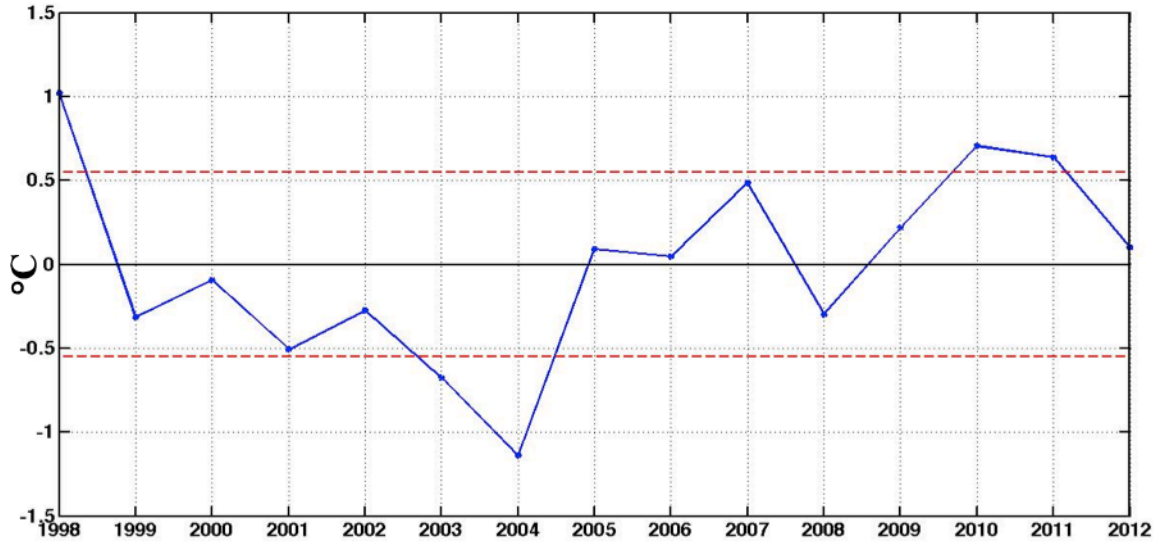

Figure 83 Great Whirl index from the SSTA (°C) (blue line) and its standard deviation (red dashed lines) for the July months between 1998 and 2012.

6.4.2 Indices of SST at the centre of the Great Whirl

Data relating to both the sea surface height anomalies (SSHA) and sea surface temperatures (SST) have been plotted for all the July months between 1998 and 2012 to provide a more comprehensive analysis of the patterns reviewed in the research. This was undertaken to try and identify both the geographic position of the Great Whirl and SST and SSHA information at the centre of this phenomenon. Figure 84 presents the data from 1998 (the year of the strong ENSO event) as an example of this form of mapping and shows the position of the Great Whirl in relation to the coastal region of Somalia.

This data seems to show a strong correlation between the SST and SSHA recorded over this time period. Figure 84 indicates a strong cooling in northern areas and warmer easterly and southeasterly Indian Ocean temperatures. This also shows the increasing sea surface heights in the warmer and more central regions of the Great Whirl. This map is a strong representation of the wider oceanographic patterns, which occur in this region, and demonstrates how the upwelling of colder waters can affect local climatic conditions and onshore temperatures.

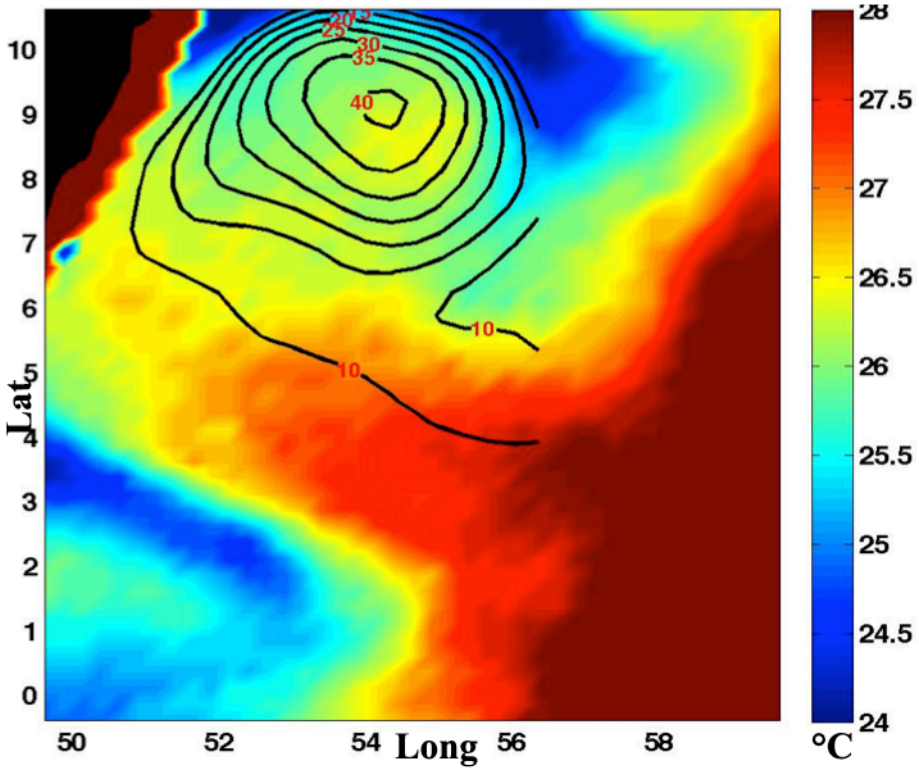

Figure 84 Map of SST (color shaded) and SSHA (contours) of July 1998 off the Somali coast showing the position of the Great Whirl gyre.

The Great Whirl moves waters from the South so it is clear to see from the data obtained how a strong ENSO event in the Indian Ocean can affect a variety of oceanographic phenomena in this area – not least the SST characteristics of the Great Whirl. The positive SSTA is clear within the 1998 data set, and may be associated with warmer sea surface temperatures as a result of an ENSO event. These El Nino conditions can reduce the strength of the southwest monsoon winds and lower the latent heat flux exchange across the air-sea interface (as discussed in Somayajulu et al., 2000). Godfrey et al. (2006) also found evidence to suggest that these waters are warmed substantially by the surface heat flux before returning to the inside edge of the Great Whirl, via the advection of cold water upwelled near the northeast corner of the eddy and strong surface heat flux. This water then sinks below the surface mixed layer and re-circulates around the Great Whirl (Godfrey et al., 2006).

Figure 85 shows time series data for SSTs at the centre of the Great Whirl for the month of July between 1998 and 2012. This shows high variability in the SST of the Great Whirl gyre centre. Indeed, the SST fluctuations appear to be more prominent than the associated data obtained for the SSHA seen in Figure 76 and may suggest that this particular characteristic is more prone to external influence. The data do again show that under stronger ENSO conditions the SST at the centre of the Great Whirl is warm when compared to data from other years when these conditions are not quite as strong or prevalent. There is a significant fall in SST from Mid-2002 to Mid-2005, before increasing to the SST mean in 2006.

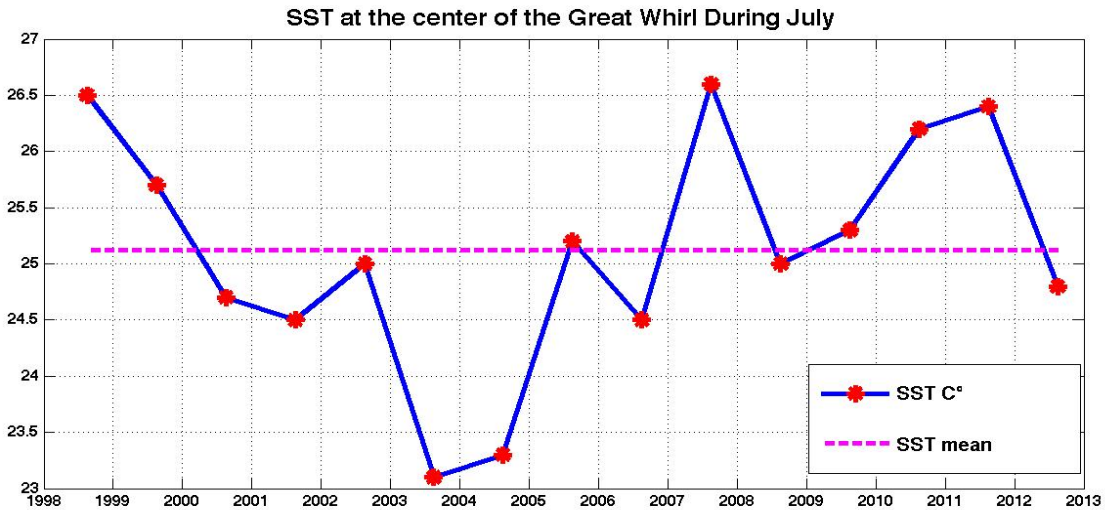

Figure 85 Time series of the SST at the center of the Great Whirl for the month of July from 1998 to 2012 using TRMM data.

6.5 Great Whirl indices using the EOFs method

The first EOF from Figure 86 has the highest percent variance of about 49% and clearly indicates that it is due to the Great Whirl phenomena, therefore we can consider the corresponding PC as the index reflecting the variability of the Great Whirl over the past two decades.

The Great Whirl is probably best represented by the 1st EOF and the corresponding PC shows the intense SSHA of 1998&2010. 2nd and 3rd EOF's have similar patterns with two adjacent circular features with opposite signs, and their PC's are also similar with one step difference in time, this pattern is most likely present because of the EOF difficulties with propagating features.

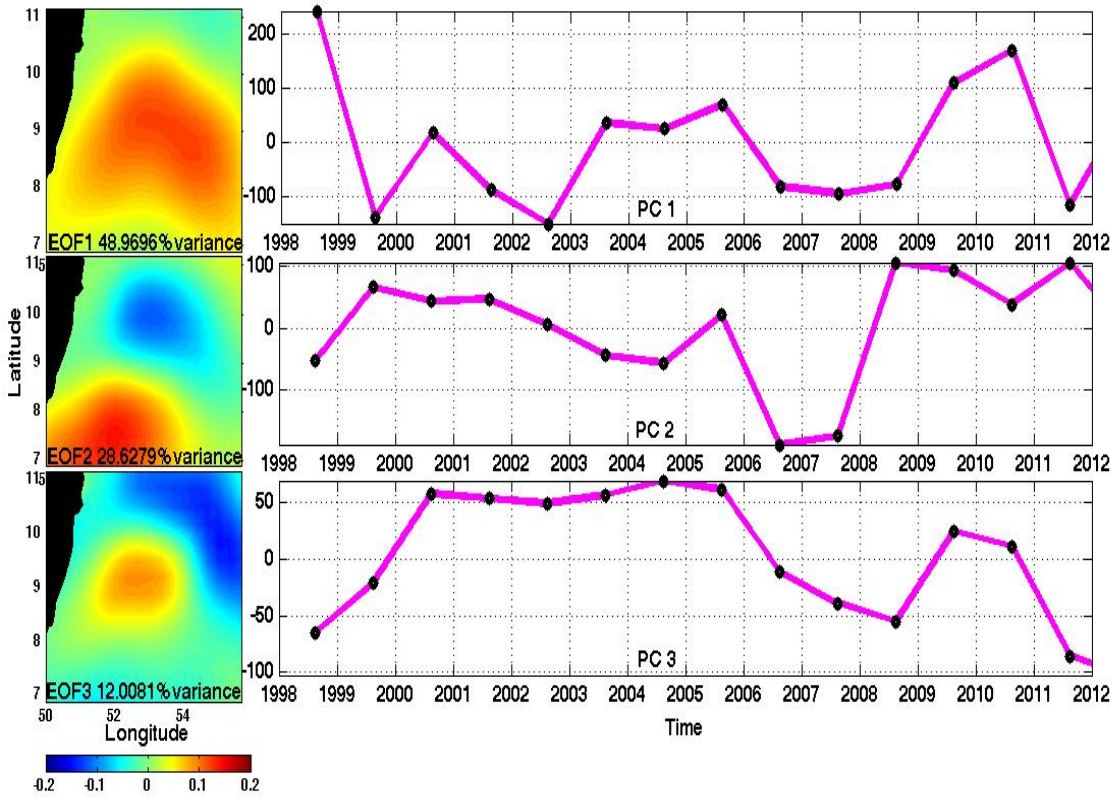

Figure 86 EOF's 1,2 and 3 (left) and the corresponding PC's (right) of SSHA for the months of July from 1993 to 2012, at 3° to 11° N and 50° to 56° E, which is the region that include the Great Whirl.

6.6 Seasonal fluctuations associated with the Great Whirl

Seasonal fluxes are also an important consideration when looking at variability indices from remote sensing data. In the Indian Ocean and Arabian Sea the prominence of the seasonal monsoon perhaps even elevates the significance of this particular issue. Although this work has focused upon inter-annual data sets, reviews of seasonal patterns are also important. This is essentially because there is also seasonal influence, which volume, intensity and area can have upon the Great Whirl and variation patterns. In addition, local wind forcing (which has significant seasonal variability) can affect the development of the Great Whirl.

For example, Brandt et al (2003) found, through time-series observations and modeling, that fluctuations over 50-day periods in the off-equatorial region of the Somalia Current had played an important role in the development of the Great Whirl. This research also showed evidence for the energy source which drives the Great Whirl – postulated to be the boundary between the Southern Gyre and the Great Whirl – with vertical shears of up to 3 m/s per 100 m have been observed during the relatively early stages of the monsoon (Brandt et al, 2003).

Figure 87 highlights typical years of the Great Whirl seasonal behavior in relation to the mean surface height anomaly, which occurs within the Somali Current region. The data presented covers the period of April to September of 1993, 1996, 1999 and 2006 which emphasis the propagation of the Great Whirl and the Socotra Gyre. During this time of the year, the Somali Current is the strongest and tends to flow northward along the coast.

The observations recorded in April indicate the manifestation of the Great Whirl looking very weak and close to the Somali Current, where it starts to turn eastward. During the period from June to September, the Great Whirl maintains its position with different strength and intensity. In the late summer monsoon phase the Somali Current flows generally northward along the coast and finally, at the end of the Southwest monsoon season, from October through December, the Somali Current turns offshore, whilst the Great Whirl shifts towards higher latitudes. During this time of the year, the flow propagates northward; however, its strength is reduced significantly.

The remote sensing data obtained in Figure 87 show clearly the migratory path of the Great Whirl. The data obtained suggests that there is a good chance of the Great Whirl presence at the end of the year in the subsurface that will not show from the SSHA and this is a critical limitation of the analysis undertaken. The data also suggests that there is a significant intensification of the Great Whirl and the Socotra Gyre throughout the summer months (July, August and September).

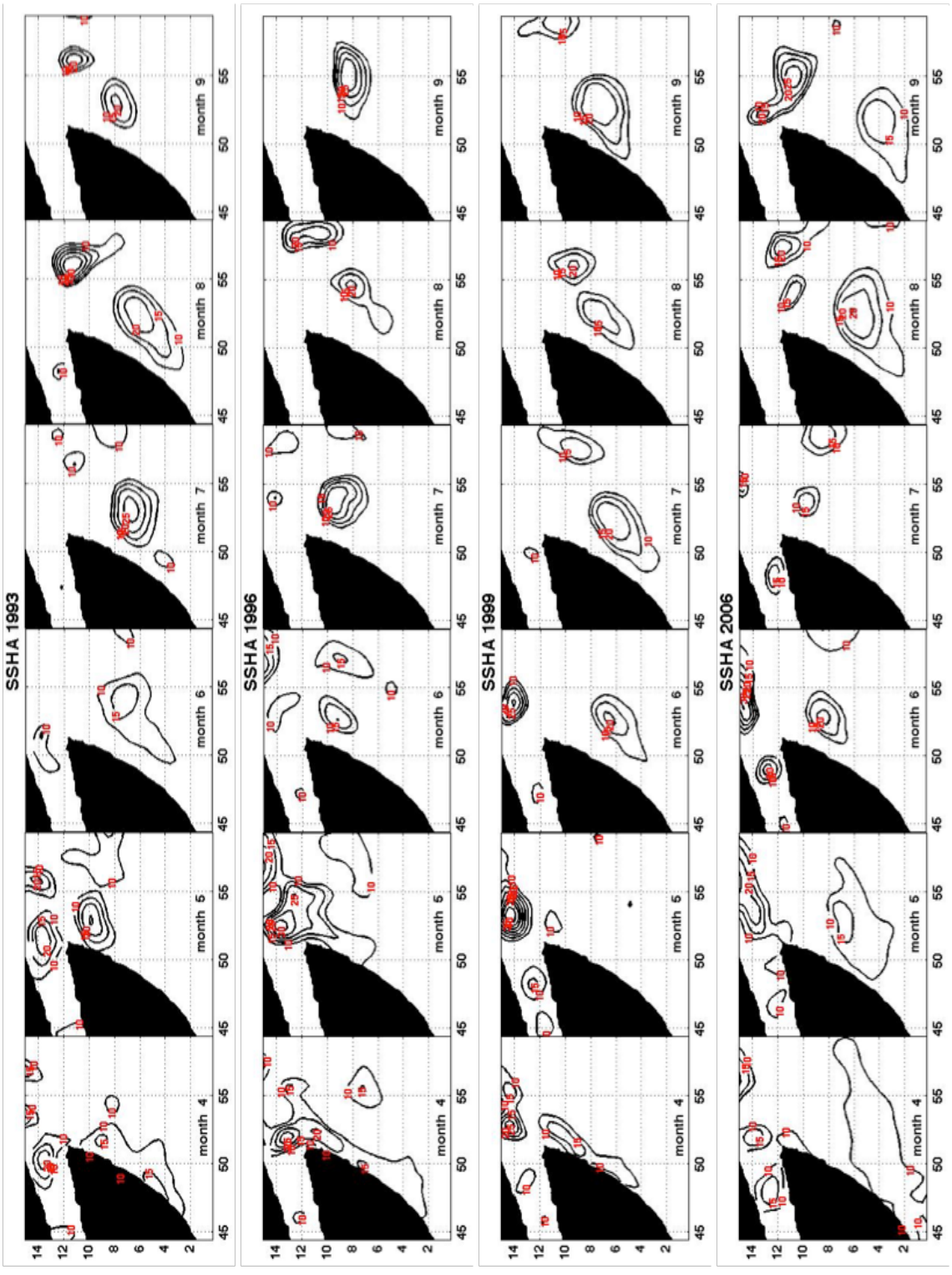

Figure 87 Contours of 5cm intervals for the mean SSHA with in the Somali Current area during a period from April to September of 1993, 1996, 1999 and 2006.

This is in-keeping with other research and observational records which demonstrate that the Great Whirl system is often still in circulation after the end of the summer monsoon period, and it is at its strongest at this time. During the winter months, the Great Whirl is typically recorded between 10°-15°N (Figure 88). Numerous observations have been made in the northern Somali Current for the winter monsoon.

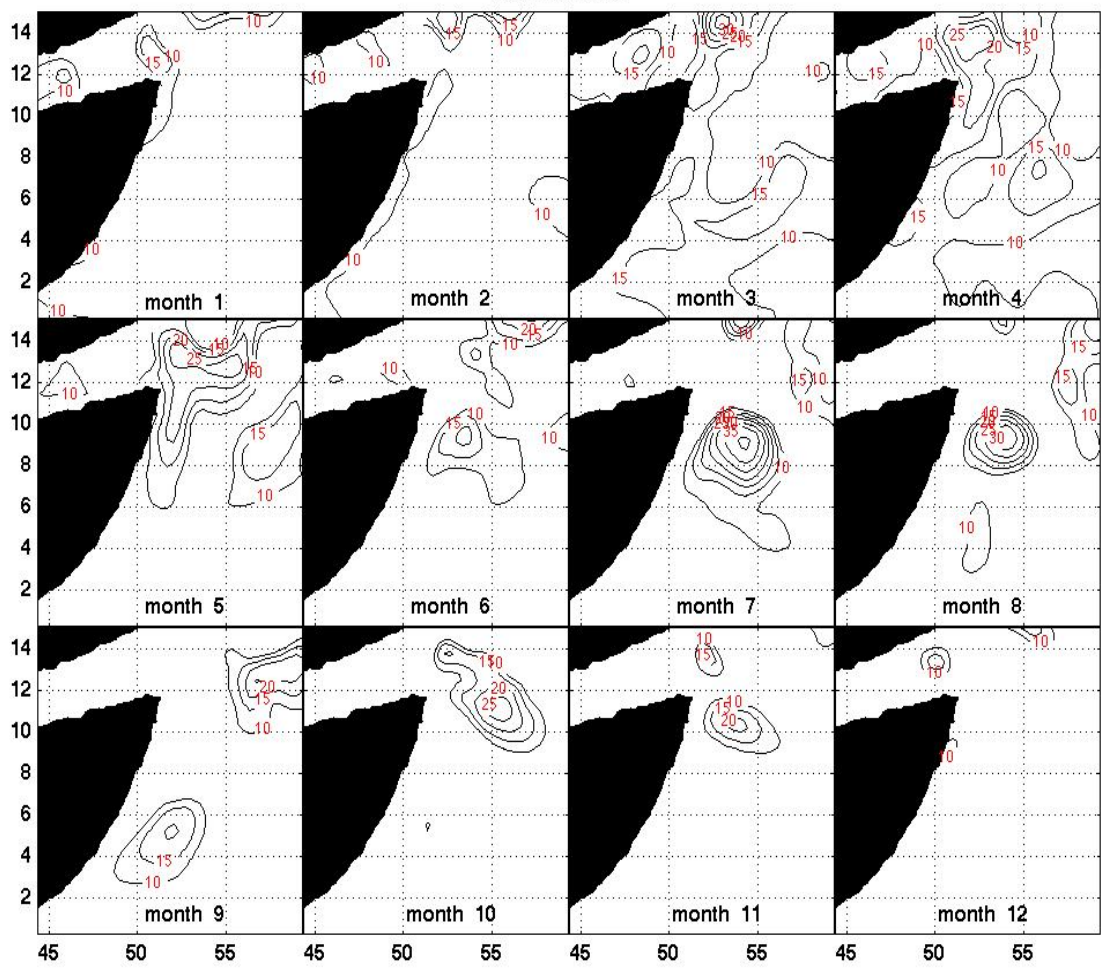

Figure 88 Mean SSHA off the Somali coast area for January to December 1998, showing the Great Whirl persisting with strong intensity through October and November at 10° to 15° N unlike the other years (Appendix C) where it normally dissipate or become very weak at the surface later in fall season.

Bruce et al. (1994), for example, reported that the Great Whirl could actually sustain summer monsoon conditions below the developing winter monsoon surface circulation for some time into the winter monsoon. Indeed, research continues to suggest that this evident intra-seasonal variability has a significant impact upon the development of seasonal cycles within the wider Somali Current. These intra-seasonal variations have also been interpreted as a product of the hydrodynamical instabilities across the Great Whirl boundary (Brandt et al., 2003).

6.7 Great Whirl indices correlation with DMI and ENSO

The Great Whirl peaks during the summer and therefore its indices is better represented by the July data and compared here with IOD and ENSO indices, which unlike the Great Whirl peak during the fall (Oct) and winter (Dec) respectively. The maximum SSHA was obtained at the centre of the GW and was used to produce an index for the gyre in section 6.3.1 and later in section 6.4.1 the SSTA within the GW area were used to get another index for the gyre. Both indices together with the DMI and El Nino 3.4 are plotted in Figure 89.

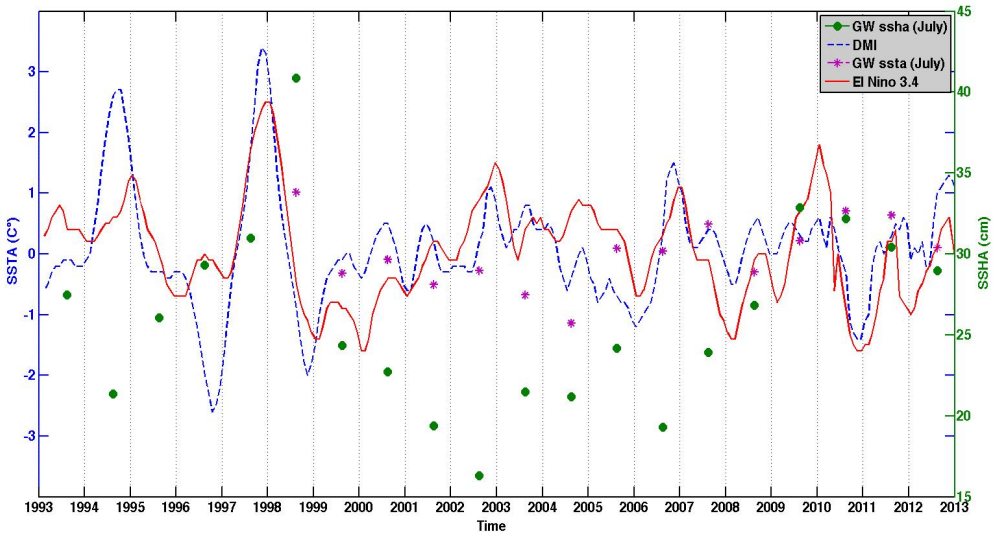

Figure 89 The GW SSHA max from 1993 to 2012 and SSTA 1998 to 2012, within the gyre area of July month plus El Nino 3.4 and DMI indices.

Clearly the gyre indices show a considerable increase in July 98 and a moderate rise in 2010, which is both an El Nino event years. With the exception of the 97/98 pIOD event most of the gyre indices fall within averaged SSHA and SSTA during the other years of IOD and ENSO events. Most likely it is because even though an El Nino event peaks during the winter its impacts last for the following summer unlike an IOD event, which peaks during fall and probably has very small if any impact on the GW during following summer. That being said we would try to correlate both climate modes to the GW indices in hopes to quantify any relationship between them.

After standardizing the GW SSHA by subtracting the mean then dividing by the standard deviation, the index is combined with the GW index for the SSTA within the eddy area to obtain an averaged index from the two (Figure 90) since both have strong correlation with each other in order to be compared against the IOD and ENSO indices along with another index that was produced for the GW based on its volume using the SSHA (Figure 91), which is why it has a stronger correlation with the GW SSHA index ($R^2 = 0.87$) than the GW SSTA index. The averaged index indicates positive figures at the early years of the index up to 1999 except for 1995, then negative observation between 2000 till 2008 and after the index go back to positive ones toward end.

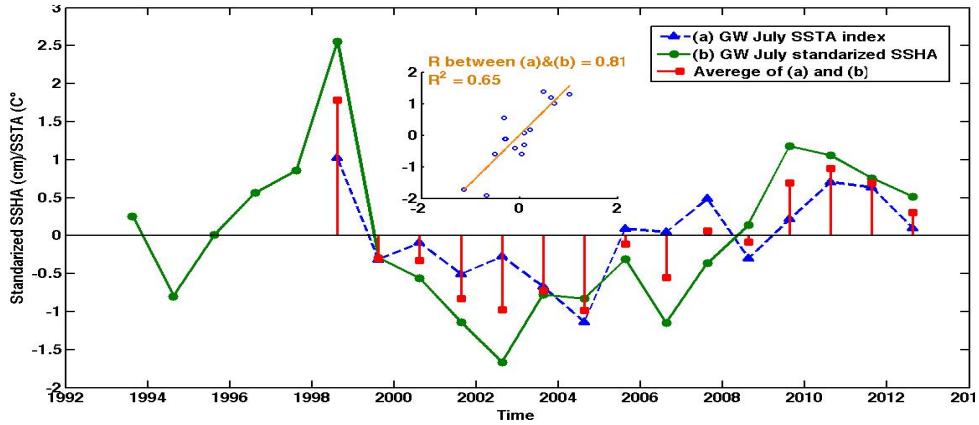

Figure 90 The combined GW index (red) from standardized SSHA and SSTA that has strong correlation (R^2= 0.65).

Figure 91 is the plot of both DMI and EL Nino 3.4 indices against the GW SSHA\SSTA and the standard deviation of the GW volume index, the gyre indices show strong positive anomalies in July 1998 then weak to moderate negative anomalies up to 2008 and for the last four years it turns positive again with the second strongest anomaly being in 2010. This in some way, can be linked to the strongest two El Nino events of 1998 and 2010, although the regression correlation is fairly small with the GW indices with R^2 being less than 0.26 and even lower with the DMI.

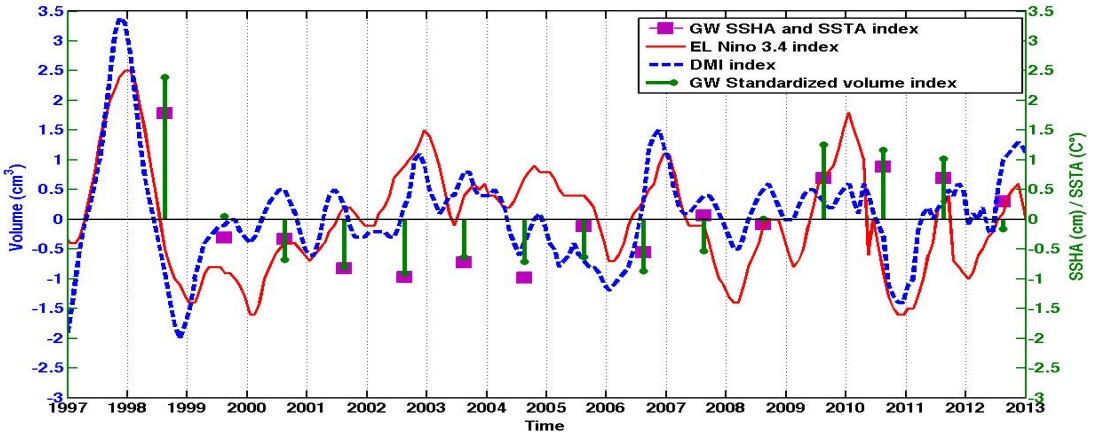

Figure 91 GW July SSHA/SSTA and standard deviation Volume index plotted against the DMI and EL Nino 3.4 indices.

6.8 Summary

Adopting remote sensing techniques can help to overcome these temporal and spatial limitations by allowing for assessments of SSHA and SSTA data in isolation and mapped together over different spatial scales. This seems to have been a successful aspect of the remote sensing data obtained, which shows strong correlations between the SSHA and SSTA data over seasons and in instances of strong climatologic shifts such as the 1998 and 2010 ENSO events. This has been further backed with the evidence obtained from the seasonal variation in the Great Whirl boundary and location, which also shows how climatologic conditions can affect this particular eddy.

Both temporal and spatial factors associated with the Somali Current and Great Whirl are thought to impact coastal flows in this region, controlling both the intensity and location of the associated coastal upwelling cold wedge – factors which are thought to have a big influence upon the heat flux budget of the North Indian Ocean and the Arabia Sea. The data obtained through this study suggests that the Great Whirl is also heavily influenced by wind and climatologic shifts, particularly the large-scale bi-annual wind forcing changes that take place in the Arabian Sea which cause the Somali Current to change.

Peng and Olson (2004) found evidence for a large degree of inter-annual variability with the Great Whirl based on numerical modeling research, particularly during June and early July, when the current along the Somali coast associated with the Great Whirl is at its strongest and again this has been backed by SSHA and SST analysis obtained through this research. The Great Whirl off the Somali coast also shows annual mean surface circulation variability, which increases during an ENSO event, where the Somali Current is more correlated with both IOD and ENSO during the winter season and with only ENSO during the summer season. Coupled with the SSHA and SST analysis, this suggests that there exists significant inter-annual variation if surface circulation under the influence of ENSO events, something which appears to be in agreement with previous works concerning ENSO events in this region (Somayajulu et al. 2000).

7 Conclusions and Recommendations

This research has placed significant emphasis on the past work of Saji et al. (1999) and Webster et al. (1999) regarding a coupled ocean-atmosphere dipole mode throughout the Indian Ocean. Relative to the unique wave patterns in this region, particularly those Kelvin and Rossby inter-annual waves which affect SST and wind stress responses on the Somali Current system, this research identified a regional, dipole-based response to climatologic conditions that uniquely operated outside of the previously believed interrelationship with ENSO.

This research highlighted a localised, regionally distinct coupling of oceanic and atmospheric variations within the NWIO region, resulting in unique phenomena that are independent of the effects of ENSO characteristics and patterning. This section offers a summary conclusion regarding the evidence captured and the relevance of these outcomes to future climate assessments, particularly in relation to the Somali Current and Great Whirl intra-annual and inter-annual variability.

7.1 Conclusions based on results and analysis

7.1.1 NWIO and equatorial Indian Ocean in relation to major climate modes

ENSO and IOD correlation shows a 0.3 to 0.35 coefficient of determination (linear regression, R^2), most likely because about third of the events of both modes co-occur during the same year between 1948 and 2012. When comparing the IOD and ENSO with the SSHA along the Indian Ocean equator using Hovmöller diagram (Figure 10), the results show a closer relationship with IOD than ENSO indicating that the two modes could be not directly associated with each other.

Comparison using regression and correlation maps (section 3.5) in particular over the Indian Ocean shows that the relationships are stronger with ENSO than IOD implying that ENSO has a broader influence on the Indian Ocean. Furthermore the relationship is almost twice as high during winter than summer season because the IOD mode peaks just before winter in October and ENSO around beginning of winter in December.

Results from plotting the SSHA along the Great Whirl latitude between the Somali coast and the south tip of the Indian subcontinent (Figure 14) show a westward propagating Rossby wave pattern. These waves reach the Somali coast around April, which is the period of the onset of the Great Whirl, accumulating energy in the region that surely has an impact on the Great Whirl explaining why it is difficult to produce the gyre in numerical modeling.

Assessment of frequency and intensity in IOD and ENSO events and their relationship with both SSHA and SSTA in the NWIO was accomplished through the use of satellite records and quantitative analysis that were described using empirical orthogonal functions. These multiple EOFs were then discussed in depth particularly to their temporal, spatial, and frequency-based significance (chapter 4). Further, their temporal variations were evaluated comparatively in order to describe correlations with key regional indications including SSTA and SSHA.

Although this investigative process began with a Matlab processing of the data, to provide full assessment the resources provided by the IRICS, 2011 were employed for the assessment of standard EOFs, and mean frequency analyses. The direct correlation between the evidence in both of these methodologies has revealed distinctive events and inter-annual phenomena that occur with remarkable consistency over time. It is this consistency that reflects the main component of this research aim, the need to assess and discuss the relationship between IOD characteristics and oceanic circulation occurring in NWIO.

The 1st leading EOF and PC of SSHA and SSTA clearly show that the highest degree of variance of the NWIO region is related to the monsoon phenomena with seasonal variability. The spatial pattern reflects a positive round feature indicating the Great Whirl and a negative strip along the coast of Somalia that is related to the Somali Current. The temporal timeseries of the PC present a seasonal fluctuation of sign every six months in January and July. The 2nd leading PC shows a change in the average of the timeseries with a higher mean of SSHA and SSTA in recent years, which is in agreement with IOD events that resulted in a basin wide worming of the IO.

In fact correlation of the 2nd PC of the SSHA with the dipole mode index (DMI) is not negligible (r=0.6), a potential indication of the effect of global climate change. The fluctuations of 1998 are the highest degree of variance, associated with the strong positive IOD event occurring in the end of 1997 and the strong ENSO event in 1998.

The 3rd significant variance seems to be associated with the changing seasons with a seesaw like spatial pattern and 3 to 4 months phase shift in the temporal timeseries from the 1st PC, moving the high peak to October and the low peak to March. This variance can be attributed to the thermodynamics systems of the atmosphere and ocean impact due to the incoming solar radiation annual cycle.

Over the course of this study, the insights from both in-situ evidence and remote sensing techniques employed by past researchers were used as a mechanism for generating and manipulating comparative outputs. On this basis it was possible to identify distinctive and linked phenomena that arise from the coupled atmospheric-oceanic system, which characterises the IOD. Further, due to the competing nature of theoretical evidence, outputs, and discussions in this field, it was possible to debate one of the most widely critiqued arguments from Saji et al. (1999) regarding the dipole elements of the Indian Ocean and their lack of correlation with ENSO-related forces.

7.1.2 The Somali Current System

7.1.2.1 Somali Current during winter and summer season climate variability

First, examining a 12 months running mean timeseries for the SSHA along Somali Current for 1993 to 2012 (Figure 44), it appears to be similar to the DMI with a considerable increase of SSHA in 1994/95, 1997/98 and toward the end of the timeseries between 2007 to 2012 with the exclusion of 2011. However when plotting SSHA of January months and July months separately, the January timeseries continue to resemble the DMI but only reflecting signals from strong IOD events (1994, 1997 and 2007), where the July timeseries reflects moderate anomalies in 1995, 2005 and 2010 with a strong anomaly in 1998, which agrees with the Nino 3.4 index.

Indices of the near-shore\offshore of SSHA along the Somali coast during January and July months from section 5.3.2 were helpful to give good characteristics of the Somali Current, most importantly regarding its reversal between winter and summer seasons, by the analysis of the slope resulting from near-shore minus offshore SSHA that was used as an indication of the Current intensity. The slope during July was steeper and with the opposite sign than January, emphasizing the stronger and reversed direction of the southwest monsoon from the northeast monsoon.

The northeast Somali Current index is very consistent throughout most of the years with a sea level difference of 10 cm and the strongest being in the winter of 2005 (17 cm) and weakest in 1994 (05), also 1997 and 2006 winter (strong IOD events years) were rather weak about 7 cm. These strongly correlate to the leading temporal timeseries (1st PC) of January SSHA over the Somali Current area. The southwest Somali Current index shows a consistency where almost half of the years represent strong (20 to 22.5 cm) and the other half weak (10 to 12.5 cm).

But interestingly the differences become exceptionally small reaching almost 0 cm in summers of 1998 and 2010 (strong ENSO events years), meaning that current is very weak. This leads us to conclude that the relationship between the Somali Current and both IOD and ENSO climate modes is an inverse one as the analysis results show (section 5.7) when comparing the Somali Current near-shore minus offshore indices with Nino 3.4 and DMI, which is clear from Figure 70.

Horizontal extension of the southwest Somali Current from SSHA from 1993 to 2013 (Figure 52) reveals that it has a large inter-annual variability where it persists as a wide current for 3 to 4 years followed by a narrow one for the next 3 to 4 years. This width represents the Somali Current being manifested away from the Shore and with the magnitude of the upwelling along the coast induced by the surface wind stress, which corresponds to the surface wind speed during late spring based on the intra-annual variability within the year due to the delay of SSHA reaction to the wind speed.

The Somali Current late spring wind speed show the same inter-annual variability and also agrees with the July SSHA leading PC of the Somali Current area suggesting that it is linked to the monsoon variability. Although SST within the Somali Current strongly reflect the seasonal variability linked to the reversal of the southwest Asian monsoon, analysis of the normalized SST anomalies from Figure 65 shows highly anomalous positive temperatures in 1997/1998 and a moderate ones in 1994/1995, 2007/2008 and 2009/2010, which are either an ENSO or an IOD event years.

7.1.2.2 The Great Whirl climate variability from its seasonal and annual behavior

Remote sensing such as the SSH departure from its long-term mean proved to be crucial in this study especially for the analysis of the Great Whirl intra-annual and inter-annual variability in examining its form, magnitude, and movement within the same season and from one year to the other.

One of the characteristics considered for the Great Whirl was the maximum SSHA at its centre during July over two decades (Figure 76), and the results showed that only one year exhibited extreme departure from the mean (1998) therefore reflecting low inter-annual variability, which leads us to believe that this aspect of the Great Whirl is more influenced by the high seasonal variability associated with the southwest monsoon. We conclude that it needs a strong ENSO companied with a strong IOD event such as the case of 1998 season to have an impact on the SSHA anomaly at the centre of the Great Whirl.

The most important use of the remote sensing application with SSHA data for the Great Whirl is to be able to identify its boundaries and whereabouts at the surface (Figure 77). The inter-annual variability of its size varied greatly between 2x2 degrees to 5x5 degrees and showed it was largest during 1998 and 2010, which is also reflected in the strong increase of the SSTA within the Great Whirl and can be attributed to the strong and moderate ENSO event occurred during those years because as we established earlier the relationship between ENSO events is proportional (r=0.6) with the SST of the NWIO and its impact cause an increase of SST in the region.

Although behavior of the Great Whirl looks random and stochastic, analysis of its position annually indicates a northeastern propagation for six to eight years then a restart back at the same position originally (section 6.3.2). The speed of this propagation is about 50 km/year, which is much slower than its seasonal propagation. Although its seasonal intra-annual variability is strongly caused by the monsoon onset, this propagation gives signs that the Great Whirl manifestation might be influenced by a slow propagating planetary Rossby waves or other climate modes such as the IOD, which would be better established by conducting an in-depth research on the subsurface data and the water column structure of the Great Whirl area. Unfortunately such observations are currently unavailable.

Comparison of spatial and temporal patterns of the Great Whirl development during the season (May to September) for several years (Figure 81), revealed that during an ENSO event year there is a shift of one to two months in the temporal pattern where the spatial pattern resembles the SSHA and SST of the Great Whirl during the next month of a typical season with no ENSO event. Therefore we can conclude that the Great Whirl would persist for a longer period during a strong ENSO year because of its delay influence on the eddy, possibly even through the winter in the subsurface.

All the Great Whirl indices produced reflect the signal from the strong ENSO events of 1998 and 2010 but not the 1994 or 2007 IOD events, which support the results found with the different influence of the two climate modes between summer and winter seasons on the Somali Current. The most significant data recording for both Somali Current and Great Whirl indices was the 1998 maximum, which showed a significantly raised SSHA and SST when compared to the mean. There was also a raised SSHA reading recorded in 2010, although this does not appear to be as significant as the 1998 result.

Despite this, both SSHA of 1998 and 2010 represent interesting results as they both corresponded with the strongest two of the four years of El Nino Southern Oscillation (ENSO) event occurring with in the period investigated. This indicates that SSHA data obtained are able to show a 'normal' year against SSHA\SST data obtained during an ENSO event through relatively simple remote sensing analysis. As for the IOD only the winter Somali Current indices show a significant relationship with strong negative SSHA observed after all three positive IOD events between 1993 and 2010, which are quantified by a correlation coefficient of 0.6. On the other hand the Great Whirl indices do not reflect any obvious relationship with the IOD that can be shown using linear regression.

Ultimately, this research has determined that some particularly anomalous events happening in this region are largely tied to the scope and scale of the ENSO manifestation, through its impact on the surface layer of the Indian Ocean with increased SSTA and SSHA in the region, where the IOD mode is more likely to impact both the surface and subsurface layers of the Indian Ocean through anomalous events that influence its inter-annual climate variability.

The relationship between the inter-annual monsoon and the oceanic features was empirically outlined over the course of this research. Consistent with past research (e.g. Wirth et al., 2002), the findings in this research have validated the development of the Great Whirl, which is predictable during the onset of the monsoon in June. However, simultaneously, it is clear from the EOF representation across the NWIO that variation in SSTA and SSHA due to climate modes events occurrence shows the consistency and geographic patterning of the Great Whirl and other formations such as the Somali Current.

One distinctive empirical trait associated with the manifestation of these hydrographic formations is their potential indication of the ocean response to the relative strength of the monsoon in any given year, a finding that requires measured assessment of pattern characteristics over time. Given the anomalies of SST and SSH exhibited during the years of extreme, decadal monsoons (e.g. 1998 and 2010), it would be beneficial for researchers to base their evidence on these particular periods and then differentiate between strength, location, and flow over the remaining intra-decadal years.

7.2 Recommendations for future studies

There are two different patterns, which have emerged within the IOD in relation to anomalous events. Firstly, there is a semi-decadal pattern which coincides with El-Nino events, suggesting that monsoonal behaviour during these El Nino years will be much more significant than in other years. Secondly, there is a three-to-four year occurrence (e.g. 2004, 2007) during which distinctive highs and lows are recorded. Such events are largely unpredictable.

Variations within the IOD have significant implications for the surrounding regions both in terms of ecology and humanity. Any variations in the monsoon, if not effectively predicted can lead to large-scale famine and drought, or conversely to unchecked flooding and degradation. Therefore, there is an underlying imperative associated with empirical assessment of monsoonal variance and, by default, climate variability, as regional populations continue to subsist according in harmony with the regular seasonal timeline of the monsoon itself. One of the important challenges and limitations faced in this study was to distinguish between the ENSO and IOD influences, especially when they occur together in the same year, it would be very interesting to undertake a study devoted to that subject.

Also to conduct research on the differences of direct or teleconnection impacts from these climate modes on regions (e.g. the severe droughts of Australia during ENSO or increase of East African rainfall from an IOD event) when the two modes coexist compared to when they occur separately. Westward propagation of Rossby waves seen here reaching the Somali coast in March/April might have an impact on both the Somali Current and Great Whirl. Research exploring this role and its influence on the onset and development of the Somali system especially the Great Whirl is crucial in clarifying its behavior and characteristics that until now have been poorly simulated in advanced numerical modeling.

An important resource for such study is the data set of the water column structure from Argo floats observations, which is currently scarce for that part of the world due to political situation regarding piracy, but hopefully this will change soon.

Although difficult to predict in nature, the forecasting based upon regional factors (e.g. strength of Great Whirl and Somali Current) may provide evidence for better predicting the manifestation of such events in the future. Somali Current indices and NWIO EOFs from SSHA/SSTA in general indicate a relative anomalous increase in recent years. A study to assess if this has any relation with climate change impact could add important assistance in predicting ocean and atmosphere phenomena related to the Indian ocean, which might be understudied compared to the Pacific and Atlantic Oceans due to its remoteness from top scientific research institutes.

References

ANDRULEIT, H. 2007. Status of the Java upwelling area (Indian Ocean) during the oligotrophic northern hemisphere winter monsoon season as revealed by coccolithophores. *Marine Micropaleontology,* 64**,** 36-51.

ARMSTRONG, E. M. An empirical orthogonal function analysis of spring summer sea surface temperature variability off northern and central California from AVHRR satellite imagery. Oceans '95 Mts/IEEE - Challenges of Our Changing Global Environment, Conference Proceedings, Vols 1-3, 1995. 2038-2045.

ASHOK, K., GUAN, Z. Y., SAJI, N. H. & YAMAGATA, T. 2004. Individual and combined influences of ENSO and the Indian Ocean Dipole on the Indian summer monsoon. *Journal of Climate,* 17**,** 3141-3155.

ASHOK, K., GUAN, Z. Y. & YAMAGATA, T. 2003. A look at the relationship between the ENSO and the Indian Ocean Dipole. *Journal of the Meteorological Society of Japan,* 81**,** 41-56.

AVISO. 2011. *'Merged Topex/Poseidon Products'. Archiving, Validation and Interpretation of Satellite Oceanographic data* [Online]. Available: http://www.aviso.altimetry.fr [Accessed July 2011].

BALDACCI, A., CORSINI, G. & MANZELLA, G. 1998. Empirical orthogonal function analysis of AVHRR Surface Temperature patterns: a case study. *IGARSS '98 - International Geoscience and Remote Sensing Symposium, Proceedings 1998 Vols 1-5***,** 903-906.

BARBER, R. T., MARRA, J., BIDIGARE, R. C., CODISPOTI, L. A., HALPERN, D., JOHNSON, Z., LATASA, M., GOERICKE, R. & SMITH, S. L. 2001. Primary productivity and its regulation in the Arabian Sea during 1995. *Deep-Sea Research Part II-Topical Studies in Oceanography,* 48**,** 1127-1172.

BAUER, S., HITCHCOCK, G. L. & OLSON, D. B. 1991. Influence of Monsoonally-forced Ekman dynamics upon surface-layer depth and plankton biomass distribution in the Arabian Sea. *Deep-Sea Research Part a-Oceanographic Research Papers,* 38**,** 531-553.

BEAL, L. M. & CHERESKIN, T. K. 2003. The volume transport of the Somali Current during the 1995 southwest monsoon. *Deep-Sea Research Part II-Topical Studies in Oceanography,* 50**,** 2077-2089.

BEAL, L. M. & DONOHUE, K. A. 2013. The Great Whirl: Observations of its seasonal development and interannual variability. *Journal of Geophysical Research-Oceans,* 118**,** 1-13.

BONDARENKO, A. L., ZHMUR, V. V., FILIPPOV, Y. G. & SHCHEV'EV, V. A. 2004. On the transport of water masses by long-period waves in seas and oceans. *Physical Oceanography,* 14**,** 275-283.

BONJEAN, F. & LAGERLOEF, G. S. E. 2002. Diagnostic model and analysis of the surface currents in the tropical Pacific Ocean. *Journal of Physical Oceanography,* 32**,** 2938-2954.

BRANDT, P., DENGLER, M., RUBINO, A., QUADFASEL, D. & SCHOTT, F. 2003. Intraseasonal variability in the southwestern Arabian Sea and its relation to the seasonal circulation. *Deep-Sea Research Part Ii-Topical Studies in Oceanography,* 50**,** 2129-2141.

BRUCE, J. G. 1984. Comparison of Eddies Off the North Brazilian and Somali Coasts. *Journal of Physical Oceanography,* 14**,** 825-832.

BRUCE, J. G., JOHNSON, D. R. & KINDLE, J. C. 1994. Evidence for Eddy Formation in the Eastern Arabian Sea during the Northeast Monsoon. *Journal of Geophysical Research-Oceans,* 99**,** 7651-7664.

CAI, W., COWAN, T. & SULLIVAN, A. 2009. Recent unprecedented skewness towards positive Indian Ocean Dipole occurrences and its impact on Australian rainfall. *Geophysical Research Letters,* Vol. 36**,** 11705.

CALEY, T., MALAIZE, B., ZARAGOSI, S., ROSSIGNOL, L., BOURGET, J., EYNAUD, F., MARTINEZ, P., GIRAUDEAU, J., CHARLIER, K. & ELLOUZ-ZIMMERMANN, N. 2011. New Arabian Sea records help decipher orbital timing of Indo-Asian monsoon. *Earth and Planetary Science Letters,* 308**,** 433-444.

CDAS1. 2014. *'Datasets Reanalysis'. Climate Data Assimilation System 1* [Online]. Available: http://iridl.ldeo.columbia.edu [Accessed February 2014].

ESA. 2011. *Radar altimetry tutorial: Coastal Applications. European Space Agency* [Online]. Available: http://earth.eo.esa.int [Accessed April 2011].

FENG, M. & MEYERS, G. 2003. Interannual variability in the tropical Indian Ocean: a two-year time-scale of Indian Ocean Dipole. *Deep Sea Research Part II: Topical Studies in Oceanography,* 50**,** 2263-2284.

FINDLATER.J 1969. A Major Low-Level Air Current near Indian Ocean during Northern Summer - Interhemispheric Transport of Air in Lower Troposphere over Western Indian Ocean. *Quarterly Journal of the Royal Meteorological Society,* 95**,** 362-380.

FISCHER, J., SCHOTT, F. & STRAMMA, L. 1996. Currents and transports of the Great Whirl-Socotra Gyre system during the summer monsoon, August 1993. *Journal of Geophysical Research-Oceans,* 101**,** 3573-3587.

FLAGG, C. N. & KIM, H. S. 1998. Upper ocean currents in the northern Arabian Sea from shipboard ADCP measurements collected during the 1994-1996 US JGOFS and ONR programs. *Deep-Sea Research Part II-Topical Studies in Oceanography,* 45**,** 1917-1959.

FRANCIS, P. A. & GADGIL, S. 2010. Towards understanding the unusual Indian monsoon in 2009. *Journal of Earth System Science,* 119**,** 397-415.

FU, L. L., CHELTON, D. B., LE TRAON, P. Y. & MORROW, R. 2010. Eddy Dynamics from Satellite Altimetry. *Oceanography,* 23**,** 14-25.

GODFREY, J. S. 2006. On Reconciling Oceanic and Atmospheric Estimates of Surface Heat Fluxes—and on Validating Greenhouse Models. *In:* JOCHUM, M. & MURTUGUDDE, R. (eds.) *Physical Oceanography.* Springer New York.

GUALDI, S., GUILYARDI, E., NAVARRA, A., MASINA, S. & DELECLUSE, P. 2003. The interannual variability in the tropical Indian Ocean as simulated by a CGCM. *Climate Dynamics,* 20**,** 567-582.

HALPERN, D. & WOICESHYN, P. M. 1999. Somali Jet in the Arabian Sea, El Nino, and India rainfall. *Journal of Climate,* 14**,** 434-441.

HASHIZUME, H., XIE, S. P., FUJIWARA, M., SHIOTANI, M., WATANABE, T., TANIMOTO, Y., LIU, W. T. & TAKEUCHI, K. 2002. Direct observations of atmospheric boundary layer response to SST variations associated with tropical instability waves over the eastern equatorial Pacific. *Journal of Climate,* 15**,** 3379-3393.

HU, R., LIU, Q. & LI, C. 2005. A heat budget study on the mechanism of SST variations in the Indian ocean dipole regions. *Journal of Ocean University of China,* 4**,** 334-342.

IRICS. 2011. *'Data Library'. International Research Institute for Climate and Society* [Online]. Available: http://portal.iri.columbia.edu [Accessed October 2011].

IZUMO, T., MONTEGUT, C. D., LUO, J. J., BEHERA, S. K., MASSON, S. & YAMAGATA, T. 2008. The Role of the Western Arabian Sea Upwelling in Indian Monsoon Rainfall Variability. *Journal of Climate,* 21**,** 5603-5623.

JAYAKUMAR, A., VIALARD, J. R. M., LENGAIGNE, M., GNANASEELAN, C., MCCREARY, J. & PRAVEEN KUMAR, B. 2010. Processes controlling the surface temperature signature of the Madden-Julian Oscillation in the thermocline ridge of the Indian Ocean. *Climate Dynamics*, 1-18.

JENSEN, T. G. 1991. Modeling the Seasonal Undercurrents in the Somali Current System. *Journal of Geophysical Research-Oceans,* 96, 22151-22167.

KALNAY, E., KANAMITSU, M., KISTLER, R., COLLINS, W., DEAVEN, D., GANDIN, L., IREDELL, M., SAHA, S., WHITE, G., WOOLLEN, J., ZHU, Y., CHELLIAH, M., EBISUZAKI, W., HIGGINS, W., JANOWIAK, J., MO, K. C., ROPELEWSKI, C., WANG, J., LEETMAA, A., REYNOLDS, R., JENNE, R. & JOSEPH, D. 1996. The NCEP/NCAR 40-year reanalysis project. *Bulletin of the American Meteorological Society,* 77, 437-471.

KANTHA, L., ROJSIRAPHISAL, T. & LOPEZ, J. 2008. The North Indian Ocean circulation and its variability as seen in a numerical hindcast of the years 1993-2004. *Progress in Oceanography,* 76, 111-147.

KEINER, L. E. & YAN, X. H. 1997. Empirical orthogonal function analysis of sea surface temperature patterns in Delaware Bay. *IEEE Transactions on Geoscience and Remote Sensing,* 35, 1299-1306.

KUG, J.S., K. Sooraj, F.F. Jin, J.J. Luo, and M. Kwon (2009), Impact of Indian Ocean dipole on high-frequency atmospheric variability over the Indian Ocean, *Atmospheric Research*, 94(1), 134–139.

KUMAR, S. P., SNAITH, H., CHALLENOR, P. & GUYMER, H. T. 1998. Seasonal and inter-annual sea surface height variations of the northern Indian Ocean from the TOPEX/POSEIDON altimeter. *Indian Journal of Marine Sciences,* 27, 10-16.

LDEO. 2012. *'Statistical Techniques in the Data Library'. Lamont-Doherty Earth Observatory* [Online]. Available: http://iridl.ldeo.columbia.edu [Accessed May 2012].

LEGRAND, P., MERCIER, H. & REYNAUD, T. 1998. Combining T/P altimetric data with hydrographic data to estimate the mean dynamic topography of the North Atlantic and improve the geoid. *Annales Geophysicae-Atmospheres Hydrospheres and Space Sciences,* 16, 638-650.

LI, C. Y., ZHOU, W., JIA, X. L. & WANG, X. 2006. Decadal/interdecadal variations of the ocean temperature and its impacts on climate. *Advances in Atmospheric Sciences,* 23, 964-981.

LUTHER, M. E. & O'BRIEN, J. J. 1989. Modelling the Variability in the Somali Current. *In:* NIHOUL, J. C. J. & JAMART, B. M. (eds.) *Elsevier Oceanography Series.* Elsevier.

MADDEN, R. A. & JULIAN, P. R. 1971. Detection of a 40-50 Day Oscillation in Zonal Wind in Tropical Pacific. *Journal of the Atmospheric Sciences,* 28, 702-708.

MANGHNANI, V., MORRISON, J. M., XIE, L. & SUBRAHMANYAM, B. 2002. Heat transports in the Indian Ocean estimated from TOPEX/POSEIDON altimetry and model simulations. *Deep Sea Research Part II: Topical Studies in Oceanography,* 49, 1459-1480.

MARCHANT, R., MUMBI, C., BEHERA, S. & YAMAGATA, T. 2007. The Indian Ocean dipole - the unsung driver of climatic variability in East Africa. *African Journal of Ecology,* 45, 4-16.

MATANO, R. P., BEIER, E. J. & STRUB, P. T. 2008. The seasonal variability of the circulation in the South Indian Ocean: Model and observations. *Journal of Marine Systems,* 74, 315-328.

MCCREARY, J. P., KUNDU, P. K. & MOLINARI, R. L. 1993. A Numerical Investigation of Dynamics, Thermodynamics and Mixed-Layer Processes in the Indian-Ocean. *Progress in Oceanography,* 31, 181-244.

MILIARESIS, G. C. & SEYMOUR, K. S. 2011. Mapping the spatial and temporal SST variations in the Red Sea, revealing a probable regional geothermal anomaly using Pathfinder V5 data. *International Journal of Remote Sensing,* 32**,** 1825-1842.

MURTUGUDDE, R., MCCREARY, J. P. & BUSALACCHI, A. J. 2000. Oceanic processes associated with anomalous events in the Indian Ocean with relevance to 1997-1998. *Journal of Geophysical Research-Oceans,* 105**,** 3295-3306.

MURTY, T. S. 2011. A. Chandrasekhar: Basics pf atmospheric science. *Natural Hazards,* 56**,** 403-405.

NAGAR, S. G., IYER, U. & SEETARAMAYYA, P. 2005. Observed variations in air, sea exchange processes over Somali basin during monsoons 1988 and 1991. *Journal of Atmospheric & Ocean Science,* 10**,** 43-60.

NAVARRA, A. & SIMONCINI, V. 2010. *Guide to Empirical Orthogonal Functions for Climate Data Analysis*, Springer.

NCAR. 2013. *'Data Analysis'. National Center for Atmospheric Research* [Online]. Available: http://www.ncl.ucar.edu [Accessed June 2013].

PENG, G. & OLSON, D. B. 2004. Simulated Somali Coastal Oceanic Response to Various Atmospheric Wind Products during Fall Transitions. *RSMAS Technical Report 2004-004*.

POLONSKII, A. B. & TORBINSKII, A. V. 2009. Velocity of propagation of temperature anomalies in the tropical zone of the Indian Ocean. *Journal of Physical Oceanography,* 19**,** 63-71.

PRASAD, T. G. & MCCLEAN, J. L. 2004. Mechanisms for anomalous warming in the western Indian Ocean during dipole mode events. *Journal of Geophysical Research-Oceans,* 109**,** C02019.

RAO, S. A., BEHERA, S. K., MASUMOTO, Y. & YAMAGATA, T. 2002. Interannual subsurface variability in the tropical Indian Ocean with a special emphasis on the Indian Ocean Dipole. *Deep Sea Research Part II: Topical Studies in Oceanography,* 49**,** 1549-1572.

RASCH, P. J. 2012. *Climate change modeling methodology : selected entries from the Encyclopedia of Sustainability Science and Technology,* New York, Springer.

REYNOLDS, R. W. & MARSICO, D. C. 1993. An improved real-time global sea-surface temperature analysis. *Journal of Climate,* 6**,** 114-119.

REYNOLDS, R. W. & SMITH, T. M. 1998: A high-resolution global sea surface temperature climatology for the 1961–90 base periods. *Journal of Climate*, 11, 3320–3323

REYNOLDS, R. W., RAYNER, N. A., SMITH, T. M., STOKES, D. C. & WANG, W. Q. 2002. An improved in situ and satellite SST analysis for climate. *Journal of Climate,* 15**,** 1609-1625.

ROBINSON, I. S. 2004. *Measuring the oceans from space : the principles and methods of satellite oceanography,* Berlin; Chichester, UK, Springer.

ROBINSON, I. S. 2010. Discovering the ocean from space the unique applications of satellite oceanography. Heidelberg, Chichester, UK: Springer.

ROJSIRAPHISAL, T., KANTHA, L. & JULIEN, K. 2007. *A study of variability in the North Indian Ocean.* Published PhD thesis. University of Colorado at Boulder.

SAJI, N. H., AMBRIZZI, T. & FERRAZ, S. E. T. 2005. Indian Ocean Dipole mode events and austral surface air temperature anomalies. *Dynamics of Atmospheres and Oceans,* 39**,** 87-101.

SAJI, N. H., GOSWAMI, B. N., VINAYACHANDRAN, P. N. & YAMAGATA, T. 1999. A dipole mode in the tropical Indian Ocean. *Nature,* 401**,** 360-363.

SALVEKAR, P. S., GANER, D. W., REDDY, P. R., BASU, S. & KUMAR, R. 2002. Numerical Simulation of North Indian Ocean State Prior to the Onset of SW Monsoon Using SSM/I Winds. *Marine Geodesy,* 25**,** 115-131.

SASAKI, H., NONAKA, M., MASUMOTO, Y., SASAI, Y., UEHARA, H. & SAKUMA, H. 2008. An Eddy-Resolving Hindcast Simulation of the Quasiglobal Ocean from 1950 to 2003 on the Earth Simulator. *High Resolution Numerical Modelling of the Atmosphere and Ocean***,** 157-185.

SCHOTT, F., FISCHER, J. R., GARTERNICHT, U. & QUADFASEL, D. 1997. Summer monsoon response of the Northern Somali Current, 1995. *Geophysical Research Letters,* 24**,** 2565-2568.

SCHOTT, F. & QUADFASEL, D. R. 1980. Development of the Subsurface Currents of the Northern Somali Current Gyre from March to July 1979. *Science,* 209**,** 593-595.

SCHOTT, F. A. & MCCREARY, J. P. 2001. The monsoon circulation of the Indian Ocean. *Progress in Oceanography,* 51**,** 1-123.

SHANKAR, D., VINAYACHANDRAN, P. N. & UNNIKRISHNAN, A. S. 2002. The monsoon currents in the north Indian Ocean. *Progress in Oceanography*.

SHI, W., MORRISON, J. M., BOHM, E. & MANGHNANI, V. 2000. The Oman upwelling zone during 1993, 1994 and 1995. *Deep-Sea Research Part II-Topical Studies in Oceanography,* 47**,** 1227-1247.

SHINODA, T., HENDON, H. H. & ALEXANDER, M. A. 2004. Surface and subsurface dipole variability in the Indian Ocean and its relation with ENSO. *Deep Sea Research Part I: Oceanographic Research Papers,* 51**,** 619-635.

SIMON, B., RAHMAN, S. H., JOSHI, P. C. & DESAI, P. S. 2008. Shifting of the convective heat source over the Indian Ocean region in relation to performance of monsoon: a satellite perspective. *International Journal of Remote Sensing*, 29 (2), 387–397.

SINGLETON, T. 2004. An Empirical Orthogonal Function (EOF) Analysis of Sea Surface Temperature, AOSC 627 'Atmospheric and Ocean Climate' Project.

SOMAYAJULU, Y. K., MURTY, V. S. N., NEELIMA, C. & JAGADEESH, P. S. V. 2006. Interannual variability of the Equatorial Jets in the Indian Ocean from the merged altimetry data - art. no. 640617. *Remote Sensing of the Marine Environment,* 6406**,** 40617-40617.

SOMAYAJULU, Y. K., MURTY, V. S. N. & SARMA, Y. V. B. 2000. Low frequency variability of the Indian Ocean from TOPEX/POSEIDON sea surface height anomalies. *The Fifth Pacific Ocean Remote Sensing Conference (PORSEC)*. NIO, Dona Paula, Goa (India): 2; 2000; 550–555.

SUBRAHMANYAM, B., MURTY, V. S. N. & HEFFNER, D. M. 2011. Sea surface salinity variability in the tropical Indian Ocean. *Remote Sensing of Environment,* 115**,** 944-956.

SUBRAHMANYAM, B. & ROBINSON, I. S. 2000. Sea Surface Height Variability in the Indian Ocean From TOPEX/POSEIDON Altimetry and Model Simulations. *Marine Geodesy,* 12**,** 167-195.

SUBRAHMANYAM, B., ROBINSON, I. S., BLUNDELL, J. R. & CHALLENOR, P. G. 2001. Indian Ocean Rossby waves observed in TOPEX/POSEIDON altimeter data and in model simulations. *International Journal of Remote Sensing*, 22 (1). 141-167.

THOMPSON, P. A., PESANT, S. & WAITE, A. M. 2007. Contrasting the vertical differences in the phytoplankton biology of a dipole pair of eddies in the south-eastern Indian Ocean. *Deep Sea Research Part II: Topical Studies in Oceanography,* 54**,** 1003-1028.

TIWARI, V. M., CABANES, C., DOMINH, K. & CAZENAVE, A. 2004. Correlation of interannual sea level variations in the Indian Ocean from Topex/Poseidon altimetry, temperature data and tide gauges with ENSO. *Global and Planetary Change,* 43**,** 183-196.

TOMCZAK, M. & GODFREY, J. S. 2003. *Regional Oceanography*, Great Britain. Parts 11–13, 175–228. Butler and Tanner Ltd.

TOMITA, H. & KUBOTA, M. 2004. Variability of surface heat flux over the Indian Ocean. *Atmosphere-Ocean,* 42**,** 183-199.

VAID, B. H., GNANASEELAN, C., POLITO, P. S. & SALVEKAR, P. S. 2007. Influence of pacific on southern indian ocean rossby waves. *Pure and Applied Geophysics,* 164**,** 1765-1785.

VALSALA, V. 2008. First and second baroclinic mode responses of the tropical Indian Ocean to interannual equatorial wind anomalies. *Journal of Oceanography,* 64**,** 479-494.

VIALARD, J., JAYAKUMAR, A., GNANASEELAN, C., LENGAIGNE, M., SENGUPTA, D. & GOSWAMI, B. N. 2012. Processes of 30-90 days sea surface temperature variability in the northern Indian Ocean during boreal summer. *Climate Dynamics,* 38**,** 1901-1916.

VINAYACHANDRAN, P. N., IIZUKA, S. & YAMAGATA, T. 2002. Indian Ocean dipole mode events in an ocean general circulation model. *Deep Sea Research Part II: Topical Studies in Oceanography,* 49**,** 1573-1596.

WAJSOWICZ, R. C. 2005. Forecasting extreme events in the tropical Indian Ocean sector climate. *Dynamics of Atmospheres and Oceans,* 39**,** 137-151.

WANG, B. 2006. *The Asian Monsoon*, Springer, ISBN 978-3-540-37722-1.

WEBSTER, P. J., MOORE, A. M., LOSCHNIGG, J. P. & LEBEN, R. R. 1999. Coupled ocean-atmosphere dynamics in the Indian Ocean during 1997-98. *Nature,* 401**,** 356-360.

WIGGERT, J. D., MURTUGUDDE, R. G. & CHRISTIAN, J. R. 2006. Annual ecosystem variability in the tropical Indian Ocean: Results of a coupled bio-physical ocean general circulation model. *Deep Sea Research Part II: Topical Studies in Oceanography,* 53**,** 644-676.

WIRTH, A., WILLEBRAND, J. & SCHOTT, F. 2002. Variability of the Great Whirl from observations and models. *Deep-Sea Research Part Ii-Topical Studies in Oceanography,* 49**,** 1279-1295.

WYRTKI, K. 1973. Equatorial Jet in Indian Ocean. *Science,* 181**,** 264-266.

YU, Y. Q., YU, R. C., ZHANG, X. H. & LIU, H. L. 2002. A flexible coupled ocean-atmosphere general circulation model. *Advances in Atmospheric Sciences,* 19**,** 169-190.

ZHOU, L. & MURTUGUDDE, R. 2010. Influences of Madden-Julian Oscillations on the eastern Indian Ocean and the maritime continent. *Dynamics of Atmospheres and Oceans,* 50**,** 257-274.

Appendices

Appendix A: Dataset Descriptions

VARIABLE	SIZE	DESCRIPTION	UNIT	RANGE
Lat	81x1	Latitude	Degrees north	[-15: 0.5: 25]
Lon	91x1	Longitude	Degrees east	[35: 0.5: 80]
Time	168x1	Decimal years	Years	[01, 1998: 30 days: 12, 2012]
SST	168x81x91	SST	Degree °C	[20: 0.5: 35]

Figure 92 SST Dataset (Source: (TMI))

VARIABLE	SIZE	DESCRIPTION	UNIT	RANGE
SSHA	208x161x181	SSHA	cm	[-40: 5: 40]
Lon	181x1	Longitude	Degrees east	[35: 0.5: 80]
Lat	161x1	Latitude	Degrees north	[-15: 0.25: 25]
Time	208x1	Decimal years	Years	[Nov, 1992 to Oct, 2010]

Figure 93 NWIO SSHA Monthly Dataset (Source: T/P+ Jason1)

VARIABLE	SIZE	DESCRIPTION	UNIT	RANGE
Time	214x1	Decimal years	Years	[07, 1997: 30 days: 12, 2010]
Lat	40x1	Latitude	Degrees north	[-15: 0.5: 25]
Lon	45x1	Longitude	Degrees east	[35: 0.5: 80]
SSTA	214x40x45	Temperature	Degree Celsius	[-3: -: 0.5:3]

Figure 94 Reynolds and Smith OIv.2 SSTA (Source: NOAA, (AVHRR))

Appendix B: Instructions for EOF/Rotated EOF Calculations Using IRICS Databases

Steps for SVD/EOF of Localised SST Time Series

- Select NOAA NCDC ERSST Dataset (Extended reconstructed global sea surface temperature) Link
- Select NOAA NCDC ERSST Version 1 (Improved extended reconstructed global SST Data).
- Choose the Sea Surface Temperature Data and Click the Filters link in the function Bar.
- Choose the Anomalies command then Click on the Data Selection link in the function bar.
- Enter the latitude (Y) and longitude (X) coordinates: Y=(15S, 25N) whilst X=(35E, 80E).
- Adjust the time (T) to reflect desired range: T=Jan 1997-Dec 2011 (Database Limited).
- Click the Expert Mode link at the top of the screen to enter the SVD code.
- Below the existing text, enter the following code sequence: (Y cosd) [XY] [T] svd and choose ok.
- This addition of the SVD code will reveal a broader range of datasets and variables as the normalised. eigenvalues, time series (PC) charts, and EOF structures are revealed.
- Capture the time series PC data by following the link to time series.
- Follow the structures link to reveal the EOF colour bar plots. Choose the chart, which reveals the colour bar data with the land in black.

Steps for Rotated EOF of SSTA Time Series

- Select a revised database representing empirical evidence from the NOAA NCEP EMC CMB GLOBAL sections with Reynolds (2002) data management applied Link
- Select the Reyn_SmithOIv2 link, which includes updated COADS datasets and accurate SST in-situ/satellite recorded datasets.
- Follow the Monthly link in the datasets and variables list and then choose the Sea Surface Temperature Anomaly Data option to reveal datasets recorded over the past 3 decades.
- Click on the Data Selection link in the function bar.

• Enter the latitude (Y) and longitude (X) coordinates: Y=(15S, 25N) whilst X=(35E, 80E)

• Adjust the time (T) to reflect desired range: T=Jan 1997-Dec 2011 (Database Limited).

• Click the Expert Mode link at the top of the screen to enter the SVD code.

• Below the existing text, enter the following code sequence: (Y cosd) [XY] [T] svd and choose ok.

• This addition of the SVD code will reveal a broader range of datasets and variables as the normalised eigenvalues, time series (PC) charts, and EOF structures are revealed.

• After reviewing the SVD/EOF datasets, input the code sequence '3 varimax' to force rotation of the EOF whilst maintaining accurate and realistic eigenvalues.

Steps for SSHA Database Access

• Follow the subsequent link to access the TOPEX NOAA SSHA assessment database. Link

Appendix C: SST, SSHA and Surface Wind Speed of May to September 2001 to 2009.

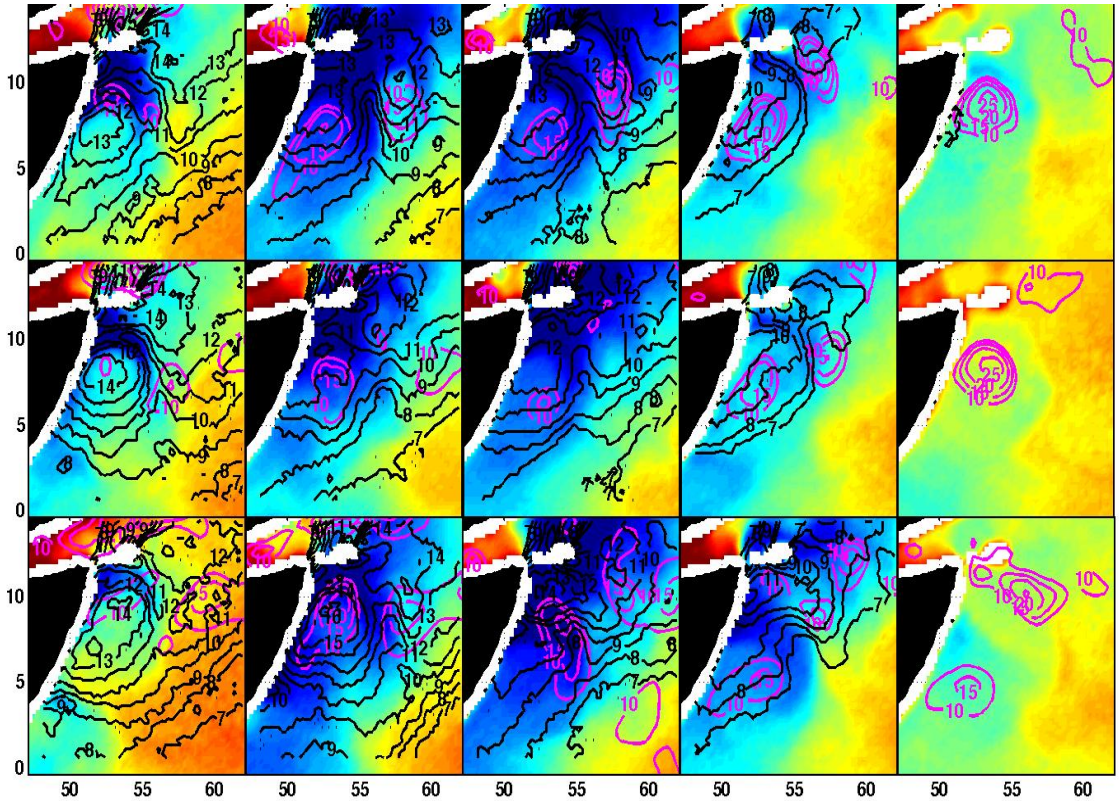

May to Sep 2001, 2002, 2003 of SSHA, SST & Wind Speed

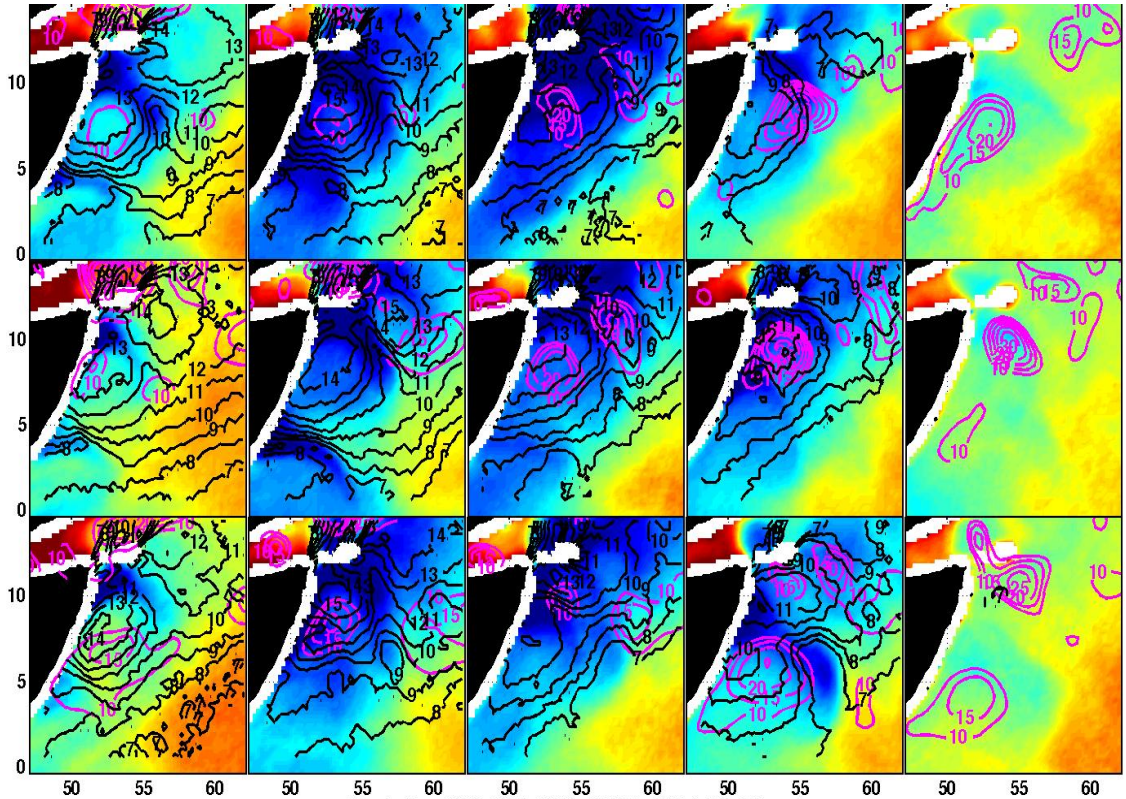

May to Sep 2004, 2005, 2006 of SSHA, SST & Wind Speed

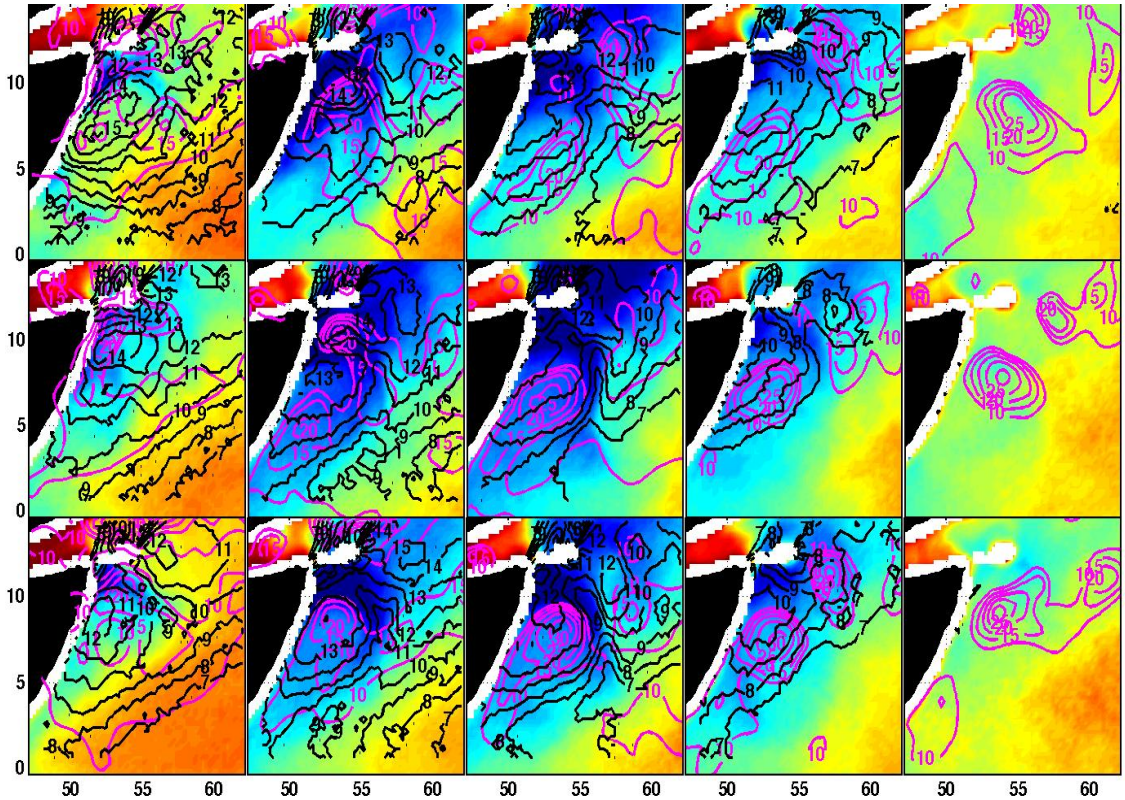

May to Sep 2007, 2008, 2009 of SSHA, SST & Wind Speed

Appendix D: Mean SSHA off the Somali coast area of 1995, 2000, 2005 and 2010.

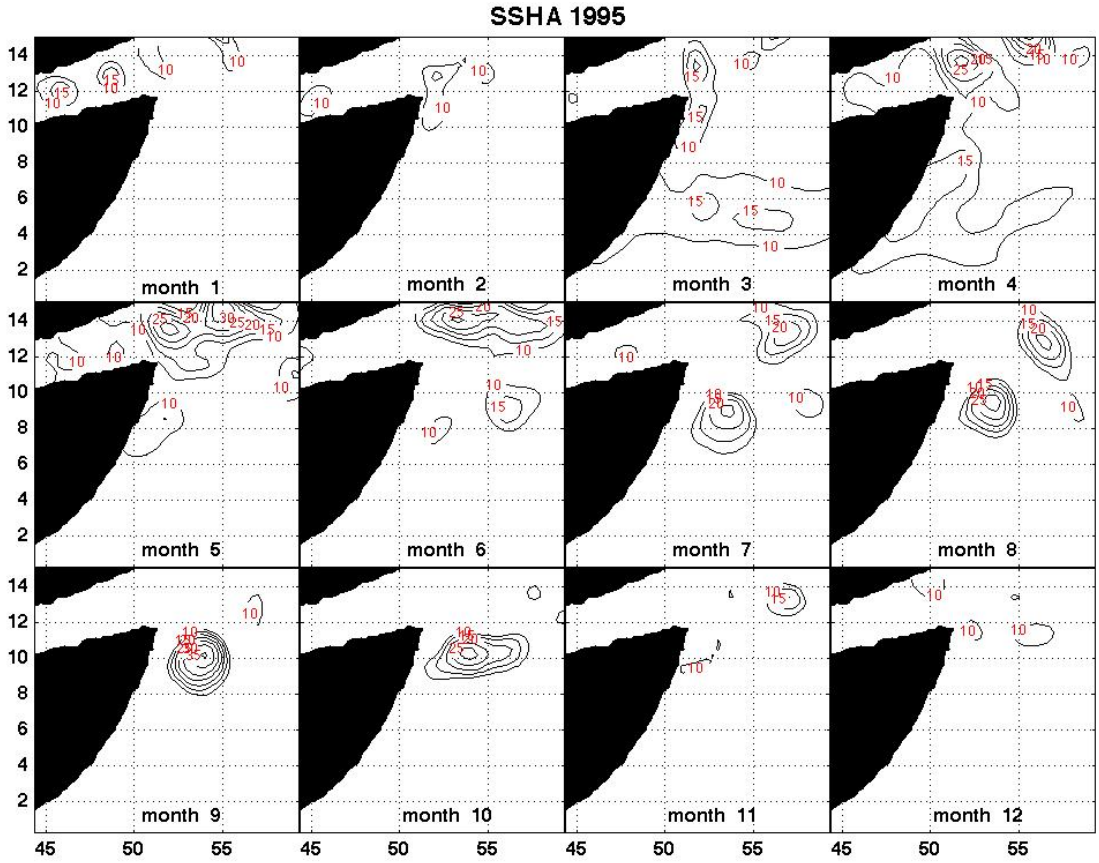

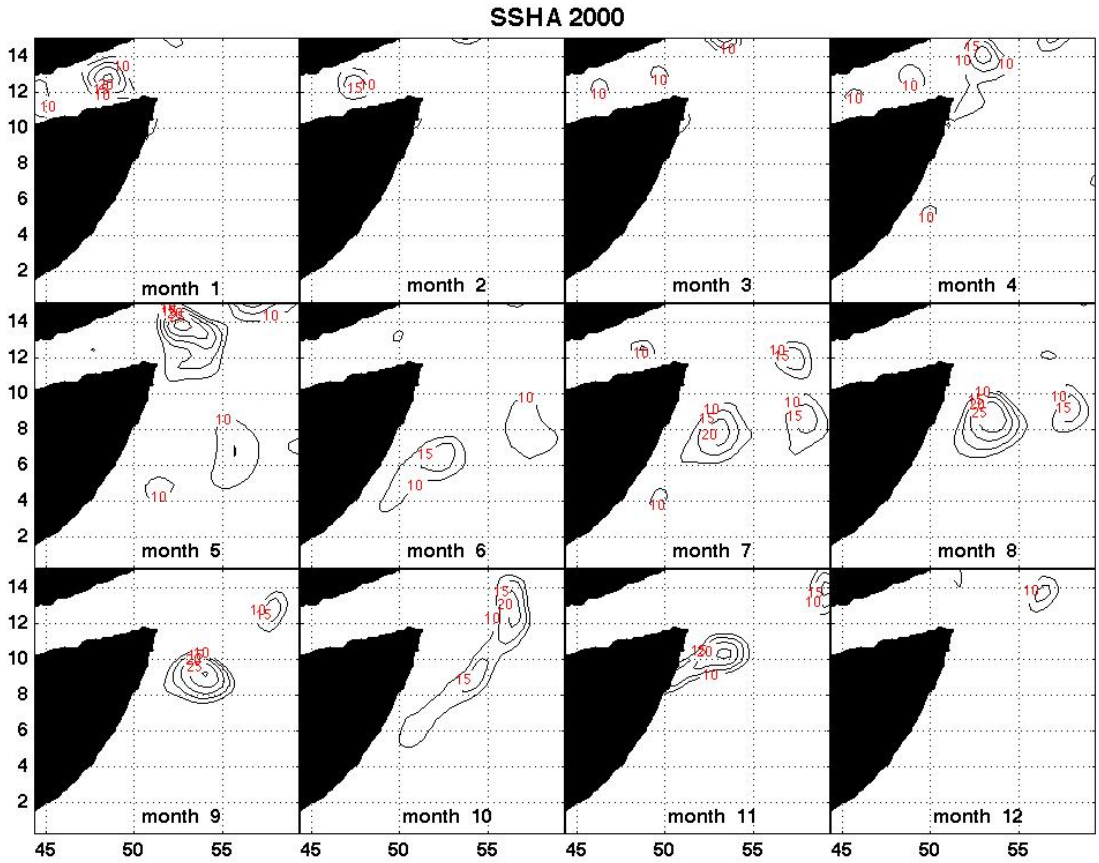

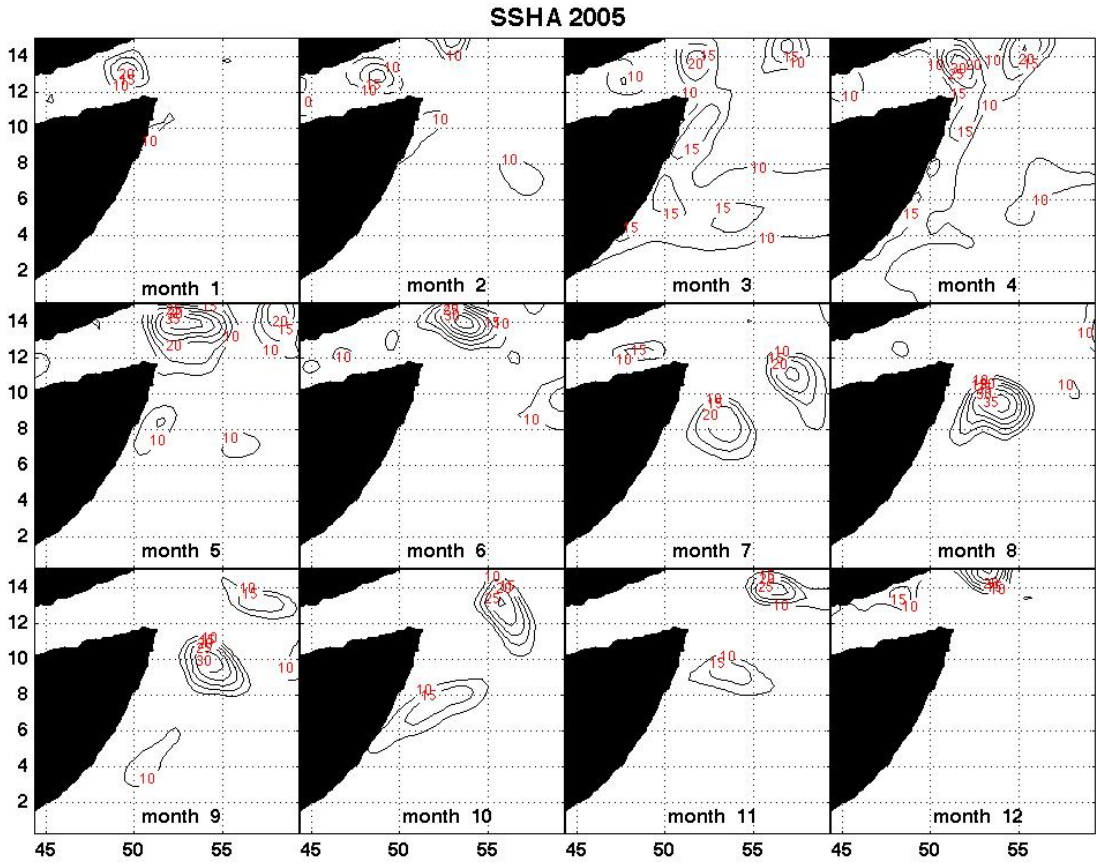
SSHA 2005
month 1
month 2
month 3
month 4
month 5
month 6
month 7
month 8
month 9
month 10
month 11
month 12

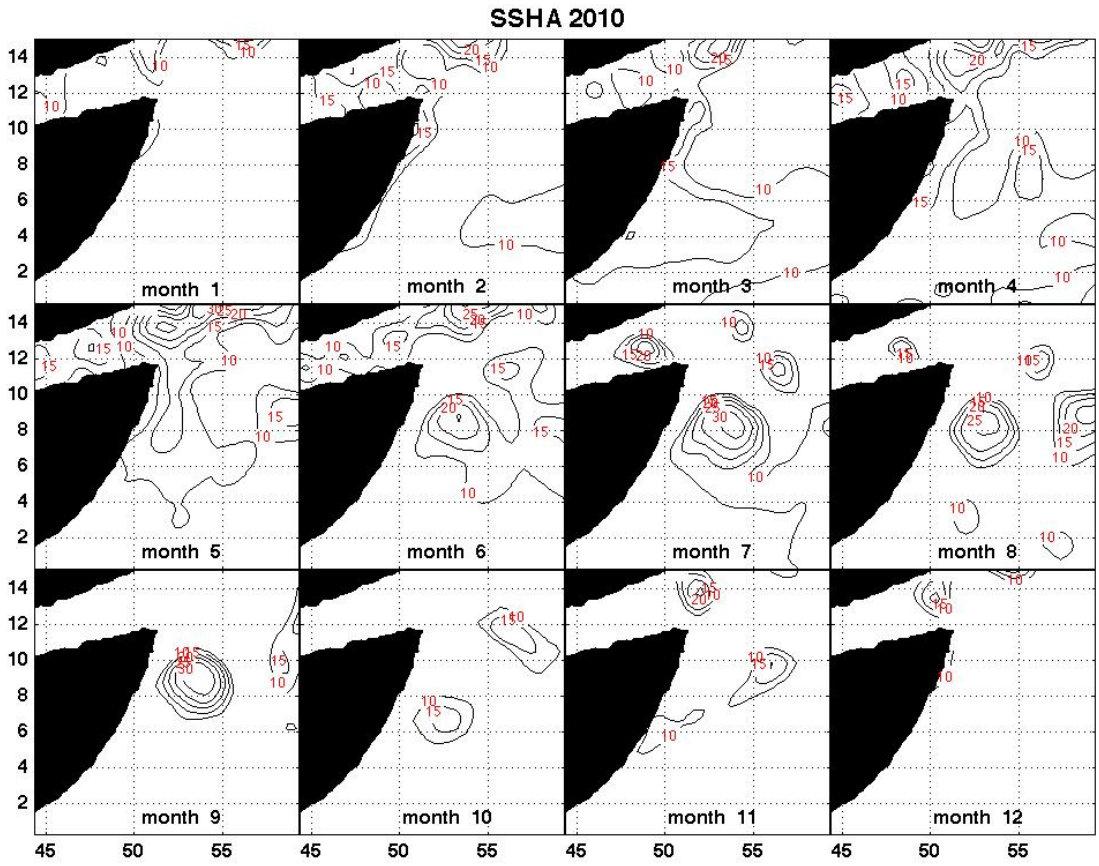
SSHA 2010
month 1
month 2
month 3
month 4
month 5
month 6
month 7
month 8
month 9
month 10
month 11
month 12

Appendix E: Matlab Routines.

EOF routine:

```
function  [EOF,tseries]=myeof(data,lon,lat,time)

% data=shiftdim(data,1);
tic
[nlats,nlons,ntimes] = size(data);
if nlats~=161
    disp('')
    disp('Just hold on, let me redimension the data')
    disp('')
    disp('before work!')
    data=shiftdim(data,1);
    [nlats,nlons,ntimes] = size(data);
end

% detrend across time
detdata=zeros(nlats,nlons,ntimes);
for i=1:ntimes
    detdata(:,:,i)=squeeze(data(:,:,i))-
squeeze(nanmean(data,3));
end

% set nans to zeros
detdata(isnan(detdata))=0;
% size(detdata)

% Reshape to 51120 x 146
D = reshape(detdata,[nlats*nlons ntimes]);
% size(D)
% ============ > C=D*D'; use for couple fields
% ------------------------
% Compute EOFs using SVD
% ------------------------
% timer = cputime;
[U,S,V] = svd(D,0); %svd(D,0);
% disp(['SVD took ' num2str(cputime-timer) ' cpu seconds'])

% Left singular vectors are the columns of U and are the EOF
loadings or
% mode patterns
 L = S*S';
 percent_variance = 100*diag(L)/trace(L);

 i = 3; % Waterfall plot of percentage variances
 percent_variance (1:i);
 figure (10)
 set(gcf,'pos',[582   108   292   225])
 plot(0:3,[0; cumsum(percent_variance(1:3))],'d--')
 title('Cumulative percent variance explained by EOF modes')

% Right singular vectors are the columns of V.
% Construct the amplitude time series from the product S*V'
```

```
then each
% row of A is the amplitude times series corresponding to
each column of U
A = S*V';

% plot the EOF patterns (a.k.a. loadings or mode structures)
 jj=[percent_variance(1) percent_variance(2)
percent_variance(3)];% percent_variance(4)
percent_variance(5)];
%  jj=ceil(jj);

EOF = reshape(U,nlats,nlons,ntimes);
for k=1:3
   figure(11)
   subplot(3,1,k)
   pcolor(lon,lat,squeeze(EOF(:,:,k)))
   shading interp;%colorbar
   %xbounds = xlim;

%set(gca,'XTick',xbounds(1):2:xbounds(2),'LineWidth',1,'font
weight','bold','fontsize',14);

%t1=['EOF  ' num2str(k),'  accounting for ' num2str(jj(k)) '
%   variance'];
fillmap
%fillmap ([.3 1 .4])
    title (['EOF  ' num2str(k),'  accounting for '
num2str(jj(k)) ' %   var
'],'fontweight','bold','fontsize',14)
     caxis ([-0.1 0.1])
     colorbar off

%set(gca,'Ytick','linewidth',3,'fontweight','bold','fontsize
',10);
end
    h = colorbar('location','southoutside','LineWidth',1);
    set(h, 'Position', [.11 .025 .8 .025])
    caxis ([-0.1 0.1])
     xh=xlabel('Longitude');
     yh=ylabel('Latitude');
     set(yh, 'position', get(yh,'position')-[0,-16,0]);
     set(xh, 'position', get(xh,'position')-[0,0,0]);
     set([xh,yh],'fontweight','bold','fontsize',14);

tseries=A(1:3,:);
% plot the EOF amplitude time series
for k=1:3
   figure(12)
   set(gcf,'pos',[   486    71   535   614])
   subplot(3,1,k)
   %plot(time,tseries(k,:),'LineWidth',4)% use plot or bar
   plot(time,tseries(k,:),'-
mo','LineWidth',1.5,'MarkerEdgeColor','k','MarkerFaceColor',
[.49 1 .63],'MarkerSize',3)
```

```
   xbounds = xlim;

set(gca,'XTick',xbounds(1):2:xbounds(2),'LineWidth',1,'fontw
eight','bold','fontsize',14);
   %set(gca,'xlim',[min(time) max(time)])
   grid on
   title(['PC '
int2str(k)],'fontweight','bold','fontsize',14)
   axis tight
end
xh=xlabel('Time');
     set(xh,'fontweight','bold','fontsize',14);

% anom=reshape(detdata,51120,37)';
% for i=1:3 % timeseries
% scores {i}=anom * V(:,i);
% end
%
% figure, plot (scores{1},'r')
```

Probability Density routine:

```
%figure(1); hist(msla_sc_06(1,:,:),50);
%title('Histogram of Somali Current SSHA');
%ylabel('Frequency');
%xlabel('SSHA (cm)');
%axis([-10 10 0 60]);

% Use [n,xout0=hist(?.) to obtain the frequency and bin
locations
%[n,xout]=hist(msla_sc_06(1,:,:),50);

% ---------------------------------------------------------
% Normalize the histogram so that the area of the histogram
equals
% one.  Use bar(xout,n) where n and xout are the vectors
found above.

%figure(2); bar(xout,n/sum(n));
%title('PDF of Somali Current SSHA');
%axis([-10 10 0 0.06]);
%ylabel('Probability Density');
%xlabel('SSHA (cm)');

%function  [julfig]=ssha_July_plot(data,lon,lat)
%julfig = data;

count = 1;
for kk=1
    figure(kk)
    %title('PDF of Somali Current SSHA');
    for k=1:20
        q=1992;
   subplot(5,4,k,'align');
```

```
   [n,xout]=hist(msla_sc_07(k,:,:),50);
   idx = xout < 0;
   bar(xout,n)
   hold on             %# Plot histogram in default color
   bar(xout(idx),n(idx),'facecolor', 'r')  %# Plot red bars
on top


    title(['July ',num2str(q+k)]);
    axis([-10 10 0 60]);
    %ylabel('Probability Density');
    %xlabel('SSHA (cm)');

     count=count+1;
    end
    %ylabel('Probability Density');
    %xlabel('SSHA (cm)');
end
```

Great Whirl SSHA boundary routine:

```
 count = 1;
for kk=1:2
    figure(kk)
    set(gcf,'pos',[   500    250   1000   750])
    ha = tight_subplot(3,4,[0.0 0.0],[0.04 0.04],[0.04
0.04]);
   for ii = 1:12; axes(ha(ii)); [c,h] =
contour(lon,lat,squeeze(msla_gw_4_9(count,:,:)),[10 15 20 25
30 35 40 ],'k');
               grid on,set(h, 'linewidth',1),axis
square;clabel(c,h,'FontSize',10,'Color','r','FontWeight','bo
ld','Rotation',0,'labelspacing',1000);fillmap;

           t1=title(['month  ' num2str(ii)]);
           set(t1, 'position', get(t1,'position')-[-
1,15,0],'fontweight','bold','fontsize',14);


set(ha(1:4),'XTickLabel','');set(ha(5:8),'XTickLabel','');

set(ha(2:4),'YTickLabel','');set(ha(6:8),'YTickLabel','');se
t(ha(10:12),'YTickLabel','');

set(ha(1:12),'ZTickLabel','','fontweight','bold','fontsize',
14);


     count=count+1;
   end

ax=axes('Units','Normal','fontweight','bold','fontsize',18,'
Position',[.0 .0 .99 0.95],'Visible','off');
set(get(ax,'Title'),'Visible','on')
```

```
title(['SSHA ' num2str( 1992 + kk )] );
if (nargout < 2)
return
end
h=get(ax,'Title');
end
```

Regression analysis routine:

```
function [r2 rmse] = rsquare(y,f,varargin)
% Compute coefficient of determination of data fit model and
RMSE
%
% [r2 rmse] = rsquare(y,f)
% [r2 rmse] = rsquare(y,f,c)
%
% RSQUARE computes the coefficient of determination (R-
square) value from
% actual data Y and model data F. The code uses a general
version of
% R-square, based on comparing the variability of the
estimation errors
% with the variability of the original values. RSQUARE also
outputs the
% root mean squared error (RMSE) for the user's convenience.
%
% Note: RSQUARE ignores comparisons involving NaN values.
%
% INPUTS
%   Y       : Actual data
%   F       : Model fit
%
% OPTION
%   C       : Constant term in model
%             R-square may be a questionable measure of fit
when no
%             constant term is included in the model.
%   [DEFAULT] TRUE : Use traditional R-square computation
%            FALSE : Uses alternate R-square computation for
model
%                    without constant term [R2 = 1 - NORM(Y-
F)/NORM(Y)]
%
% OUTPUT
%   R2      : Coefficient of determination
%   RMSE    : Root mean squared error
%
% EXAMPLE
%   x = 0:0.1:10;
%   y = 2.*x + 1 + randn(size(x));
%   p = polyfit(x,y,1);
%   f = polyval(p,x);
%   [r2 rmse] = rsquare(y,f);
%   figure; plot(x,y,'b-');
```

```
%   hold on; plot(x,f,'r-');
%   title(strcat(['R2 = ' num2str(r2) '; RMSE = '
num2str(rmse)]))
%
% Jered R Wells
% 11/17/11
% jered [dot] wells [at] duke [dot] edu
%
% v1.2 (02/14/2012)
%
% Thanks to John D'Errico for useful comments and insight
which has helped
% to improve this code. His code POLYFITN was consulted in
the inclusion of
% the C-option (REF. File ID: #34765).

if isempty(varargin); c = true;
elseif length(varargin)>1; error 'Too many input arguments';
elseif ~islogical(varargin{1}); error 'C must be logical
(TRUE||FALSE)'
else c = varargin{1};
end

% Compare inputs
if ~all(size(y)==size(f)); error 'Y and F must be the same
size'; end

% Check for NaN
tmp = ~or(isnan(y),isnan(f));
y = y(tmp);
f = f(tmp);

if c; r2 = max(0,1 - sum((y(:)-f(:)).^2)/sum((y(:)-
mean(y(:))).^2));
else r2 = 1 - sum((y(:)-f(:)).^2)/sum((y(:)).^2);
    if r2<0
    %
http://web.maths.unsw.edu.au/~adelle/Garvan/Assays/GoodnessO
fFit.html
        warning('Consider adding a constant term to your
model') %#ok<WNTAG>
        r2 = 0;
    end
end

rmse = sqrt(mean((y(:) - f(:)).^2));
```

Appendix F: De-seasoned SSHA/SSTA EOF patterns

T/P+Jason De-seasoned SSHA (Jan 1993 - Dec 2011)

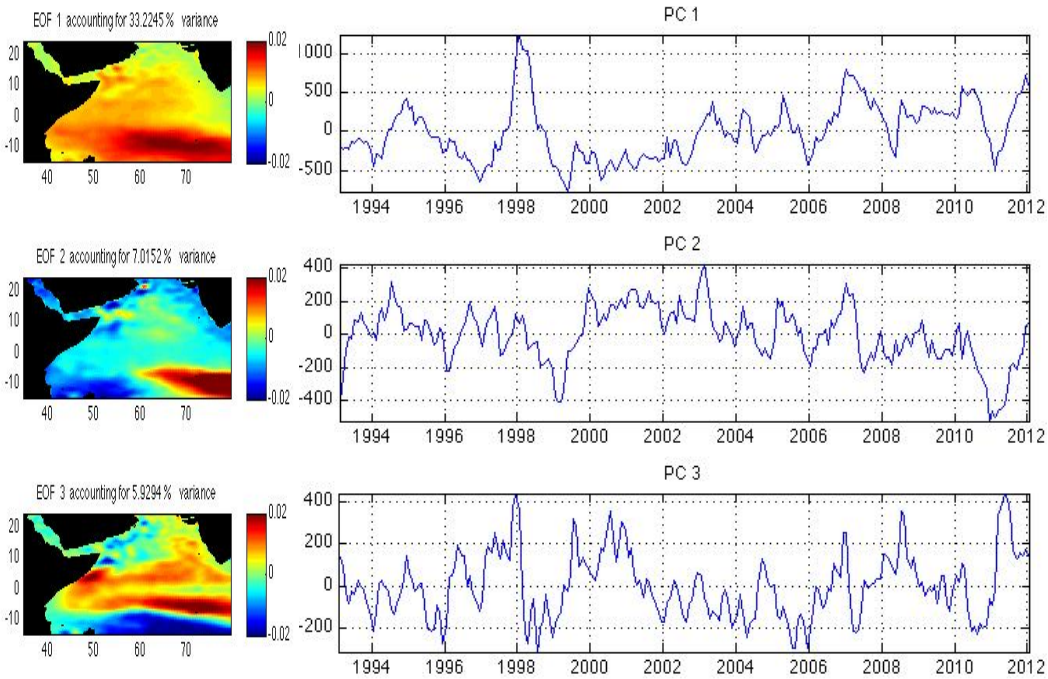

TMI De-seasoned SSTA (Jan 1998 - Dec 2011)